Structure and dynamics in polystyrene/single-walled carbon nanotube nanocomposites via neutron scattering techniques

BIRD, VICTORIA,JANE

How to cite:

BIRD, VICTORIA,JANE (2016) *Structure and dynamics in polystyrene/single-walled carbon nanotube nanocomposites via neutron scattering techniques*, Durham theses, Durham University. Available at Durham E-Theses Online: http://etheses.dur.ac.uk/11863/

Structure and dynamics in polystyrene/single-walled carbon nanotube nanocomposites *via* neutron scattering techniques

Vikki Bird

A thesis presented for the degree of

Doctor of Philosophy

Department of Chemistry

Durham University

May 2016

Abstract

Small angle and quasielastic neutron scattering (SANS and QENS) were used to investigate the cause of the minimum in the diffusion coefficient for polystyrene (PS)/single walled carbon nanotube (SWCNT) nancomposites (M. Mu, N. Clarke, R. J. Composto and K. I. Winey, *Macromolecules*, 2009, **42**, 7091–7097). Radius of gyration (R_g) values for PS/SWCNT nanocomposites were obtained by fitting SANS data with the Debye equation, and were found to increase by ~450% (110 kg mol^{-1}) and ~500% (230 kg mol^{-1}), indicating agglomeration or incomplete contrast-matching of the matrix and the nanotubes.

Elastic scans recorded *via* QENS on ring and chain-labelled samples indicated that the PS rings were more mobile in both the polymer and the nanocomposite, and that adding SWCNTs increased the mobility of the chain at SWCNT concentrations above 1 wt%, especially around the glass transition temperature (T_g). Slower motions of the ring also increased, but only at 4 wt% loading. The stiffness values for the chain and ring were isolated for the first time, indicating reduced chain stiffness on addition of increasing levels of SWCNTs.

QENS peaks were Fourier transformed and the decay curves fitted with the KWW function. Only the data recorded at 177 °C returned relaxation times that could be resolved, suggesting that the motions at lower temperatures are slower than could be detected.

T_g values were extracted calorimetrically and from neutron data. The calorimetric T_g had a minimum at ~1 wt%. The neutron T_g was recorded from data on two spectrometers, IRIS (2-200 ps) and HFBS (100 ps–10 ns); the ring data recorded on IRIS increased relative to the bulk on loading, while the chain data recorded on HFBS decreased, indicating that the chain and rings are affected by SWCNTs on different timescales.

The neutron static structure factor was affected at loading levels of 0.1–3 wt%, and the effect was more pronounced for the chain than the ring.

This work clearly indicates that adding nanoparticles influences the local structure and fast local dynamics of PS/SWCNTs, and while it does not identify the origin of the minimum in the diffusion coefficient, it does narrow the time window where the origin must lie.

Structure and dynamics in polystyrene/single-walled carbon nanotube nanocomposites *via* neutron scattering techniques

Vikki Bird

A thesis presented for the degree of Doctor of Philosophy

Department of Chemistry

Durham University

May 2016

Table of Contents

List of tables

List of figures

List of abbreviations

$\frac{R_g{}^2}{3}$	Debye function
$\langle a_{\mathrm{pp}}\rangle^{-2}$	tube diameter
$\langle u^2\rangle$	mean-squared displacement
$\frac{\mathrm{d}\Sigma}{\mathrm{d}\Omega}(Q)$	differential scattering cross-section normalised by a unit volume
$\frac{B}{1+CQ^2}$	single chain contribution
τ_{d}	tube diameter
τ_{KWW}	Kohlrausch–Williams–Watts decay constant
2D	two-dimensional
AFM	atomic force microscopy
a-PS	amorphous polystyrene
APTES	3-aminopropyltriethoxysilane
AQ^{-n}	small angle upturn
$B_{\mathrm{x,inc}}$	incoherent scattering cross-section
CNT	carbon nanotube
CVD	chemical vapour deposition
D	background
D	diffusion coefficient
d	wall-to-wall distance
D_0	bulk diffusion coefficient
d3 PS	chain-deuterated polystyrene
d5 PS	ring-deuterated polystyrene
DMF	dimethyl formamide
D_{min}	minimum value of the diffusion coefficient
dPS	deuterated polystyrene
EISF	elastic incoherent structure factor
FENE	finite extensible non-linear elastic

FWHM	full-width half-maximum
$g(\omega)$	density of states
GBP	Great British pound
$\hbar$	Planck's constant
h3 PS	chain-hydrogenated polystyrene
h5 PS	ring-hydrogenated polystyrene
h8 PS	fully-hydrogenated polystyrene
hPS	hydrogenated polystyrene
HWHM	half width at half maximum
$\mathrm{I}(\mathrm{Q})$	scattering intensity
$I(Q,t)$	intermediate decay function
$I(Q,\omega)$	intermediate scattering function
$I_{\mathrm{el}}(Q)$	elastic intensity as a function of neutron wavevector
INS	inelastic neutron scattering
k_{B}	Boltzmann's constant
KWW	Kohlrausch–Williams–Watts stretched exponential function
m	chiral integer (nanotube)
MC-RIS	Monte Carlo random isometric state
MD	molecular dynamics
MWCNTs	multi-walled carbon nanotubes
n	chiral integer (nanotube)
PDMS	poly(dimethyl siloxane)
PEO	poly(ethylene oxide)
PMMA	poly(methacrylate)
PS	polystyrene
Q	neutron/X-ray wavevector
QENS	quasielastic neutron scattering
R	size of the polymer chain
$R(Q,\omega)$	spectrometer resolution function

R_g	radius of gyration
R_{g0}	radius of gyration of bulk polymer
$\mathrm{R}_{\mathrm{MWCNT}}$	multi-walled carbon nanotube radius
R_{NP}	nanoparticle radius
$\mathrm{R}_{\mathrm{SWCNT}}$	single-walled carbon nanotube radius
$S(Q,\omega)$	incoherent structure factor
s.d.	standard deviation
SANS	small angle neutron scattering
SAXS	small-angle X-ray scattering
SC/PRISM	self-consistent polymer reference interaction site model
SSF	static structure factor
SWCNTs	single-walled carbon nanotubes
T	temperature
TEM	transmission electron microscopy
T_g	glass transition temperature
THF	tetrahydrofuran
T_m	melting temperature
T_{peak}	temperature of maximum weight loss
vol%	volume percent
WAXS	wide-angle X-ray scattering
WAXS	wide-angle X-ray scattering
Z_{kink}	number of entanglements per chain
α	fraction of immobilised chain segments
κ	effective local stiffness
λ	neutron wavelength
φ	volume fraction of polymer nanoparticles
φ_{crit}	critical volume fraction
β	stretching exponent
τ	relaxation time

ω	frequency
θ	scattering angle
η	viscosity

Statement of copyright

The copyright of this thesis rests with the author. No quotation from it should be published without the author's prior written consent and information derived from it should be acknowledged.

Acknowledgements

First, enormous thanks go to Professor Nigel Clarke at The University of Sheffield for supervising the first two years of this PhD, and to Dr Richard Thompson at Durham University for taking over when Nigel relocated. Your help has been invaluable.

Second, thank you to my collaborators at the University of Pennsylvania, Philadelphia, particularly Professor Karen Winey and Professor Russell Composto, for useful scientific discussion and warm hospitality.

Thirdly, thank you to everyone who helped with sample preparation, neutron experiments and sample characterisation, especially: Dr Serena Agostini and Dr Paul Brooks for introducing me to living anionic polymerisation (and being so excited when I finally managed to get the synthesis right); Dr Michelle Seitz for making me feel so welcome and being so helpful when I came over to prepare nanocomposite samples; Wei-Shao 'Walter' Tung for assistance with nanocomposite preparation; Dr Sangah Gam for running the AFM on my behalf; Dr Mike Weir for helping out with the neutron experiments when I couldn't be there, for running the SAXS on my samples, and for lots of very helpful discussions; Doug Carswell for running the DSC on my samples; Dr Madhusudan Tyagi for running the samples at HFBS; and Dr Isabelle Grillo for helping with the SANS experiments at ILL.

Special thanks go to Dr Victoria Garcia-Sakai at ISIS for direction and assistance with the neutron experiments, and a huge amount of guidance with the analysis. This thesis would have been pretty thin without your comments and suggestions.

Thank you to the EPSRC for funding me over the past seven years.

When I started this PhD, I did not anticipate it taking seven years, but sometimes life gets in the way. During that time I have been grateful for the academic and non-academic support of the assorted residents of MC105 and the Materials Chemistry building; you have all kept me going through this, so thank you. My Monday night knitters deserve a special mention, for always being there for me, and only occasionally reminding me that I ought to be working rather than knitting. As does Amy, whose friendship is the most valuable thing I have ever gained from an academic course; thank you for all the Wednesday lunches, and for never attempting to convince me to like tea. And my friends from way back, both Yeovil and Durham, and the friends I have met through my children, particularly Abi, Debra and Lesley; your ongoing friendship is always appreciated. I would also like to thank the Bird family for being so welcoming.

And finally, thank you to Mum and Dad, Adam, Sarah and Liz for all your love and support.

To David, Aidan and Jessica

and

Marc and Mary Chapman; I like to think you would have been proud

Chapter 1: Literature review

This thesis concerns the influence of carbon nanotube (CNT) fillers on the structure and dynamics of polystyrene (PS). In order to study the effect of the filler, it is first necessary to review the properties of both the nanotubes in the absence of a supporting matrix, and the matrix in the absence of filler. First a background on carbon nanotubes and their scientific interest is presented, including a discussion of their effect on polymer matrices. Second, the polymer chain conformation in polymer nanocomposites is reviewed. Third, the dynamics of polystyrene, both in the bulk and as thin films is considered; followed by a review of the literature concerning the dynamics in polymer nanocomposites.

1.1 Carbon nanotube nanocomposites

1.1.1 Carbon nanotubes

Carbon nanotubes (CNTs) were first identified in 1991 by Iijima,[1] and consist of rolled up sheets of carbon atoms end-capped with hemispherical carbon shells (hemifullerenes). There are two basic types of carbon nanotube: (i) single-walled carbon nanotubes (SWCNTs), which consist of a single graphene sheet rolled into a seamless cylinder, and (ii) multi-walled carbon nanotubes (MWCNTs), which are made up of nested cylinders of graphene with interlayer separations of 0.34 nm, which corresponds to the inter-plane spacing in graphite. The properties of carbon nanotubes are dependent upon their morphology, size and diameter, and CNTs can be metallic or semi-conducting.

1.1.1.1 Synthesis

Carbon nanotubes can be synthesised by a variety of methods, including arc discharge, laser ablation and chemical vapour deposition.[2, 3]

1.1.1.1.1 Arc discharge

Arc discharge was the method used by Iijima in the first synthesis of carbon nanotubes, which were MWCNTs.[1] In this method, the CNTs are formed *via* hot plasma discharge between two graphitic electrodes connected to a power supply in the presence of gaseous helium. Gaseous carbon is formed by evaporation of the solid carbon, which then condenses to form nanotubes.

1.1.1.1.2 Laser ablation

In 1995, Guo *et al*. used this method to create the first reported SWCNTs.[4] For laser ablation, a carbon source is doped with small amounts of a mixed metallic catalyst (0.6 at% each of Co and Ni) for nucleating CNT growth, then the doped carbon is vaporised using a pulsed laser beam at very high temperatures and pressures in the presence of an inert gas. The nanotubes condense away from the laser, in regions that are comparatively cool. This method of nanotube production is very energy intensive, and thus expensive.

1.1.1.1.3 Chemical vapour deposition

For chemical vapour deposition (CVD), a catalyst is used to decompose a gaseous carbon source (*e.g.* a hydrocarbon or carbon monoxide), and the nanotubes grow on a metallic substrate. While this method requires high temperatures (500–1000 °C), it is conducted at atmospheric pressure, making it commercially viable for the production of large volumes of CNTs. Plasma-enhanced CVD, first used by Ren *et al*. in 1998 uses a direct current plasma to align the nanotubes,[5] and this variant of CVD is used to produce CNT-based flat panel displays and solar cells.

1.1.1.2 Properties

Carbon nanotubes have been shown to have unique properties, including excellent mechanical, electrical, thermal and optical properties.[2, 3, 6, 7] This combination of properties is not seen in any other individual material, except graphene.

1.1.1.2.1 Mechanical properties

Carbon nanotubes exhibit high stiffness, high moduli, and excellent tensile strength. Yu *et al*. reported stress–strain values for individual MWCNTs of 0.27–0.95 TPa, fracture of MWCNTs at strains up to 12%, and strengths of 11–63 GPa, corresponding to nanotube toughness values of ~1200 J g^{-1}. The nanotubes were found to fracture *via* a sword and sheath failure mechanism, with the outer layer of the nanotube fracturing and the inner layers telescoping out.[8]

It has proven difficult to obtain the mechanical properties of individual single walled carbon nanotubes,[9] as it is difficult to isolate them, but good results have been achieved for small bundles of SWCNTs: Salvetat *et al*. described tensile modulus values of 1 TPa for small bundles of SWCNTs *via* bending methods in an atomic force microscope.[10] The properties of larger bundles were poorer owing to slippage between the nanotubes. Yu *et al.* determined SWCNT moduli of 0.32–1.47 TPa, strength values of 10–52 GPa, and failure strains of 5.3%, giving toughness values of ~770 J g^{-1}.[8] The bundles were found to fail at their perimeters.

1.1.1.2.2 Electrical properties

The arrangement of atoms in an individual nanotube can be described by the chiral vector (n, m), where n and m are integers of the vector equation $R = na_1 + ma_2$. Carbon nanotubes may be metallic or semi-conducting, and their conductivity is determined by the values of n and m. A SWCNT is metallic when $n - m$ is divisible by three, otherwise, it is semiconducting.[11] Ebbensen *et al*. measured the conductivity of individual nanotubes, reporting values of 10^7–10^8 S m^{-1},[12] but also reported that the conductivity varied widely from nanotube to nanotube. The electrical properties of carbon nanotubes are affected by defects in the CNTs, with defects leading to a large increase in electrical resistance.[13]

1.1.1.2.3 Thermal properties

Individual carbon nanotubes display excellent thermal conductivity, achieving values (6000 W m^{-1} K^{-1}) comparable to diamond or a monolayer of graphene,[14] and significantly higher than copper, which has thermal conductivity of ~400 W m^{-1} K^{-1} at room temperature,[15] and is widely used for its good thermal conductivity, *e.g.* in saucepans.

1.1.2 Nanocomposites

Polymer nanocomposites are polymer matrices containing fillers that have at least one dimension of less than 100 nm. A wide variety of fillers, including nanoclays, nano-oxides, carbon nanotubes, metallic particles and silsesquioxanes can be used. The nanoscale dimensions of the particles in nanocomposites result in a high specific surface area, leading to increased physical interactions and physico-chemical and chemical interfaces, which can in turn lead to enhanced electrical, optical, mechanical, thermal and barrier properties at much lower loading levels than can be achieved with conventional fillers.[16, 17]

1.1.3 Carbon nanotube nanocomposites

The first carbon nanotube polymer nanocomposites were produced by Ajayan *et al.* in 1994.[18] Since then CNT polymer nanocomposites have been widely researched, with new papers being published on them every day. Carbon nanotube polymer nanocomposites are of interest because they can exhibit large enhancements in the mechanical, electrical, thermal properties relative to the base matrix, conventional composites containing microscale fillers and other nano-filled composites.[2, 3] Carbon nanotube polymer nanocomposites have been used in the automotive, microelectronics, aeronautic and aerospace sectors.[19]

1.1.3.1 Synthesis

Unfortunately the surface properties of CNTs cause them to agglomerate, forming bundles of 10–100 nm in diameter,[20] making them difficult to disperse in polymer matrices. As composites in which the nanotubes are well dispersed tend to display greater improvements in properties than those in which the nanoparticles are poorly dispersed, the key aim when preparing CNT–polymer nanocomposites is to ensure that the CNTs are as well dispersed as possible.[2] In addition, the aspect ratio of the CNTs should not be detrimentally affected by the preparation process, as aspect ratio is one of the key properties of CNTs. For certain properties of CNT–polymer composites, *e.g.* load transfer, it is also necessary for good interfacial bonding to be achieved between the polymer matrix and the CNTs.

There are three major categories of CNT–polymer nanocomposite production: melt processing, solution blending and *in situ* polymerisation,[2, 20] each of which are covered in the following section.

1.1.3.1.1 Pre-processing

The methods currently used for the preparation of CNTs tend to mean that a sample of CNTs will contain other species, so pre-processing is required to eliminate these contaminants.[20] This pre-processing usually consists of up to three steps: (i) purification, (ii) de-agglomeration, and (iii) chemical functionalisation.

The intention of the purification steps is to remove any amorphous carbon, fullerenes, non-crystalline graphitic species and catalyst residue from the CNTs. In general, this is done by thermally annealing the CNTs in air or oxygen, which selectively etches the amorphous carbon, then washing the CNTs in acid to eliminate the catalyst residues. Alternatively mechanical techniques, *e.g.* centrifugal separation, size exclusion chromatography and microfiltration, may be used. Unfortunately all current methods tend to reduce the amount of material by ~50%, so more efficient methods (of CNT production and purification) must be developed in order for CNTs to be considered for routine industrial application; at present carbon nanotubes cost of the order of hundreds of pounds (GBP) per gram, with SWCNTs costing significantly more than MWCNTs.[21]

A wide variety of methods are available for the de-agglomeration of CNTs, including ultrasonication, electrostatic plasma treatment, polymer wrapping (where a polymer is wrapped round a CNT *via* non-covalent association, in a way that does not affect the structure of the individual nanotube)[22, 23] and electric field manipulation. Of these, sonication is the most widely used, but it has been shown that this can reduce the aspect ratio of the CNTs.[24-26]

Chemical functionalisation is a common technique that can be used to improve the interactions between the CNTs and the polymer matrix, leading to improved processability and property enhancement. In addition, through surface functionalisation, the nanotubes can be covalently bonded to the polymer matrix, which further improves the interaction at the polymer–CNT interface.[27-29]

1.1.3.1.2 Melt processing

Melt processing methods of preparing CNT–polymer nanocomposites are commonly used for industrial-scale nanocomposite preparation as they make use of conventional industrial techniques, *e.g.* extrusion, internal mixing, and injection and blow moulding, to incorporate the CNTs into the polymer matrix.[20] Melt processing methods rely on the high temperatures and shear forces inherent in these techniques to disperse the CNTs in the polymer matrix, but they are still less effective than solution blending at dispersing the CNTs, and are limited to low nanoparticle concentrations due to the viscosity increasing rapidly as the CNT concentration is increased.[2, 20]

Melt processing methods do, however, have some advantages. As no solvent is required for these methods the final composite is purer and the risk of introducing contaminants is reduced; in addition, if elongational flow is part of the processing technique, the CNTs are aligned during processing, which can lead to improved properties.[20]

1.1.3.1.3 Solution blending

Solution blending classically involves three key steps: (i) the CNTs are dispersed in a solvent; (ii) the CNT–solvent dispersion is mixed with a polymer solution; (iii) the composite is recovered *via* either precipitation or film casting. Solution blending is the most commonly used method of CNT–polymer nanocomposite preparation in the academic literature, partly because the presence of solvent significantly lowers the viscosity of the solution compared to melt blending, but also because it is possible to produce small samples, which is ideal for most laboratory techniques.[2] However, the presence of solvent also has disadvantages: unless they are chemically modified, CNTs are insoluble in all solvents, so ultrasonication is necessary to produce a metastable solution of CNTs, but, as mentioned previously, this can reduce the aspect ratio of the CNTs, particularly if long periods of sonication are required. In addition, during solvent evaporation, the CNTs have a tendency to agglomerate, however, this can be reduced by using spin-casting (where a droplet of CNT–polymer–solvent mixture is spun at high speeds to rapidly remove the solvent) or drop-casting (where the CNT–polymer–solvent mixture is dropped onto a heated substrate causing the solvent to evaporate rapidly).

For the work presented in this thesis on CNT–polystyrene (PS) nanocomposites, the coagulation method was used. This method was first demonstrated by Du *et al*.[30] in 2003 and is a variation on the solution blending methodology. Du *et al*. used poly(methyl methacrylate) (PMMA) due to its good spinning properties, and its high solubility in dimethyl formamide [DMF, a solvent which disperses single-walled CNTs (SWCNTs) well] and single-walled CNTs, but the method has also been shown to work well for SWCNT–PS nanocomposites.[24] The method involves 5 key steps: (i) purification of the SWCNTs; (ii) dispersion of the SWCNTs in DMF; (iii) dissolution of polymer into the DMF–SWCNT suspension; (iv) coagulation into water; (v) drying the final composite.

1.1.3.1.4 *In situ* polymerisation

In situ polymerisation occurs *via* a two-step process. First, the CNTs are dispersed in the monomer, then the monomers are polymerised. This method leads to improved dispersion of the nanotubes in the polymer matrix, especially when combined with chemically-functionalised CNTs—the functionalisation improves the dispersion in the monomers and thus in the final polymer. In addition, chemical-functionalisation can lead to covalent bonding between the CNTs and the matrix, providing reinforcement on a molecular level. This method was not used for the production of the nanocomposites in this thesis as the analysis of neutron scattering data is simplified if the polymer has very low polydispersity;[31] in order to achieve a polymer with a low polydispersity, living anionic polymerisation was used, a method which requires the elimination of all impurities or the reaction fails.[32] It is not possible to make the nanotubes sufficiently pure to be incorporated during a living anionic polymerisation reaction.

1.1.3.1.5 Other methods

There are several other methods which may be used for incorporating CNTs into polymer matrices. Solid-state mechanical pulverisation (*e.g.* pan milling and twin-screw pulverisation) essentially involves grinding the polymer and nanotubes together. This method can result in the nanotubes becoming grafted to the polymer, leading to good dispersion, improved interfacial adhesion, and improved tensile modulus.[33, 34]

In the latex fabrication method, CNTs are dispersed in water, then a suspension of latex nanoparticles is added, followed by freeze-drying and processing. This method is good for using with highly viscous polymer matrices as a good level of dispersion is produced without having to worry about viscosity issues.[35-37]

1.1.3.2 Properties

1.1.3.2.1 Mechanical properties

The excellent mechanical properties of carbon nanotubes (*i.e.* high Young's modulus, high tensile strength, high aspect ratio, low density, *etc.*) make them ideal candidates as reinforcement materials for polymer matrices. In addition, their low density, high aspect ratio and large surface area mean that only low loading levels are required to see some improvement in mechanical properties. Nanotubes also have the advantage of offering multifunctionality, *e.g.* reinforcement plus electrical conductivity.[2, 3, 38]

The tensile modulus and strength of CNT composites have been seen to increase with nanotube loading, with the CNT dispersion, aspect ratio, length and alignment all affecting the resulting material properties.[9] Homogeneous dispersion and alignment of the CNTs prevents agglomeration and gives better load transfer between the filler and the matrix, leading to a greater improvement in mechanical properties. The level of improvement is not as great as theoretical predictions suggest could be achieved; this arises from imperfect dispersion and poor load transfer. Even low levels of agglomeration increase the diameter and length distributions of the CNTs, leading to a decrease in aspect ratio and a reduction in the filler modulus.

In order to be used for mechanical reinforcement, a good interface between the nanotube and the polymer is required in order to facilitate load transfer. This requires aggregation to be minimised to prevent slippage between the individual nanotubes. Chemically modifying the surface of the CNTs can lead to improved compatibility between the CNT and the matrix, with a

0.3% grafting density between carbon nanotubes and a polyethylene matrix (6 crosslinks with two methylene units each) resulting in an increase in the shear strength of the nanocomposite of over an order of magnitude.[39] Covalent bonding at the CNT/polymer interface can be very effective in improving compatibility and strengthening the material.

Schadler *et al*.[40] and Ajayan *et al*.[41] found that slippage occurred between the shells of MWCNTs, and within SWCNT ropes (bundled nanotubes), limiting stress transfer in CNT/polymer nanocomposites. Nucleation of cracks occurs at low CNT density regions in the nanocomposite, then cracks propagate along weak CNT/polymer interfaces.[42]

One disadvantage of adding CNTs to a polymer matrix to increase tensile strength and modulus, is that this can be coupled with reduced strain at break, indicating a reduction in polymer toughness and flexibility. Also after a critical CNT loading level, the matrix mechanical properties can decrease with increasing loading, sometimes to levels below those of the neat matrix as the nanocomposite becomes more powder-like at high filler concentrations.[43-46]

1.1.3.2.2 Electrical properties

Individual carbon nanotubes conduct electricity, and a CNT-polymer nanocomposite becomes electrically conducting when the filler content exceeds a critical value, the percolation threshold.[2, 3] At this concentration, the nanotubes form a continuous three-dimensional network within the matrix, leading to a conductive path through the material. The CNT loading levels required to create an electrically conductive nanocomposite depend on the aspect ratio, dispersion and alignment of the fillers, but typically less than a few vol% of CNTs is required because of the large aspect ratio and excellent electrical conductivity of the CNTs. As only small levels of CNTs are needed to induce conductivity, nanocomposites can retain the optical clarity, mechanical properties and low viscosity of the matrix. Electrically conducting nanocomposites are used in electrically conducting adhesives, antistatic coatings and films and electromagnetic interference shielding materials for electronic devices, *etc*.

Nanotubes conduct through their extended π-network, and well-dispersed nanotubes can induce conductivity in an insulating polymer matrix. While chemical functionalisation can improve the dispersibility of carbon nanotubes in the polymer matrix, a factor that should reduce the percolation threshold, chemical functionalisation can increase the electrical percolation threshold of CNT-polymer nanocomposites as the extended π-network is disrupted.

1.1.3.2.3 Thermal properties

The thermal conductivity of a material is dominated by atomic vibrations (phonons), and nanocomposites with good thermal conductivity are of use in printed circuit boards, heat sinks and other high-performance thermal management systems. Adding nanotubes to a polymer matrix can lead to modest increases in thermal conductivity, with matrices generally exhibiting 2.5-fold increases in thermal conductivity relative to the pure matrix at loading levels of 7–9 vol%,[47, 48] although these increases are not to the same extent as the improvements seen in electrical conductivity.[2] This lack of enhancement in thermal conductivity is primarily due to the large interfacial thermal resistance between the polymer and the nanotubes, which hinders the phonon transfer that dominates heat conduction in polymer/CNT nanocomposites.[49]

CNT-containing nanocomposites have shown increased thermal stability, with higher decomposition temperatures and temperatures of maximum weight loss rate (T_{peak}). This may be due to the dispersed nanotubes hindering the flux of degradation product, thereby delaying the onset of degradation, or the polymer near the nanotubes degrading more slowly, thus shifting T_{peak} to higher temperatures. These improvements in thermal stability properties open the possibility of using CNT polymer nanocomposites for flame retardency.

1.2 Polymer chain conformation in polymer nanocomposites

While the conformation of polystyrene chains in the bulk has been thoroughly characterised using neutron scattering techniques,[50] the influence of nanofillers on polymer chain conformation is still not fully understood. The vast majority of the work conducted on chain conformations in filled polymer nanocomposites has been for systems where the filler is spherical, and the majority of those studies are simulation based, rather than experimental; these studies will be covered first in this section. Recently, some work, both computational and experimental, has been published on nanocomposites containing cylindrical fillers. These works have particular relevance to CNT-filled polymers and will be examined in some detail at the end of this section.

1.2.1 Measuring the size of a polymer chain

The physical size of a polymer chain can be defined in several ways, and will depend on the molecular weight (*i.e.* the length of the polymer chains) and the morphology (*i.e.* the shape adopted by the polymer) of the polymer. The two measures of polymer size used in this thesis are the polymer radius of gyration and the mean squared end to end distance.

1.2.1.1 Polymer radius of gyration

The square radius of gyration (${R_{\mathrm{g}}}^2$) is the average square distance between monomers in a given conformation and the polymer's centre of mass,[51] given by Equation 1.

$${R_{\mathrm{g}}}^2 = \frac{1}{N}\sum_{i=1}^{N}(\boldsymbol{R}_i - \boldsymbol{R}_{\mathrm{cm}})^2$$

Equation 1

where N is the degree of polymerisation, $\boldsymbol{R}_i$ is the position vector of the ith monomer, and $\boldsymbol{R}_{\mathrm{cm}}$ is the position vector of the centre of mass of the polymer, defined by the number average of all the monomer position vectors (Equation 2).

$$\boldsymbol{R}_{\mathrm{cm}} \equiv \frac{1}{N}\sum_{j=1}^{N} \boldsymbol{R}_j$$

Equation 2

where $\boldsymbol{R}_j$ is the position vector of the jth monomer.

1.2.1.2 The mean squared end to end distance

The end-to-end vector, $\boldsymbol{R}$, measuring the distance between the ends of a polymer chain can also be used to indicate the size of a polymer coil.[52] If a polymer chain is made up of N bonds, with $\boldsymbol{r}_n$ the vector of the nth bond, then $\boldsymbol{R}$ can be found using Equation 3:

$$\boldsymbol{R} = \sum_{n=1}^{N} \boldsymbol{r}_n$$

Equation 3

As there is an equal probability of the end to end vector being equal to $\boldsymbol{R}$ or $-\boldsymbol{R}$, the average value of $\boldsymbol{R}$ within a polymer matrix is zero, therefore, the average of the square of $\boldsymbol{R}$, the mean squared end to end distance $\langle R^2 \rangle$ (Equation 4), is used to measure the size of the polymer instead:

$$\langle R^2 \rangle = \sum_{n=1}^{N} \langle {\boldsymbol{r}_n}^2 \rangle = Nl^2$$

Equation 4

where l is the bond length.

The mean squared end to end distance is related to the radius of gyration *via* Equation 5.

$$\langle {R_{\mathrm{g}}}^2 \rangle = \frac{Nl^2}{6} = \frac{\langle R^2 \rangle}{6}$$

Equation 5

1.2.2 Systems containing spherical nanoparticles

For systems containing spherical nanofillers, the work falls into three categories: (i) systems where the radius of gyration of the bulk polymer (R_{g0}) is smaller than the radius of the nanoparticle (R_{NP}), *i.e.* $R_{\mathrm{NP}} > R_{\mathrm{g0}}$; (ii) systems where R_{g0} is of similar size to R_{NP}, *i.e.* $R_{\mathrm{NP}} \approx R_{\mathrm{g0}}$; and (iii) systems where nanoparticles are smaller than R_{g0}, *i.e.* $R_{\mathrm{NP}} > R_{\mathrm{g0}}$.

1.2.2.1 Large nanoparticles: $R_{NP} > R_{g0}$

For systems where the nanoparticle size is greater than the chain conformation, three different system behaviours have been reported: (i) polymer R_g is unchanged on addition of nanoparticles;[53, 54] (ii) polymer R_g decreases when nanoparticles are added;[55-58] and (iii) the polymer radius of gyration reaches a maximum value before decreasing to levels higher than the bulk R_g.[57]

1.2.2.1.1 Systems where R_g is unperturbed

Two experimental studies have reported that adding spherical nanoparticles to a polymer has no influence on the chain conformation relative to that of the bulk polymer, irrespective of filler concentration.[53, 54] Both works used small angle neutron scattering to extract the dimensions of single chains within the system.

Sen *et al*.[53] studied a system of polystyrene with spherical silica nanoparticles; the paper displays transmission electron microscopy images of the samples, and for all samples containing more than 2.9 vol% nanoparticles, the dispersion is poor, with the particles existing in clusters surrounded by ‘voids’. This situation is worse at higher nanoparticle concentrations, with only very few lone nanoparticles, and the cluster size is very large. It was also noted that in the low-*Q* region, corresponding to larger length scales, the small angle neutron scattering intensity increases dramatically with increasing silica content, especially at concentrations below 10 vol%, indicating that the matrix is not properly contrast-matched, so scattering from the filler particles is being counted alongside the scattering from the single deuterated chains in the matrix. Both these factors call into question the conclusions drawn from this paper.

Nusser *et al*.[54] examined a nanocomposite with an apolar polymer component, poly(ethylene-*alt*-propylene), and a hydrophobically-modified silica nanofiller component as a model system for a nanocomposite with repulsive interactions. The nanoparticles used in this system have a core–shell structure, and Nusser *et al*. found that the hydrophobic surface layer on the nanofiller particles scattered strongly, independent of incorporation into the nanocomposite system, and contributed significantly to the nanocomposite scattering signal, even with the best possible contrast-matching, owing to the core and the shell having different scattering length densities. This additional scattering makes it hard to say whether the lack of change in chain conformation on addition of nanoparticles is real, or is in fact caused additional scattering masking a different effect.

1.2.2.1.2 Systems where R_g decreases

The majority of the works conducted on systems where the nanoparticles are larger than the polymer chains indicate that the polymer radius of gyration decreases on addition of a nanofiller;

all studies on this regime that come to this conclusion are based on computational simulations.[55-58]

In 2001, Vacatello[55] conducted Monte Carlo simulations on a dense polymer melt containing solid nanoparticles that were 10 and 16 times the size of the transverse diameter of the polymer chains. Vacatello followed this in 2002 with a second series of MC simulations, this time on a polymer system containing randomly-arranged spherical particles that were 8 times the transverse diameter of the polymer chains at filler levels of 10–50%.[56] Both works indicate that the chain dimensions were always slightly smaller for the filled matrices than for those that were unfilled, an effect that was seen both globally and locally, with chain segments of between 10 and 20 units in length in the filled matrix also being shorter than those in the unfilled matrix.

Vacatello's work showed that at the polymer/filler interface the polymer chains arranged themselves in densely-packed and ordered shells of polymer units, and the size of these shells was almost twice the diameter of the unit size. The polymer chains in these systems assembled themselves into a series of interface segments (chain segments totally running in the interface shell of a given particle), bridge segments (sequences of non-interface units with the two adjoining units in the interface shells of two different particles) and loop segments (sequences starting and ending in the interface shell of the same particle). It was found that the polymer chains visit the interface shell of several filler particles, and that each particle is in contact with many different particles. This results in the filler particles behaving as highly functional physical cross-links. The average number of different chains visiting an individual particle decreases with increasing particle volume fraction, an effect that is more pronounced at higher filler volume fractions.

Sharaf and Mark[57] published Monte Carlo random isometric state (MC-RIS) simulations on amorphous polyethylene containing spherical filler particles arranged on a cubic lattice. Their study measured the influence of the volume excluded by the rigid nanoparticles and the distribution of the filler particles, but did not take into account filler–matrix and matrix–filler interactions. This work[57] showed that the root mean squared end-to-end distance of the polymer always reduced compared to the unfilled matrix with increasing filler concentration. This decrease was attributed to a decrease in the effective free volume available within a unit cell as the filler volume fraction was increased. When the particle filler size was varied, a reduction in radius of gyration was seen for all particle sizes, but the scale of the decrease was less significant as the particles became larger; when the unit cell dimensions became greater than the root mean squared end-to-end distance of the polymer chains, the effects of volume exclusion by the filler particles became negligible. How realistic this system is compared to a real polymer nanocomposite is questionable, as really nanofillers do not tend to organise themselves in cubic lattices, and generally might be randomly arranged, or if aggregated, form fractals with dimensions that depend on their tendency to be attracted to other particles.[59, 60]

Sharaf *et al*.[58] followed Sharaf and Mark's 2004 paper[57] with a study on the same system, but with polymer chains five times longer than those previously examined (2500 *vs*. 500 bonds), and only randomised matrices were looked at, rather than those where the particles were sat on a lattice, a consideration that makes the results more easily applicable to a real polymer system. It was found that for larger nanoparticles (20 nm), chain dimensions decreased with increasing filler volume.

1.2.2.1.3 Systems where R_g reaches a maximum value

One computational study produced a result that differed from the others presented so far, suggesting that the polymer radius of gyration increased to a maximum value before falling to levels that were still greater than the radius of gyration of the bulk polymer: having considered the effect of nanoparticles arranged on a cubic lattice, Sharaf and Mark's 2004 paper went on to evaluate what would happen if the particles were instead arranged randomly in the matrix.[57] For this scenario, they found that the root mean squared end-to-end distance of the matrix chains increased relative to the unfilled matrix, and the magnitude of this change was affected by the volume fraction and size of the nanoparticles. For each particle size series investigated, a maximum in the root mean squared end-to-end distance was seen with increasing volume fraction. This maximum value was attributed to the polymer chains being stretched out in the nanocomposite up to the point where the nanoparticles form a percolated network, which traps the polymer chains in pockets, leading to a reduction in the effective free volume in the system, and causing the polymer chains to collapse.

1.2.2.2 Intermediate nanoparticles: $R_{NP} \approx R_{g0}$

As for nanocomposite systems containing nanoparticles that were larger than R_{g0}, nanocomposite systems containing intermediate sized nanoparticles, *i.e.* particles whose size approximately matches that of the polymer chains, also failed to show a consistent trend, with R_g being seen to remain constant with addition of nanoparticles;[53, 61] decrease with increasing nanoparticle concentration;[54, 57, 58, 62-64] or increase to a maximum value before declining again, depending on the system under examination, and the method used to examine the system.

1.2.2.2.1 Systems where R_g is unperturbed

For nanoparticles that are approximately the same size as the bulk polymer radius of gyration, two studies, one computational[61] and one experimental[53] suggest that the bulk radius of gyration is unperturbed by the addition of nanofillers.

Ozmusul *et al.*[61] used Monte Carlo simulations to study the polymer chain conformation in a monodisperse melt of self-avoiding chains containing spherical nanoparticles. They found that the chain statistics remained the same irrespective of filler loading levels up to the limit investigated (27 vol%). Their work also indicated that while small segments of the chain exhibited strong non-Gaussian behaviours, and the bridges, loops and tails were strongly stretched, this occurred in such a way that the system as a whole maintained the Gaussian behaviour of the bulk polymer, and there was no effect on the overall equilibrium melt chain dimensions.

Sen *et al.*,[53] in their work previously discussed in terms of systems for which $R_{\mathrm{NP}} > R_{\mathrm{g0}}$, found *via* SANS that no change in polymer R_{g} occurred relative to the bulk on addition of spherical silica nanoparticles to polystyrene. As before, the TEM images within their paper suggest that the particle dispersion in their samples was poor, so their results cannot be relied upon.

1.2.2.2.2 Systems where R_{g} decreases

A reduction in polymer R_{g} relative to the bulk value has been found both experimentally[54, 62, 63] and computationally[57, 58, 64] for systems containing nanoparticles that are the same size as the polymer dimensions.

In 2001, Nakatani *et al.*[62] used SANS to measure the single chain dimensions of poly(dimethyl siloxane) (PDMS) chains being used as a matrix with trimethylsily-treated polysilicate filler particles. Their work showed that when the radius of gyration of the polymer matched that of the filler, the chain radius of gyration decreased with increasing filler concentration for all filler concentrations. This study was followed in 2002 with a second study on the same system within the same group.[63] This second study increased the filler concentration up to 50% and again found that the chain dimensions decreased at all concentrations.

The work of Nusser *et al.*,[54] whose work also examined chain conformations in nanocomposites where $R_{\mathrm{NP}} > R_{\mathrm{g0}}$, found that for a system of poly(ethylene-alt-propylene) and silica nanofiller the radius of gyration decreased, but, as discussed previously, the group questioned whether additional scattering arising from the core–shell structure of the nanoparticles was influencing the results.

As part of a study on the elastomeric properties of PDMS matrices containing crosslinked chains and randomly arranged spherical particles, Yuan *et al.*[64] used MC-RIS simulations to measure the distribution of the end-to-end vectors of the polymers in these systems. When the system had polymer chains that were approximately the same size as the filler particles, the polymer chains contracted, with the change in R_{g} becoming more significant with increasing filler concentration. Yuan *et al.* argued that for systems where $R_{\mathrm{g0}} \approx R_{\mathrm{NP}}$, the nanoparticles act as large obstacles for the polymer chains, and the free volume between particles in insufficient for the polymer chain to expand, thus it contracts.

Sharaf and Mark's MC-RIS study,[57] which was previously considered for systems where the nanoparticles are larger than the polymer chain dimensions, found that when the nanoparticles were of comparable size to the chain dimensions, and were arranged on a cubic lattice, the root mean squared end-to-end distance of the polymer decreased relative to that of the bulk. As before, this decrease was attributed to a reduction in the effective free volume available within a unit cell as the filler volume fraction was increased. Again, whether these results are applicable to a 'real' system is questionable as nanoparticles do not tend to align themselves to a cubic lattice; however, Sharaf *et al.*'s 2006 paper,[58] examining the same system as before, but with a more realistic random arrangement of nanoparticles and longer chains and larger nanoparticles, also found a decrease in polymer dimensions with increasing filler volume fraction.

1.2.2.2.3 Systems where R_g reaches a maximum value

One computational study found a different result to the others: Sharaf and Mark's 2004 paper,[57] found that when the spherical nanoparticles were arranged randomly in the amorphous polyethylene matrix, the root mean squared end-to-end distance of the matrix chains increased relative to the unfilled matrix up to a maximum value, as discussed previously for systems where $R_{NP} > R_{g0}$. As before, this maximum value was attributed to the increasing volume fraction leading to a percolated network, which in turn leads to a reduction in the effective free volume in the system, which causes the polymer chains to collapse.

1.2.2.3 Small nanoparticles: $R_{NP} < R_{g0}$

This regime is the most widely studied size regime for spherical nanoparticles in polymer matrices, but as for the other regimes, there is no consistent conclusion on the effect of nanofillers on chain dimensions, with the polymer R_g being seen to remain constant[53, 65-67] or increase on addition of spherical nanoparticles.[68, 69]

1.2.2.3.1 Systems where R_g is unperturbed

Several studies have identified that the polymer chain dimensions do not change on addition of spherical nanoparticles, both using simulations[65, 66] and experimentally.[53, 67]

In 2002, Vacatello[65] modelled a series of realistically dense polymer melts containing randomly-distributed solid nanoparticles using only excluded volume arguments and found that there was no large increase in chain dimensions when the radius of gyration of the chain was larger than the diameter of the nanoparticles.

Vacatello argued that the polymer/nanoparticle systems modelled could be compared to polymer systems at the interface with a solid, with previous computational work[56, 70-74] showing that significant changes in R_g with respect to the bulk are only observed for nearly two-dimensional chains that are close to the solid wall (the centre of mass should be less than $R_{g0}/2$ from the solid surface for R_g to be affected), and confirmed by Jones *et al.*[75] who conducted small angle neutron scattering studies on ultrathin (<100 nm) films of PS and found that chain swelling only occurred for the very thinnest films. Vacatello stated that a situation where all the polymer chains in a system would be sufficiently close to a nanoparticle surface for their radius of gyration to be affected would not occur for systems with large nanoparticles and low filler volumes, and Vacatello's calculations suggest that the chain dimensions should also be unperturbed for small particles and higher filler volumes, where the polymer chains are simultaneously in contact with several filler particles.

Dionne *et al.*[66] used a coarse-grain model and MC simulations to investigate a system of monodisperse linear polyethylene with a homogeneous dispersion of spherical nanoparticles (filler size was equal to $0.7R_g$), in an attempt to model a system that was representative of a real polymer system rather than an idealised model one. Their work showed that the average size, average shape and average orientation of the polyethylene chains did not differ significantly from the melt on addition of nanoparticles, but did note significant changes to the localised sub-chain segments within the system. First, the number of bridges decreased rapidly with increasing wall-to-wall distance (d), until at a wall-to-wall distance of $3R_g$, there were no bridges. Second, as d was increased, the number of dangling segments (segments where one end is connected to a nanoparticle and the other is free) also increased; this is directly associated with the reduction in the number of bridges with increasing d. Third, the number of loops and trains (segments that snake along the surface of the nanoparticle) remains constant as $d \geq 1.83\ R_g$.

Sen *et al.*'s 2007 paper,[53] already discussed for the $R_{NP} > R_{g0}$ and $R_{NP} \approx R_{g0}$ regimes, found no change in polymer chain dimensions for a system of polystyrene with spherical silica nanoparticles when investigated *via* small angle neutron scattering. As previously stated, the dispersion of the nanoparticles within this system suggests that their observations may be misleading.

Another series of PS/silica nanocomposites was investigated by Jouault *et al.*[67] The nanocomposites were first characterised using small angle X-ray scattering and transmission electron microscopy, and at low filler concentrations the samples contained small discrete silica aggregates that did not form a network. At higher concentrations (>15 vol%), the silica nanoparticles formed a connected network that extended throughout the sample. For all matrix molecular weights investigated, no change in R_g between the pure PS and the PS/silica nanocomposites was seen. As for the work of Sen *et al.*,[53] the dispersion of the silica particles within the polymer matrix is poor, with large clusters of particles being seen in the TEM images shown in the paper. This suggests that the SANS is actually measuring the scattering of regions of pure polymer (and large aggregates), rather than that of a well-dispersed PS/silica matrix.

1.2.2.3.2 Systems where R_g increases

A number of studies indicated that the R_g of the polymer within the nanocomposite increased on addition of nanofillers; this result was obtained through both experiment[68, 69] and computational simulation.[64, 76-79]

In 2006, Mackay *et al.*[68] investigated the dispersion of tightly-crosslinked PS nanoparticles into a melt of linear PS chains and found that the addition of nanoparticles led to a swelling of the polymer chains with increasing nanoparticle concentration. They argued that excluded volume arguments could not fully account for the increase observed in R_g, as if it was assumed that the polymer and nanoparticle densities did not change on mixing, the R_g relative to that of the pure matrix polymer would be expected to vary as $(1 + \varphi)^{1/3}$, where φ is the volume fraction of polymer nanoparticles; for their system they found the R_g varied as $1 + c\varphi$, where $c \approx 1$.

In a follow-up paper, Tuteja *et al.*[69] presented a second study on cross-linked PS nanoparticles in a polystyrene matrix. In this paper they report a 10-20 % increase in radius of gyration compared to bulk PS on the addition of the nanoparticles when the radius of gyration of the polymer chains is greater than the size of the nanoparticles. They also noted that polymer chains with lower molecular weights were swollen by the nanoparticles more than those with higher molecular weights in relative terms.

The choice to investigate the effect of PS nanoparticles in a PS polymer matrix was a prudent one on the part of Mackay and his collaborators. In small angle neutron scattering, individual chains can be studied by deuterating a small portion of the matrix, and only scattering from the deuterated species is recorded; if a system contains nanoparticles made from a material other than the matrix material, the resultant scattering is a convolution of the scattering from the nanoparticle and the scattering from the deuterated polymer chains. By using PS nanoparticles in a PS matrix, the system is automatically contrast-matched, with both the nanoparticles and the hydrogenated part of the matrix having scattering lengths that are either the same or very close in value, so the only scattering species are the individual deuterated polymer chains. This simplifies analysis of the data and allows for greater confidence in the conclusions that are drawn.

In both papers by Mackay's group, the importance of good dispersion is highlighted, and they conclude that a good dispersion can only be achieved if the radius of gyration of the matrix is larger than that of the filler particles. If the nanoparticles are poorly dispersed, chain swelling should not occur as the effective size of the aggregated particles would be bigger than the R_g. Mackay *et al.* also suggested that Sen *et al.*'s[53] result that adding silica nanoparticles to a polystyrene matrix resulted in no change in the polymer radius of gyration was due to phase separation of the filler from the matrix.

In Yuan *et al.*'s[64] MC-RIS study on PDMS crosslinked matrices containing spherical nanoparticles, previously discussed for the intermediate nanoparticle regime, chain expansion was found when the radius of gyration of the polymer was much larger than that of the filler particle radius, a change that was more significant with increasing filler concentration. It was suggested that the increase in chain conformation was caused by there being considerable free volume in the system in this regime, allowing the polymer chains to snake between particles.

In 2006 Erguney *et al.*[76] used Monte Carlo simulations to consider dense one-component melts of polyethylene and polyoxyethylene chains containing nanoparticles made from parent chains that had been completely collapsed intramolecularly to make filler particles, such that the filler particles could not be penetrated by the matrix chains; this choice of nanoparticle suppresses any influence of special particle–matrix effects. Their model allowed the particles to be mobile, rather than fixed, and indicated an increase in matrix chain dimensions when the particles were smaller than the matrix chains. This was followed in 2008 by Erguney and Mattice with a second study on the same polyoxyethylene system.[77] On this occasion their aim was to refute any suggestion that the chain expansion seen in the earlier paper was caused by an extra volume effect arising from the collapsing of the polymer chains to produce the nanoparticles; the nanoparticles in this system were produced by enhancing the attractive part of the Lennard–Jones potential. This work tested the proposal by artificially inserting some extra free volume into the filled and unfilled systems, and found that the simulated behaviour did not change significantly in magnitude relative to the system originally measured. This led Erguney and Mattice to the conclusion that the chain expansion found in 2006 could not be explained by additional free volume from the collapse of the linear polymer chains into nanoparticles.

Monte Carlo simulations on nanoparticles in a dense, high molecular weight matrix were presented by Termonia.[78] It was found that a thin interfacial region of between 1 and 2 nm existed adjacent to the nanoparticles, in which the polymer segments are oriented perpendicular to the polymer surface. This interfacial region had lower polymer density than the rest of the matrix, and an accumulation of chain ends. For small nanoparticles, Termonia found chain swelling when the distance between the centres of mass of the nearest neighbour nanoparticles was less than the radius of gyration of the polymer chains: for low particle volumes fractions, swelling occurred when the particle radius was less than 3 nm, and at high particle volume fractions, swelling occurred when the nanoparticle radius was less than 4 nm.

In 2010, Frischknecht *et al.*[79] conducted a self-consistent polymer reference interaction site model (SC/PRISM) simulation on polymer melts with spherical nanoparticle fillers. The nanoparticles and polymer were modelled as having an attractive interaction so that the nanoparticles would be fully miscible and easily dispersed in the polymer matrix. It was found that the nanoparticles perturbed the chain dimensions, leading to an increase in radius of gyration with increasing nanoparticle loading. The authors identified that the attractive interaction between the monomers and the nanoparticles was a partial cause of the chain swelling, with the nanoparticles acting as a good solvent for the polymer chains and swelling the chains. The nanoparticles were seen to induce long range disruptions to the packing of the polymer chains up to length scales of approximately three nanoparticle diameters, and to attract a weakly bound polymer layer around them, thus reducing the size of the monomer–monomer attraction.

1.2.2.3.3 Systems where R_g decreases

One computational study identified a reduction in polymer radius of gyration when the nanoparticles were smaller than the chain dimensions. Picu and Ozmusul[80] conducted a Monte Carlo simulation on a matrix of linear polymers containing impenetrable spherical fillers at levels up to 6%. The work investigated a size effect by scaling the radius of the filler particles at constant filler volume fraction, and found that when the wall-to-wall distance between fillers was decreased to below $2R_{g0}$, the chain size decreased in the direction of its large semi-axis, independent of energetic interactions.

Picu and Ozmusul based their work on the argument that macromolecular conformation is restricted close to an impenetrable interface, with the polymer conformation being determined by the configurational entropy between polymer chains, the nature and strength of the interactions between the polymer and the confining wall, and the temperature and density of the system. When a chain approaches a wall, the configurational entropy of the system decreases due to a reduction in the number of accessible chain conformations, and this entropic driving force retracts the chain from the interface. This generates a low density polymer layer along the interface, and affects chain mobility, glass transition temperature and small molecule diffusion. The retraction from the interface is balanced by increased packing in the bulk.

1.2.2.3.4 Systems where R_g reaches a maximum value

One experimental study (across two papers)[62, 63] indicates a different result in this regime to that obtained from other systems: an increase in polymer dimensions up to a maximum value, followed by a decrease to values that are still higher than those of the pure polymer.

Nakatani *et al.*’s 2001 paper,[62] in which SANS was used to measure the single chain dimensions of PDMS chains with trimethylsily-treated polysilicate filler particles, showed that when the radius of gyration of the polymer was larger than the radius of the filler particles, the radius of gyration of the matrix chains increased with increasing filler concentration up to a maximum R_g value, then decreased to values that were still higher than the radius of gyration of the unfilled polymer. These results were confirmed in a second SANS paper published by Nakatani *et al*. in 2002,[63] in which the result was explained in terms of an excluded volume model where the nanoparticle concentration is increased so much that the particles touch and interconnect. At these concentrations, a large portion of the volume available at the start of any calculation is not available to the chain, and the chain goes from expanded to collapsed: the loss of entropy that the polymer chain suffers by collapsing is smaller than the loss of entropy imposed by the restricted volume available to the extended chain. This could result in R_g either increasing or decreasing depending on the relationship between particle distribution, size and volume fraction.

1.2.3 Systems containing cylindrical nanoparticles

Information on the polymer chain conformation in polymer systems containing cylindrical fillers is most relevant to the work on CNT-filed polymers presented in this thesis, but is very limited, with only a handful of computational studies and two experimental studies available. These studies are summarised here.

1.2.3.1 Computational studies

Karatrantos *et al*.[81] simulated a monodisperse polymer/SWCNT system where the SWCNT spans the simulation cell and represents an isolated SWCNT with infinite aspect ratio. In all simulations the radius of the SWCNT was smaller than R_{g0}, and the maximum volume fraction explored was 0.8%. It was found that while the nanotube affected the local arrangements of the monomers, it had no influence on the average radius of gyration of the polymer relative to that of the bulk, independent of polymer molecular weight, interaction strength and SWCNT radius. An exception to this was found for the shortest chains, where a slight increase in the radius of gyration parallel to the SWCNT was found for chains in contact with the SWCNT.

In 2012, Zaminpayma and Mirabbaszadeh[82, 83] conducted molecular dynamics (MD) simulations on SWCNTs in a variety of semi-crystalline polymers that are used in the fabrication of solar cells: poly(3-hexythiophene); poly(2-methoxy-5-(3-7-dimethyloctyoxy)-1,4-phenylenevinylene); and poly((((2-ethylhexyl)oxy)methoxy-1,4-phenylene)-1-2-ethendiyl). They found that the system temperature, SWCNT radius and chirality of the nanotubes had no influence on the polymer radius of gyration.

The minimum energy structures of a SWCNT/polyethylene nanocomposite, at a volume fraction of 7% were simulated by Haghighatpanah and Bolton.[84] They found that the PE chains prefer to align themselves along the SWCNT axis, leading to the polymer chains stretching out relative to the bulk chains and an increase in R_g.

Eslami and Behrouz used an atomistic molecular dynamics simulation to investigate polyamide 6,6 oligomers (10 molecular repeat units long) at a carbon nanotube interface.[85] At the interface, the oligomers arranged themselves into cylindrical shells that appeared as layered structures. It was found that close to the nanotube interface, the polymer chains wrapped the CNT surface, while further out they oriented themselves parallel to the CNT. The specific localised chain conformation was affected by the radius of the nanotubes: nanotubes with a greater radius lead to increased wrapping, while nanotubes with smaller radii, and therefore a greater surface curvature, exhibit an energetically more favourable extended conformation along the nanotube. This paper reports perturbations in the local chain properties up to 2–3 nm from the nanotube surface, but the global R_g is affected up to a few times the R_g of the unperturbed polymer.

The hydrogen-bonding within the polyamide is also influenced by interaction with the nanotube surface, and close to the nanotube surface the hydrogen bonds are weaker than those in the bulk, and are less numerous. In the layered interface region, the H-bonds are stronger and occur more frequently than in the bulk.

1.2.3.2 Experimental studies

In 2013, Tung *et al*.[86] presented the first small angle neutron scattering study on a polymer matrix containing carbon nanotubes. Two systems were studied: single-walled carbon nanotubes (SWCNTs) in PS [the ratio of the radius of the carbon nanotubes (R_{SWCNT}) to the polymer R_g was approximately 0.4], and multi-walled carbon nanotubes in PS ($R_{MWCNT}/R_g \approx 1$). The paper presented a model that incorporated scattering contributions from the polymer chains (the chains were assumed to be Gaussian), rod networks, defects and incoherent scattering (Equation 6).

$$\frac{\mathrm{d}\Sigma}{\mathrm{d}\Omega}(Q) = A \times \mathrm{Debye}(Q, R_g) + B \times Q^{-2} + C \times Q^{-4} + D$$

Equation 6

where $\mathrm{d}\Sigma/\mathrm{d}\Omega(Q)$ is the differential scattering cross-section normalised by a unit volume, commonly referred to the as the intensity, $I(Q)$. As the fitting parameter A is proportional to the volume fraction of polymer chains in the sample, in the fitting of the scattering curves, A was replaced by $A'(1\text{-}\varphi_{CNT})$; in addition, the incoherent term was found to be negligible, so was not used in the fittings. After these modifications, the data were fitted with Equation 7.

$$\frac{\mathrm{d}\Sigma}{\mathrm{d}\Omega}(q) = A'(1 - \varphi_{\mathrm{CNT}}) \times \mathrm{Debye}(q, R_g) + B \times q^{-2} + C \times q^{-4}$$

Equation 7

The scattering length scales of carbon nanotubes and polymer chains overlap, so Equation 7 was first applied to the scattering curves of a series of nine PS nanocomposite samples containing 1 wt% SWCNTs with dPS/hPS ratios of 79/21 to 63/37 to determine a contrast-matched condition of 72.5/27.5 for the PS/SWCNT system. Having hydrogenous and deuterated PS at this ratio tunes the average scattering length density of the matrix to that of the SWCNTs, thus only scattering from the deuterated chains should be seen in the scattering experiments. It was assumed that the contrast matching conditions for the MWCNTs should be similar to those of the SWCNTs, but the scattering length density depends on both the radius and number of layers in a MWCNT, so the contrast matching for the MWCNT samples was not perfect.

Following contrast matching, the scattering from samples made at the contrast-matched PS ratio containing a series of weight fractions of SWCNTs and MWCNTs was recorded and fitted. From these fittings it was found that below 2 wt%, R_g is approximately constant for both SWCNT and MWCNT systems, while above 2 wt%, R_g in the PS/MWCNT nanocomposites decreases slightly, while that of the PS/SWCNT nanocomposites increases significantly, and at 10 wt% SWCNT the R_g increased by 36% over the bulk value.

The rod network term used in the fitting model increased with increasing CNT concentration, and the values were higher for nanocomposites containing SWCNTs than MWCNTs. The increase in the value of B for the PS/SWCNT nanocomposites was attributed to SWCNTs having a smaller mesh size at a given concentration, due to SWCNTs having a much higher number density than MWCNTs for a given weight fraction.

In 2015, Tung *et al.*[87] followed up their 2013 work with a study using small angle neutron scattering and small angle X-ray scattering to explore the radius of gyration parallel and perpendicular to the direction of nanotube alignment in polystyrene nanocomposites containing 0–10 wt% aligned SWCNTs. The nanotubes were aligned in the nanocomposites using melt fibre spinning, which forced the nanotubes to align in the direction of extrusion, then annealed to allow the polymer chains to relax; 2D SAXS was used to demonstrate that the annealing process allowed the polymer chains to relax without influencing the alignment of the pre-aligned nanotubes.

The $I(Q)$ SANS data were fitted with the same model that was used in Tung's earlier paper[86] (Equation 7) and it was found that as the SWCNT concentration was increased, the radius of gyration perpendicular to the direction of alignment increased significantly more than that parallel to the alignment direction, and the extent of anisotropy increased with increasing SWCNT concentration. Compared to the radius of gyration of isotropic PS/SWCNT nanocomposites, the radius of gyration perpendicular to the direction of extrusion is slightly higher, whilst that parallel to the alignment direction is much lower, falling to values close to those of bulk PS. These results indicate that the polymer chains in the nanocomposite expand in the direction perpendicular to extrusion, and that the PS and the nanotubes are not strongly attracted to one another (if this was the case, the polymer would expand along the long axes of the nanotubes).

Tung *et al*. accounted for their results in terms of the mesh size of the nanotubes: with increasing nanotube concentration, the SWCNT mesh becomes more compact, and when the mesh size becomes smaller than the radius of gyration of the bulk polymer (9.50 ± 0.03 nm), the polymer expands to find a way around the SWCNTs. On alignment, the mesh sizes perpendicular to the direction of extrusion become smaller than those parallel to the direction of alignment, an effect that is exaggerated at higher SWCNT concentrations, especially above ~5 wt%.

1.3 Polymer dynamics in polymer nanocomposites

1.3.1 Introduction

Dynamics in polymer chains span a huge time range from approximately 10^{-13} s to many years. These dynamics range from terminal relaxations at the slow end to fast vibrational dynamics including methyl rotations at the fast end, and in between these two extremes lie conformational rearrangements, segmental dynamics and side group rotations.[88]

1.3.2 Use of neutron scattering to examine polymer dynamics

Quasielastic and inelastic neutron scattering (QENS and INS, respectively) can both be used to investigate the dynamics in polymer systems. When a beam of neutrons interacts with a sample, most of the neutrons are scattered elastically, *i.e.* the neutron is scattered by the sample without an energy transfer occurring; however, occasionally, a neutron may be scattered inelastically, *i.e.* the neutron rebounds having exchanged energy with the sample, resulting in the neutron undergoing an energy change during the collision. In quasielastic scattering, both the neutrons that are scattered elastically and those that are scattered inelastically are recorded. This leads to a large elastic peak in the spectrum, which is broadened by the neutrons that are scattered inelastically. In inelastic neutron scattering, only the neutrons that are scattered inelastically are measured. In both cases it is the inelastically scattered neutrons that provide information on the dynamic processes occurring in the sample.

1.3.3 Dynamics in polystyrene

In this section the literature regarding the use of QENS and INS in studying polystyrene (PS), both in the bulk[89-93] and in thin films,[94-100] is reviewed. In order to consider the effect of the filler on the dynamics, the dynamic properties of the pure matrix must be considered first. Thin films are significant because they introduce the influence of a surface and an interface to the polymer. These interfaces affect the packing of the polymer chains, potentially leading to confinement effects similar to those experienced in nanocomposites.

1.3.3.1 Bulk PS dynamics

A pictorial summary of the dynamics in polystyrene is shown in Figure 1.

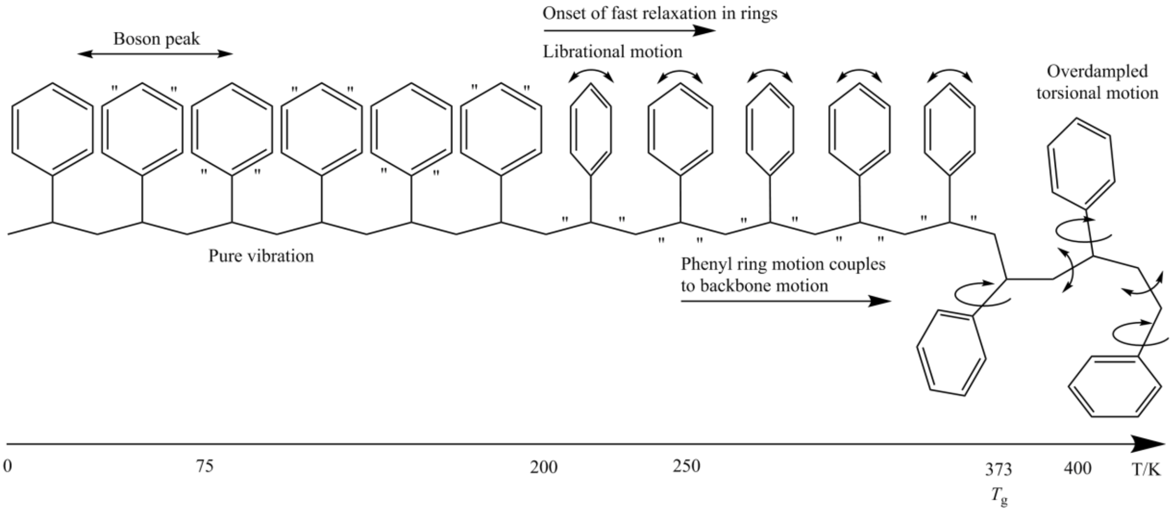

Figure 1: Schematic describing the dynamics in polystyrene as a function of temperature.

1.3.3.1.1 Dynamics below T_g

1.3.3.1.1.1 Low temperature dynamics

At temperatures below ~200 K inelastic scattering increases with T according to the Bose factor (Equation 8):[101]

$$n = \frac{1}{exp(\hbar\omega/k_B T) - 1}$$

Equation 8: Bose factor

where ħ is Planck's constant, ω is the frequency, and k_B is Boltzmann's constant, indicating that motion in this temperature-region is vibrational.[91] At very low temperatures (21 and 75 K), the $S(Q,\omega)$ peak for PS exhibits an enhancement of the density of states $g(\omega)$ over Debye's $g(\omega) \propto \omega^2$ law,[102] *i.e.* the Boson peak, corresponding to low-energy excitation, at ~1.5 meV.[89, 92] This peak is characteristic of amorphous materials, and Kanaya *et al.* attributed the peak to an anomalous excess heat capacity of amorphous materials at very low T.[92] Frick *et al.* found that the position of the peak was only very weakly influenced by the phenyl ring deuteration (used to separate the motions of the whole molecule and the ring).

1.3.3.1.1.2 Intermediate temperature dynamics

Neutron scattering elastic scans (elastic intensity *vs*. temperature) for PS experience deviations from linearity at $T \approx 200$ K,[91, 92] with Frick *et al*. identifying such a deviation at temperatures as low as T = 150 K for fully-hydrogenated PS (h8 PS).[89] Deviations from linearity in the elastic scans were stronger in h8 PS than h3 PS,[89, 91] indicating that this decrease was caused by motion of the phenyl ring. However the weak decrease for h3 PS indicates that phenyl ring motions were not completely independent of main chains motions. Kanaya *et al.*[92] found that for h8 PS, the decrease in elastic intensity did not occur until ~250 K, suggesting that the chain may exhibit a drop in the scattering intensity triggered by the phenyl ring motion that starts at ~200 K, *i.e.* the motion of the main chain begins to couple with that of the phenyl motion at ~250 K. On comparing the scattering of PS and h3 PS, the authors concluded that the fast motion could be assigned to librational motion of the phenyl rings, which couples with main chain motion *via* bonds to the polymer backbone.

Kawaguchi *et al.*[91] and Kanaya *et al.*[92] both identified that at $T \approx 200$ K, the shape of $S(Q,\omega)$ changed from inelastic-like to quasielastic-like; while Frick *et al.*[89] and Kanaya *et al.*[92] found a deviation in the mean squared displacement, $\langle u^2 \rangle$, *vs*. T. Both results indicate the onset of a fast relaxation process. Kanaya *et al.*[92] noted that this process occurred at much lower temperatures in PS than in other polymers, and that the change in $\langle u^2 \rangle$, *vs*. T was hardly observed at $\delta\varepsilon = 2$ meV, indicating that the fast process had an energy < 2 meV.

1.3.3.1.2 Dynamics around T_g

Kanaya *et al.*[90, 92] used QENS to explore the dynamics of amorphous PS, fitting $S(Q,t)$ from fully-hydrogenated PS and chain-hydrogenated PS, to identify that the scattering from the side groups and main chain was strongly coupled. The work identified a slight decrease in $S(Q,t)$ at $\sim T_g + 20$ K, *i.e.* 393 K, indicating the onset of a fast localised process; the half width at half maximum (HWHM) of the peak from PS was approximately equal to that of h3 PS, suggesting that the motion of the phenyl ring was the same as that of the main chain and that side chain motion was strongly coupled with that of the main chain near the T_g. Kanaya *et al.*[90] did not observe the α-relaxation of PS as the experiments were conducted in a much lower energy region and at a slower time; however, they did observe a change in the slope of $I_{el}(Q)$ around T_g, which was most pronounced at $\delta\epsilon = 0.2$ meV indicating that the glass transition influences processes that are much faster than the α-relaxation.

Kanaya *et al.*[92] suggested that the motion starting around 400 K corresponds to overdamped torsional motion around the C–C bond. Below T_g, this motion is hindered by the surrounding polymer segments, and is only able to begin when the free volume exceeds a critical value for the motion. This additional motion leads to a weakening of the cooperativity of motion.

1.3.3.1.2.1 Quasielastic behaviour

Arrese-Igor *et al.*[93] used QENS to investigate the dynamics of h3 PS and h5 PS below the glass transition temperature. Their work had its emphasis on relaxations with a characteristic time greater than 2 ps, and the partial hydrogenation of polystyrene chains allowed the scattering contributions from the chain (h3 PS) and the phenyl rings (h5 PS) to be separated out.

The intermediate scattering function, $I(Q,t)$, obtained by Fourier transform of the $S(Q,\omega)$ peaks, exhibited pronounced decay at $t < 1–2$ ps. At times greater than 2 ps, decay was almost zero at low T and very small at high T. This crossover between fast and slow motions at ~1–2 ps is common in polymeric systems[103-106] and usually evolves to clear 2-step decay at higher temperatures when slower relaxation enters the experimental window. From the behaviour of $I(Q,t)$, Arrese-Igor *et al.* concluded that the increase in $\langle u^2 \rangle$ with temperature was mostly due to motions faster than 2 ps.

From the quasielastic scattering, Arrese-Igor *et al.* calculated the average derivative of the intermediate scattering function between 2 and 20 ps for different T and Q (Equation 9).

$$A(Q,T) = \left| dS_{exp}(Q,t) \right| d(logt) \right|$$

Equation 9

This value is proportional to [1 – EISF(Q)], and plotting $A(Q,T)$ *vs*. Q provides information on both the slow and fast processes in a system, as EISF(Q) has peaks corresponding to particular motions. For h5 PS there were no maxima, indicating small oscillations of the phenyl rings, not generalised phenyl ring flips. The authors calculated that this motion had an activation energy of 0.21 meV ± 0.08 meV. This broad distribution indicates that the activation energy does not represent an intra-molecular energy barrier over which phenyl rings jump, but rapid fluctuations of a single particle potential. For d5 PS, decay above 2 ps is smaller than for the d3 PS sample, and no useful analysis could be conducted.

1.3.3.2 Thin film PS dynamics

Thin films have been shown to have properties that differ from those in the bulk, including a reduction in the glass transition temperature[107] and negative thermal expansivity.[108] The properties of thin films of PS are worth considering here as preparing a polymer as a thin film can alter the packing of the polymer chains and lead to confinement and interface effects similar to those seen in nanocomposites.

The scattering behaviour observed for thin films of polystyrene is broadly similar to that of bulk PS with the observation of the Boson peak, a change from inelastic to quasielastic behaviour arising with increasing temperature, and $\langle u^2 \rangle$ increasing linearly with temperature up to the point at which anharmonic motions began and then deviating from linearity.[96] However, PS thin films have been reported to display some confinement effects relative to the bulk: decreasing mean squared displacement with decreasing film thickness in the meV energy region;[94-100] a decrease in the T_g obtained from ellipsometry, until 100 Å, when the T_g became thickness-independent, while that obtained from neutron measurements increased with decreasing film thickness;[99] and the elastic intensity decreased with increasing temperature more rapidly perpendicular than parallel, with a 20% difference at 323 K.[98] These results all indicate confinement-induced hardening.

The decrease in mean squared displacement with decreasing film thickness[94-100] indicates confinement-induced hardening as polymer stiffness is inversely proportional to $\langle u^2 \rangle$.[109] The decrease in $\langle u^2 \rangle$ was greater with increasing temperature,[95] confirming that the PS thin films experienced hardening relative to the bulk.

Kanaya and coworkers investigated the glass transition temperatures in the films, with the T_g being obtained from the change in thermal expansivity of the samples measured using ellipsometry.[94, 99] It was found that T_g decreased with thickness in the PS thin films, but became thickness-independent and maintained a constant value of 355 K below 100 Å, indicating that the surface T_g was less than that of the bulk[110] (~373 K). The T_g began to decrease at ~400 Å, and was molecular weight dependent, with a more pronounced decrease in T_g for higher molecular weight films (2890 kg mol^{-1} *vs*. 303 kg mol^{-1}). The authors attributed this to deGennes sliding motion.[111]

In contrast, T_g values from $\langle u^2 \rangle$ obtained from neutron measurements increased with decreasing film thickness.[99] This was attributed to the different time scales evaluated by the two techniques: ellipsometry evaluates the thermal expansivity, which is driven by the α-process and free volume, so is dominated by slow motion, whereas inelastic neutron scattering is dominated by fast motion, suggesting that the films exhibit a timescale dependent T_g. Based on these results it was concluded that a higher T_g value always results from lower mobility and *vice versa*, in spite of the apparent contradiction from the ellipsometry results.

The dynamic anisotropy of PS thin films on Al foil in the glassy state was investigated by measuring the scattering intensities parallel and perpendicular to the film surface as a function of T.[98] For a 200 Å film, the elastic intensity decreased with increasing temperature more rapidly perpendicular than parallel, with a 20% difference at 323 K, suggesting higher mobility in the perpendicular direction.

Confinement-induced hardening could easily be explained when the film was thinner than $2R_g$ (~300 Å in the systems investigated), at which point normal chain conformations cannot be sustained, chain deformation occurs and a higher restoring force is required than for normal coils. However, hardening was also seen for 1000 Å films,[98] thicker than $2R_g$, which leads to the possibility that hardening was being caused instead by a hard ‘dead layer’ at the surface.[95]

The molecular weight dependence of $\langle u^2 \rangle$ in PS thin films was examined in thin films by maintaining the film thickness between samples but varying the molecular weights, leading to different ratios of film thickness, d, to R_g.[97] Kanaya *et al.* argued that if a confinement effect were dominant, a decrease in $\langle u^2 \rangle$ would be seen with decreasing $d/2R_g$ as a consequence of increased spatial confinement. If, however, an interface effect was dominant, $\langle u^2 \rangle$ would remain constant with $d/2R_g$ because the layer/bulk ratio would be constant under the same film thickness. The $\langle u^2 \rangle$ data for samples at three molecular weights were virtually identical within experimental error, indicating that confinement was not the main reason for the decrease in mobility with film thickness.

If the hard layer were small relative to the bulk, its influence would also be small. The work of Kanaya and co-workers concluded that the hard layer was approximately 130 Å, and that it became non-negligible below ~1000 Å, and attributed the hard layer to the tendency of phenyl rings to orient parallel to the interface between polystyrene and the substrate,[97] and this orientation of the rings resulting in lower chain mobility than in the bulk.

1.3.3.3 Static structure factor of PS

The static structure factor (SSF) of a material describes how that material scatters incident radiation, without resolving the energy of the scattered radiation. The SSF of polymers can be obtained using X-ray or neutron radiation and provides information on the structure of a material as a function of Q. While the SSF is related to structure rather than dynamics, it is relevant here as it can form a coherent background to dynamic neutron scattering, and can in turn affect the analysis of dynamic neutron scattering data.

The X-ray SSF of polystyrene (PS) has been widely investigated, both *via* experiment[112-115] and simulation.[116] The SSF features several peaks, at Q = 0.75, 1.4, 3.1, 5.6, 9 and 10 Å^{-1}, with the two primary peaks falling at Q = 0.75 and 1.4 Å^{-1}. [114]

The peak at Q = 0.75 Å^{-1} is called the polymerisation peak as it does not appear in the WAXS spectra of styrene monomer.[112, 113] This peak exhibits unusual behaviour: on stretching, the peak intensifies equatorially and the peak significantly increases in intensity with increasing temperature, especially above the T_g.[114] For most materials, increasing the sample temperature leads to an increase in thermal disorder and a corresponding decrease in electron density due to thermal expansion, so the changes responsible for the increase in peak intensity must compensate for the increase in thermal disorder and override them. Ayyagari and co-workers[116] used comparisons between molecular dynamics simulations and Schubach and co-workers' WAXS experimental data[115] to assign the polymerisation peak primarily to intermolecular backbone–backbone correlations, with the addition of the low-Q tail of the intermolecular phenyl–phenyl and phenyl–backbone correlations. They found that the phenyl–backbone and phenyl–phenyl contributions both increase in intensity and shift to lower Q with increasing temperature, leading to the apparent anomalous temperature-dependence of the polymerisation peak.

The most intense peak in the SSF occurs at $Q = 1.5$ Å^{-1}, and is sharper for a-PS than for styrene or benzene, indicating that the polymer has a greater degree of packing order than the monomer. This peak is referred to as the amorphous peak. Ayyagari and co-workers[116] assigned the amorphous peak primarily to phenyl–phenyl correlations from both intra- and intermolecular interactions, with smaller, but still significant, nearly temperature-independent intramolecular phenyl–phenyl and phenyl–backbone contributions; this combination explains the weak temperature-dependence of the amorphous peak.

1.3.4 Dynamics in polymer nanocomposites

1.3.4.1 Introduction

While the previous section has shown that the dynamics in both bulk PS and thin films has been fully characterised, this is not the case for PS nanocomposites, where only a few filled PS systems have been examined. As this is the case, this literature review examines works on filled systems with a variety of matrix polymers, and the majority of the work reviewed involves systems that contain spherical fillers and systems where the polymer is confined, as these areas are more widely explored than systems containing cylindrical fillers. This review primarily covers the short range, fast dynamics uncovered by neutron scattering, but also features some discussion of long-range dynamics revealed by the glass transition temperature. In addition, the long range diffusion of polymer chains in nanocomposites is considered as these works were the direct inspiration for the work contained within this thesis.

1.3.4.2 Dynamics in nanocomposites containing non-cylindrical fillers

1.3.4.2.1 Spherical fillers

1.3.4.2.1.1 Experimental studies: rigid nanoparticles

In the context of polymer nanocomposite research, rigid nanoparticles are filler particles that form impenetrable barriers to polymer chains in the melt. These particles can hinder the dynamics of the polymer chains as the chains have to find paths around the filler particles. The rigid nanoparticles considered here are silica and fullerenes.

1.3.4.2.1.1.1 Silica nanocomposites

In 1998, Arrighi *et al.* presented the first QENS study on polymer–filler nanocomposites.[117] They conducted QENS on a nanocomposite composed of a PDMS matrix [polydimethyl siloxane, a semi-crystalline polymer with a glass transition temperature of approximately 150 K and a melting temperature (T_m) of approximately 235 K] and a silica filler component. The elastic scattering up to 275 K was recorded, and showed that the molecular mobility decreased in the filled polymer relative to the bulk at temperatures above the melting temperature; this was attributed to a reduction in the free energy and entropy of the system through loss of translational and rotational degrees of freedom arising from some polymer segments being adsorbed to the surface of the filler component.

The elastic scan showed that the filler had little effect on the dynamics up to T_g; between T_g and T_m a small effect was seen, but the dynamics of the PDMS chains were largely unperturbed by the presence of the filler up to the melting temperature. This behaviour was expected as PDMS is semi-crystalline below the melting temperature, so large scale motions are hindered below the melting point. Having identified that the filler had little effect below the melting point, Arrighi *et al.* measured the QENS only above the T_m. The QENS spectra exhibited elastic and quasielastic components, with the quasielastic components arising from methyl group reorientation. The filled samples produced narrower QENS peaks, indicating decreased chain mobility. From analysis of the QENS peaks, it was determined that at 40 wt% silica, the fraction of immobilised segments was 7.2% at 250 K and 6.2% at 275 K for a filler with 90 m^2 g^{-1} surface area, corresponding to an adsorption layer ~50 Å thick. This result indicated that any reinforcement effect depends on the properties of the interfacial region, and is analogous to the hard layer identified by Kanaya and co-workers at the interface in PS thin films.[94-100] Kanaya and co-workers argued that the hard layer is influential if it is large relative to the bulk, it will have a significant influence on the properties of the system; if a system contains particles that are surrounded by hard layers that overlap at high concentrations, it would be reasonable to expect that the system as a whole would experience hardening.

In 2001, Gagliardi *et al.* used INS to examine the mobility in nanocomposites containing silica nanoparticles in a PDMS or poly(vinyl acetate) matrix.[118] They identified reduced polymer mobility in both matrices on addition of silica relative to the bulk, and a progressive slowing down of motion with increasing surface area.

Masui *et al.* used QENS to record the dynamics in a polybutadiene and silica nanocomposite.[119] They identified a damped vibrational mode of polybutadiene and jump diffusion motion of segments. Both motions were unaffected by the presence of silica, while the residence time of the jump diffusion motion became longer at high filler loadings. The authors suggested that this effect may be due to microstructural confinement, or a molecular weight effect between the filled and unfilled samples.

1.3.4.2.1.1.2 Fullerene nanocomposites

Sanz *et al.* used inelastic incoherent neutron scattering on C_{60} nanocomposites based on PS-related macromolecules to investigate the effects of C_{60} (0–4 %; C_{60}, ~1 nm diameter) on the fast molecular dynamics.[120] Elastic window scan measurements were conducted on the composites between 2 and 450 K. Sanz *et al.* found that adding C_{60} led to an increase in $\langle u^2 \rangle$ relative to the neat polymer over the whole temperature range examined; the effect was larger for larger C_{60} concentrations.

From the relationship between $\langle u^2 \rangle$ and T, the authors extracted the effective local stiffness, κ. The value of κ decreased with increasing concentration, indicating that the addition of the fullerene nanoparticles caused the 'fast' (~10^{-15} s) local (~1 Å) dynamics of the polymer chains to plasticise. The authors suggested that this reduction in the resistance to displacement of the protons of polymer segments arose from increased free volume caused by enhanced packing frustration on the introduction of the marginally soluble C_{60} nanoparticles into the melt.

Kropka *et al.* used incoherent elastic neutron scattering to assess the influence of C_{60} on the dynamics of PS, PMMA and tetramethyl bisphenol A polycarbonate in polymer nanocomposites.[121] All three nanocomposites exhibited an increase in T_g relative to the bulk on addition of the nanoparticles. In contrast to the work presented by Sanz *et al.*,[120] it was found that the local polymer chain motions were suppressed relative to the pure polymer, but that the influence was limited to the vicinity of the particles at nanosecond timescales; this indicates that the nature of the filler particle may be significant.

The work identified that the elastic scattering increased relative to the bulk for all nanocomposites, indicating a decrease in the atomic motions on addition of C_{60}. For polystyrene, adding the nanoparticles suppressed the drop in elastic intensity corresponding to harmonic vibrations, indicating that the presence of C_{60} suppressed these motions. Both PMMA and TMPC displayed a drop in the elastic intensity associated with methyl vibrations at 50–100 K; this drop was not affected by the addition of C_{60}, indicating that C_{60} did not affect these motions. The intensity drop associated with local backbone motion was, however, suppressed on addition of C_{60} in all the systems investigated, with higher elastic intensity being recorded for the nanocomposites relative to the bulk polymer, indicating reduced mobility. The magnitude of suppression of motions was comparable for all systems.

Kropka *et al.*'s analysis focused on PS as this polymer exhibits no anharmonic behaviour below 200 K, so the data were not contaminated by the methyl group rotations seen from 50 K in PMMA and TMPC. Below 200 K, the work showed that PS and the PS/C_{60} nanocomposite exhibited equivalent $\langle u^2 \rangle$, and a stiffness value was calculated. Above 200 K, $\langle u^2 \rangle$ of PS has stronger T-dependence than that of the nanocomposite. While the harmonic approximation is not strictly valid in this region, Kropka *et al.* applied it heuristically and found a 24% increase in local stiffness for the nanocomposite as compared to the pure polymer. The authors stated that the suppression of local relaxation dynamics was consistent with enhanced cohesive interactions, and speculated that this may be the source of the increase in T_g with the system needing to acquire more thermal energy for polymer segments to overcome local energy barriers and enable centre of mass motion. The authors plotted $I_{\mathrm{el(polymer\ nanocomposite)}} - I_{\mathrm{el(polymer)}}$ for the nanocomposites and identified a diffuse peak at $T = T_g + 50$ K for all the systems examined. The presence of the peak was taken to indicate that at higher temperatures the polymer dynamics homogenise towards those of the pure polymer. The authors identified the diffuse nature of the peak as an indication that the polymer chains were undergoing transient immobilisation at the particle surfaces, a process that became less significant at higher temperatures as the nearest neighbour distances increased and the polymer–filler interactions became weaker relative to the thermal energy of the system, rather than being due to the sudden onset of diffusive motions associated with a fraction of polymer chains being strongly influenced by the particle surfaces.

The QENS peaks of PMMA and PMMA/C_{60} nanocomposites were examined and the nanocomposites showed an increase in $S(Q,t)$ relative to pure PMMA over the whole Q range examined. Kropka *et al.* found that the $S(Q,t)$ of the polymer and the nanocomposite could to be made to match over all Q by applying Equation 10:

$$S(Q,t)_{PNC} = \alpha + (1-\alpha)S(Q,t)_{PMMA}$$

Equation 10

with α, the fraction of immobilised chain segments, taking a value of 0.025. The difference in the scattering between the polymer and the nanocomposites was attributed to immobilisation of polymer segments at the polymer–filler interface, with all other polymer chains in the system retaining homopolymer-like dynamics. The authors described the effect of the particles in terms of an increased segmental friction coefficient for the polymer in the presence of the nanoparticles.

In a follow-up to Sanz *et al.*'s 2008 paper,[120] in 2010 Wong *et al.* published a paper on the effect of C_{60} nanoparticles on the T_g of PS.[122] Wong *et al.* found that the glass transition temperature, approximated by recording the temperature of the apparent kink in the elastic intensity, increased by ~6 °C on addition of C_{60}, indicating a slowing of the α-relaxation. This antiplasticisation effect was also found for the calorimetric and dielectric glass transition temperatures. The authors suggested that the presence of the particles modified the polymer packing causing an increase in the fragility of glass formation, *i.e.* at the glass transition temperature the polymer undergoes a more dramatic departure from Arrhenius behaviour on addition of C_{60}; a polymer is classed as fragile if the deviation at T_g is large and strong if the deviation is small. Polymers with sterically hindered side groups and rigid backbones, such as PS, tend to be 'fragile'.

The increase in glass transition found by Wong *et al.* indicates a decrease in segmental motion, while the elastic scattering behaviour identified by Sanz *et al.* suggested an increase in the amplitude of the fast proton motion,[120] therefore the addition of C_{60} locally softened (plasticised) the polymer in the glassy state while simultaneously slowing down (antiplasticising) the segmental dynamics. These results imply that C_{60} alters the dynamics of PS in two different directions depending on the time scale under examination, which is not entirely implausible as T_g is primarily affected by the backbone rigidity and side group bulkiness while fragility is largely determined by relative flexibility between the side groups and the backbone, and polycarbonate diluted with a polychlorinated biphenyl mixture with 60% chlorine has been found to exhibit plasticisiation/antiplasticisiation at an 'antiplasticisation temperature'.[123]

Wong *et al.* also discussed the importance of particle distribution in the nanocomposites: the bulk nanocomposite properties are due to the small interparticle distances of adequately dispersed nanoparticles and the total amount of exposed surface area (cohesive interactions), with the nanoparticles causing confinement of the polymer chains. Higher nanoparticle concentrations should lead to smaller interparticle distances provided no clustering occurs, but this may not be the case at higher concentrations as thermodynamically driven agglomeration can occur.[124] The authors obtained a good dispersion below 2 wt% C_{60}; above this concentration, agglomeration of nanoparticles was seen on annealing, and as the nanoparticle loading and temperature increased, so did the polydispersity of the cluster sizes.

In 2015, Sanz *et al.* followed Wong *et al.*'s 2010 paper[125] on the glass transition temperature in PS/fullerene nanocomposites with a second paper on the same topic, with this second paper focusing on the effects of annealing and the methods used for sample preparation.[126] It was found that adding C_{60} to composites prepared *via* rapid precipitation led to an increase in T_g at nanoparticle concentrations of up to 4 wt%, but at higher concentrations the T_g gradually reverted to the value for neat PS. The maximum increase in T_g was 4 °C, lower than that found by Wong *et al.* Thermally annealing the samples, or preparing them *via* a solvent evaporation method, reversed the effects in nanocomposites containing more than 1 wt% C_{60} as the dispersion in these sample was poorer than in the as-prepared rapidly precipitated samples.

The rapid precipitation method included sonication of a 10 wt% PS–C_{60}/toluene solution prior to stirring for two days at room temperature before precipitation of the solution into an excess of methanol. Sanz *et al.* varied the time of this sonication step from 0 to 150 min, and found that sonication time had no effect on the thermal properties of the composite at concentrations up to 2 wt% C_{60}, as measured by DSC.

The structure and dispersion of the fullerenes in spun cast nanocomposites was investigated using optical microscopy and atomic force microscopy. These films displayed uniform and homogeneous dispersions up to 4–5 wt% C_{60}, however, annealing the samples at 180 °C led to cluster nucleation within minutes for fullerene loadings greater than 1 wt%. Small angle neutron scattering was used to monitor the dispersion in composites containing 1 and 4 wt% C_{60} prepared *via* rapid precipitation. Upon annealing, the scattering increased as precipitation occurred; this did not happen for the 1 wt% sample, indicating polymer–fullerene miscibility for loadings up to 1 wt%. Wide angle X-ray scattering confirmed that uniform composites could be produced with up to 5 wt% C_{60} *via* either rapid precipitation or solvent casting methods; the authors referred to 5 wt% as the 'dipersibility limit'; above this concentration the composites were no longer uniform. At concentrations higher than 1–2 wt% crystalline C_{60} peaks grew rapidly after 2–5 min of annealing at 180 °C, indicating that thermally stable composites are only achievable at loadings of 1–2 wt%.

1.3.4.2.1.2 Experimental studies: Soft nanoparticles

Soft nanoparticles are nanoparticles made by crosslinking polymer chains so they exist as compact clusters. As they are not fully solid, and the surrounding polymer chains have the potential to diffuse within the space occupied by the nanoparticle, with this chain mixing potentially leading to interesting properties, including plasticisation of the less mobile component and slowing down of the more mobile component, and alteration of T_g values.[127]

Carbon nanotubes are relatively hard, so chain mixing is not an option, however one result from the field of soft nanoparticles may be relevant to a CNT/polymer nanocomposite: Miller *et al.* used neutron reflectivity to measure the diffusion coefficients in PS linear chain nanocomposites filled with soft PS nanoparticles with different levels of crosslinking determining their softness.[128] Using SANS the authors identified that the particles exist as a gel-like core and a corona of free chain ends and loops. Nanoparticles with a lower crosslink density (1% crosslink density) increased the diffusion coefficient of the matrix more than nanoparticles with a higher crosslink density (2% crosslink density), and softer nanoparticles increased the extent of the rise in polymer diffusion rate. This indicates that the nanoparticle softness is crucial in determining the impact of the nanoparticles on polymer diffusion; and if this is extrapolated to carbon nanotubes, which for comparative purposes can be considered as nanoparticles with very high crosslink density, either a smaller increase in polymer diffusion rate, or a reduction in diffusion rate should be expected, echoing the result of Clarke *et al.*, who identified a minimum in the diffusion coefficient in PS with increasing CNT concentration.[129, 130]

1.3.4.2.1.3 Simulation studies

All MD simulations conducted on polymer nanocomposites containing spherical fillers consider how the addition of the filler affects the entanglements of the polymer chain. Entanglements are topological constraints imposed on polymer chains by their neighbouring chains they cannot pass through one another; entanglements are important as they limit the dynamics of the polymer.

Li *et al.* conducted isobaric MD simulations using a conventional finite extensible non-linear elastic (FENE) spring model to investigate the primitive path of the polymer in a nanocomposite made up of a polymer and spherical non-attractive nanoparticles.[131] The work identified that highly entangled chains significantly disentangle on increasing nanoparticle levels from 0 to 42%, but that the chains exhibit Gaussian statistics at all φ.

The critical volume fraction, or percolation threshold, φ_c = 31% led to a crossover from polymer chain entanglements to 'nanoparticle entanglements.' The authors found that below φ_c the polymer relaxed faster on adding nanoparticles, due to disentanglement, and the reduction in disentanglement time, τ_d, was linearly proportional to the reduction in the number of entanglements per chain (Z_kink) or tube diameter, $\langle a_\mathrm{pp}\rangle^{-2}$. Below φ = 31%, τ_d decreased with increasing φ.

Above φ_c the polymer became geometrically constrained on adding the nanoparticles and the relationship between disentanglement time and Z_kink and $\langle a_\mathrm{pp}\rangle^{-2}$ broke down. For φ > 31%, τ_d was suddenly much larger than that of the pure chains (φ = 0%): τ_d was 60% larger at φ = 42% than at φ = 0%.

Karatrantos *et al.* conducted stochastic MD simulations to investigate nanoparticle diffusivity and entanglements in a system of spherical nanoparticles in a polymer matrix from the percolation threshold, φ = 31%, to 40.9%.[132] The nanoparticle diffusivity was found to follow the Stokes–Einstein equation (Equation 11) in nanocomposites containing short chains in the dilute regime. Above the percolation threshold the nanoparticle diffusivity decreased dramatically, in contrast to the work of Li *et al*.[131] It was also noted that the diffusivity of small nanoparticles deviated from the Stokes-Einstein relation, with small nanoparticles diffusing much faster than predicted by Equation 11:

$$D = \frac{k_\mathrm{B}T}{4\pi\eta R_\mathrm{NP}}$$

Equation 11

where *D* is the diffusion coefficient, η is the viscosity. Adding nanoparticles increased the number of entanglements seen, as measured by the large contour length of primitive paths. This increase in the number of entanglements was accompanied by a decrease in the entanglement length, which results in more topological constraints and hindered polymer diffusivity. The entanglement length decreased with increasing volume fraction of nanoparticles. Attraction between the nanoparticles and the polymer was seen to affect the entanglements and alter the primitive path.

Kalathi *et al.* conducted molecular dynamics simulations on the internal relaxations and Rouse modes of polymer chains in polymer/nanoparticle nanocomposites where the polymer and nanocomposite were weakly interacting.[133] When the nanoparticles were smaller than the entanglement mesh size the effective monomeric relaxation rates were faster than in the neat melt. The introduction of small nanoparticles led to a reduction in monomer friction and a decrease in entanglement density, *i.e.* plasticisation. The effect was akin to adding solvent molecules to a polymer resulting in the entanglement length increasing by 20%. The effect was nanoparticle size dependent and decreased to ~10% for nanoparticles approximately half the bulk tube diameter or larger.

For nanoparticles larger than half the entanglement mesh size, the effective monomer relaxation was essentially unaffected for low nanoparticle concentrations. A strong reduction in entanglements was seen for larger nanoparticle loadings. When the nanoparticles were larger than the entanglement mesh size, the dominant effect comes from the fact that some part of the volume is taken up by the nanoparticles (entanglement dilution).

The authors concluded that nanoparticles always reduce the number of entanglements, but that the effect is only pronounced for small nanoparticles or at high concentrations of nanoparticles; the entanglement length was found to have a strong dependence on nanoparticle size at fixed nanoparticle loading. From this result, it would be expected that the polymer radius of gyration should increase with increasing nanoparticle concentration, which is largely borne out by the experimental work conducted on similar systems: for nanoparticles smaller than the polymer radius of gyration, Mackay *et al*.[68] and Tuteja *et al*.[69] both found a pronounced increase in R_g in a system of tightly-crosslinked PS nanoparticles in a PS matrix, while Nakatani *et al*. found the R_g to achieve a maximum value, then fall to levels that were still greater than the bulk R_g beyond the percolation threshold, in a system of PDMS/trimethylsily-treated polysilicate particles.[62, 63] Some experimental studies suggest the R_g was unperturbed on addition of small nanoparticles, but both studies had issues with dispersion, so the nanoparticles were acting as clusters, resulting in higher effective R_g values for the polymer.[53, 67]

1.3.4.2.2 Confinement

Confining a polymer in a layered system such as a silicate can be considered as an extreme case of introducing a nanofiller to a polymer system: in both cases the ‘filler’ component introduces a large additional surface area with which the polymer chains must interact, leading to a potential alteration of polymeric behaviour from that in the bulk. The interface effects arising from confinement would generally be expected to be more extreme and extensive than from adding a filler.

Chrissopoulou *et al.* used QENS to investigate poly(methyl phenyl siloxane) (PMPS) in the bulk and under confinement.[134] The polymer was confined in the 1–2 nm interlayer spacing of intercalated (chains evenly distributed between layers of inorganic material) polymer/layered organosilicate. The work examined a broad temperature range above and below T_g. The temperature-dependence of the elastic scattering for the homopolymer and the nanohybrids exhibited two distinct relaxation processes, the first due to methyl group rotations and the second from phenyl ring flips and segmental motions. The segmental motion and phenyl flip were coupled from T_g + 40 K until T_g + 60 K, when segmental motion became dominant.

Chrissopoulou *et al.* showed *via* analysis of the mean square displacement and QENS that the methyl group relaxations were not affected by confinement, were insensitive to the glass transition and had a *Q*-dependent relaxation time and low activation energy.

The temperature-dependence of the mean squared displacement showed that phenyl ring motion started just above the glass transition temperature, in contrast to PS, where phenyl ring libration starts at *ca*. 200 K, well below the T_g,[91, 92] and at T_g + 60 K, segmental motion started to occur. $\langle u^2 \rangle$ indicated that segmental motion was faster under confinement than in the bulk, even after the contribution from the stabilising surfactant chains was taken into account.

The authors concluded that under confinement, the chains adopted a preferentially parallel configuration near the walls, resulting in a region of enhanced monomeric mobility. Under severe confinement this region was found to extend to the whole film, leading to faster relaxation.

Barroso-Bujans *et al.* examined the inelastic neutron spectroscopy of poly(ethylene oxide) under extreme 2D confinement in graphite oxide, with the polymer being intercalated into the subnanometer graphite oxide layers.[135] This confinement eliminated the α-relaxation because of the lack of cooperativity among the intercalated chains. The β-relaxation modes slowed, as under confinement they required greater activation energies than in the bulk. Under confinement the PEO adopted a planar zig-zag conformation, very different to the standard helical structure adopted in the bulk crystal.

1.3.4.2.3 Complex systems

In 2003, Karlsson *et al.* investigated the dynamics of a solid polymeric electrolyte system *via* QENS.[136] The system comprised the amorphous copolymer trihydroxy poly(ethylene oxide-*co*-propylene oxide) (3-PEG), a salt to increase conductivity ($LiClO_4$), and a filler (TiO_2) that induced some structural changes. The results identified slow relaxations that presented as elastic scattering, and two dynamic processes: fast local chain motion and slower diffusive segmental motion. Karlsson *et al.* saw no changes in the widths of the QENS peaks between the filled and unfilled composites, but the elastic scattering increased on the addition of filler, which they took to indicate the presence of a ~5 nm thick immobilised polymer layer (~5 vol%) around the filler particles, while the bulk dynamics (~95 vol%) were unaffected.

Karlsson *et al.* fitted the elastic intensity using two Lorentzians: one narrow and one broad. The authors attributed the broad component to a fast, local chain motion, primarily rapid rotational conformational fluctuations of chain segments, or fast local hydrogen motions in the polymer backbone. The narrow component was identified as diffusive segmental motion and methyl group rotation. The polymer in the nanocomposite was crosslinked, so any motions were localised.

For pure 3-PEG, the FWHM of the narrow component of the spectrum decreased with increasing Q, and was temperature-dependent, while the FWHM of the broad component was Q-independent with only a weak T-dependence. When 1.5 mol kg^{-1} $LiClO_4$ was added, the FWHM of the narrow component was smaller than that of pure 3-PEG, indicating that the corresponding process was slowed down by the presence of the salt. The FWHM of the broad component of the spectrum was unaffected by the presence of the salt. The FWHM of both peaks was unaffected by the addition of 10 and 20 wt% TiO_2.

The elastic scattering, which is due to polymer immobility on the length scales probed, increased when the salt was added, indicating a slowing down of the dynamics, confirmed by the narrowing of the FWHM of the narrow component. Adding 10 wt% filler led to a further increase in the elastic scattering. The authors considered whether this increase may be due solely to the elastic scattering contribution arising from the filler, but as the filler contributed only 0.25% of the total scattering cross section, the authors concluded that some polymer must be immobilised on addition of the filler. Karlsson *et al.* suggested that this may be due to the polymer interacting strongly with the surface of the filler particles. Adding 20 wt% TiO_2 filler resulted in a small/negligible increase in elastic scattering, which the authors attributed to aggregation having occurred, resulting in no significant increase in the total filler surface with the addition of extra filler.

1.3.4.3 Dynamics in carbon nanotube nanocomposites

While the dynamics observed in nanocomposites containing non-cylindrical nanoparticles can in theory be extrapolated to those containing nanotubes, in practice this is non-trivial owing to the significant increase in aspect ratio contributed by cylindrical particles.

1.3.4.3.1 Long range dynamics: polymer diffusion

The majority of the dynamics literature on polymer/CNT nanocomposites focuses on the long range dynamics within the systems, primarily diffusion, investigating how the diffusion of labelled polymer chains into a polymer matrix containing both single-walled and multi-walled carbon nanotubes is affected by the size and concentration of the filler particles, and the molecular weights of both the tracer and matrix.

1.3.4.3.1.1 Experimental studies

In 2009, Mu *et al.*[129] published the first experimental results regarding the diffusion of polymer chains in carbon nanotube nanocomposites. The experiment examined a system of SWCNTs in PS and used elastic recoil detection (ERD, an ion beam technique that provides a concentration profile of the diffusing species as a function of depth into a matrix) to follow tracer diffusion of a 20 nm dPS layer into a >40 µm hPS/SWCNT nanocomposites on annealing at 150 °C for different periods of time. The system did not undergo a change in T_g on addition of the nanoparticles, indicating an absence of interaction between the PS and SWCNTs. Mu *et al.* identified a minimum in the diffusion coefficient in the region of the percolation threshold found from rheology: initially the tracer diffusion coefficients were suppressed with increasing SWCNT volume fraction, then increased beyond a critical concentration, $\varphi_{crit} < 1$ vol%; further increases in SWCNT concentration led to the diffusion coefficient gradually increasing from D_{min} to D_0.

Shorter chains experienced a greater slowing than larger chains, and longer matrix chains reduced the value of φ_{crit}. The minimum was seen for all molecular weights investigated (matrix molecular weights: 125k and 480k g/mol; tracer molecular weights: 75k, 140k and 680k g/mol). The result presented by Mu *et al.* contradicts that predicted by deGennes reptation,[137] which anticipates the filler acting as a diluent and smoothly increasing both the free volume and diffusion coefficient with increasing filler concentration.

Mu *et al.*[129] devised a trap model to account for the minimum, and proposed that the centre of mass diffusion of the polymer chains was anisotropic near the nanotubes, being slower perpendicular to the nanotube surface than along it. In the model this anisotropy was modelled by assigning a single jump probability for motion parallel to the nanotubes, and a second, lower, jump probability for motion involving entering or leaving a trap, *i.e.* motion perpendicular to the trap. The traps form cylinders around the nanotubes, and when the traps are isolated, *i.e.* at low nanoparticle concentrations, movement is slowed. When the volume fraction of nanoparticles is increased, the traps percolate and the network spans the sample. As the polymer chains can move as freely within the trap as outside it, the influence of the traps diminishes with increasing nanotube concentration, and D recovers. The trends of sharper minimum and smaller value of φ_{crit} observed for higher matrix molecular weights were both mirrored in the model by using an increase in the trap radius as a proxy for increased matrix molecular weight, indicating that at higher matrix molecular weights the region around the nanotube that has an influence on the motion of the nanotubes is larger.

Mu *et al.* followed their initial work with a second study, this time on PS/MWCNT nanocomposites.[130] This work showed that when the dPS tracer had a molecular weight of 680 kg mol^{-1} (R_g 21.3 nm), diffusion was suppressed at low MWCNT concentrations, and increased with higher loadings, as was found for the PS/SWCNT nanocomposites; again the minimum in the diffusion coefficient occurred at the rheological percolation threshold for the system. However, no minimum was observed for tracer molecular weights of 10 and 75 kg mol^{-1} (R_g 2.5 and 7.2 nm, respectively); in this case, dPS diffusion was independent of MWCNT loading.

Mu *et al.* identified that when the radius of gyration of the tracer was smaller than the radius of the nanotubes, tracer diffusion was independent of nanoparticle loading, and no minimum was observed. When $R_{\mathrm{MWCNT}} > R_g$, diffusion was in line with the predictions of Maxwell,[138] and consistent with diffusion parallel and perpendicular to the nanotube surface being of the same order. Mu *et al.*[130] suggested that in such cases the tracer polymer was too small to be significantly entangled with the nanotubes and the excluded volume from the impenetrable nanoparticles was negligible at these low loadings (<5 vol%), so the nanotubes had no significant effect on diffusion in these nanocomposites.

In 2013, Tung *et al.*[139] followed Mu *et al.*'s earlier works[129, 130] with a study on the temperature dependence of the diffusion minimum in PS/MWCNT nanocomposites. The diffusion of a 20 nm 680 kg mol^{-1} dPS tracer layer into a >100 μm MWCNT/hPS nanocomposite after annealing at seven temperatures between 152 and 214 °C was recorded using ERD. It was found that the value of $(D/D_0)_{\min}$ was much smaller at higher temperatures (0.9 at 214 °C compared to 0.6 at 152 °C), but that the value of φ_{crit} was temperature-independent. Mu *et al.*'s trap model[129] was applied to this system, with an increase in temperature being modelled by increasing the probability of a polymer chain leaving or entering the tube, indicating that the difference in tracer diffusion parallel and perpendicular to the MWCNT surface was smaller at higher temperature.

At fixed MWCNT concentrations (0.5, 2 and 6 wt%), the temperature-dependence of the diffusion coefficient was found to follow Williams–Landel–Ferry (WLF),[51] indicating that the polymer dynamics in the nanocomposites arose from changes in the free volume with temperature, and the minimum in D/D_0 is associated with a minimum in the thermal expansion coefficient of free volume.

The works of Mu *et al.*[129, 130] and Tung *et al.*[139] were followed in 2014 by Lin *et al.*,[140] who used ERD to measure the diffusion of tracer layers of dPS into a PS nanocomposite matrix containing ‘chained’ nanoparticles grafted with PS. These nanoparticles were made of strings of five spherical Fe_3O_4 nanoparticles, each 5 nm in diameter, fused to make string-like aggregates, then grafted with 132 kg mol^{-1} PS, and are closer in structure to those nanoparticles used in technological applications than the model nanoparticles used in the earlier experiments. The grafting chains ensure that the chained nanoparticles are easily and stably dispersed in the polymer matrix as they are made of the same material as the matrix.

The diffusion coefficients in the chained nanoparticle (cNP) nanocomposites exhibited a minimum with increasing nanoparticle concentration when $2R_g/L \leq 1.5$, where L is the mean length of the impenetrable core of the chained nanoparticles; when $2R_g/L > 1.5$, D was seen to decrease monotonically with increasing cNP concentration. As with the SWCNT and MWCNT nanocomposites, D_{min} was attributed to anisotropic diffusion near the nanoparticle surface, and requires the long dimension of the nanoparticle to be longer than the radius of gyration of the tracer molecule.

Lin *et al.*’s work also investigated the influence of the polymer brushes on the diffusion coefficient. When the data were normalised with an effective diffusion coefficient accounting for distinct dynamics in the PS matrix and the brushes, D/D_e, the transition between D_{min} behaviour and monotonic behaviour is gradual, whereas when the data are normalised with the diffusion coefficient in the bulk polymer, D/D_0, the transition between the two regimes is sharp. Lin *et al.* suggested that this difference occurs because the polymer brush grafted to the nanoparticles provides an alternative pathway to control the polymer dynamics, whereas the ungrafted nanoparticles act as an impenetrable obstacle for polymer diffusion.

1.3.4.3.1.2 Simulation studies

Inspired by the experimental results of Mu *et al.*,[129, 130] in 2011 Karatrantos and Clarke[141] presented a theoretical model to predict the diffusion of polymer chains around a single SWCNT. The model modifies reptation theory[137] to take into account the polymer/nanoparticle interaction and size of the polymer/nanoparticle interface for a system where the radius of gyration of the polymer is much greater than the nanotube radius. Karatrantos and Clarke’s model agreed quantitatively with Mu *et al.*’s experimental diffusion study on a PS/SWCNT system below the percolation threshold,[129] however, as the model considered only an isolated nanoparticle, no results above the percolation threshold could be obtained.

In 2012, Karatrantos *et al.*[142] published MD simulations on a polymer/single SWCNT system. The work presented data on the contour length of the primitive path (the shortest path connecting the two ends of the polymer chain, subject to entanglements), which provides information about the entanglements in the system. Irrespective of whether or not there were attractive interactions between the PS and the SWCNT, adding the SWCNT to the polymer led to an increase in the contour length of the primitive path, and a corresponding decrease in entanglement length. A greater decrease in entanglement length was identified when the nanotube and the polymer experienced attractive interactions; this was attributed to higher monomer density in the vicinity of the nanotube.

The mean squared displacement of polymer chains in contact with the nanotube surface (*i.e.* those chains that diffuse along or around the nanotube) was compared to that of those polymer chains that were not in contact with the nanotube. Large heterogeneities were found, and for an entangled polymer melt, $\langle u^2 \rangle$ of chains not in contact with the nanotube surface was smaller than that in the bulk, suggesting that the motion of chains not adsorbed to the nanotube surface was affected by those chains interacting with the SWCNT surface.

The dynamics of the polymer chains was estimated through the self-diffusion coefficient, D_0, extracted from the mean squared displacement. When there was no attraction between the nanotube and the polymer chains, the addition of the nanotube did not affect the diffusivity, contradicting Mu *et al.*'s experimental results.[129, 130] When there was attraction, a reduction in diffusivity was seen with increasing chain length, and below the entanglement length, *N*, was around 10, diffusivity retained the bulk value.

Later in 2012, Karatrantos *et al.* presented further results from their MD simulations.[143] The work examined the effect of the interaction strength between the polymer and the SWCNT, and identified an excluded volume repulsion between the nanotube and the polymer chains when there was no attraction. Chain diffusion close to the nanotube was approximately the same as that in the melt, and no alteration in the chain diffusivity due to geometric effects was identified when $R_g >> R_{SWCNT}$, *i.e.* diffusion was the same parallel and perpendicular to the SWCNT.

When there was attraction between the nanotube and the polymer chains, the number of entanglements went up on addition of the SWCNT, leading to a reduction in chain diffusivity. A large heterogeneity in polymer dynamics was seen near the nanotube, with $\langle u^2 \rangle$ of chains 'not always in contact with the SWCNT' being smaller than in the bulk, indicating that the chains were influenced by interaction with the nanotube surface. This change occurred close to the interface, and at a distance of 1 R_g from the surface, the polymer number density was found to be the same as the melt value, independent of chain length. The chain diffusivity was smaller perpendicular to the SWCNT surface than parallel to it; this difference was smallest for unentangled polymer chains.

Increasing the radius of the carbon nanotube at a constant volume fraction led to a reduction in the surface to volume ratio, reduced contact and a smaller interfacial area. Karatrantos *et al.*

found that for the largest SWCNT radius examined (r_{SWCNT} = 0.85) in an entangled polymer melt the diffusion value was only slightly lower than that of the bulk, and decreasing the SWCNT radius led to a reduction in the diffusion.

In 2013, Karatrantos *et al.*[144] used dissipative particle dynamics simulations to model polymer matrices containing 0–11 vol% hexagonal nanorods; the nanorods were non-attractive with respect to the matrix and had diameters smaller than the polymer radius of gyration, and an aspect ratio of 7.5.

The system displayed an increase in the number of entanglements on addition of the nanorods, which was attributed to larger contour lengths of the primitive path. A 50% reduction in the entanglement length was found on addition of 11 vol% nanorods: increasing the number of nanorods and retaining the same free volume led to more topological constraints and hindered chain dynamics. These results contradict those found for a simulation by Li on a system of nanocomposites containing repulsive spherical nanospheres,[131] where the nanosphere radius was the same as the polymer radius of gyration. In Li's system, the entanglement length increased with volume fraction of nanospheres due to a reduction in the contour length of the primitive path, indicating that entangled chains gradually disentangle on addition of spherical nanoparticles. For spherical nanoparticles of the same radius as the polymer radius of gyration, but with an attractive interaction with the matrix, no change in entanglement length was seen.[145]

Karatrantos *et al.*[144] also investigated the effect of the nanorods' radii. Increasing the radii of the nanorods at a constant nanorod length and volume fraction led to a decrease in the surface area to volume ratio, and a larger depletion area around the nanorod surface was identified. Increasing the nanorod radius led to a slightly smaller decrease in the entanglement length than when a smaller nanorod was examined, and no disentanglement in the vicitiny of the nanorod was found.

1.3.4.3.2 Short range dynamics

At the time of writing, only one experimental study had been conducted on the short range dynamics in a polymer/SWCNT nanocomposite.[146] Ashkar *et al.* used neutron scattering and neutron spin echo to investigate the dynamics of a PMMA/SWCNT nanocomposite beyond the percolation threshold (1, 8, 15 vol%); this system exhibits strong interfacial binding. The authors recorded elastic window scans across a wide temperature range and identified a reduction in elastic intensity with temperature for both PMMA and the nanocomposite, but the decrease was not as rapid for SWCNT composites as for pure PMMA, indicating that the nanotubes limit the fraction of hydrogen atoms whose relaxation time is shorter than 2 ns (the time resolution of the elastic scan). The mean squared displacements extracted from the elastic scan at different nanofiller loading levels were largely unaffected by the level of SWCNT loading. At higher loadings, polymer chains are expected to have more contacts with the SWCNT network, so even non-interfacial polymer units might be expected to be more constrained. However, the absence of a concentration effect in the mean squared displacement indicates that localised hydrogen motions are not further affected by proximity to the interface. Combined with a decrease in the total hydrogen mobility, a result confirmed by neutron spin echo spectroscopy on dPMMA and dPMMA + 8% nanotubes at $Q = 0.9$ Å^{-1} (where chain-chain relaxations are most prominent), the authors concluded that two separate polymer regions exist: (a) regions with effectively frozen dynamics around the nanotubes and (b) regions with faster motions away from the interface. The work suggested that slow interfacial segments arrest the faster non-interfacial segments and restrict the extent of their local mobility.

Aim of this thesis

The aim of this thesis is to understand the structure and dynamics of polymers and how they are affected by SWCNT fillers, in particular to identify the origin of the minimum in the diffusion coefficient in PS/SWCNT nanocomposites. To achieve this, well defined samples must be prepared (Chapter 2: Experimental), and their structure (Chapter 3: Small angle neutron scattering) and dynamics (Chapter 4: Quasielastic neutron scattering) analysed in detail before and after addition of nanotubes.

Chapter 2: Experimental

2.1 Introduction

This chapter introduces the experimental techniques used in the work presented in this thesis. The chapter covers living anionic polymerisation, nanocomposite synthesis, and characterisation of the polymers and nanocomposites produced. Small angle neutron scattering and quasielastic neutron scattering are also introduced, including sample data sets.

2.2 Polymer synthesis

2.2.1 Introduction

All polymers for small angle neutron scattering (SANS) and quasielastic neutron scattering (QENS) were synthesised *via* living anionic polymerisation, which allows high control over the molecular mass and polydispersity of the polymers produced.[147] For the SANS experiments, two sets of polymers whose molecular masses are matched to within 10% [100 000 and 250 000 g mol^{-1} hydrogenated and fully-deuterated polystyrene (hPS and dPS, respectively)] were required. The QENS experiments required one batch of ring-hydrogenated PS (h5 PS) and one batch of chain-hydrogenated PS (h3 PS), ideally of matching molecular weight.

2.2.2 Materials

The monomers [styrene, (Sigma Aldrich, St Louis, Missouri, USA), d8 (fully-deuterated) styrene, h5 (ring-hydrogenated/chain-deuterated) and h3 (chain-hydrogenated/ring-deuterated) styrene (all Cambridge Isotope Laboratories, Andover, Massachusetts, USA)] were each dried over CaH_2 (Acros Organics, Geel, Belgium) under high vacuum (5×10^{-8} mbar; the monomer was frozen, then this level of vacuum was applied to remove any unfrozen impurities) for at least 36 h, and a minimum of three freeze–evacuate–thaw cycles were conducted to remove any impurities or inhibitors prior to use. The d8, h3 and h5 monomers were further purified by adding dibutyl magnesium solution (1.0 M in heptane, Sigma Aldrich, St. Louis, Missouri, USA) immediately prior to transfer to the reaction vessel [~0.5 ml $(t\text{Bu})_2\text{Mg}$ per 5 g of monomer].

The polymerisations were all conducted in benzene (Sigma Aldrich, St. Louis, Missouri, USA) that had been dried over CaH_2, and purified *via* three freeze–evacuate–thaw cycles, as for the styrenes. *sec*-BuLi (1.4 M in cyclohexane, Sigma Aldrich, St. Louis, Missouri, USA) was used as the initiator; the amount of initiator used was calculated according to Equation 12:

$$\text{mol}_{\text{initiator}} = \frac{g_{\text{monomer}}}{M_{\text{n, polymer}}}$$

$$\text{ml}_{\text{initiator solution}} = \frac{\text{mol}_{\text{initiator}} \times 1000\ \text{ml}}{\text{molarity}_{\text{initiator solution}}}$$

Equation 12

where $\text{mol}_{\text{initiator}}$ is the number of moles of initiator required to give a polymer of the required molar mass; g_{monomer} is the mass of monomer (g) being used; $M_{\text{n, polymer}}$ is the number average molar mass of the target polymer; $\text{ml}_{\text{initiator solution}}$ is the volume (ml) of initiator solution required; and $\text{molarity}_{\text{initiator solution}}$ is the molarity of the initiator solution.

2.2.3 Method

Each polymerisation was carried out under high vacuum conditions (5×10^{-4} mbar) in a glass reaction vessel (a ‘Christmas tree’) sealed with Young’s taps and Suba Seal silicone rubber septa (see Figure 2). Before starting each reaction, the sealed reaction vessel was pre-washed with a living PS solution (styrene monomer in benzene, initiated with *sec*-BuLi,) then with benzene that had been distilled under vacuum from the living solution.

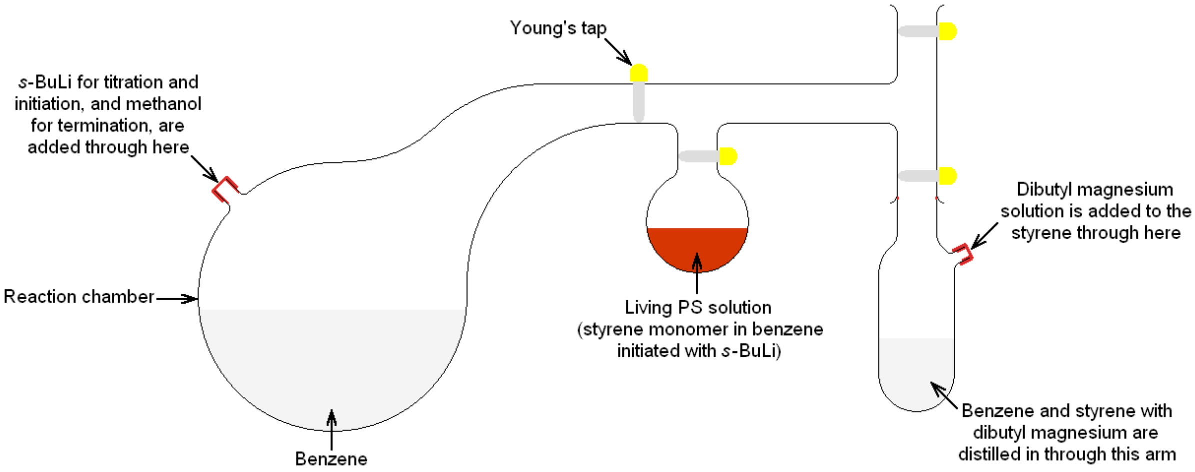

Figure 2: Schematic of the Christmas tree experimental set-up used for the polymerisation reaction

Once the reaction vessel had been cleaned, benzene (~10 ml of benzene per g of monomer), then styrene, were distilled, under vacuum, into the reaction vessel.

Prior to initiation, the reaction mixture was ‘titrated’ with a small amount of the initiator solution (*sec*-BuLi, 1.4 M in cyclohexane), *i.e.* *sec*-BuLi was added dropwise *via* a syringe through the septum until the benzene–styrene solution exhibited a persistent yellow colour; this step ensured that all impurities that would otherwise react with the initiator had been used up prior to adding the measured dose of initiator, allowing greater control over the final molecular weight of the polymer. Once this colour had been achieved, the amount of *sec*-BuLi solution required to initiate the reaction was injected *via* the septum, with constant stirring. The amount of initiator solution required was calculated using Equation 12.

Following addition of the required volume of initiator solution, the reaction mixture was stirred overnight at room temperature; the colour of the reaction solution was indicative of whether the reaction had worked: a yellow–orange–red hue (with the depth of the colour depending on the concentration of polymer chains in the solution) indicated success, while a colourless solution indicated the absence of living anions, therefore a failed reaction. The living polymer chains were terminated by injecting an excess of methanol, which had been degassed with N_2, into the reaction mixture, again *via* the septum. The polymer was recovered by precipitation into methanol. The product was filtered and re-dissolved in tetrahydrofuran (THF) before being re-precipitated into methanol, filtered, then washed with further methanol and dried *in vacuo*, until the mass of the final polymer was constant.

For the h5 PS, the reactants were transferred under vacuum, but the reaction itself was conducted under nitrogen, other than this the reaction procedure was as described above.

2.2.4 Characterisation

The molar masses of the polymers were analysed *via* size exclusion chromatography (SEC) using a Viscotek TDA 302 with refractive index, viscosity and light scattering detectors (with a 690 nm wavelength laser). Two 300 mm PLgel 5 μm mixed C columns (with a linear range of molecular weight from 200 to 2 000 000 g mol^{-1}) were employed. THF was used as the solvent at a flow rate of 1.0 ml/min at room temperature.

Details of the polymers produced can be seen in Table 1.

Table 1: Details of PS samples synthesised *via* living anionic polymerisation

Sample	Polymer	M_n/kg mol^{-1}	M_w/kg mol^{-1}	PDI (M_w/M_n)
PS(110k)[a,b]	PS	111 000	117 000	1.05
dPS(110k)[a]	dPS	113 000	116 000	1.03
PS(220k)[c]	PS	220 000	225 000	1.02
PS(230k) [c]	dPS	235 000	246 000	1.05
h5 PS[d]	h5 PS	397 000	425 000	1.07
h3 PS[d]	h3 PS	229 000	262 000	1.14

[a] Samples PS(110k) and dPS(110k) were paired for used in SANS experiments. [b] This sample was synthesised by Prof. Lian Hutchings at Durham University. [c] Samples PS(220k) and dPS(230k) were paired for use in SANS experiments. [d] These samples were prepared for use in QENS experiments.

2.3 Nanocomposite synthesis

2.3.1 Introduction

The nanocomposites required for both SANS and QENS were prepared *via* a modified version of the coagulation method described by Du *et al.*[30] This method has been shown to produce an excellent dispersion of nanotubes at the mass fractions levels required.

2.3.2 Materials

Raw, unpurified HiPco (high-pressure carbon monoxide conversion) single-walled carbon nanotubes (SWCNTs; Unidym, Sunnyvale, California, USA) were purified as outlined in the next section. Hydrochloric acid (HCl, for analysis, *ca*. 37% solution in water) and dimethyl formamide [DMF, pure, for high-performance liquid chromatography (HPLC)] were purchased from Acros Chemicals. The matrix polymers [PS(110k), dPS(110k), PS(220k), dPS(230k), h5 PS and h3 PS] were all produced *via* living anionic polymerisation; details of the polymer compositions can be found in Table 1.

2.3.3 Method

2.3.3.1 Nanotube purification

As made, the HiPco nanotubes contain approximately 32 wt% Fe [verified by thermogravimetric analysis (TGA) using a TA Instruments Thermal Gravimetric Analyser SDT Q600. TGA was conducted by Dr Michelle Seitz (h5 PS) and Wei-Shao (Walter) Tung (h3 PS) at the University of Pennsylvania. All TGA was run in air with a flow rate of 100 ml min^{-1} and using platinum pans. The temperature was ramped to 120 °C at a rate of 5 °C min^{-1} and held at this temperature for 60 min in order to evaporate any residual water, then ramped to 800 °C, again at 5 °C min^{-1}]. In order to lower the iron content, the nanotubes were purified *via* a modified version of the method described by Zhou *et al*:[148] as-received nanotubes (~1.35 g) were placed in a glass dish and covered with aluminium foil, then heated in an oven in stagnant air at 250 °C for 24 h to allow the Fe to oxidise to Fe_2O_3. Following cooling to room temperature, the nanotubes were transferred to a glass jar and ~200 ml concentrated HCl (37%, 1 g nanotubes per 125 ml HCl) was added. This mixture was sonicated for 30 min in a water bath at 80 °C. As soon as the nanotubes came into contact with the acid the mixture turned yellow and gas was evolved. Once the sonication step had been completed, the mixture was filtered through a Buchner funnel with glass fritted disc filter, and thoroughly rinsed with deionised water until the pH of the filtrate matched that of the original deionised water. The clean nanotubes were then transferred to a jar and covered with deionised water (*ca*. 125 ml water per g nanotubes), sonicated for ~20 min in a water bath, then filtered. At this point a small amount of the purified material was removed and TGA run as before to determine the final amount of Fe present in the nanotubes (~5.4 wt%). To remove any residual water, the filtered nanotubes were transferred to a new jar and topped up with DMF (*ca*. 125 ml per g nanotubes), sonicated for 20 min, filtered and rinsed with DMF.

2.3.3.2 Nanotube suspension

A nanotube–DMF suspension was created by transferring the DMF-rinsed nanotubes to a clean jar and topping the jar up with DMF (again *ca*. 125 ml per g nanotubes); this mixture was then sonicated for 24 h in a water-filled sonicator bath. Care was taken to stop the nanotubes from drying in order to prevent irreversible aggregation.

In order to determine the concentration of nanotubes in the suspension, an aluminium dish was weighed, then a sample of the stock solution was pipetted into the dish and the dish re-weighed. The aluminium dish was placed on a hot plate to remove the solvent, and the dish containing the dry nanotubes was then weighed again. The concentration of nanotubes in the DMF solution was determined *via* the following calculation:

$$(\text{Mass of Al dish} + \text{solution}) - (\text{mass of Al dish}) = \text{solution mass}$$

$$(\text{Mass of Al dish} + \text{dry nanotubes}) - (\text{mass of Al dish}) = (\text{nanotube mass})$$

$$(\text{Solution mass}) - (\text{nanotube mass}) = \text{mass of DMF}$$

$$\frac{(\text{Mass of DMF})}{(\text{Density of DMF, } 0.95 \text{ g ml}^{-1})} = \text{Volume of DMF}$$

$$1000 \times \frac{(\text{Nanotube mass})}{(\text{Volume of DMF})} = \text{Concentration of CNT–DMF suspension}$$

Equation 13

Details of the nanotube–DMF suspensions are detailed in Table 2.

Table 2: Concentration of SWCNTs in the DMF–SWCNT suspensions used in nanocomposite coagulation

Solution	Nanotube concentration (mg ml^{-1})	Standard deviation (mg ml^{-1})	Standard deviation (%)
A[a]	2.04	0.236	11.6
B[b]	2.78	0.262	9.42

[a] Used to prepare the PS(110k):dPS(110k), PS(220k):dPS(230k), and h5PS nanocomposites; 2010. See Table 3 and Table 4. [b] Used to prepare the h3PS nanocomposites and a second h5PS 0.4 wt% sample; 2013—see Table 3 and Table 4 for details.

For coagulation, the suspension should be at a concentration of *ca*. 0.25 mg CNTs per ml of DMF.[30] Rather than dilute the entire solution, the approximate amount of stock solution required for each sample was transferred to 20 ml glass vials of known mass; the filled vials were then weighed and their contents transferred to jars sufficiently large to hold the volume of DMF needed at the more dilute concentration, rinsing thoroughly to ensure all the nanotubes were transferred. The larger jars were then topped up with sufficient DMF to reach a concentration of *ca*. 0.25 mg per ml of DMF. Once the solutions had been diluted to the required concentration, they were sonicated for 24 h; the sonication periods were timed such that there was no standing time between the end of the sonication and the start of coagulation process.

2.3.3.3 Preparation of polystyrene–DMF solutions

Two types of PS–DMF solutions were prepared: those containing one type of PS (h3 or h5 PS), and those containing two types of PS (dPS and PS in a 9 : 1 mass ratio). For the single polymer solutions, the polymers were weighed into glass vials of known mass; for the solutions containing two types of polymer, one polymer was weighed into a glass vial of known mass, then the mass of the second polymer required to create a 9 : 1 ratio was calculated, and the second polymer was weighed into a second vial. For both types of solution, the polymers were then transferred to a larger jar, and a known mass of DMF was added to create PS–DMF solutions of known concentration, with concentrations between 5 and 10 wt% [accurate concentrations were calculated using a method analogous to that described for calculating the concentrations of the nanotube–DMF suspensions (Equation 13)]. These solutions were stirred overnight to ensure full dissolution.

2.3.3.4 Coagulation

Prior to removing the nanotube–DMF solutions from the sonicator, the amount of polystyrene–DMF solution necessary to make a nanocomposite containing the desired nanotube concentration was weighed into a glass vial. Having removed the nanotube–DMF solution from the sonicator, the weighed polystyrene–DMF solution was then rapidly pipetted into the nanotube–DMF solutions, taking care to rinse any residue from the pipette into the nanotube–DMF solutions using fresh DMF. The nanotube–DMF–polystyrene solution was swirled by hand for ~30 s, then sonicated for ~30 s. Next, the nanotube–DMF–polystyrene solution was pipetted quickly into a beaker containing a 5× excess of deionised water, and vigorously stirred with a magnetic stirrer, causing the nanocomposite to precipitate. The nanocomposite–water–DMF mixture was filtered and rinsed with deionised water, transferred to an aluminium dish, loosely covered with aluminium foil, and dried for at least a day at room temperature in a fume hood. The nanocomposite was transferred to a vacuum oven at 125 °C for 24 h for further drying. For a list of all the compositions synthesised, see Table 3 and Table 4.

Table 3: Details of the two-polymer samples prepared *via* the coagulation method[a]

Sample name	wt% SWCNT in composite	Error in wt%	Mass of composite made (g)
110A(0)[b]	0	0	>0.5
110B(0.5)[b]	0.5	0.06	0.46
110C(1)[b]	1	0.12	0.5
110D(1.5)[b]	1.48	0.17	0.55
110E(2)[b]	2.04	0.24	0.47
110F(2.5)[b]	2.51	0.30	0.56
110G(3)[b]	3.05	0.37	0.59
110H(3.5)[b]	3.54	0.43	0.49
110I(4)[b]	3.98	0.48	0.55
230A(0)[c]	0	0	>0.4
230B(0.5)[c]	0.5	0.06	0.37
230C(1)[c]	0.99	0.12	0.42
230D(1.5)[c]	1.5	0.18	0.42
230E(2)[c]	1.99	0.24	0.36
230F(3)[c]	3.01	0.36	0.43
230G(4)[c]	3.91	0.47	0.47

[a] All samples were prepared in 2010. [b] Samples with labels containing the prefix 110 were composed from a 9 : 1 ratio of *ca*. 110 000 g mol^{-1} dPS : hPS. [c] Samples with labels containing the prefix 230 were composed from a 9 : 1 ratio of *ca*. 230 000 g mol^{-1} dPS : hPS.

Table 4: Details of the single-polymer composites synthesised *via* the coagulation method

Sample name	wt% SWCNT in composite	Error in wt%	Mass of composite made (g)
h5A(0)[a,b]	0	0	>0.4
h5B(0.1)[a,b]	0.09	0.01	0.36
h5C(0.4) [a,b]	0.44	0.05	0.41
h5H(0.4)[b,c]	0.41	0.04	0.60
h5D(1)[a,b]	1.06	0.12	0.40
h5E(2)[a,b]	1.97	0.23	0.43
h5F(3)[a,b]	2.8	0.33	0.42
h5G(4)[a,b]	3.93	0.48	0.42
h3A(0)[c,d]	0	0	0.51
h3B(0.1)[c,d]	0.10	0.01	0.58
h3C(0.4)[c,d]	0.40	0.04	0.51
h3D(1)[c,d]	1.01	0.09	0.51
h3E(2)[c,d]	2.01	0.19	0.50
h3F(3)[c,d]	3.02	0.27	0.50
h3G(4)[c,d]	4.02	0.36	0.50

[a]This sample was prepared in 2010. [b]Samples with labels containing the prefix h5 were composed from h5 PS (M_n 397 000 g mol^{-1}, M_w 425 000 g mol^{-1}, PDI 1.07). [c]This sample was prepared in 2013. [d]Samples with labels containing the prefix h3 were composed from h3 PS (M_n 229 000 g mol^{-1}, M_w 262 000 g mol^{-1}, PDI 1.14).

2.3.4 Characterisation

2.3.4.1 Nanoparticle dispersion

2.3.4.1.1 Atomic force microscopy: Determining CNT bundle size

Silicon wafers coated with carbon nanotubes (CNTs) were prepared by Michelle Seitz, using a method outlined by Brand and co-workers,[48, 149] in order to determine the size of the nanotube bundles within the CNT nanocomposites. Silicon wafers were functionalised with 3-aminopropyltriethoxysilane (APTES) to yield an amine-terminated surface (the wafers were prepared by Hyun-Su Lee in Prof. Russell Composto's lab at the University of Pennsylvania). The wafer was dipped briefly (~1 s) into a sample of the *ca*. 0.25 mg ml^{-1} SWCNT–DMF solution that had the same sonication history as that used for the nanocomposite preparation. The sample was immediately rinsed with methanol, and then blown dry with argon.

Several different areas of the CNT-coated silcon wafer were imaged in tapping mode with a SiN tip using an atomic force miscroscope [Molecular Imaging PicoPlus + Agilent MAC III AFM; atomic force microscopy (AFM) was conducted by Sangah Gam at the University of Pennsylvania]. The bundle diameters were measured using line scans across the topology, while the bundle lengths were determined from amplitude images using Photoshop image software. Ten scans of 5 μm × 5 μm were collected from various parts of the sample and the average bundle diameter was determined to be 4 nm (standard deviation 2.55 nm) from 117 measurements; the average length was found to be 410 nm (standard deviation 280 nm) from 285 measurements (Figure 3).

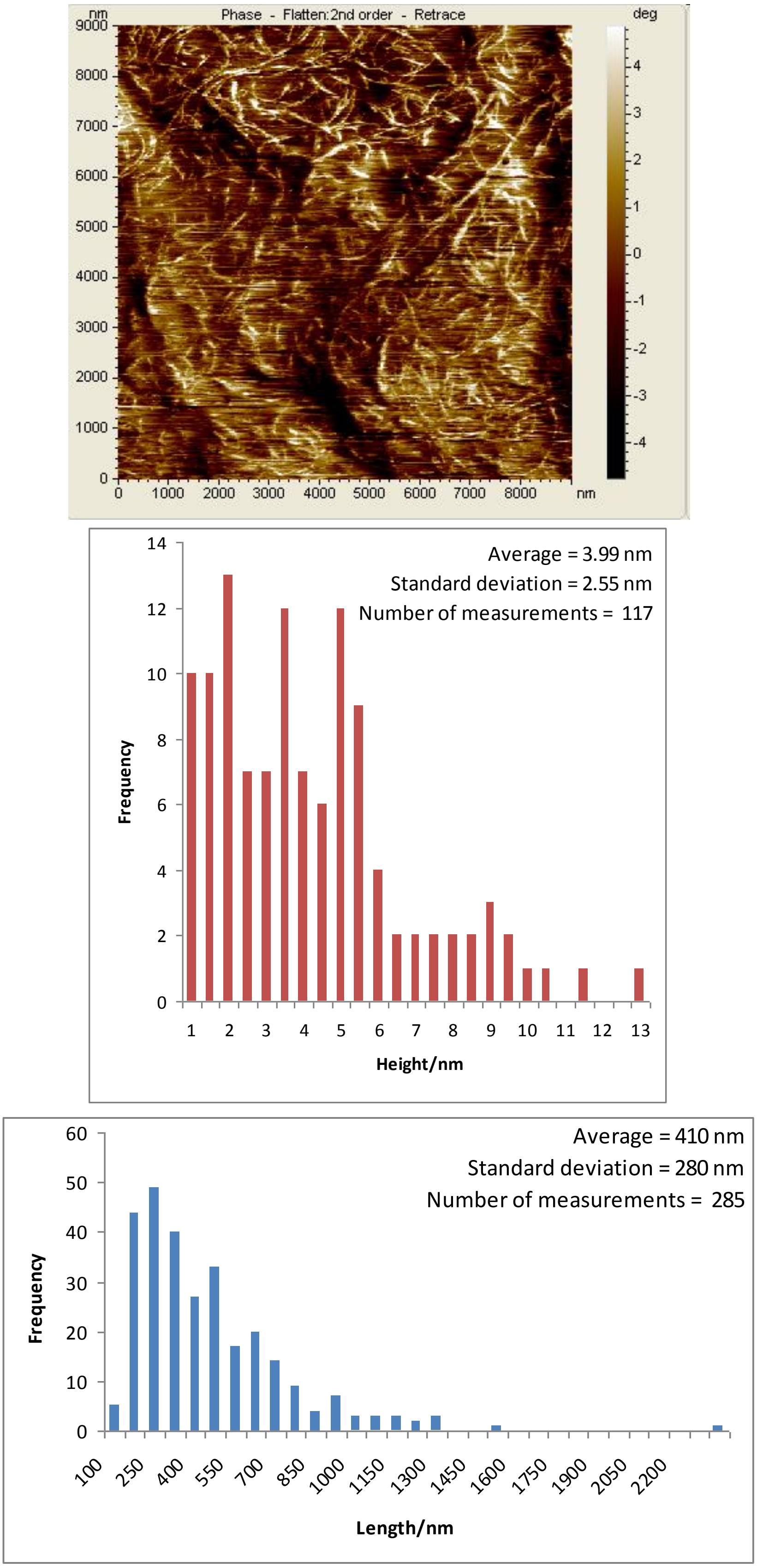

Figure 3: (Top) Representative AFM image of a SWCNT-coated silicon wafer used to determine the extent of nanotube bundling in the samples. Histograms of nanotube bundle diameter (middle) and length (bottom).

2.3.4.1.2 Small angle X-ray scattering

SAXS measurements were carried out by Dr Michael Weir at The University of Sheffield on a laboratory SAXS instrument (NanoStar, Bruker) equipped with a microfocus Cu Kα X-ray source, collimating system with motorised scatterless slits (Xenocs, France), and HiStar 2D multiwire gas detector (Siemens/Bruker). Scattering patterns were collected with a beam size of 1 × 1 mm, and corrected for the detector's dark current, spatial distortion, flat field, sample thickness, exposure time, sample transmission, and the detector normalisation coefficient by Dr Michael Weir; the intensity units are arbitrary. Data were recorded for d3 PS with 0, 0.4 and 4 wt% SWCNTs and d5 PS with 0, 0.1, 0.4, 1, 2, 3 and 4 wt% SWCNTs.

2.3.4.2 Calorimetric glass transition temperatures

The calorimetric glass transition temperatures of the nanocomposites were determined using differential scanning calorimetry (DSC). DSC measurements were conducted by Doug Carswell at Durham University using a Perkin Elmer DSC 8500 differential scanning calorimeter. Samples were taken from the d3 PS and d5 PS nanocomposite samples that were used for the QENS experiments, and weighed between 0.818 and 4.289 mg. Each sample was (i) heated from 0 to 160 °C at 300 °C min^{-1}, (ii) cooled from 160 °C to 0 °C at 100 °C min^{-1}, (iii) heated from 0 to 160 °C at 300 °C min^{-1}, (iv) cooled from 160 °C to 0 °C at 100 °C min^{-1}, (v) heated from 0 to 160 °C at 300 °C min^{-1}. Data were analysed by Vikki Bird using PYRIS,[150] and a T_g value was extracted from the second and third heating ramps. The values reported in Table 5 are the average of the two runs.

Table 5: Calorimetric T_g values for the d3 and d5 PS SWCNT nanocomposites used in the QENS experiments

Sample	**Calorimetric T_g/°C**	**s.d.**
d3 PS + 0 wt% SWCNTs	123	0.00707
d3 PS + 0.4 wt% SWCNTs	125	0.184
d3 PS + 1 wt% SWCNTs	122	0.0141
d3 PS + 2 wt% SWCNTs	121	0.481
d3 PS + 3 wt% SWCNTs	122	1.07
d3 PS + 4 wt% SWCNTs	122	0.184
d5 PS + 0 wt% SWCNTs	126	1.58
d5 PS + 0.1 wt% SWCNTs	126	0.332
d5 PS + 0.4 wt% SWCNTs	123	1.54
d5 PS + 1 wt% SWCNTs	118	0.481
d5 PS + 2 wt% SWCNTs	122	1.92
d5 PS + 3 wt% SWCNTs	124	2.18
d5 PS + 4 wt% SWCNTs	123	1.19

2.4 Neutron scattering

2.4.1 The basics of neutron scattering

Neutron scattering (incorporating small angle neutron scattering and quasielastic neutron scattering) is the primary technique used in the body of this thesis. The sections that follow provide a brief introduction to the fundamentals of neutron scattering techniques.

2.4.1.1 Why use neutrons?

Neutrons exhibit wave–particle duality, and follow the deBroglie relationship[31] (Equation 14):

$$\lambda = h/mv$$

Equation 14

where λ is the neutron wavelength, *h* is Planck's constant, *m* and *v* are the mass and velocity of the neutron, respectively. Neutrons from thermal reactors have energies of the order k_BT (where k_B is Boltzmann's constant) *i.e.* ~4–5 x 10^{-21} J, corresponding to a wavelength of ~10^{-10} m, which is ideal for exploring interatomic distances.

2.4.1.1.1 Neutron scattering length

Neutrons are scattered by nuclei, with the strength of interaction being governed by the scattering length, *b*, which defines the amplitude of the wave scattered by a nucleus with respect to the amplitude of the incident wave. The square of the amplitude at a point in space determines the probability that a neutron will be found at that point, thus b^2 gives the probability that a neutron from the incident beam will be found in the scattered beam and represents the probability of a neutron being scattered per nucleus, per incident neutron, per solid angle (measured in steradians; there are 4π steradians in a sphere). The scattering length varies throughout the periodic table and does not disadvantage smaller atoms, *e.g.* hydrogen. In addition, the scattering lengths of hydrogen and deuterium differ markedly, so these atoms can be used for labelling with little effect on the material properties, allowing molecules to be examined in their 'natural state'.

2.4.1.1.2 Neutron scattering cross section

The neutron scattering cross section of a nucleus, σ, is related to the scattering length (Equation 15), and gives the probability of a neutron being scattered in all space.[31]

$$\sigma = 4\pi b^2$$

Equation 15

In an assembly of nuclei, the probability of a beam of neutrons being scattered depends on the sum of the wavelengths scattered by each nucleus. If the assembly contains nuclei with different values of *b*, these must be averaged before squaring to obtain the net probability of the beam being scattered.

2.4.1.2 The wavevector Q

In a neutron scattering experiment, a beam of neutrons of known wavelength, λ, is fired at a sample; the neutrons are scattered by the atoms in the sample, and the scattered neutrons are recorded in terms of their wavevectors, Q. Q corresponds to the modulus of the vector resulting from the incident and scattered wavevectors, $\boldsymbol{k}_i$ and $\boldsymbol{k}_f$, given by Equation 16, and has units of inverse length.[151]

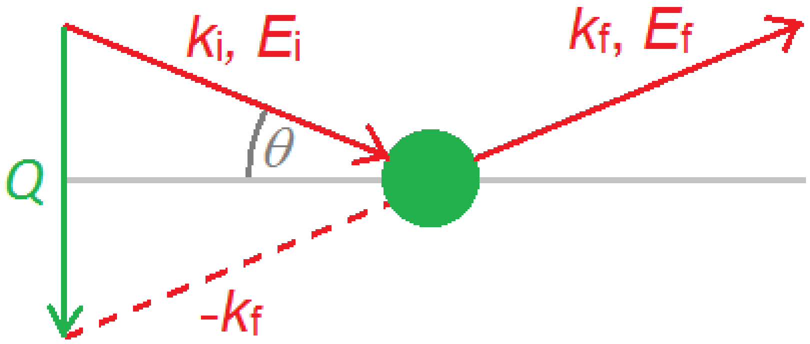

Figure 4: Schematic of a scattering experiment

$$|\boldsymbol{k}_\mathrm{i}| = |\boldsymbol{k}_\mathrm{f}| = \frac{2\pi}{\lambda}$$

$$Q = \left|\boldsymbol{k}_i - \boldsymbol{k}_f\right| = \frac{4\pi n}{\lambda}\sin\theta$$

Equation 16

Substituting Equation 16 into Bragg's Law of Diffraction (Equation 17) gives Equation 18, which can be used to calculate the lengthscales within a molecule that are being probed by the neutrons, *d*, with small values of *Q* corresponding to large-scale structures, while large values correspond to small-scale structures.

$$\lambda = 2d\sin(\theta/2)$$

Equation 17

$$d = \frac{2\pi}{Q}$$

Equation 18

2.4.1.3 Coherent vs. incoherent scattering

2.4.1.3.1 Coherent scattering

Coherent scattering arises from spatial correlations between nuclei of the same scattering length. This gives rise to structure factors, $S(Q)$, that are characteristic of the spatial arrangement of the nuclei and allows information about the structure of a system to be identified.

2.4.1.3.2 Incoherent scattering

Incoherent scattering does not contain any information about the structure in a system and instead describes the dynamics of individual particles. Incoherent scattering arises from two sources: isotopic and spin.

2.4.1.3.2.1 Isotopic incoherent scattering

Isotopic incoherent scattering happens when there is no correlation between the position of a scatterer in the sample and its scattering length, *e.g.* natural isotopic variation. This leads to a random scattering probability that forms a background under coherent scattering.

2.4.1.3.2. 2 Spin incoherent scattering

Both nuclei and neutrons have spin, and the interaction between these spins may alter the scattering length. For example, hydrogen has two very different scattering lengths depending on its spin state. The spin of a nucleus is not related to its position, therefore this scattering is incoherent. Spin incoherence can, however, provide useful information about the dynamics within a system *via* energy changes that occur on scattering.

2.4.1.4 Elastic scattering **vs.** ***inelastic scattering***

If a neutron is scattered by a vibrating, rotating or translating molecule, there is a finite probability of an energy exchange (loss or gain) occurring when a neutron interacts with a molecule. A collision in which an energy change occurs is described as inelastic. A collision in which no energy change occurs is described as elastic.

Elastic scattering provides information about the structure of a molecule, while inelastic scattering provides information about the dynamics. Energy changes will occur at all temperatures greater than absolute zero, therefore purely structural experiments require that the experimental set-up is designed such that elastic and inelastic scattering can be distinguished. This can be done either by screening out inelastic events and examining purely the elastic scattering, or by ignoring inelastic events.

2.4.1.4.1 Types of inelastic scattering

Inelastic scattering arising from different types of motions has different effects on the appearance of plots of the elastic intensity [$I(E)$] *vs*. energy (E).[31]

2.4.1.4.1.1 Vibrational motion

The energy levels within a molecule are quantised, and for vibrational motions the spacings between the quantised energy states are large compared to the thermal energies of the neutrons. This large spacing results in energy gains and loses appearing as distinct shifts in the neutron energy (Figure 5); this is true inelastic scattering. The chances of a neutron gaining energy from a vibrating molecule are smaller than the chances of the neutron imparting energy to the molecule, as energy gain depends on the occupation of excited states, which is governed by the Boltzmann factor.

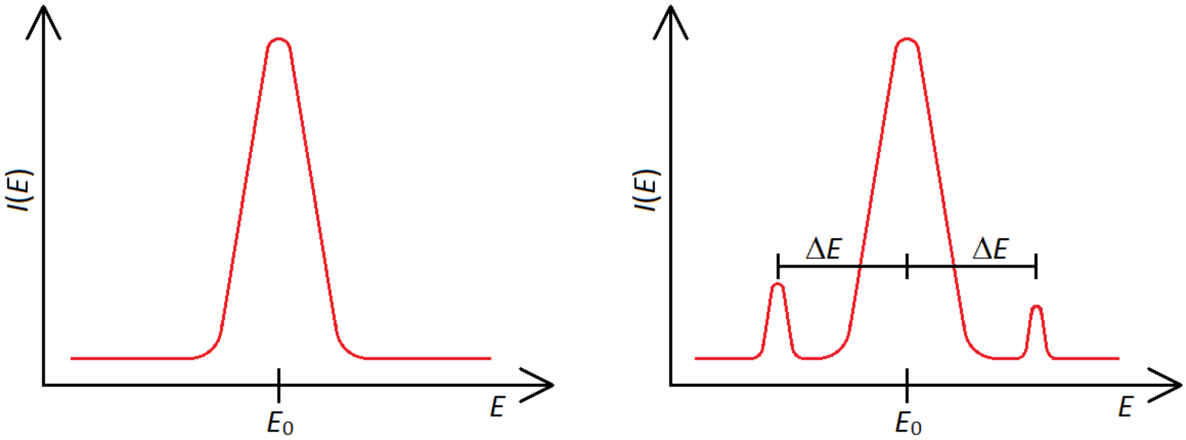

Figure 5: Schematic showing the neutron energy when all scattering is elastic (left) and the neutron energy when energy exchange to and from vibrational states occurs (right).

2.4.1.4.1.2 Rotational and translational motion

The quantisation of rotational and translational states is negligible compared to thermal and neutron energy, so energy exchange between the neutron and these energy states results in a broadening of the initially sharp energy distribution (Figure 6); this is quasielastic scattering. The width of the peak, δE, is related to the energy of the motion involved.

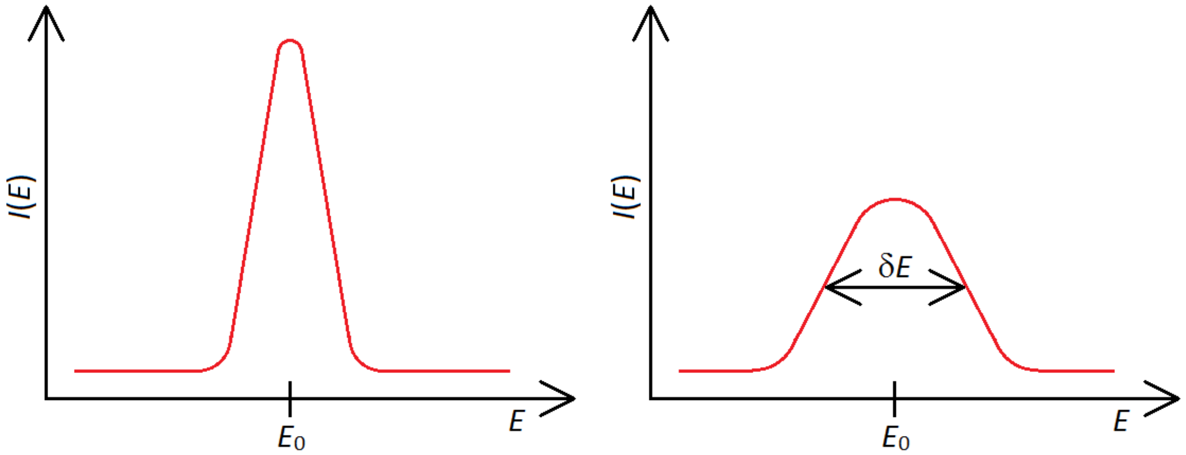

Figure 6: Schematic showing neutron energy when all scattering is elastic (left) and neutron energy when energy exchange to and from rotational and translational states occurs (right).

2.4.1.5 Debye–Waller factor

Even at very low temperatures, nuclei vibrate, causing a decrease in the elastic peak during quasielastic neutron scattering experiments, with the decrease becoming more pronounced as the temperature increases. If it is assumed that the vibrations are harmonic and isotropic, the drop in intensity follows the Debye–Waller factor (Equation 19).[152]

$$\text{Debye–Waller factor} = \langle exp(i\boldsymbol{Q}\cdot\boldsymbol{u})\rangle = exp(-\langle(\boldsymbol{Q}\cdot\boldsymbol{u})^2\rangle) = \frac{1}{3}exp(Q^2\langle u^2(T)\rangle)$$

Equation 19

2.4.1.6 Structural studies: differential scattering cross section

The differential scattering cross section normalised by a unit volume, $(\mathrm{d}\Sigma/\mathrm{d}\Omega)(Q)$, contains all the structural information about a system, including the size, shape, and interactions between the scattering centres in the sample. $(\mathrm{d}\Sigma/\mathrm{d}\Omega)(Q)$ is related to the scattering intensity, $I(Q)$, *via* Equation 20.

$$I(Q) = I_0(\lambda)\Delta\Omega\eta(\lambda)T(\lambda)V_s\frac{\partial\Sigma}{\partial\Omega}(Q)$$

Equation 20

$I_0(\lambda)$, the incident neutron flux, $\Delta\Omega$, the solid angle element determined by the size and position of the detector, and $\eta(\lambda)$, the detector efficiency, are instrument-dependent, while $T(\lambda)$, the neutron transmission of the sample, V_s, the sample volume impinged by the neutron beam, and $(\mathrm{d}\Sigma/\mathrm{d}\Omega)(Q)$ are sample-dependent. $(\mathrm{d}\Sigma/\mathrm{d}\Omega)(Q)$ is obtained by measuring the scattering from the sample, an empty cell, a calibration sample, and background noise; these are then used to calibrate the instrument using Equation 21.

$$\frac{\mathrm{d}\Sigma}{\mathrm{d}\Omega}(Q)_{\mathrm{sa}} = \frac{\left[\left(\frac{I(Q)_{\mathrm{sa}}}{\mathrm{count}_{\mathrm{sa}}} - \frac{I(Q)_{\mathrm{ba}}}{\mathrm{count}_{\mathrm{ba}}}\right) - \frac{T_{\mathrm{sa}}}{T_{\mathrm{ec}}} \times \left(\frac{I(Q)_{\mathrm{ec}}}{\mathrm{count}_{\mathrm{ec}}} - \frac{I(Q)_{\mathrm{ba}}}{\mathrm{count}_{\mathrm{ba}}}\right)\right]}{\left[\left(\frac{I(Q)_{\mathrm{ca}}}{\mathrm{count}_{\mathrm{ca}}} - \frac{I(Q)_{\mathrm{ba}}}{\mathrm{count}_{\mathrm{ba}}}\right) - \frac{T_{\mathrm{ca}}}{T_{\mathrm{ec}}} \times \left(\frac{I(Q)_{\mathrm{ec}}}{\mathrm{count}_{\mathrm{ec}}} - \frac{I(Q)_{\mathrm{ba}}}{\mathrm{count}_{\mathrm{ba}}}\right)\right]} \times \frac{{L_{\mathrm{sa}}}^2 t_{\mathrm{ca}} T_{\mathrm{ca}}}{{L_{\mathrm{ca}}}^2 t_{\mathrm{sa}} T_{\mathrm{sa}}} \times \frac{\partial\Sigma}{\partial\Omega}(Q)_{\mathrm{ca}}$$

Equation 21

where the subscripts ca, sa, ec and ba refer to the calibration standard, the sample, the empty cell, and the background, respectively; *L* is the sample–detector distance, *t* is the sample thickness, and *T* is the transmission.[86]

2.4.1.7 Dynamic studies: the dynamic structure factor

The dynamic structure factor, $S(Q,\omega)$, contains all the dynamic information about a system, and is measured during a QENS experiment; $\mathrm{S}(Q,\omega)$ relates the dynamics to the probability of a neutron being scattered with frequency ω and momentum change *Q*. The overall structure factor (Equation 22) is made up of the incoherent structure factor, $S_{\mathrm{inc}}(Q,\omega)$ (Equation 23), arising from incoherent scattering, and the coherent structure factor, $S_{\mathrm{coh}}(Q,\omega)$ (Equation 24), which arises from coherent scattering.[152]

$$S(Q,\omega) = S_{\mathrm{inc}}(Q,\omega) + S_{\mathrm{coh}}(Q,\omega)$$

Equation 22

$$S_{inc}(Q,\omega) = \frac{1}{2\pi}\int_{-\infty}^{+\infty}\sum_{i}\langle exp\big(-i\boldsymbol{Q}\cdot\boldsymbol{R}_i(0)\big)exp\big(-i\boldsymbol{Q}\cdot\boldsymbol{R}_i(t)\big)\rangle exp(-iwt)\mathrm{d}t$$

Equation 23

$$S_{coh}(Q,\omega) = \frac{1}{2\pi}\int_{-\infty}^{+\infty}\sum_{i,j}\langle exp\big(-i\boldsymbol{Q}\cdot\boldsymbol{R}_i(0)\big)exp\left(-i\boldsymbol{Q}\cdot\boldsymbol{R}_j(t)\right)\rangle\, exp(-iwt)\mathrm{d}t$$

Equation 24

$S_{\mathrm{inc}}(Q,\omega)$ describes the dynamics of individual particles, and contains no structural information, while $S_{\mathrm{coh}}(Q,\omega)$ describes correlations between nuclei, allowing access to the collective dynamics of the nuclei. However, the coherent scattering also results in a background arising from the elastic signal arising from the structural correlations.

2.4.1.8 Elastic incoherent structure factor

The elastic incoherent structure factor (EISF) measures the area of the elastic curve divided by the total area under the scattering curve, *i.e.* the fraction of the elastic contribution.

$$\mathrm{EISF} = A_0 = \frac{S_{\mathrm{inc}}^{\mathrm{el}}(Q)}{S_{\mathrm{inc}}^{\mathrm{el}}(Q) + S_{\mathrm{inc}}^{\mathrm{qel}}(Q)}$$

Equation 25

When localised motions occur, *e.g.* side group rotation, the scattering peak returns a finite value for the EISF, while diffusive behaviour results in an EISF of zero as the elastic peak experiences full broadening.

2.4.2 Small angle neutron scattering

Small angle neutron scattering (SANS) can be used to obtain structural information about a polymer system. SANS measures the coherent scattering of atoms, and the large difference in coherent scattering lengths for hydrogen and deuterium ($b_{\mathrm{H,coh}} = -0.37 \times 10^{-12}$ cm and $b_{\mathrm{D,coh}} = 0.66 \times 10^{-12}$ cm)[153] means that isotopic substitution can be employed to provide time-averaged information about a polymer’s structure.

2.4.2.1 Sample preparation

2.4.2.1.1 Sample pressing

For SANS, the nanocomposites had to be pressed into discs 15 mm in diameter and 0.5 mm thick. The following method was used for pressing the samples: the amount of composite required (~130 mg) was weighed into an aluminium dish, then transferred to a circular brass mould 15.8 mm diameter and 0.53 mm thick (see Figure 7). The die was sandwiched between two polished stainless steel plates and placed in a press that had been heated to 150 °C. The composite was allowed to equilibrate for 10 min; during this time the press was gradually closed so the hot plates were always in contact with the steel plates on both the top and bottom of the sample. After 10 min, the pressure was increased to 1.5 metric tons and the sample held at this temperature and pressure for 30 min. The press was cooled while maintaining the pressure on the sample; once cool, the sample was removed from the press. On removal from the press the composite discs were visually inspected for defects, such as air bubbles and cracks. If a sample was deemed to be faulty, additional composite was added to the die and the sample was returned to the press as before for a second pressing period. If a sample required annealing it was left in the mould, if not it was gently pressed out of the mould; in both cases, any excess composite was removed with a razor blade.

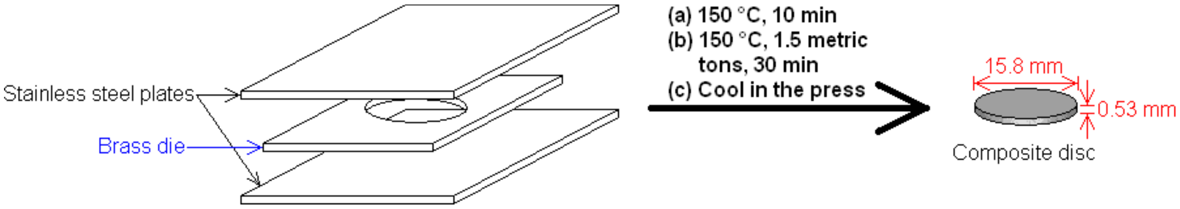

Figure 7: Schematic showing how the composite samples were pressed in preparation for SANS.

2.4.2.1.2 Sample annealing

Following pressing, several of the SANS samples were annealed to remove any stresses introduced during their processing. The samples that required annealing were left in their moulds following pressing, and laid, uncovered, on a stainless steel pressing plate and heated under vacuum in an oven at 150 °C for 3 h. After 3 h, the composites were removed from the oven and cooled to room temperature. The annealing times for the samples are recorded in Table 6; the times are significantly longer than the reptation times (longest relaxation times) for PS (42 s for 230 kg mol^{-1} PS at 150 °C).[154] One sample, 230A(0)_annealed2, was annealed twice (*i.e.* 6 h annealing time) in order to eliminate a large air bubble on the surface of the sample. Following annealing the composites were carefully pressed from their moulds.

Table 6: Annealing histories for the SWCNT–PS nanocomposite SANS samples

Sample name	**Annealing time (h)**
230A(0)_annealed1	3
230A(0)_annealed2	6^{a}
230C(1)_annealed	3
230E(2)_annealed	3
230F(3)_annealed	3
^{a}This sample was annealed twice to eliminate a large air bubble.	

2.4.2.2 Data collection

The SANS measurements were carried out using beamline D11 at Institut Laue Langevin (ILL), Grenoble, France;[155] this instrument is laid out as shown in Figure 8. The scattering from 20 samples was measured [110A(0)–110I(4), 230A(0)–230G(4) (see Table 4 for details of sample composition) and annealed versions of four 230k molecular weight samples: 230A(0)_annealed1, 230C(1)_annealed, 230E(2)_annealed and 230(3)_annealed (see Table 6 for further information)]; the samples were arranged in a 22-hole sample holder, as shown in Figure 9. Scattering was measured at three different sample–detector distances (1.502 m, 8.002 m and 38.999 m. These distances were chosen to allow the largest possible range of *Q* values to be covered; there is a slight overlap between the *Q* ranges for the three distances to make it easier to ensure the vertical alignment of the traces), using a neutron wavelength (λ) of 6 Å, giving a *Q*-range of 0.00147–0.428 Å^{-1}, where *Q* is the neutron wavevector.

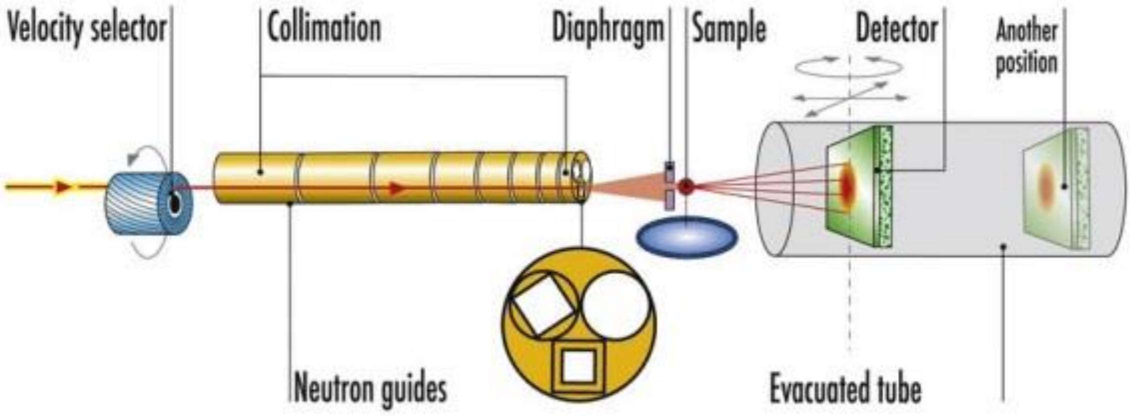

Figure 8: Schematic diagram of beamline D22 at ILL, Grenoble, France. This instrument set-up is the same as for beamline D11, which was used in the SANS experiment.

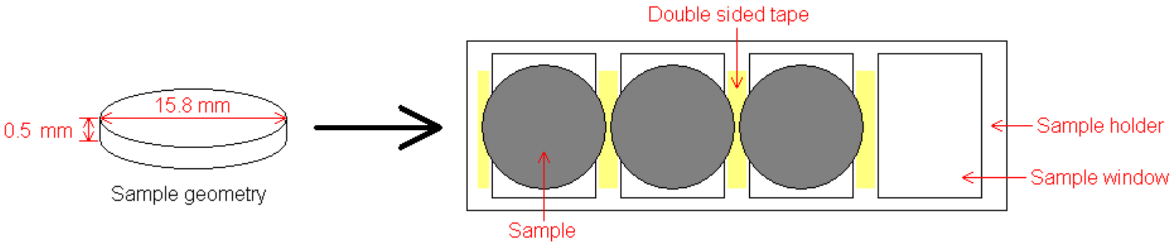

Figure 9: Schematic diagram of the sample holding arrangement for the SANS experiments. The sample holder had 22 sample positions, of which the first two were empty and the samples were inserted in the remaining 20 holes in the following order: 110A(0)–110I(4) (9 samples), 230A(0)–230G(4) (7 samples), 230A(0)_annealed1, 230C(1)_annealed, 230E(2)_annealed and 230(3)_annealed.

2.4.2.3 Sample data

Scattering was recorded as 2D detector images (Figure 36), which were then radially-averaged to give the differential scattering cross-section normalised by a unit volume, $d\Sigma/d\Omega(Q)$ (Figure 11), after reduction to correct for detector efficiency, normalisation against a water standard, and subtraction of the background (from background radiation hitting the detector and electronic leakage). The reduction and radial averaging were conducted by Isabelle Grillo, a beam scientist at ILL using the LAMP data reduction programme.[156, 157]

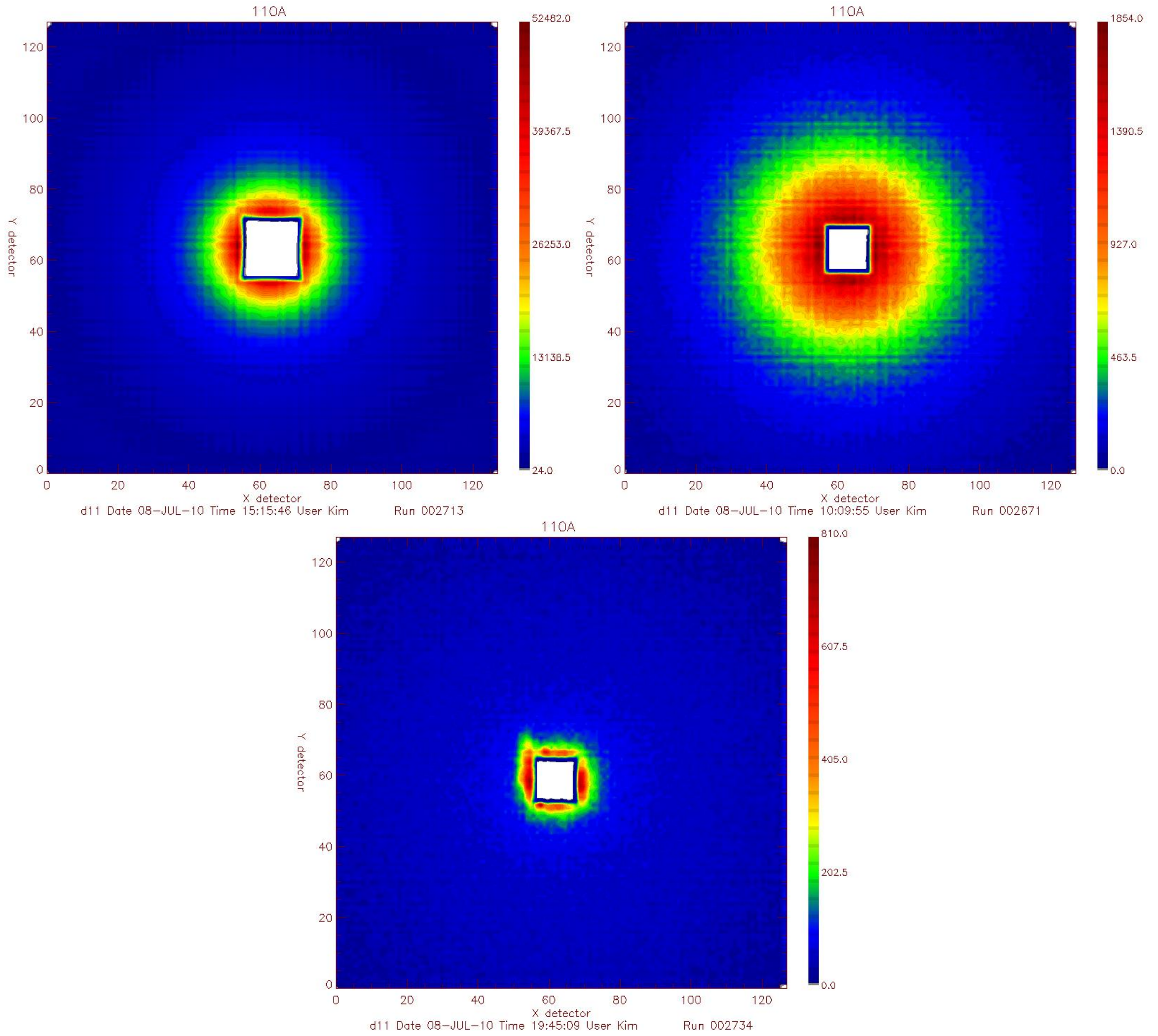

Figure 10: 2D SANS detector images for 110A (110 kg mol^{-1} with 0 wt% SWCNTs). Sample–detector distances: top left: 1.50 m; top right: 8.00 m; bottom: 39.0 m.

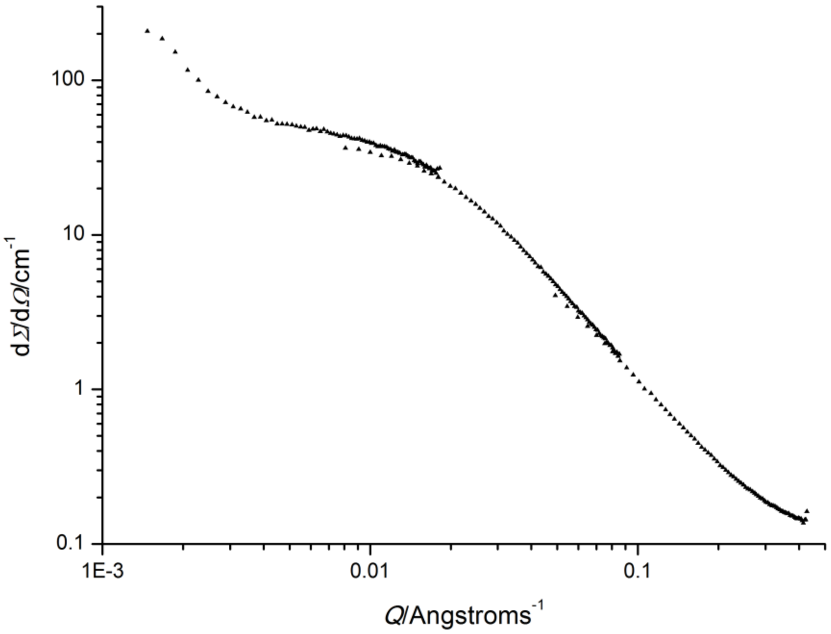

Figure 11: Plot of the unshifted SANS data for 110k PS with 0 wt% SWCNTs.

2.4.3 Quasielastic neutron scattering

Quasielastic neutron scattering (QENS) can be used to provide information about the dynamics within a polymer system as a function of length scale.[93, 120] In QENS, the scattering signal is dominated by the incoherent scattering cross-section of hydrogen ($b_{\mathrm{H,inc}}$ = 25.2 × 10^{-12} cm and $b_{\mathrm{D,inc}}$ = 4.0 × 10^{-12} cm)[158], and selective deuteration allows us to elucidate different parts of the monomer unit.

2.4.3.1 Sample preparation

In order to be used for QENS, the nanocomposites had to be pressed into *ca*. 6.5 cm × 3.2 cm rectangular films, 0.1 mm in thickness; this requires approximately 0.3 g of powdered nanocompsite. This sample thickness was chosen to give a neutron transmittance of around 90%, preventing multiple scattering and ensuring sufficient scattering to obtain data at an acceptable rate.

The nanocomposite films were prepared as follows: the nanocomposite was sandwiched between the centres of two aluminium foil covered stainless steel plates. These plates were placed in a heated press (B13142 Graseby Specac 15.011 15 ton IR press) held at 150 °C. The plates were closed and tightened, and the sample was allowed to equilibrate for 5–10 minutes before between 2 and 5 tons of pressure was applied for between 5 and 45 minutes. The samples were cooled in the press, then removed from the press between pressings and broken up; the pieces were rearranged as necessary for the polymer to cover the entire sample area. This process was repeated until the sample had formed a single uniform film. None of the samples produced were entirely even, and were often slightly thicker in the centres than at the edges, however, all samples covered the entire sample area required.

2.4.3.2 Data collection

QENS experiments were carried out on the time-of-flight inverted-geometry crystal analyser backscattering spectrometer, IRIS, at ISIS Neutron and Muon Facility, Rutherford Appleton Laboratory, Oxford, UK; this instrument is laid out as shown in Figure 12. A comprehensive list of data recorded is shown in Table 7 and Table 8. The configuration selected – using the 002 reflection of a pyrolytic graphite analyser – gives an energy resolution of 17.5 μeV, energy window $-0.56 \leq \Delta E \leq 0.68$ meV, and wavenumber range $Q = 0.442$–1.85 Å^{-1}. This set-up allows us to probe motions at timescales ranging from 0.4 to 200 ps and lengthscales from 4 to 16 Å. The as-pressed film samples were wrapped in Al foil and rolled into annular aluminium cans of 20 mm diameter to ensure full detector coverage. Resolution spectra, fixed window (elastic) scans ($\Delta E \approx 0$) and inelastic spectra were recorded.

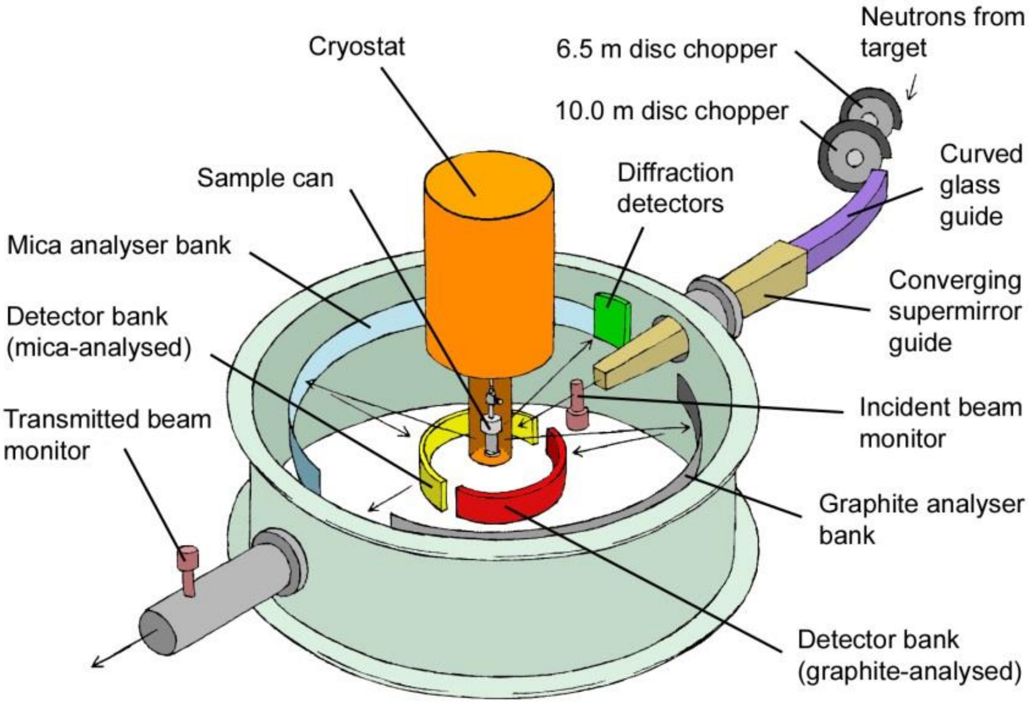

Figure 12: Schematic of the IRIS beamline at ISIS, Oxford, UK. Figure taken from the ISIS website.[159]

Table 7: Details of data recorded on ring-hydrogenated PS at ISIS and NIST between 2010 and 2014

Sample		**h5A(0)**	**h5B(0.1)**	**h5C(0.4)**	**h5H(0.4)**	**h5D(1)**	**h5E(2)**	**h5F(3)[a]**	**h5G(4)**
Resolution[b]		2010	—	—	2013	—	—	—	—
Elastic scan	**IRIS**	2010	2010	2010	2013	2011	2011	—	2010
	HFBS	Y	—	—	Y	—	—	—	Y
QENS (IRIS)	**250 K[c]**	2010	2011	2010	—	2011	2011	—	2010
	280 K[c]	2010	2011	2010	—	2011	2011	—	2010
	310 K[c]	2010	2011	2010	—	2011	2011	—	2010
	340 K	2010	2011	2010	2013	2011	2011	—	2010
	370 K	2010	2011	2010	2013	2011	2011	—	2010
	400 K	2010	2011	2010	2013	2011	2011	—	2010
	425 K	2010	2011	2010	2013	2011	2011	—	2010
	450 K	2010	2010	2010	2013	2011	2011	—	2010
QENS (HFBS)		—	—	—	Y	—	—	—	—

[a]This sample was made, but no data were recorded for it. [b]No resolution run was recorded for the h5 2011 data. [c]Data were recorded only for some samples at these temperatures as it was concluded that nothing really happens before T_g.

Table 8: Details of data recorded on chain-hydrogenated PS at ISIS and NIST between 2013 and 2014

Sample		**h3A(0)**	**h3B(0.1)**	**h3C(0.4)**	**h3D(1)**	**h3E(2)**	**h3F(3)**	**h3G(4)**
Resolution		2013	2014	—	—	—	—	—
Elastic scan	**IRIS**	2013	2014	2013	2014	2014	2014	2013
	HFBS	Y	Y	Y	—	—	—	Y
QENS (IRIS)	**340 K**	2013	2014	2013	2014	2014	2014	2013
	370 K	2013	2014	2013	2014	2014	2014	2013
	400 K	2013	2014	2013	2014	2014	2014	2013
	425 K	2013	2014	2013	2014	2014	2014	2013
	450 K	2013	2014	2013	2014	2014	2014	2013

Additional elastic scans were conducted on the backscattering spectrometer HFBS[160] at the National Institute of Standards and Technology (NIST), Gaithersburg, MD, USA (see Table 8 for details on which samples were run). The configuration selected gives an energy resolution of 1 μeV (FWHM, full width at half maximum) and wavenumber range Q = 0.25–1.75 Å^{-1}; a neutron wavelength of 6.271 Å was used. As for the IRIS experiments, the film samples were mounted in annular aluminium cans to ensure full detector coverage.

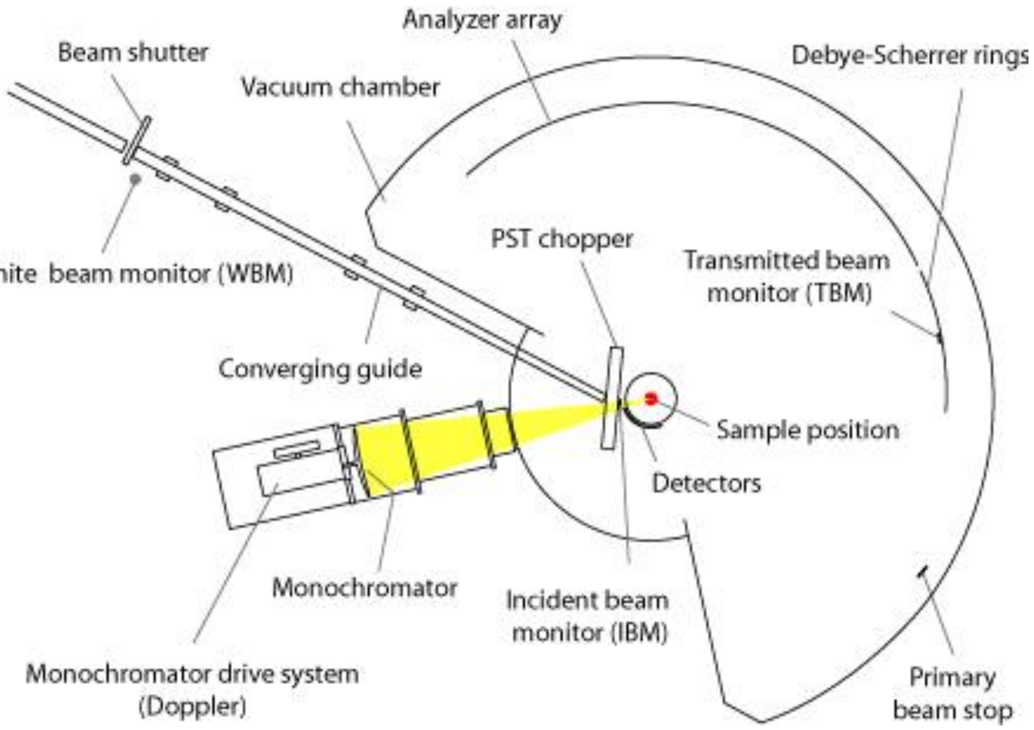

Figure 13: Schematic of the HFBS beamline at NIST, MD, USA. Figure taken from the NIST website.[161]

2.4.3.3 Sample data

2.4.3.3.1 Elastic scans

Elastic scans were recorded over a temperature range 41–453 K (IRIS: 43–453 K; NIST: 41–450 K), obtained using a cryofurnace, with measurements being taken every 10 K up to 303 K and every 5 K from 308 K onwards (IRIS), or approximately every 1 K (NIST); full details can be seen in Table 7 and Table 8. These measurements record the integrated intensity within a narrow energy window as a function of T and Q. As the temperature increases, the scattering goes from being purely elastic to having an inelastic component arising from rotational and translational motions within the polymer chain; these motions cause the peak to broaden and the intensity of the fixed window scan to drop (Figure 14). A sample elastic scan is shown in Figure 15. The root mean square amplitude $\langle u^2\rangle^{1/2}$ can be obtained from the fixed window scan as the intensity should decrease as $\exp(Q^2\langle u^2\rangle/3)$.[31]

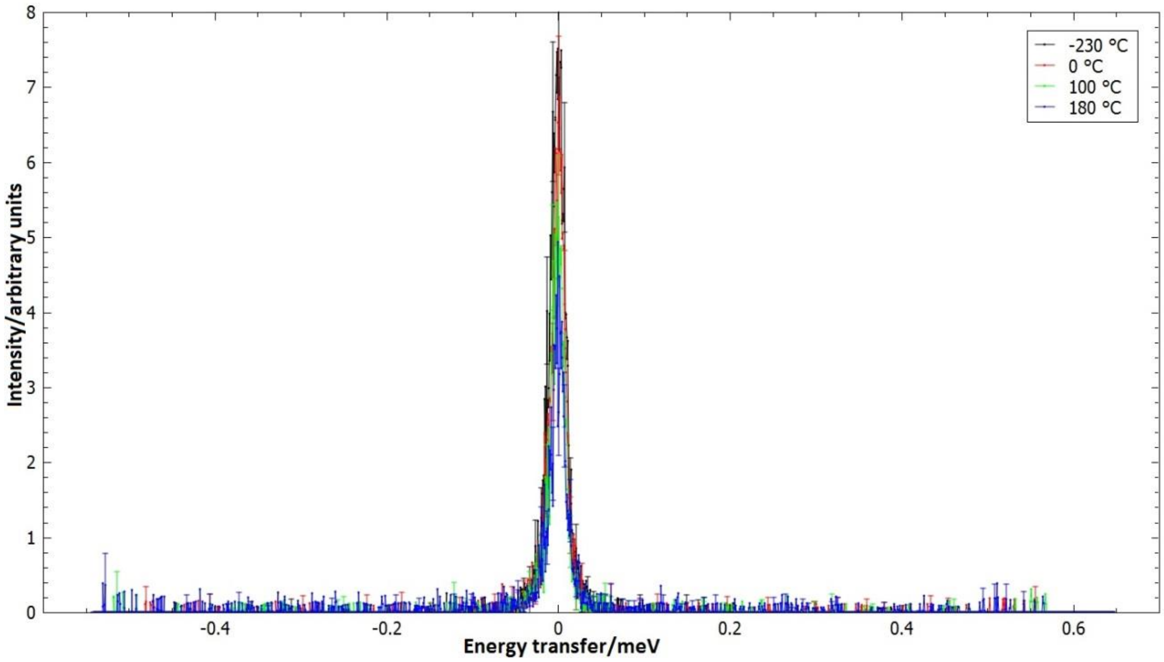

Figure 14: Sample elastic scan peaks from chain-hydrogenated PS with 0.1 wt% SWCNTs at *Q* = 1.725 Å^{-1} and four different temperatures (–230 °C, black; 0 °C, red; 100 °C, green; 180 °C, blue). The reduction in intensity is caused by the scattering changing from elastic to quasielastic with increasing temperature. The data is noisy because of low sampling statistics.

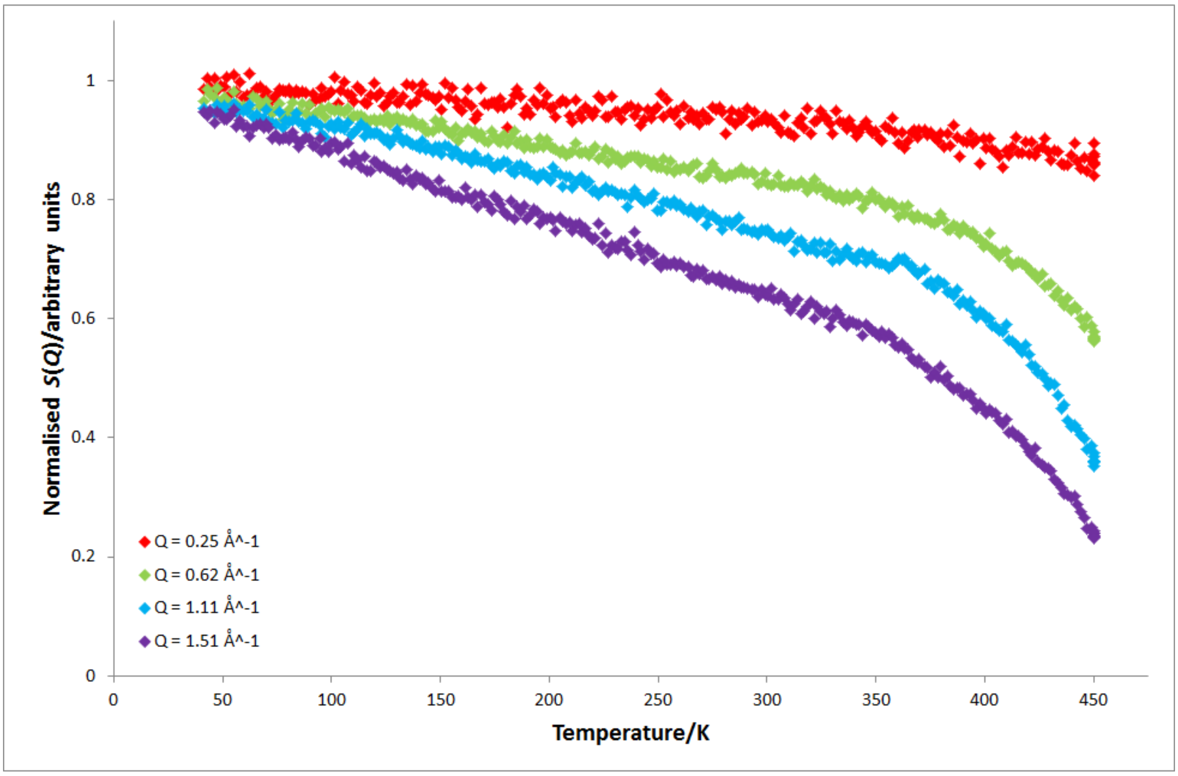

Figure 15: Sample elastic scan (at 1 μeV resolution) of pure chain-hydrogenated (h3) PS from *T* = 41.57–450.14 K, at selected wavenumbers *Q* ranging from 0.25 to 1.51 Å^{-1}. The data were recorded at NIST and the results are normalised by the elastic intensity extrapolated to 0 K.

2.4.3.3.2 Quasielastic scans

Full details of the data recorded for each sample are shown in Table 7 and Table 8. The QENS temperatures explored were chosen based on the elastic scan from the pure h5 PS sample recorded from 45 to 453 K (Figure 16). At all *Q* values this plot is linear in appearance after *ca*. 100 K, indicating a localised motion with an Arrhenius temperature dependence and an activation temperature of approximately 100 K. As the plot did not display any regions that had features of specific note, it was decided that each sample should be characterised in detail, and therefore QENS experiments were run at 250, 280, 310, 340, 370, 400, 425 and 450 K for the h5 PS 0%, 0.1%, 0.4%, 1%, 2% and 4% samples. The experiments on the h3 PS samples were conducted at a later date, by which point it had been concluded that the QENS data collected far below T_g (the T_g of PS is 373 K)[110] did not provide any more information than could be obtained from a QENS experiment run at 340 K, and for these samples QENS runs were conducted at 340, 370, 400, 425 and 450 K, omitting the lower temperatures.

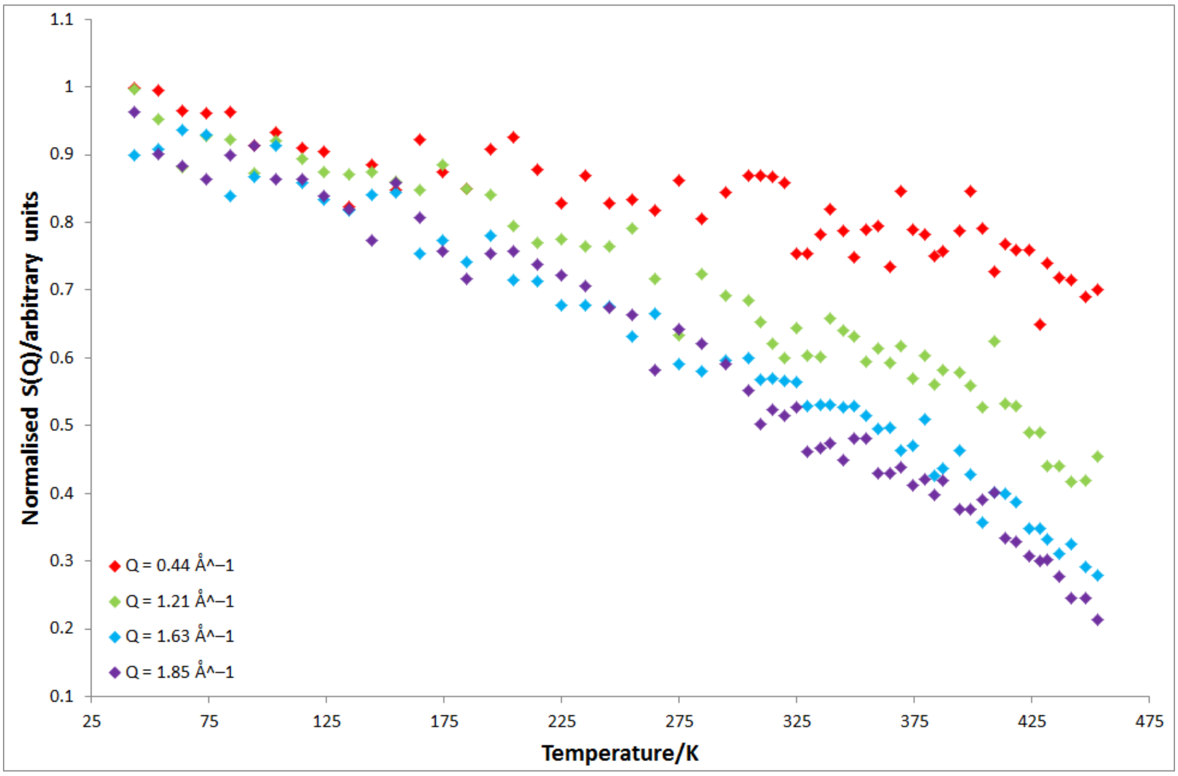

Figure 16: Elastic scan of pure chain-hydrogenated polystyrene from *T* = 45–453 K, at selected wavenumbers *Q* ranging from 0.44 to 1.85 Å^{-1}. The data were recorded at ISIS and the results are normalised by the elastic intensity extrapolated to 0 K. The linear nature of the plot indicates a localised motion with Arrhenius temperature dependence and an activation energy around 100 K.

A sample quasielastic neutron scan can be seen in Figure 17; this figure shows the broadening of the peak from the polymer sample relative to the resolution peak. This broadening can provide information about the dynamic processes occurring in a system.

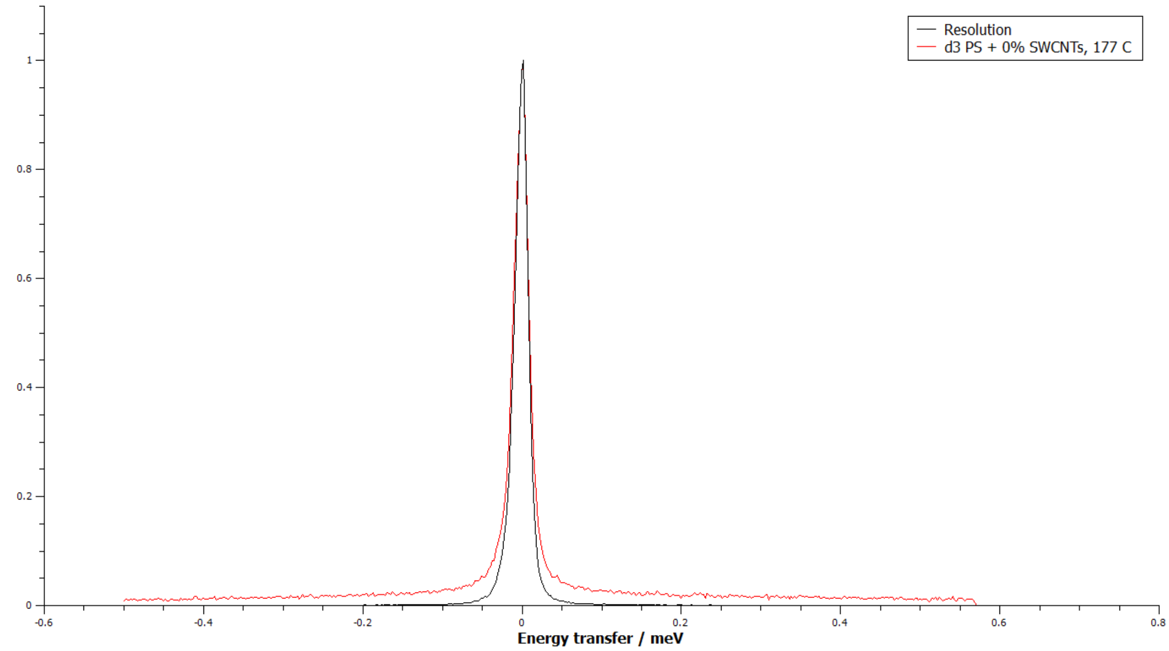

Figure 17: Sample normalised QENS peaks comparing ring-hydrogenated PS at 177 °C to the resolution scan at Q = 1.85 Å^{-1}. Peak broadening in the polymer sample is indicative of dynamic processes occurring. The data is less noisy that that in Figure 14 because of much higher sampling statistics

Chapter 3: Small angle neutron scattering

3.1 Introduction

Inspired by the work of Mu *et al.*, which identified a minimum in the diffusion coefficient of a system of polystyrene and carbon nanotubes at the percolation threshold,[129, 130] this chapter begins to address whether single walled carbon nanotubes affect the polymer chain conformation in a series of PS/SWCNT nanocomposites. According to the reptation model, the diffusion coefficient is proportional to the size of the polymer chain (R), and inversely proportional to the relaxation time (τ) for the polymer to diffuse from its original tube (Equation 26).[51]

$$D \propto \frac{R^2}{\tau}$$

Equation 26

If it is assumed that τ is not affected by the addition of carbon nanotubes to a polymer matrix, the measure of polymer size used here, the radius of gyration, R_g, should be expected to exhibit a similar trend to that seen in D on increasing CNT concentration, *i.e.* a minimum followed by a gradual return towards bulk values.

Small angle neutron scattering records the coherent scattering from a sample to provide information about the structure within that sample. In a system containing both hydrogenous and deuterated polystyrene, the coherent scattering is dominated by the scattering from the deuterium atoms (Table 9); here a mixed system of 10% deuterated PS and 90% hydrogenated PS is used to highlight 'isolated' polymer chains in their natural state. By fitting the scattering data the radius of gyration can be obtained and the effect of the nanotubes on this value can be identified.

Table 9: Coherent scattering lengths of hydrogen, carbon and polystyrene[162]

Species	b_{coh}**/1E–15 m**
Hydrogen	–3.7406
Deuterium	6.671
Carbon[a]	6.6460
hPS (C_8H_8)[b]	23.2432
dPS (C_8D_8)[b]	106.5384

[a] Average value based on the natural abundances of C12 and C13.

[b] Calculated from the scattering length densities of the individual atoms in a repeat unit.

3.2 Results and analysis

3.2.1 Data reduction

All SANS data were reduced to correct for detector efficiency, normalised against a water standard, and the background (from background radiation hitting the detector and electronic leakage) was subtracted by Isabelle Grillo at ILL using the LAMP data reduction programme.[156, 157]

3.2.2 Vertical shifting of data

For each sample, data were collected across three Q ranges, where Q is the neutron wavevector, calculated using Equation 27, where λ is the neutron wavelength and θ is the scattering angle.

$$Q = \left(\frac{4\pi}{\lambda}\right)\sin\theta/2$$

Equation 27

The three data sets can be combined to produce one continuous data set that crosses the full Q range. Following data reduction, the data acquired from the three different Q ranges [$\mathrm{d}\Sigma/\mathrm{d}\Omega$ the differential scattering cross-section normalised by a unit volume, which is commonly reported as the intensity, $I(Q)$] do not align vertically (see Figure 18), but can be vertically aligned by applying a multiplication factor, as follows.

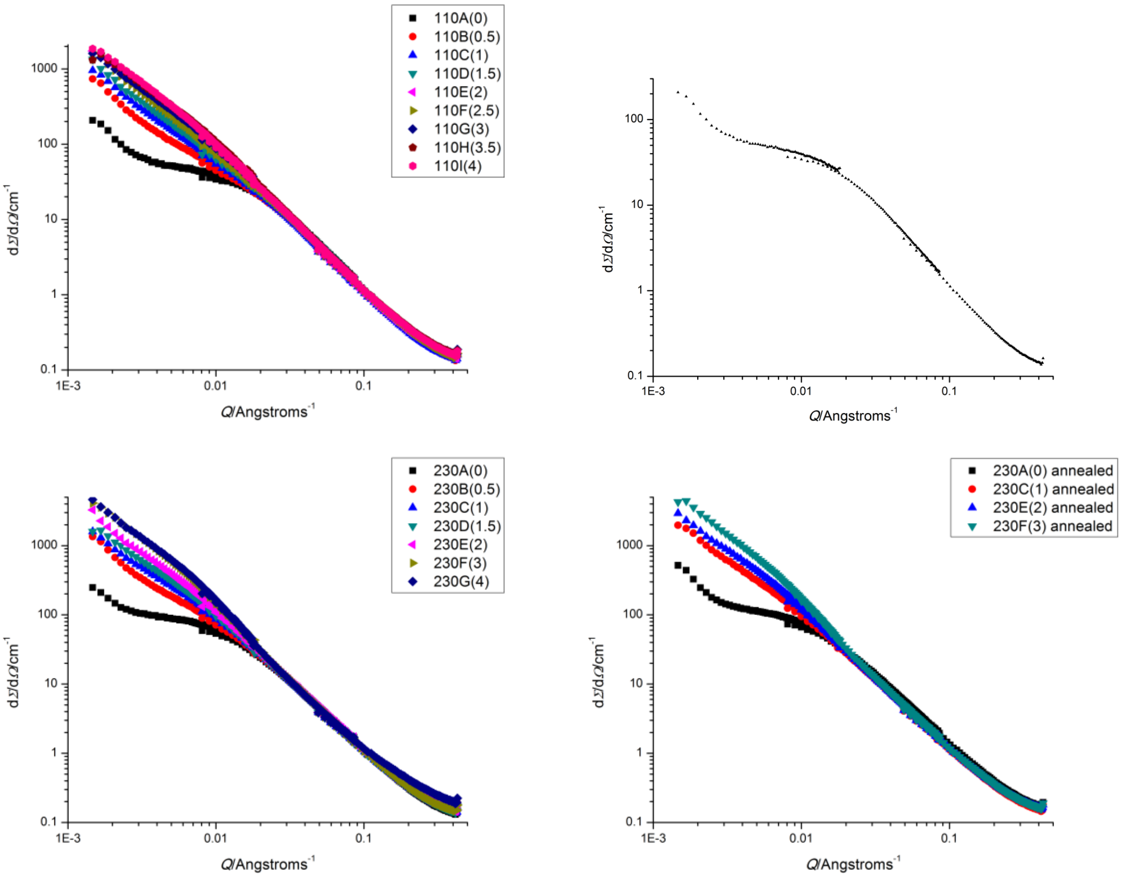

Figure 18: Plots of the unshifted SANS data; top left: 110k PS with 0–4 wt% SWCNTs; top right: 110k PS with 0 wt% SWCNTs; bottom left: 230k PS with 0–4 wt% SWCNTs; bottom right: annealed 230k PS with 0–3 wt% SWCNTs. The 110k PS with 0 wt% SWCNTs plot (top right) highlights the vertical misalignment of the three *Q* regions.

First, the high-*Q* data, which has the smallest error in scattering intensity of the three data sets, are compared to the intermediate-*Q* data. For each value of *Q* for which there is equivalent $d\Sigma/d\Omega$ data (the *Q* values are not necessarily exactly the same, but are the same within 1% and the difference is generally much lower) in both data sets, a multiplication factor is calculated, and these values are averaged. All the intermediate-*Q* values are then multiplied by this average multiplication factor to give shifted $d\Sigma/d\Omega$ values that overlay the high-*Q* values, with the high-*Q* tail of the intermediate-*Q* data overlaying the low-*Q* end of the high-*Q* data. Once this has been completed, the shifted intermediate-*Q* values are compared to the low-*Q* data, and the low-*Q* data are shifted in a manner analogous to the shifting of the intermediate-*Q* data. See Table 10 and Table 11 for the averaged multiplication factors for both the intermediate and low-*Q* data; the vertically aligned data are shown in Figure 19.

Table 10: Averaged multiplication applied to the intermediate and low-*Q* 110k PS $d\Sigma/d\Omega$ data to ensure vertical alignment with the high-*Q* data

Sample	**Intermediate-*Q***			**Low-*Q***		
	Multiplication factor	**Standard deviation**	**% error**	**Multiplication factor**	**Standard deviation**	**% error**
110A(0)	0.903	0.032	3.5	0.815	0.037	4.5
110B(0.5)	0.909	0.037	4.1	0.825	0.027	3.2
110C(1)	0.920	0.038	4.1	0.838	0.023	2.8
110D(1.5)	0.907	0.042	4.6	0.834	0.052	6.3
110E(2)	0.895	0.034	3.8	0.851	0.019	2.3
110F(2.5)	0.895	0.036	4.0	0.842	0.038	4.5
110G(3)	0.901	0.039	4.3	0.827	0.024	2.9
110H(3.5)	0.917	0.033	3.6	0.886	0.038	4.3
110I(4)	0.920	0.042	4.5	0.853	0.034	4.0

Table 11: Averaged multiplication applied to the intermediate and low-*Q* neat and annealed 230k PS dΣ/dΩ data to ensure vertical alignment with the high-*Q* data

Sample	**Intermediate-*Q***			**Low-*Q***		
	Multiplication factor	**Standard deviation**	**% error**	**Multiplication factor**	**Standard deviation**	**% error**
Unannealed samples						
230A(0)	0.891	0.039	4.3	0.806	0.041	5.0
230B(0.5)	0.895	0.036	4.0	0.822	0.025	3.0
230C(1)	0.902	0.037	4.1	0.842	0.040	4.7
230D(1.5)	0.901	0.031	3.4	0.842	0.017	2.1
230E(2)	0.894	0.044	5.0	0.832	0.054	6.4
230F(3)	0.903	0.038	4.2	0.852	0.031	3.6
230G(4)	0.920	0.046	5.0	0.860	0.054	6.3
Annealed samples						
230A(0) annealed	0.903	0.034	3.8	0.811	0.034	4.2
230C(1) annealed	0.907	0.035	3.8	0.831	0.033	4.0
230E(2) annealed	0.909	0.040	4.4	0.853	0.043	5.1
230F(3) annealed	0.915	0.034	3.7	0.880	0.022	2.4

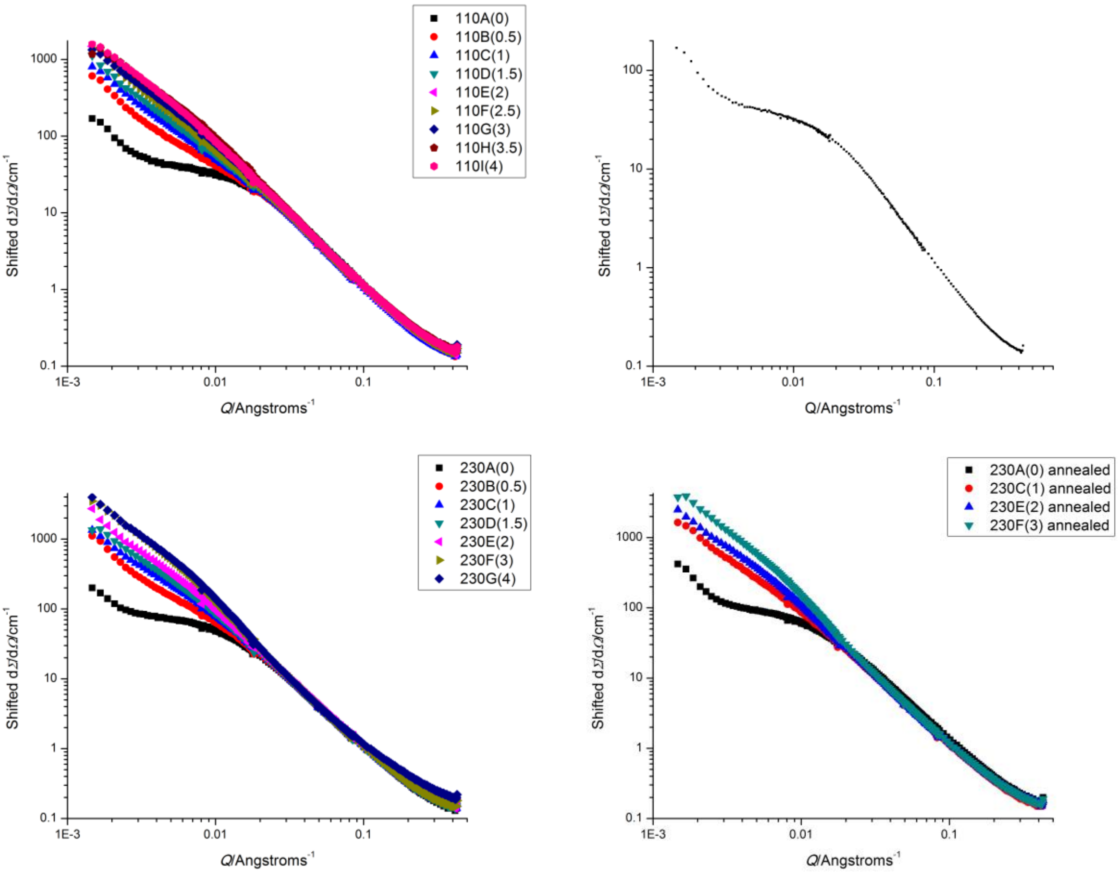

Figure 19: Plots of the shifted SANS data; top left: 110k PS with 0–4 wt% SWCNTs; top right: 110k PS with 0 wt% SWCNTs; bottom left: 230k PS with 0–4 wt% SWCNTs; bottom right: annealed 230k PS with 0–3 wt% SWCNTs. The 110k PS with 0 wt% SWCNTs plot (top right) highlights the improved vertical of the three *Q* regions.

3.2.3 Data fitting

3.2.3.1 Aim and equations used

The primary aim in fitting the SANS data was to obtain the radius of gyration, R_g, and see how it changes as a function of nanotube concentration. The R_g can be obtained by fitting the scattering data.

The scattering intensity of Gaussian polymer chains is given by Equation 28:[86]

$$\begin{aligned} \frac{\mathrm{d}\Sigma}{\mathrm{d}\Omega} &= V\varphi\Delta\rho^2 P(Q)_{\mathrm{polymer}} \\ &= V\varphi\Delta\rho^2 \frac{1}{N^2}\left[N\frac{1+b}{1-b} - 2b\frac{1-b^N}{(1-b)^2}\right] \\ b &= \exp\left(-l_{\mathrm{K}}{}^2 Q^2/6\right) \end{aligned}$$

Equation 28

where $P(Q)_{\mathrm{polymer}}$ is the single chain form factor, N is the number of Kuhn monomers, l_{K} is the Kuhn length, φ is the polymer volume fraction and $\Delta\rho^2$ is the scattering length density contrast between the polymer chains and the matrix.

$\frac{\mathrm{d}\Sigma}{\mathrm{d}\Omega}$ can be approximated using the Zimm approximation, which is a limited development of $\frac{\mathrm{d}\Sigma}{\mathrm{d}\Omega}$,[163] given in Equation 29.

$$\frac{1}{\frac{\mathrm{d}\Sigma}{\mathrm{d}\Omega}} = \frac{1}{V\Phi_{\mathrm{polymer}}\Delta\rho^2}\left(1 + \frac{{R_g}^2}{3}Q^2\right)$$

Equation 29

The first approach taken was to fit the experimental data with the Zimm equation, including contributions to scattering from the nanotubes, defects, and incoherent scattering (Equation 30).

$$\frac{\mathrm{d}\Sigma}{\mathrm{d}\Omega} = AQ^{-n} + \frac{B}{1 + CQ^2} + D$$

$$\text{where } C = \frac{{R_\mathrm{g}}^2}{3}$$

Equation 30: Zimm equation

In , AQ^{-n} represents the small angle upturn from the nanotubes and defects in the sample, *e.g.* microbubbles and voids: at very low scattering angles the scattering is dominated by scattering from voids and defects in the samples, which is given by Porod's law[164, 165] (Equation 31):

$$\frac{\mathrm{d}\Sigma}{\mathrm{d}\Omega} = \frac{2\pi(\Delta\rho)^2 S}{Q^4}$$

Equation 31

where $\Delta\rho$ is the difference in scattering length density between the matrix and the void, and S is the total surface area of boundaries in the sample. The scattering from defects and voids varies as Q^{-4}. The prefactor A in Equation 30 is proportional to $\Delta\rho$ and S, but also depends on the volume fraction of nanotubes in the sample and AQ^{-n} will vary with Q^{-2} if a rod network is present in the sample,[166, 167] as would be contributed by the nanotubes. $\frac{B}{1+CQ^2}$ corresponds to the single chain contribution, with the pre-factor B taking into account scattering length densities, monomer volumes, the degree of polymerisation and the volume ratio of polymers (as described in Equation 29). The final term, D, represents the constant background contributed by incoherent scattering from the hydrogen atoms present in the nanocomposites; this scattering does not provide any structural information. The Zimm equation is more stable than the Debye equation (Equation 32), and was therefore used to give an indication of whether the Debye equation is likely to fit the scattering data, and to provide appropriate starting values for the Debye fitting.

The second equation used to extract the R_g from the data is the Debye equation (Equation 32). This equation has a very similar form to the Zimm equation:

$$\mathrm{d}\Sigma/\mathrm{d}\Omega = AQ^{-n} + B\left\{\frac{2}{u^2}[u - 1 + exp(-u)]\right\} + D$$
$$\text{where } u = Q^2 {R_\mathrm{g}}^2$$

Equation 32: Debye equation

As for the Zimm equation, AQ^{-n} represents the small angle upturn from the nanotubes and defects in the sample, and D corresponds to incoherent scattering arising from the hydrogen atoms present in the nanocomposites. The only difference between the two equations is that the central term of the Zimm equation, $\frac{B}{1+CQ^2}$, is replaced by the expanded term $B\left\{\frac{2}{u^2}[u - 1 + \exp(-u)]\right\}$, which corresponds to Debye approximation[31, 165] of the single chain contribution (Equation 28), which applies for large N.

3.2.3.2 Data truncation

Prior to conducting any fitting, the data were examined, and any irregularities at low and high Q eliminated. The data for sample 110A(0) is shown in the left hand image in Figure 20 as an example. This data set displays a slight plateau at low Q, and a slight upturn at high Q. As these irregularities are at the extremes of the data, they may be due to instrumental error: at very low Q the blocking of the beam by the beamstop is not perfect, and at very high Q, the radial average of the data on a square detector only takes into account very few of the detector's pixels; however, the slight upturn at high Q may in fact be due to monomer–monomer interactions. In order to make the fitting simpler, for this data set, the first two (Q = 0.00147 and 0.00167 Å^{-1}) and final three (Q = 0.42, 0.424 and 0.428 Å^{-1}) data points were omitted from the fitting range, this removed the slight plateau at low Q, and the slight upturn at high Q, as can be seen in the right hand image in Figure 20. This process was repeated for all data sets, and details of the data points omitted can be found in Table 12 and Table 13.

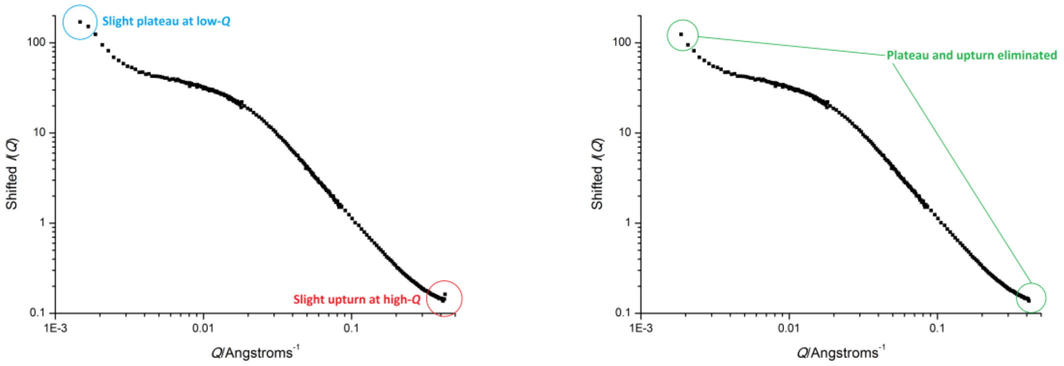

Figure 20: Plot of the shifted data for sample 110k PS with no nanotubes: left: before truncation the data shows a slight plateau at low *Q* and a slight upturn at high *Q*; right: after truncation the plateauing and upturn have been eliminated.

Table 12: Details of the data points omitted from the 110k PS SANS data sets in order to eliminate any low and high *Q* irregularities

Sample	**Low-*Q* points omitted/Å^{-1}**	**High-*Q* points omitted/Å^{-1}**
110A(0)	0.00147, 0.00167	0.42–0.428
110B(0.5)	0.00147	0.415–0.428
110C(1)	0.00147	0.415–0.428
110D(1.5)	0.00147	0.428
110E(2)	0.00147	0.42–0.428
110F(2.5)	0.00147	0.407–0.428
110G(3)	0.00147	0.428
110H(3.5)	0.00147, 0.00167	0.428
110I(4)	0.00147	0.428

Table 13: Details of the data points omitted from the 230k PS SANS data sets in order to eliminate any low and high *Q* irregularities

Sample	**Low-*Q* points omitted/Å^{-1}**	**High-*Q* points omitted/Å^{-1}**
Unannealed samples		
230A(0)	—	0.415–0.428
230B(0.5)	0.00147	0.42–0.428
230C(1)	—	0.428
230D(1.5)	0.00147	0.42–0.428
230E(2)	—	0.42–0.428
230F(3)	—	0.428
230G(4)	—	0.424, 0.428

3.2.3.3 110A(0) fitting

The protocol for fitting the Zimm and Debye functions to all the $d\Sigma/d\Omega$ data was established using the data from the 110A(0) sample, *i.e.* the 110k PS sample with no nanotubes.

3.2.3.3.1 110A(0) data: Zimm fitting

Once any irregular points had been omitted, the 110kA(0) data set was fitted to the Zimm equation (); fitting was conducted in Origin.[168] The fitting was conducted in two steps: the first step was to allow Origin to automatically fit all the parameters. The starting values and limits for the fitting are given in Table 14; the initial values are 'best guesses' for the system. This approach produced a fit that was good at low and intermediate *Q*, but poor at high *Q*, because of an underestimation of *D* (Figure 21, left). In order to improve the fit at high *Q*, a more realistic value of *D* (*ca*. 0.1) was selected, fixed (as allowing this value to vary consistently resulted in an over or underestimation), and the remaining parameters were refitted, using the values of the parameters from the first round of fitting as the starting values for the second round of fitting. The value of *D* was systematically varied at 0.005 intervals around 0.1 until the fit at high *Q* had been improved as far as possible, then the value of *D* was varied at smaller increments to further improve the fit (Figure 21, right).

Table 14: Starting values and limits for the initial fitting of the Zimm function to the $\mathrm{d}\Sigma/\mathrm{d}\Omega$ for 110A(0)

Parameter	**Units**	**Lower limit**	**Initial value for the first round of fitting**	**Initial value for the second round of fitting**
A	—	0	0	7.61E-9
n	—	0	1	3.67
B	—	0	10	43.1
C	Å^2	0	3333[a]	3430
D	cm^{-1}	0	0	Variable[b]

[a] Based on an R_g value of 100 Å for 110k PS:[169] $\langle R_0\rangle^2 = 0.434M$; $\langle R_0\rangle_{110\mathrm{k}}{}^2 = 47740\ \text{Å}^2$; $R_\mathrm{g}{}^2 = \frac{\langle R_0\rangle^2}{6} = 7957\ \text{Å}^2$; $R_\mathrm{g} = 89.2\ \text{Å}$.

[b] The value of *D* was varied in 0.005 increments starting with a value of 0.1; once the fit had been improved as far as possible, the increment was reduced to 0.001 until the fit had been optimised.

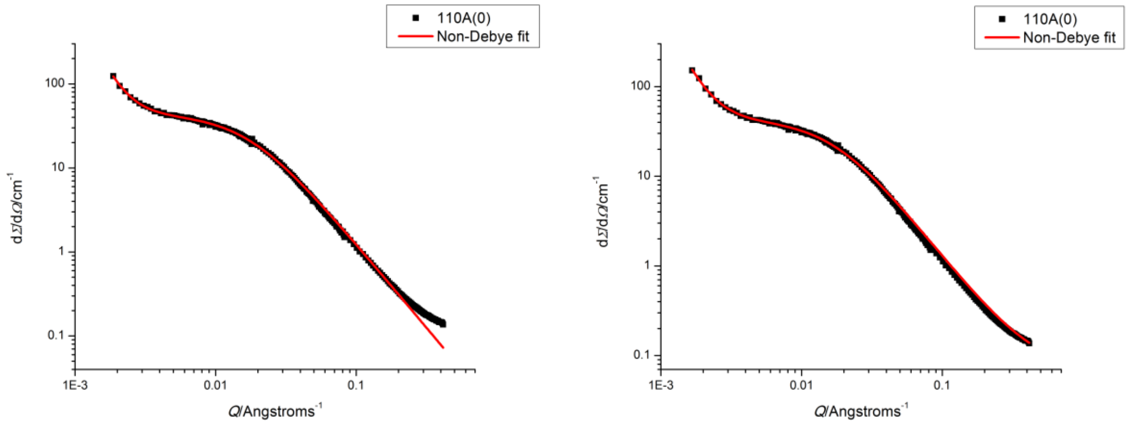

Figure 21: Left: first attempt at the Zimm fitting of the 110A(0) data set. All parameters were allowed to vary freely. The fit is good at low and intermediate *Q*, but poor at high *Q* due to an underestimation of the value of *D* (*D* = 0). Right: second attempt at the Zimm fitting of the 110A(0) data set. *D* was fixed at 0.065, and all other parameters were allowed to vary freely around starting parameters extracted from the first round of fitting.

3.2.3.3.2 110A(0) data: Debye fitting

Following optimised fitting to the Zimm function, the 110A(0) data was fitted with the Debye function (Equation 32). The fitting was conducted in Origin.[168] Again the fitting was conducted in two steps: first Origin automatically fitted all the parameters simultaneously, but rather than using the 'best guesses' that were used for the Zimm fitting, the final fitted values from the Zimm fit were used (Table 15). As for the Zimm fitting, this first round of fitting produced a good fit at low and intermediate *Q*, but the fit was poor at high *Q*, because the value of *D* was overestimated (Figure 22, left). Following the first round of fitting to the Debye function, the value of *D* was varied as in the Zimm fitting to optimise the fit (Figure 22, right). The final values for the Debye fitting to the 110A(0) sample data are given in Table 16.

Table 15: Starting values and limits for the fitting of the Debye function to the $d\Sigma/d\Omega$ for 110A(0)

Parameter	Units	Lower limit	Initial value for the first round of fitting	Initial value for the second round of fitting
A	—	0	7.61E-9	3.36E-8
n	—	0	3.67	3.44
B	—	0	43.1	82.0
R_g	Å	0	101[a]	88.8
D	cm^{-1}	0	0.065	Variable[b]

[a] Based on $C = R_g^2/3 = 3430$ Å^2 from the fitting of the Zimm function to the 110A(0) data.

[b] The value of *D* was varied in 0.005 increments starting with a value of 0.1; once the fit had been improved as far as possible, the increment was reduced to 0.001 until the fit had been optimised.

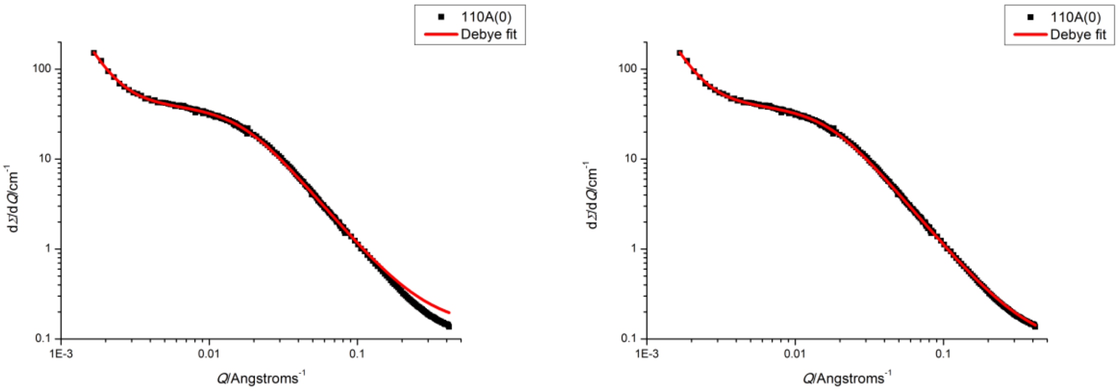

Figure 22: Left: first attempt at the Debye fitting of the 110A(0) data set. All parameters were allowed to vary freely. The fit is good at low and intermediate *Q*, but poor at high *Q* due to an overestimation of the value of *D* (*D* = 0.132). Right: second attempt at the Debye fitting of the 110A(0) data set. *D* was fixed at 0.082, and all other parameters were allowed to vary freely around starting parameters extracted from the first round of fitting.

Table 16: Final parameters obtained from fitting the Debye function (Equation 32) to the 110A(0) data set

Parameter	**Units**	**Fitted value**
A	—	1.35E-7
n	—	3.21
B	—	40.4
R_g	Å	87.4
D	—	0.082

Figure 23 shows the contributions from the different components in the Zimm and Debye equations (and Equation 32, respectively) to the total scattering of the neat 110k PS. In both cases the scattering at low *Q* is primarily due to the AQ^{-n} term, which in this sample corresponds to defects such as microbubbles. The weaker scattering at high *Q* arises from the polymer chains in the sample.

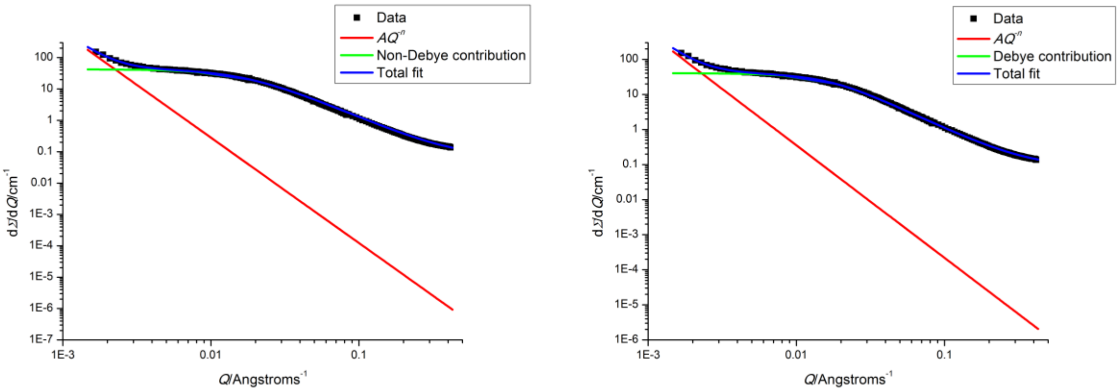

Figure 23: Small-angle neutron scattering data for 110k PS with 0 wt% SWCNTs. The best fit (blue) combines the contribution from the nanotubes and defects (red) and the single chain contribution and background (green). The left hand data is fitted with the Zimm equation (); the right hand data is fitted with the Debye equation (Equation 32).

3.2.3.3.3 Establishing a fitting protocol

The final fit of the Debye function to the 110A(0) data set is good across all values of Q (Figure 22, right). The R_g value obtained from the fit (87.4 Å) is good (polystyrene with a molecular weight of 110 kg mol^{-1} would be expected to have an R_g value of ~89.2 Å).[169] Based on these two factors, the fitting procedure used to fit the Zimm and Debye functions to the 110A(0) data set was used to set-up the following protocol for fitting the remaining data sets:

1. Remove any irregular data points as outlined earlier.
2. Fit the Zimm function to the truncated data using the parameters obtained from the successful Zimm fitting of the 110A(0) data set. Allow all the parameters to vary freely.
3. Refit the Zimm function to the data set using the parameters found in the first fitting as the starting values, but fixing the background D to a value close to 0.1 and varying this value systematically at 0.005 increments until a good fit is achieved at high-Q. When a good fit has been achieved, further vary the value of D by increments of 0.001 to optimise the fit.
4. Fit the Debye function to the data using the parameters obtained from the Zimm fitting of the same data set. Allow all the parameters to vary freely.
5. Refit the Debye function to the data set using the parameters found in the first fitting as the starting values, fixing the background D as in Step 3.

3.2.3.4 Final fittings: 110k and 230k PS samples

All data were fitted in Origin.[168] For the 230k series of samples, the 230A(0) sample was fitted as given for the 110A(0) sample. The starting values for the first round of the Zimm fitting were taken from the final fitted values of the Zimm function to the 110A(0) data; full details are given in Table 17. The final fits are shown in Figure 24 and Figure 25; all further 230k PS samples were fitted as for the 110k PS data series, but using the final parameters for the Debye fits to the 230A(0) sample (Table 18), rather than those from the 110A(0) sample.

Table 17: Starting values and limits for the fitting of the Zimm function to the dΣ/dΩ for 230A(0)

Parameter	Units	Lower limit	Initial value for the first round of fitting	Initial value for the second round of fitting
A	—	0	3.36E-8	3.23E-8
n	—	0	3.44	3.38
B	—	0	82.0	81.6
C	Å^2	0	6000[a]	6840
D	cm^{-1}	0	0.082	Variable[b]

[a] Based on an R_g value of 134 Å for 230k:[169] PS$\langle R_0\rangle^2 = 0.434M$; $\langle R_0\rangle_{110\mathrm{k}}{}^2 = 99820\ \text{Å}^2$; $R_\mathrm{g}{}^2 = \frac{\langle R_0\rangle^2}{6} = 16637\ \text{Å}^2$; $R_\mathrm{g} = 129\ \text{Å}$.

[b] The value of *D* was varied in 0.005 increments starting with a value of 0.1; once the fit had been improved as far as possible, the increment was reduced to 0.001 until the fit had been optimised.

Table 18: Starting values and limits for the fitting of the Debye function to the dΣ/dΩ for 230A(0)

Parameter	Units	Lower limit	Initial value for the first round of fitting	Initial value for the second round of fitting
A	—	0	3.23E-8	1.44E-7
n	—	0	3.38	3.16
B	—	0	81.6	77.4
R_g	Å	0	143[a]	124
D	—	0	0.060	Variable[b]

[a] Based on the parameter $C = R_g^2/3 = 6840$ from the final Zimm fitting of sample 230A(0).

[b] The value of D was varied in 0.005 increments starting with a value of 0.1; once the fit had been improved as far as possible, the increment was reduced to 0.001 until the fit had been optimised.

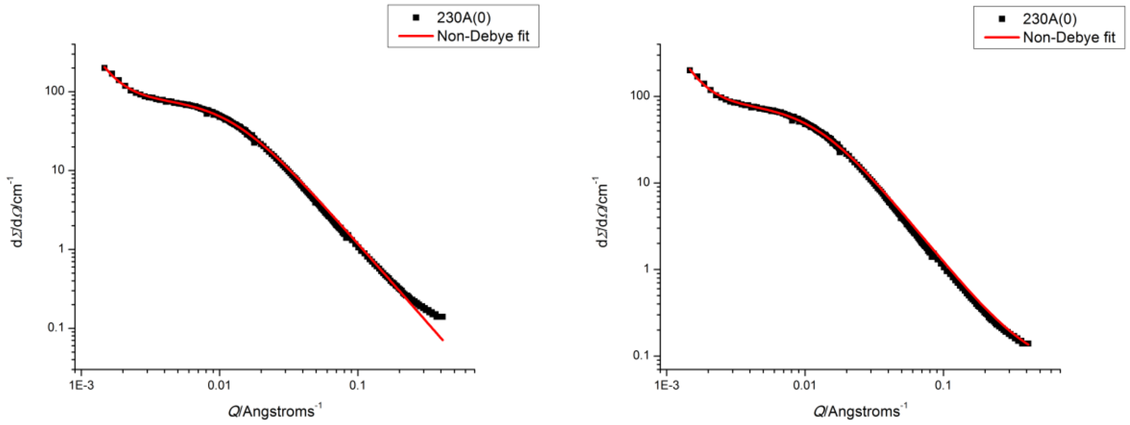

Figure 24: Left: first attempt at the Zimm fitting of the 230A(0) data set. All parameters were allowed to vary freely. The fit is good at low and intermediate *Q*, but poor at high *Q* due to an underestimation of the value of *D* (*D* = 8.2E-16). Right: second attempt at the Zimm fitting of the 230A(0) data set. *D* was fixed at 0.060, and all other parameters were allowed to vary freely around starting parameters extracted from the first round of fitting.

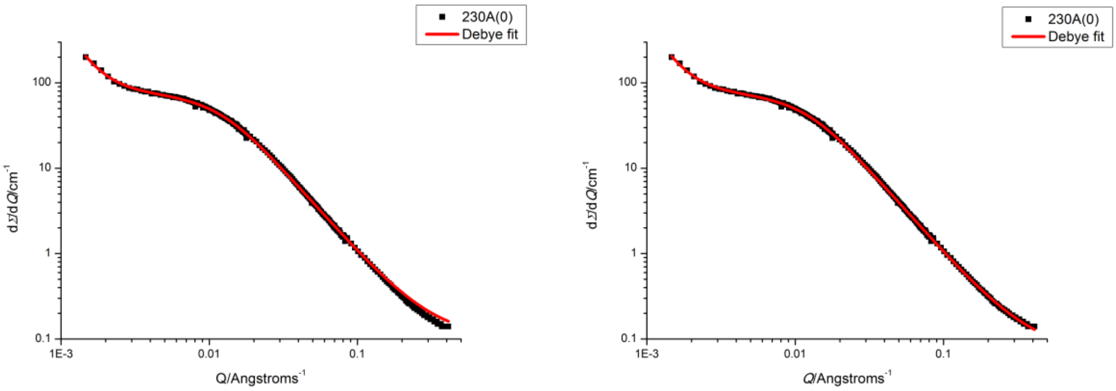

Figure 25: Left: first attempt at the Debye fitting of the 230A(0) data set. All parameters were allowed to vary freely. The fit is good at low and intermediate *Q*, but poorer at high *Q* due to an overestimation of the value of *D* (*D* = 0.10215). Right: second attempt at the Zimm fitting of the 230A(0) data set. *D* was fixed at 0.07, and all other parameters were allowed to vary freely around starting parameters extracted from the first round of fitting.

Table 19: Final parameters obtained from fitting the Zimm and Debye functions to the 230A(0) data set

Parameter	**Units**	**Zimm fitted parameters**	**Debye fitted parameters**
A	—	3.25E-8	1.46E-7
n	—	3.38	3.16
B	—	81.6	77.4
C	$Å^2$	6830	—
R_g	Å	—	124
D	—	0.06	0.07

The fitted scattering curves and final fitted parameters for the Zimm and Debye fittings of the 110k PS nanocomposite series are shown in Figure 26,

Table 20 and Table 21; the fitted scattering curves and final fitted parameters for the Zimm and Debye fittings of the 230k PS nanocomposite series are show in Figure 27, Table 22 and Table 23. In the majority of cases the fits are reasonable to good; in some cases the fit in the mid to high-*Q* region is poor, in part because of the fixing of the value of *D* to improve the fit at high-*Q*, and the shape of the fitted curve is not appropriate to capture the data.

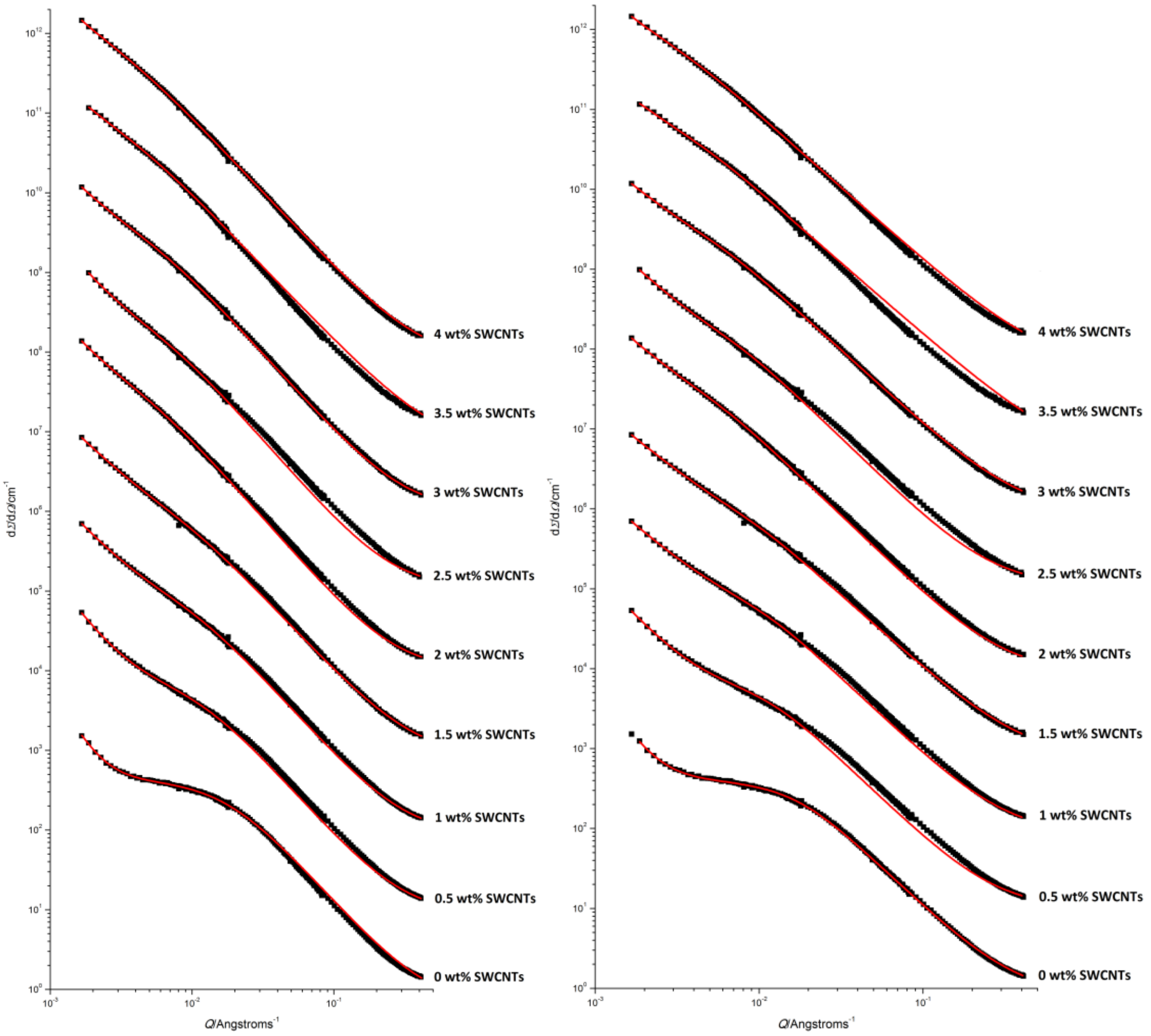

Figure 26: Zimm (left) and Debye (right) fits for the 110k PS series of nanocomposite samples. The bottom curve corresponds to scattering from the sample containing 0 wt% SWCNTs, with the weight fraction of SWCNTs increasing with each curve up to the top curve, which corresponds to the scattering from the sample containing 4 wt% SWCNTs. Data have been vertically offset for clarity.

Table 20: Final fitted Zimm parameters for the 110k PS data series

Sample	Parameter								
	A	**Error**	***n***	**Error**	***B***	**Error**	***C***	**Error**	***D***
Units	—	—	—	—	—	—	$Å^2$	$Å^2$	—
110A(0)	5.36E-8	1.03E-3	3.36	0.9	42.2	0.214	3320	47.8	0.065
110B(0.5)	7.44E-5	8.89E-6	2.44	0.0178	70.4	1.43	8710	280	0.090
110C(1)	2.32E-3	2.22E-4	1.96	0.0141	71.4	2.51	11 100	413	0.090
110D(1.5)	7.81E-3	1.21E-3	1.80	0.0227	65.6	6.1	13 700	1020	0.085
110E(2)	1.01E-3	2.08E-4	2.17	0.0293	314	16	49 000	1530	0.110
110F(2.5)	5.93E-4	1.36E-4	2.25	0.0336	189	11	28 700	1330	0.110
110G(3)	4.21E-3	5.65E-4	1.93	0.0193	225	9	36 100	723	0.105
110H(3.5)	1.55E-2	3.28E-3	1.75	0.0311	323	17	61 500	3630	0.065
110I(4)	1.08E-2	1.30E-3	1.81	0.0174	364	12	80 100	2480	0.080

Table 21: Final fitted Debye parameters for the 110k PS data series

Sample	Parameter								
	A	**Error**	***n***	**Error**	***B***	**Error**	R_g	**Error**	***D***
Units	—	—	—	—	—	—	Å	Å	—
110A(0)	1.35E-7	2.34E-8	3.21	0.0260	40.4	0.193	87.4	0.583	0.082
110B(0.5)	1.30E-4	1.56E-5	2.36	0.0181	61.4	1.32	132	2.20	0.10
110C(1)	3.62E-3	3.11E-4	1.89	0.0127	57.1	2.03	146	2.67	0.10
110D(1.5)	1.12E-2	1.37E-3	1.75	0.0181	48.8	4.32	161	5.57	0.075
110E(2)	4.24E-3	4.85E-4	1.96	0.0166	181	7.84	281	3.02	0.09
110F(2.5)	2.33E-3	3.62E-4	2.04	0.0231	113	6.55	212	4.24	0.11
110G(3)	1.10E-2	9.43E-4	1.79	0.0124	145	5.14	256	2.22	0.085
110H(3.5)	2.25E-2	3.22E-3	1.70	0.0212	223	11.2	332	8.91	0.04
110I(4)	1.75E-2	1.30E-3	1.75	0.0108	250	7.26	389	6.03	0.06

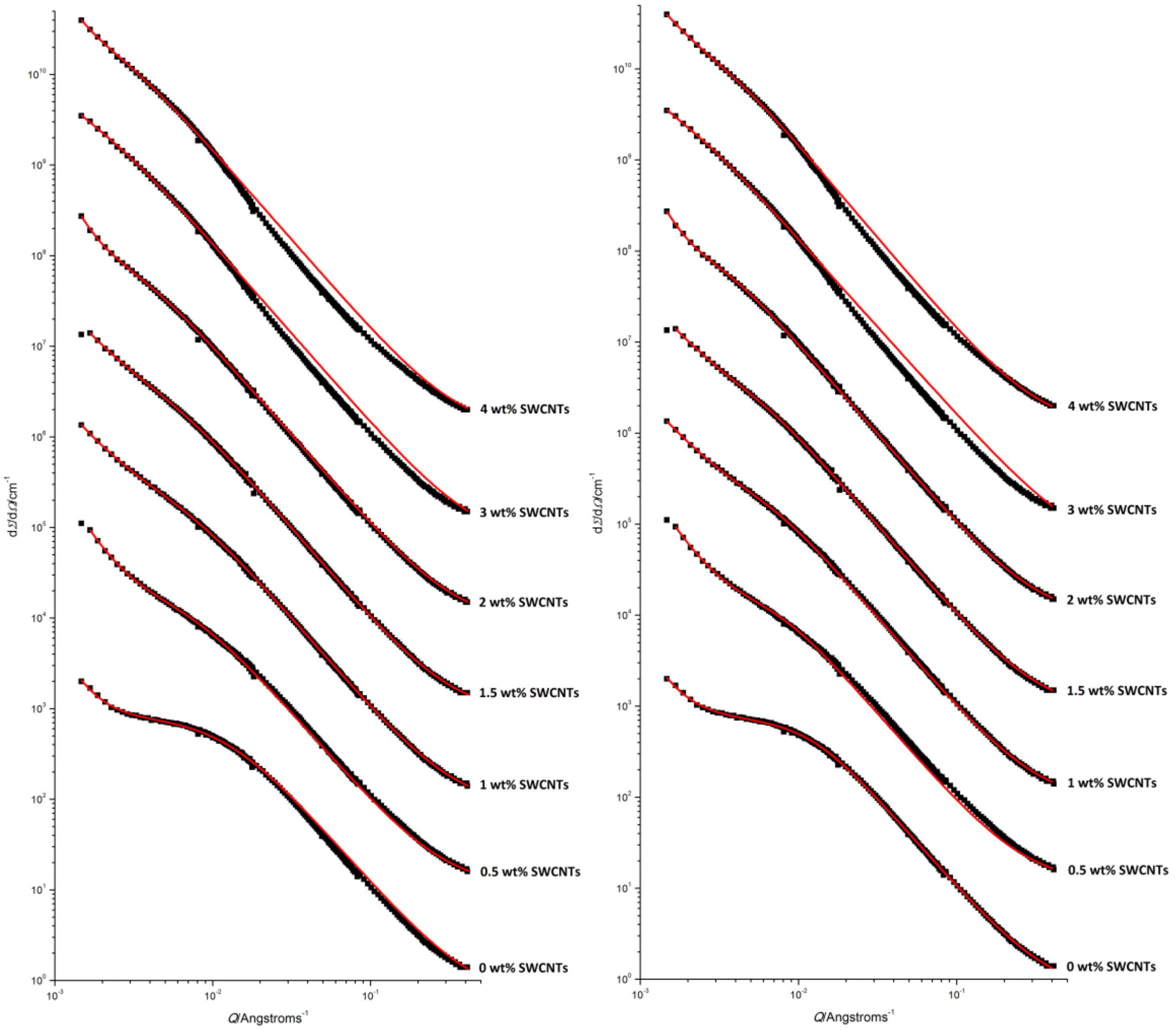

Figure 27: Zimm (left) and Debye (right) fits for the 230k PS series of nanocomposite samples. The bottom curve corresponds to scattering from the sample containing 0 wt% SWCNTs, with the weight fraction of SWCNTs increasing with each curve up to the top curve, which corresponds to the scattering from the sample containing 4 wt% SWCNTs. Data have been offset for clarity.

Table 22: Final fitted Zimm parameters for the 230k PS data series

Sample	**Parameter**								
	A	**Error**	***n***	**Error**	***B***	**Error**	***C***	**Error**	***D***
Units	—	—	—	—	—	—	Å^2	Å^2	—
230A(0)	3.23E-8	1.22E-8	3.38	0.055	81.6	0.543	6840	105	0.065
230B(0.5)	3.09E-6	4.14E-7	3.02	0.0197	191	2.75	20 800	429	0.11
230C(1)	9.21E-4	1.32E-4	2.15	0.0205	232	7.55	27 000	810	0.085
230D(1.5)	9.10E-4	2.02E-4	2.19	0.0319	338	15.6	41 300	1330	0.09
230E(2)	3.59E-9	1.85E-9	4.12	0.0720	1282	42.3	122 000	4850	0.09
230F(3)	5.00E-3	2.17E-3	1.97	0.0622	2540	170	274 000	24 800	0.07
230G(4)	6.16E-8	1.12E-7	3.70	0.251	3120	342	208 000	23 400	0.12

Table 23: Final fitted Debye parameters for the 230k PS data series

Sample	**Parameter**								
	A	**Error**	***n***	**Error**	***B***	**Error**	***R*$_g$**	**Error**	***D***
Units	—	—	—	—	—	—	Å	Å	—
230A(0)	1.46E-7	4.23E-8	3.16	0.0424	77.4	0.433	124	0.759	0.07
230B(0.5)	9.15E-6	1.34E-6	2.86	0.0217	159	2.71	197	2.29	0.115
230C(1)	1.99E-3	2.18E-4	2.04	0.0158	178	5.20	222	2.74	0.09
230D(1.5)	3.39E-3	4.40E-4	2.00	0.0189	218	8.23	262	2.82	0.09
230E(2)	9.24E-9	4.16E-9	3.99	0.0632	1030	28.5	461	7.37	0.095
230F(3)	1.17E-2	2.33E-2	1.88	0.0292	1480	86.5	654	23.2	0.05
230G(4)	8.71E-4	2.83E-4	2.32	0.0458	926	61.6	403	7.78	0.12

Figure 28 is analogous to Figure 23 and shows the contributions from the different components in the Zimm and Debye equations (and Equation 32, respectively) to the total scattering of the 110k PS with 1 wt% SWNCTs [110C(1)]. Again the scattering at low Q arises from the AQ^{-n} term, while the weaker scattering at high Q is from the polymer chains in the sample. The AQ^{-n} contribution is several orders of magnitude larger for this sample than for the neat 110k PS sample (Figure 23), and the single chain contribution is relatively smaller, indicating that the nanotubes contribute significantly to the scattering from the nanocomposite.

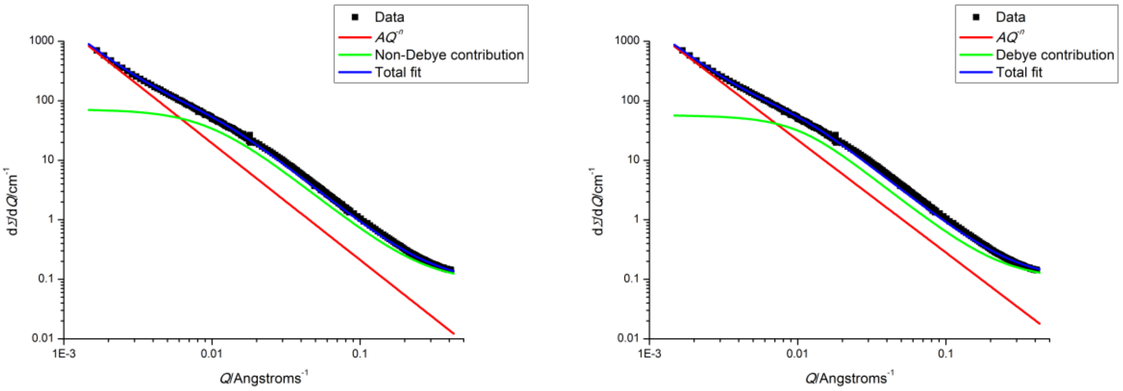

Figure 28: Small-angle neutron scattering data for 110k PS with 1 wt% SWCNTs (bottom row). The best fit (blue) combines the contribution from the nanotubes and defects (red) and the single chain contribution and background (green). The left hand data is fitted with the Zimm equation (); the right hand data is fitted with the Debye equation (Equation 32).

Figure 29 and Figure 30 show the individual contributions to the overall scattering from the AQ^{-n} and single-chain and background components of the Zimm and Debye equations (and Equation 32, respectively) for the neat 230k PS sample and the 230k PS sample containing 1 wt% SWCNTs [230C(1)]. As for the 110k PS samples (Figure 23 and Figure 28) the scattering at low Q arises from the AQ^{-n} term, and is significantly larger for the sample containing nanotubes than for the neat sample. Again the weaker scattering at high Q is from the polymer chains in the sample, and shows a smaller relative contribution when the nanotubes are added than when they are not present.

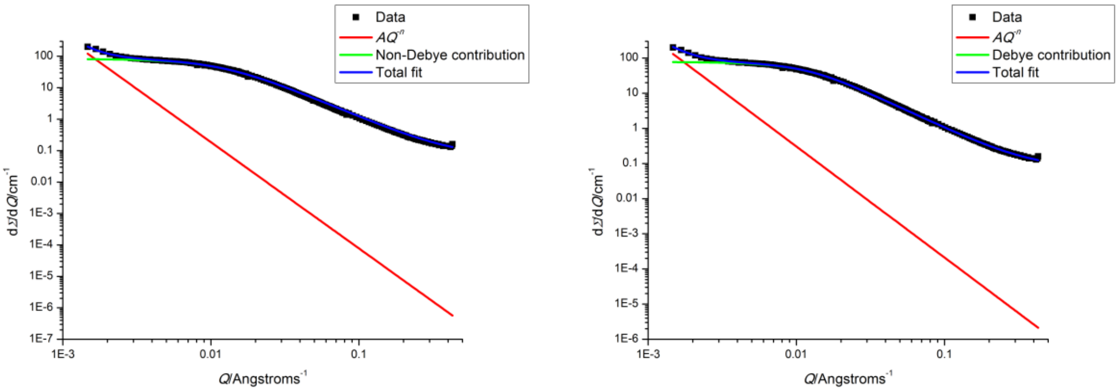

Figure 29: Small-angle neutron scattering data for 230k PS with 0 wt% SWCNTs. The best fit (blue) combines the contribution from the nanotubes and defects (red) and the single chain contribution and background (green). The left hand data is fitted with the Zimm equation (); the right hand data is fitted with the Debye equation (Equation 32).

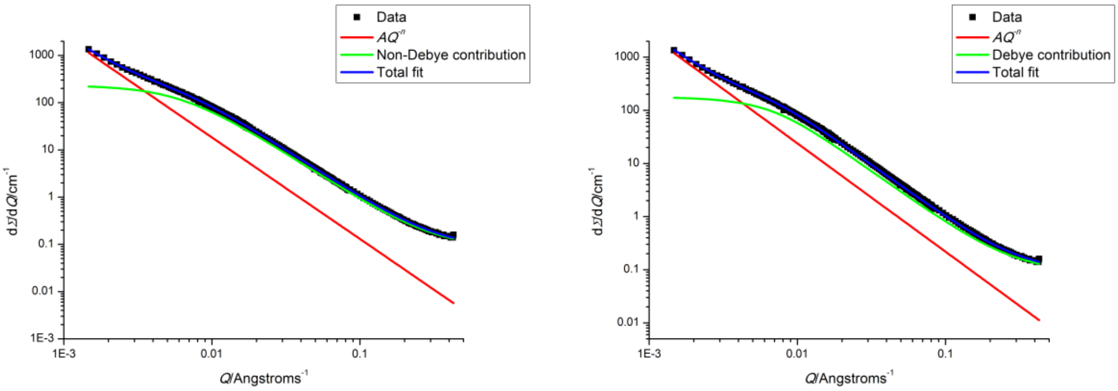

Figure 30: Small-angle neutron scattering data for 230k PS with 1 wt% SWCNTs (bottom row). The best fit (blue) combines the contribution from the nanotubes and defects (red) and the single chain contribution and background (green). The left hand data is fitted with the Zimm equation (); the right hand data is fitted with the Debye equation (Equation 32).

3.2.3.5 Trend in n

The value of n in both the Zimm and Debye fittings for the 110k and 230k PS series of samples plateau to an approximate value of 2 with increasing CNT concentration (Figure 31). At high Q

($QR_g >> 1$), the Debye function, the form factor of an ideal chain, $P(Q,N)$, scales as Q^{-2} (Equation 33):[51]

$$P(Q,N) \cong \frac{12}{Q^2 N b^2}$$

Equation 33

where N is the degree of polymerisation, and b is the Kuhn length. The value of $n = 2$ at higher nanotube concentrations (≥ 1 wt% SWCNTs) results in the first term of the Zimm () and Debye (Equation 32) equations used to fit the data masking the Debye scattering, so unfortunately this scattering cannot be resolved from the scattering of the filled samples.

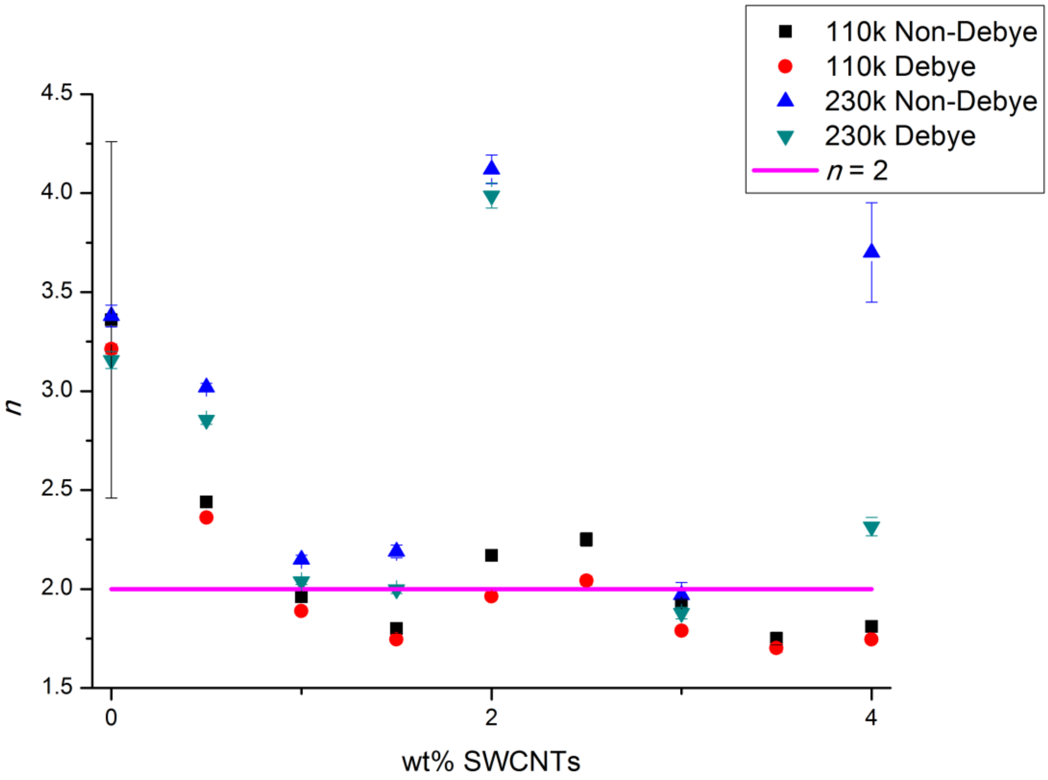

Figure 31: *n* extracted from the Zimm and Debye fits to the 110k and 230k PS series of samples. The pink horizontal line indicates n = 2.

3.2.4 Annealed samples

$d\Sigma/d\Omega$ data were recorded for four annealed 230k PS samples, and these data reduced and vertically shifted in preparation for fitting (Figure 18 and Figure 19). However, during the scattering experiment itself, it was noted that the annealed samples were scattering anisotropically, with the 2D scattering exhibiting a lozenge-shaped scattering ring (Figure 32–Figure **35**), suggesting that the nanotubes were scattering more in one direction than the other. This was also true for some of the unannealed samples at nanotube concentrations above 1 wt% (examples are shown in Figure 36 and Figure 37 for 110 kg mol^{-1} samples, and Figure 38 and

Figure 39 for 230 kg mol^{-1} samples; the 2D scattering for all samples is shown in Appendix 1). This observation suggests that the nanotubes were aligning at higher nanotube concentrations and on annealing, a phenomenon that can presumably be attributed to the attractive forces between the nanotubes causing the CNTs to aggregate at higher concentrations and as they became mobile in the nanocomposite at high temperatures. For both the unannealed and the annealed samples, anisotropy was only observed at intermediate and long sample–detector distances (8 m and 39 m, respectively), indicating that agglomeration and alignment were occurring at the low-*Q* end of the measurements, corresponding to longer distances in the samples, *i.e.* the large dimensions of the CNTs.

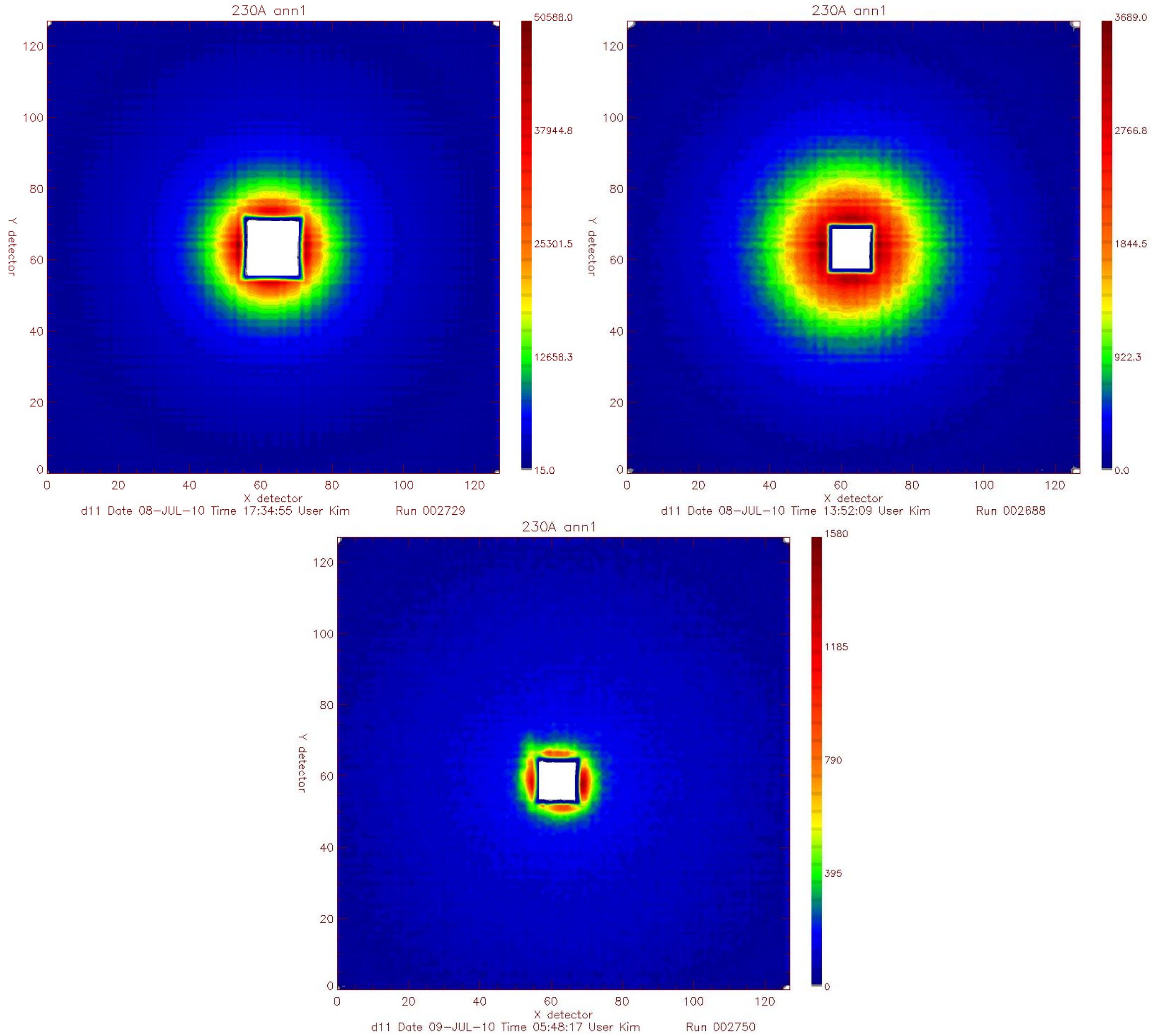

Figure 32: 2D SANS detector images for 230A_ann (230 kg mol^{-1} with 0 wt% SWCNTs, annealed). Sample–detector distances: top left: 1.50 m; top right: 8.00 m; bottom: 39.0 m.

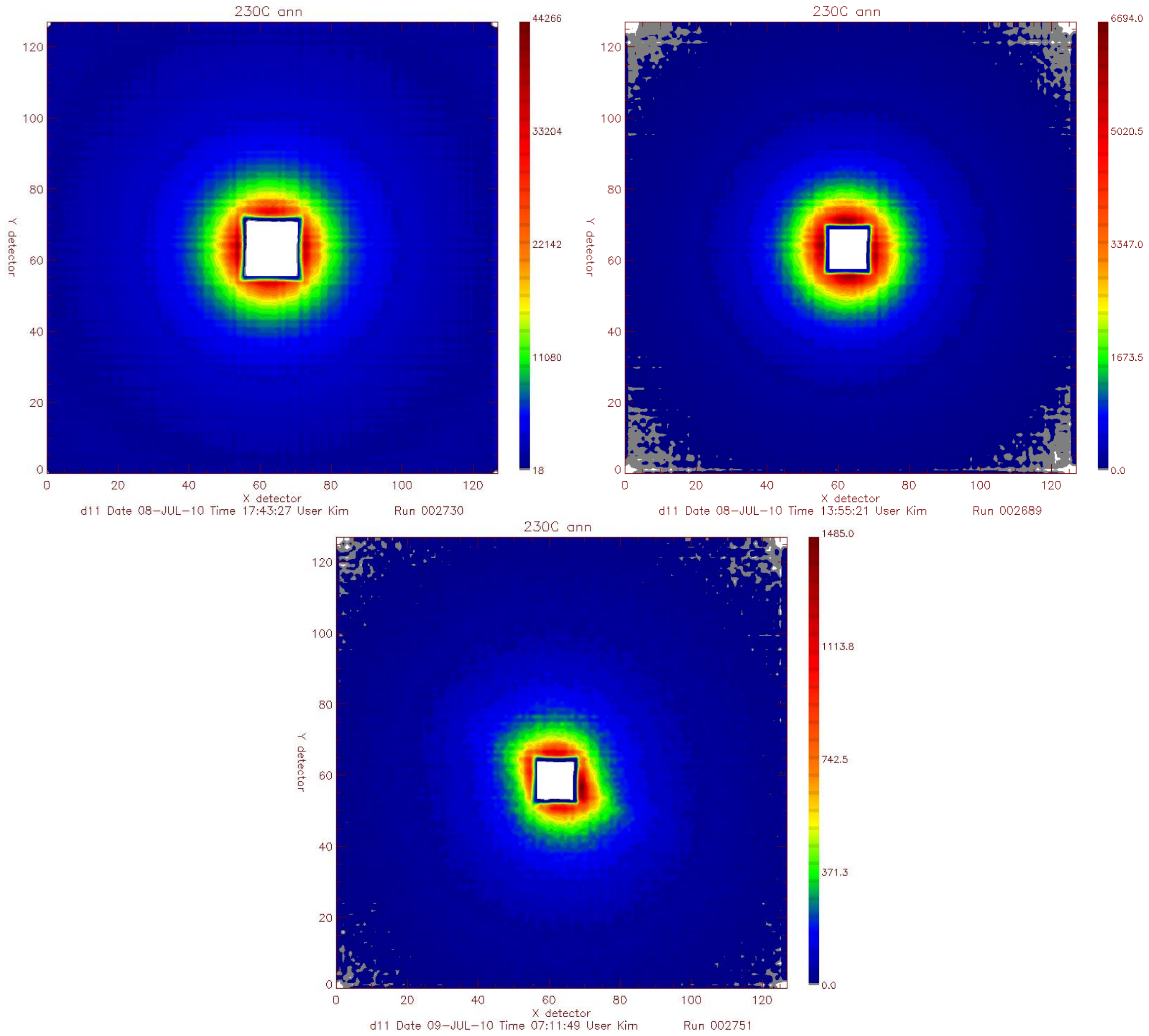

Figure 33: 2D SANS detector images for 230C_ann (230 kg mol^{-1} with 1 wt% SWCNTs, annealed). Sample–detector distances: top left: 1.50 m; top right: 8.00 m; bottom: 39.0 m.

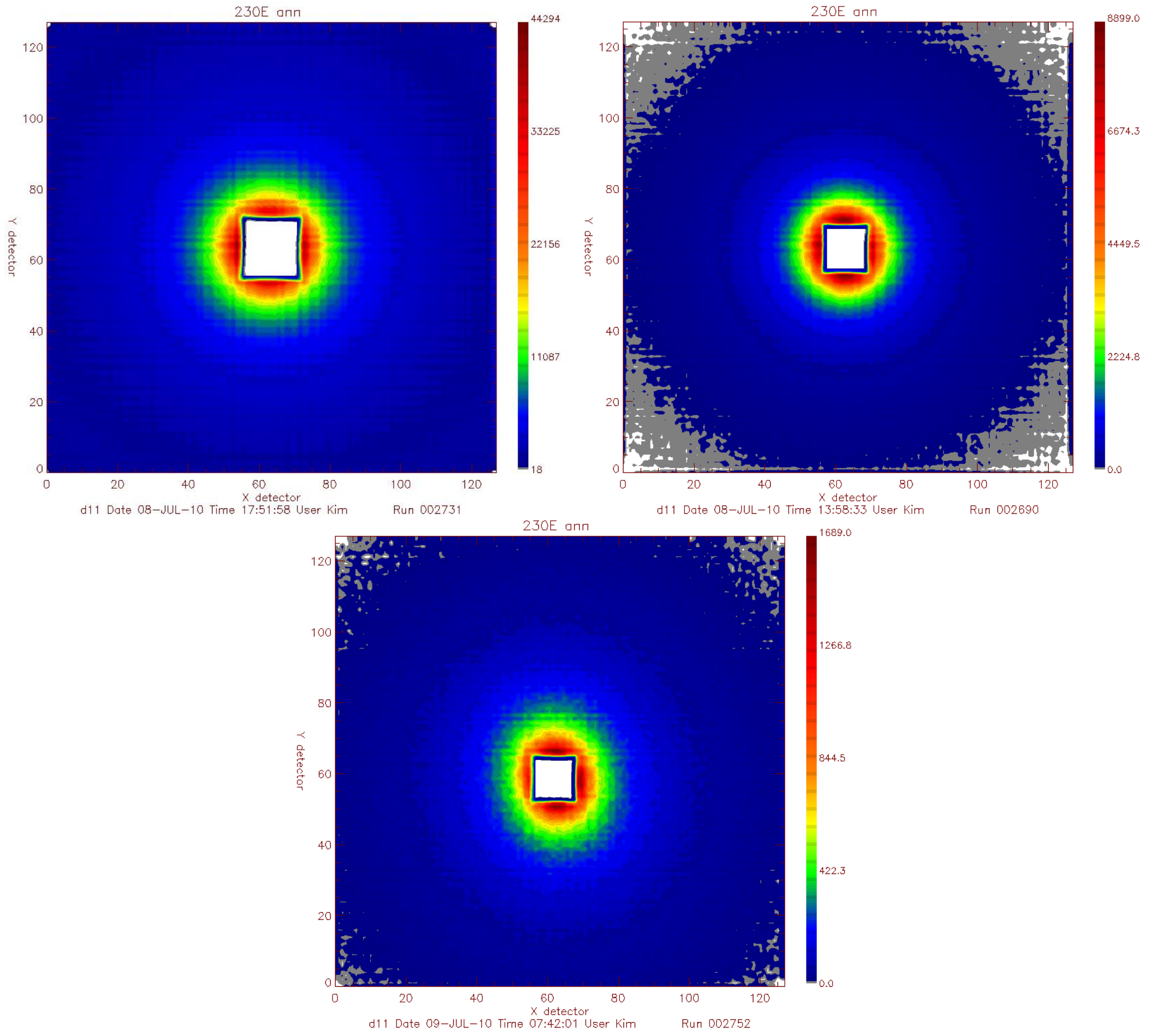

Figure 34: 2D SANS detector images for 230E_ann (230 kg mol^{-1} with 2 wt% SWCNTs, annealed). Sample–detector distances: top left: 1.50 m; top right: 8.00 m; bottom: 39.0 m.

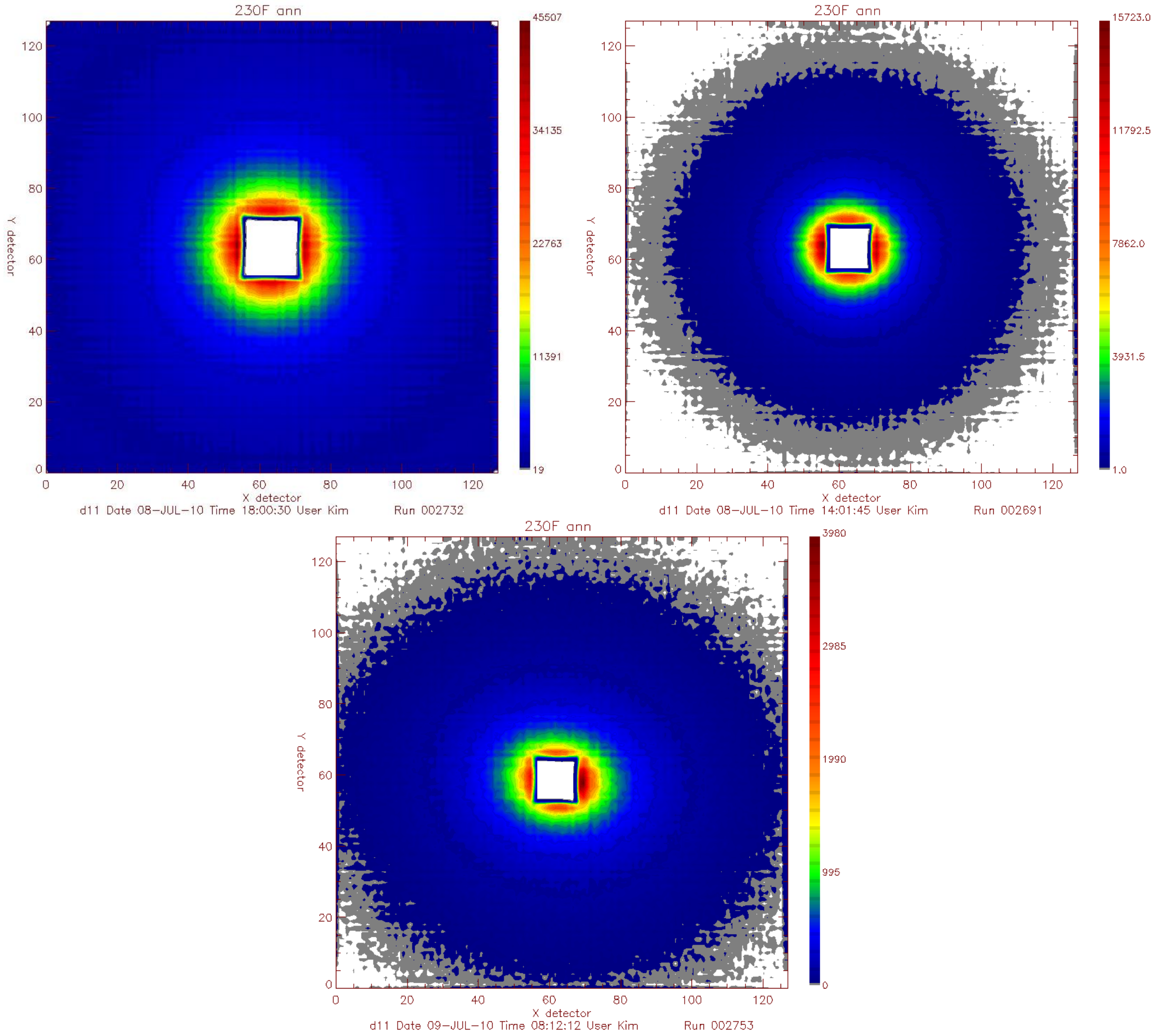

Figure 35: 2D SANS detector images for 230F_ann (230 kg mol^{-1} with 3 wt% SWCNTs, annealed). Sample–detector distances: top left: 1.50 m; top right: 8.00 m; bottom: 39.0 m.

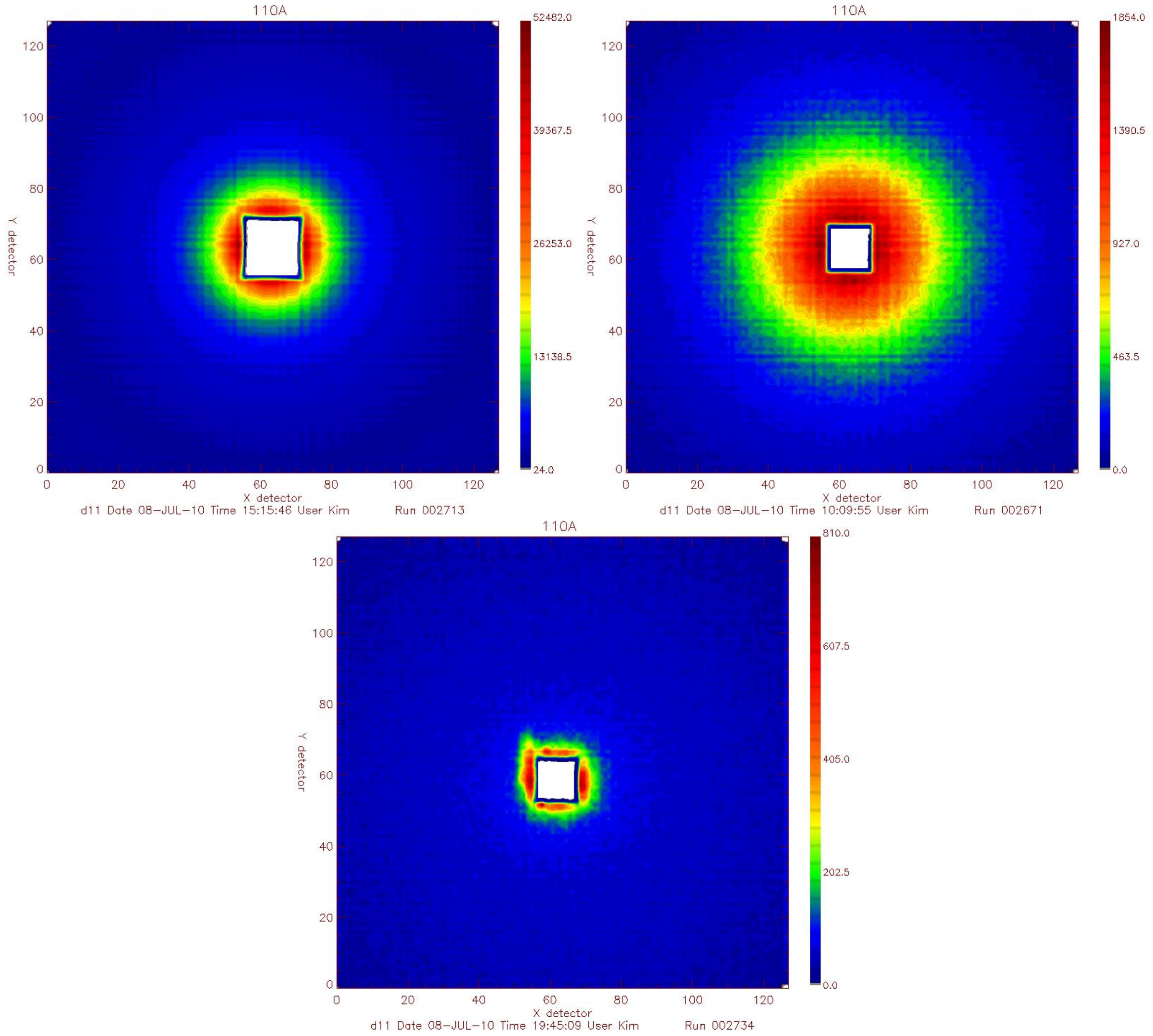

Figure 36: 2D SANS detector images for 110A (110 kg mol^{-1} with 0 wt% SWCNTs). Sample–detector distances: top left: 1.50 m; top right: 8.00 m; bottom: 39.0 m.

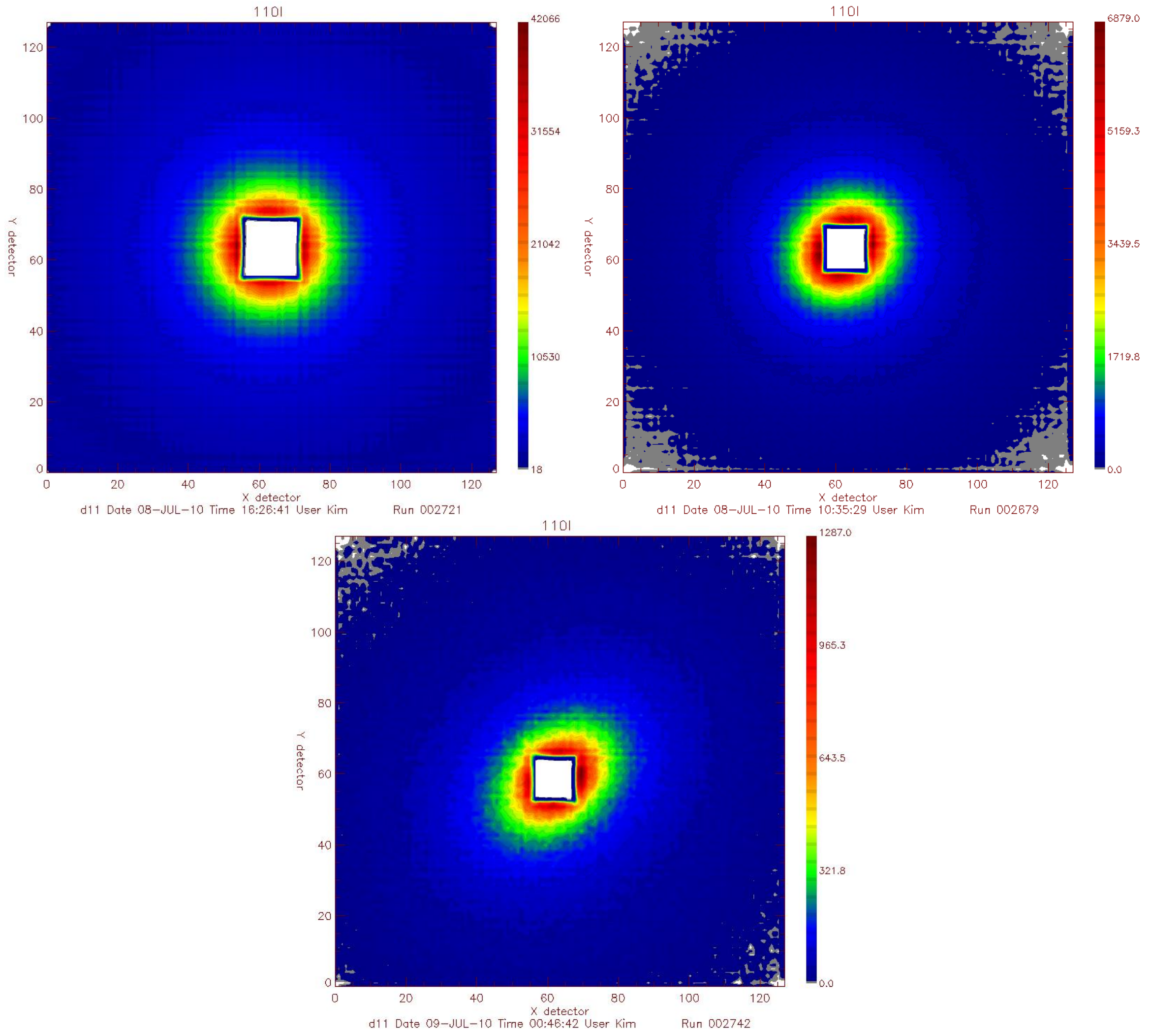

Figure 37: 2D SANS detector images for 110I (110 kg mol^{-1} with 4 wt% SWCNTs). Sample–detector distances: top left: 1.50 m; top right: 8.00 m; bottom: 39.0 m.

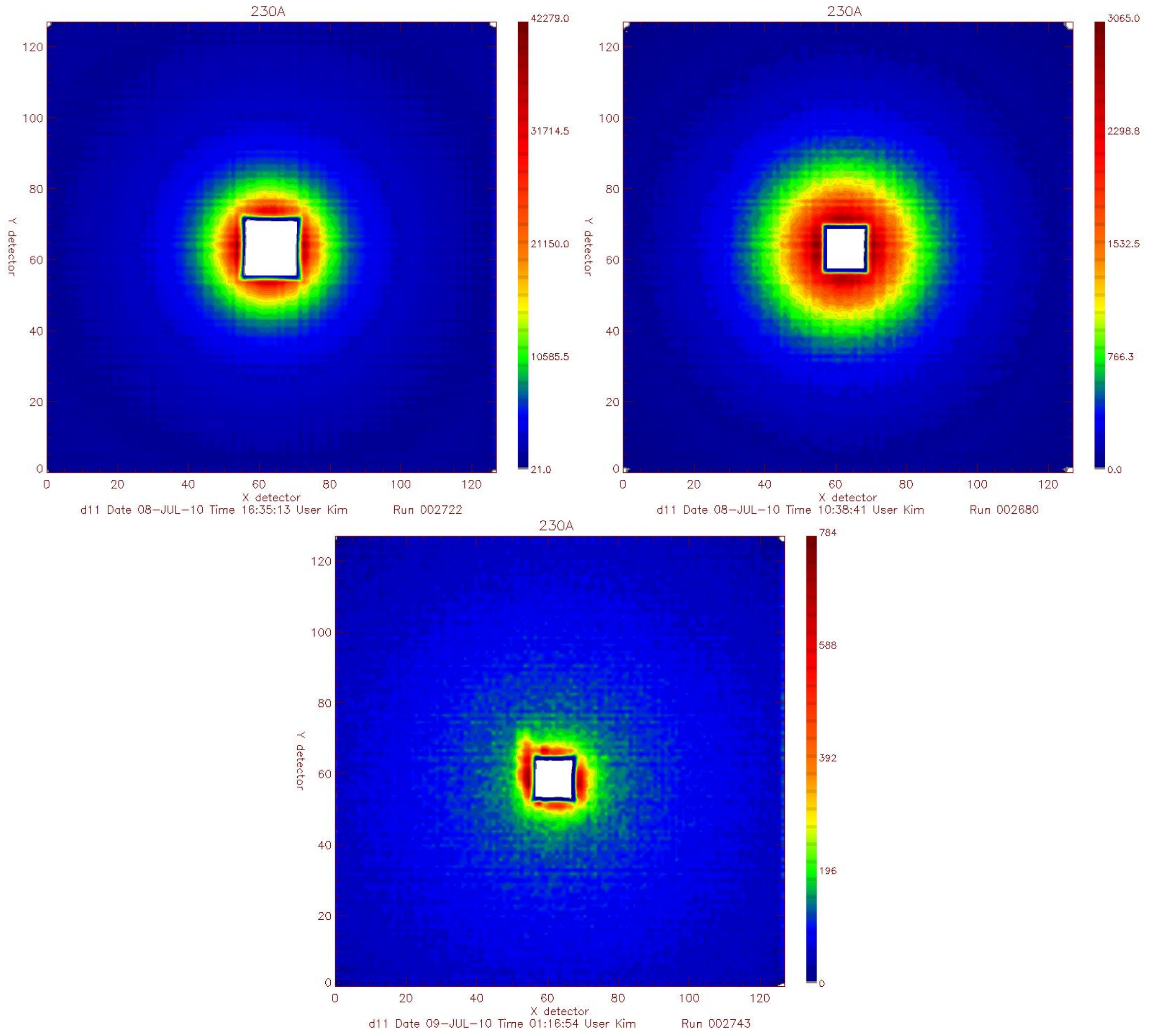

Figure 38: 2D SANS detector images for 230A (230 kg mol^{-1} with 0 wt% SWCNTs). Sample–detector distances: top left: 1.50 m; top right: 8.00 m; bottom: 39.0 m.

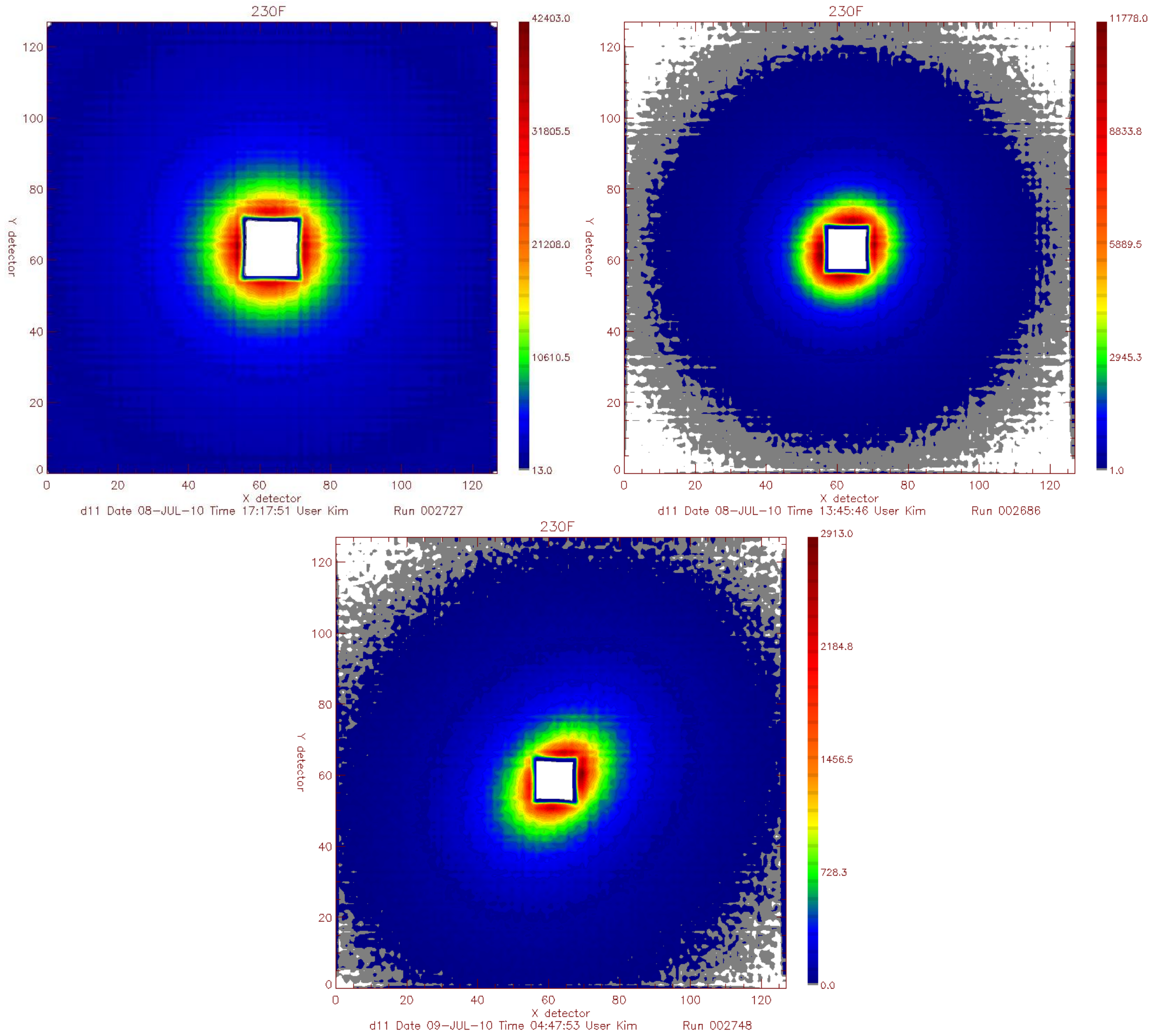

Figure 39: 2D SANS detector images for 230F (230 kg mol^{-1} with 3 wt% SWCNTs). Sample–detector distances: top left: 1.50 m; top right: 8.00 m; bottom: 39.0 m.

The data sets for the annealed samples were never fitted as the fitting of the 110k and 230k series of samples indicated that the experiment required contrast-matched samples for any valuable information to be obtained (see the discussion that follows). The anisotropy in the nanocomposites with higher nanotube concentrations also decreases the reliability of the R_g values extracted from the nanocomposite samples with nanotube concentrations greater than 1 wt%, as the radial averaging conducted to convert the 2D detector data into a plot of $d\Sigma/d\Omega$ *vs*. Q is not consistent across the 2D scattering.

3.3 Discussion

The apparent R_g values obtained by fitting the Zimm and Debye functions to the 110k and 230k PS data series are shown in Figure 40 and Figure 41, respectively. For both matrix molecular weights the Zimm data returns larger values of R_g, but with greater associated error, however, both fitting approaches provide the same trends. For the 110k data series, an increase in R_g is seen with increasing nanotube concentration, with the exception of the data point for the 2 wt% sample, which has a higher R_g than would be predicted from looking at the other samples. For the 230k data series, the R_g values increase for concentrations up to 3 wt%, then decrease at 4 wt%, to a value that is significantly larger than the R_g of neat PS.

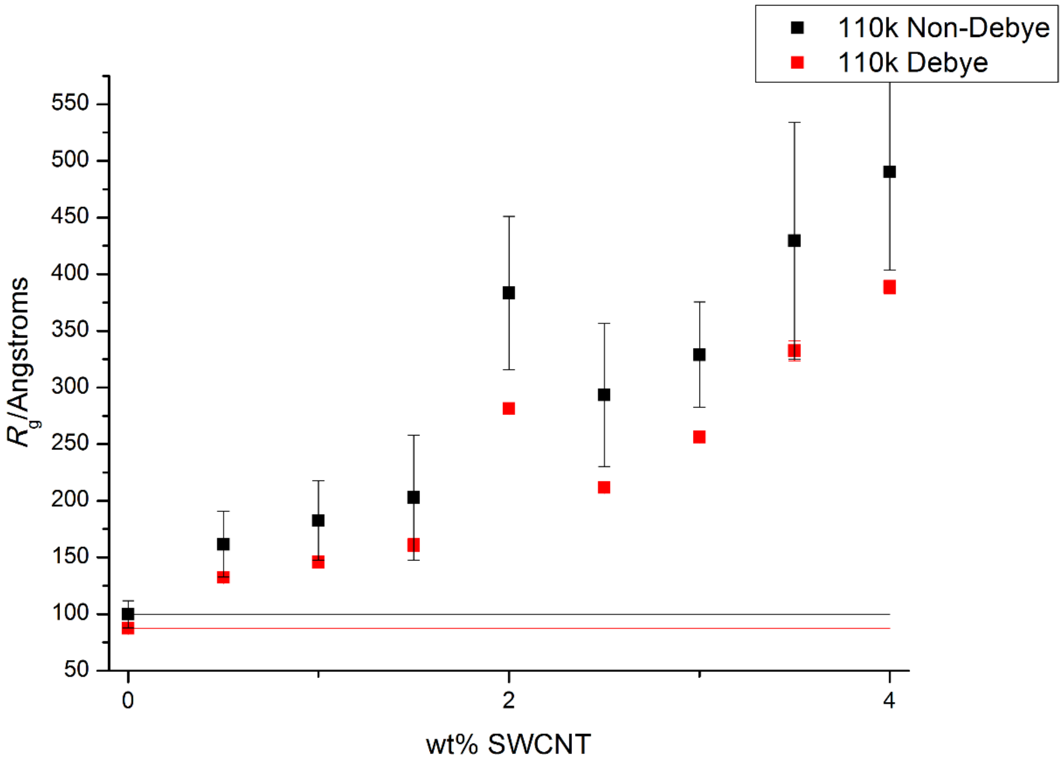

Figure 40: Apparent R_g as a function of nanotube concentration for the 110k PS series of samples obtained from the fits of the Zimm (black squares) and Debye (red squares) functions to $d\Sigma/d\Omega$ *vs.* Q. The black and red horizontal lines indicate the unperturbed dimensions found from fitting the data with the Zimm and Debye functions, respectively.

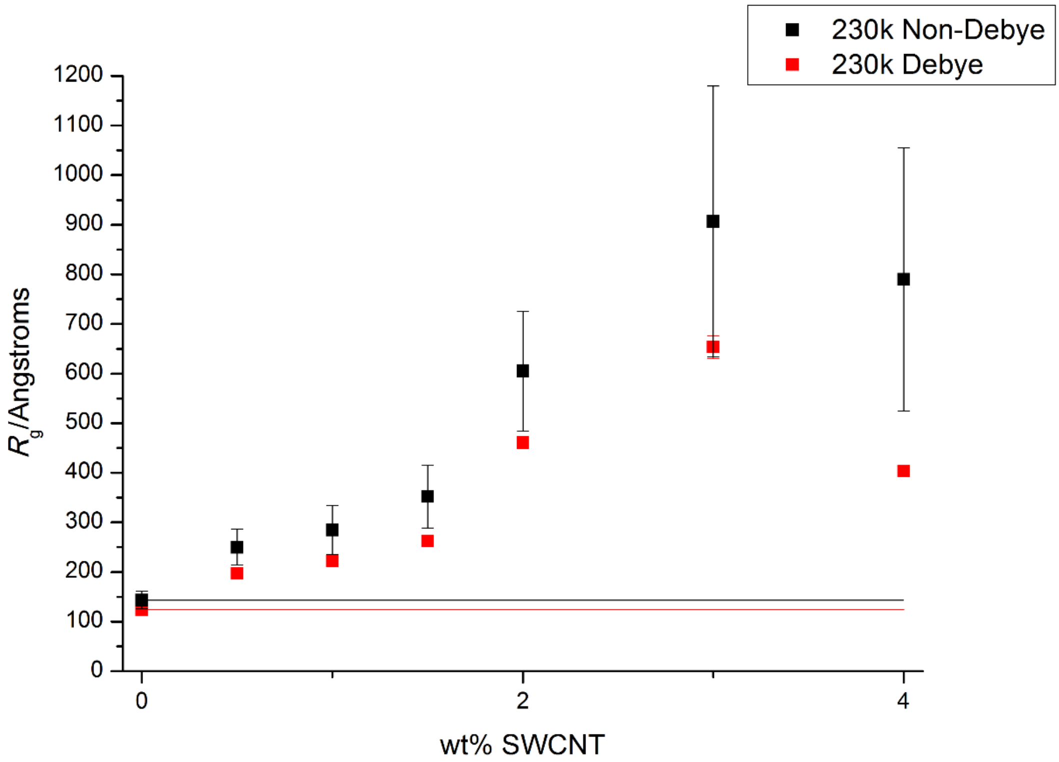

Figure 41: Apparent R_g as a function of nanotube concentration for the 230k PS series of samples obtained from the fits of the Zimm (black squares) and Debye (red squares) functions to $d\Sigma/d\Omega$ *vs. Q*. The black and red horizontal lines indicate the unperturbed dimensions found from fitting the data with the Zimm and Debye functions, respectively.

At the time this work was conducted (up to the summer of 2011), there was virtually no literature looking at the polymer radius of gyration in polymer nanocomposites containing cylindrical nanoparticles; the only directly relevant work was a simulation conducted by Karatratos *et al.*,[81] which indicated that no increase in R_g should occur on adding nanotubes to a polymer matrix up to the highest loading level investigated, 0.8%. The work presented here clearly suggests an increase in polymer radius of gyration at loading levels as low as 0.5%, contrary to Karatrantos *et al.*'s simulation studies.

To see whether any further insight could be gained into what was happening in the system, the literature on spherical nanoparticles in polymer matrices, which has been studied in greater detail than cylindrical nanotubes, was examined. In this work, the nanotube bundles have a radius of ~4 nm, which is smaller than the polymer radius of gyration in either system under examination ($R_{g,110k\ PS} \approx 89$ Å^{-1}; $R_{g,230k\ PS} \approx 129$ Å^{-1})[169], and several papers reported an increase in the radius of gyration of the polymer matrix relative to the bulk R_g in this regime from both simulations[64, 76-79] and small angle neutron scattering experiments.[68, 69]

The increase in polymer radius of gyration seen in the experiments presented here is large, with the 110k PS nanocomposite samples exhibiting up to a 4.5-fold increase in polymer R_g when compared to the bulk, and the 230k PS nanocomposite samples returning a five-fold increase at 3 wt%. While it could be suggested that these increases in chain size are caused by the nanotubes being very well dispersed among the polymer chains, expanding the polymer coils and causing the radii of gyration to increase with increasing nanotube concentration, none of the literature on systems containing spherical nanoparticles has suggested that such a large increase should occur. Mackay's group saw that the increase in the R_g of PS containing soft PS nanoparticles varied as $1 + c\varphi$, where φ is the volume fraction of nanoparticles and $c \approx 1$.[68, 69] While Mackay's system is not the same as that presented here, featuring soft nanospheres rather than solid nanotubes, the radii of the nanoparticles is comparable; the scale of the increase in R_g is significantly different between that found in the work presented by Mackay's group and the work presented here: Mackay's empirical relationship would suggest a maximum increase in R_g of 40% at 4 wt% filler; here an increase of ~450% at 4 wt% with the 110k PS samples, and ~500% with the 230k PS at 3 wt% filler is seen. This comparison could lead to the conclusion that what is being seen here is not a real result, and that something else must be happening in this system, however, any explanation other than chain stretching is thermodynamically very implausible. Aubouy *et al.*'s scaling theory used to calculate polymer chains stretching in brushes suggests that the free energy penalty for stretching a polymer chain by an amount equal to its unperturbed dimensions is about k_BT (where k_B is Boltzmann's constant and T is temperature).[170] Increasing the extent of stretch to 4.5 to 5 times the unperturbed dimensions (corresponding to the 450 to 500% stretches calculated from the fits) would come at a cost of around 4.5 or $5k_BT$. This is a huge energy penalty, which could be minimised by excluding the nanotubes from the polymer matrix *via* aggregation. Agglomeration is also suggested by the SAXS results presented in Figure 42, which were recorded on the d5 PS samples that were prepared for the QENS experiments (for more details, see section 2.3 Nanocomposite synthesis), and are analogous to the samples used in the SANS experiments. The SAXS data show a marked change in lineshape when the nanotube concentration reaches 1 wt%. Below 1 wt% SWCNTs, the data presents a curved line shape when potted on a log–log scale, while at nanotube concentrations of 1 wt% and above the data follow a much shallower curve, suggesting a fundamental change in the distribution of the nanoparticles in the system.

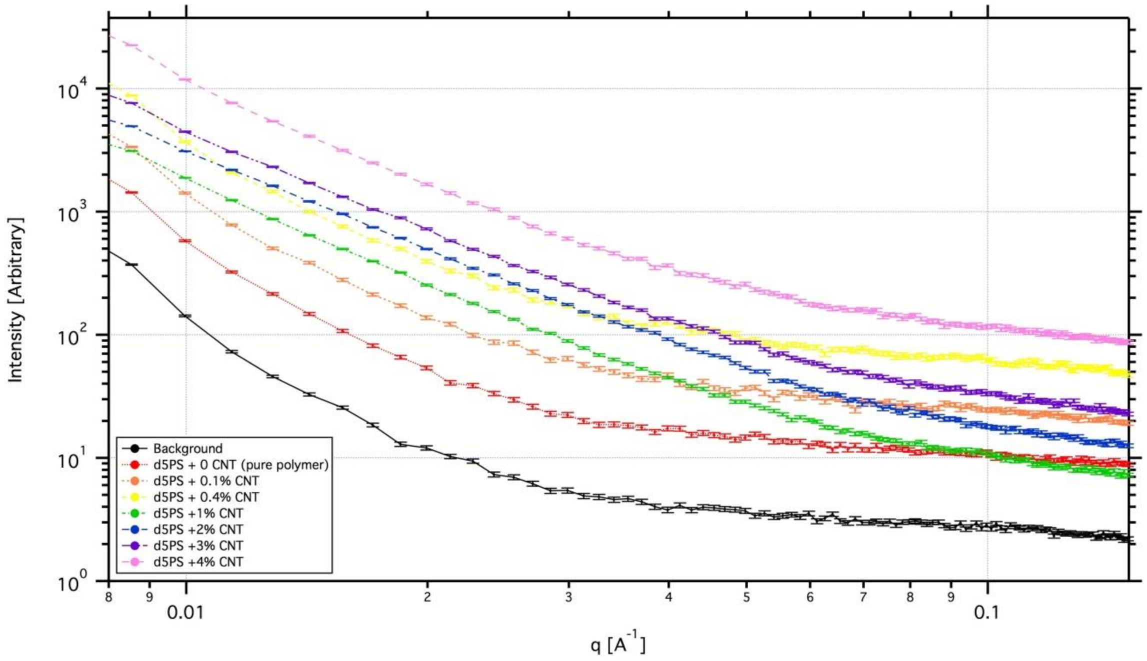

Figure 42: SAXS data for d5 PS with 0, 0.1, 0.4, 1, 2, 3 and 4 wt% SWCNTs, prior to background subtraction.

Several papers investigating the effect of adding nanospheres to a polymer stress the importance of good contrast-matching.[53, 54, 68, 69] The SANS work of Sen *et al*. and Nusser *et al*. on nanospheres that were larger than the polymer radius of gyration found no increase in polymer R_g relative to the bulk on addition of nanospheres to the system, contrary to all other literature on this size regime. While Sen *et al*.'s anomalous results may have been due to the poor dispersion of filler in the nanocomposites under study, it was also noted that the scattering intensity at low-*Q* increased dramatically with increasing silica nanoparticle loading levels, indicative of poor contrast-matching.[53] Nusser *et al*.'s work[54] concerned small angle neutron scattering on nanocomoposites containing core–shell particles where the core and the shell had different scattering length densities. This excess made it impossible for scattering from the particles to be removed entirely from the scattering of the system as a whole. The SANS study by Mackay's group[68, 69] on tightly-crosslinked PS spheres in a PS matrix stated that this system had been deliberately chosen to avoid contrast-matching issues – as the hydrogenated PS nanoparticles and hydrogenous PS chains have the same scattering length density, the scattering from the deuterated chains in the system is highly visible, simplifying analysis and making it easier to draw generalised conclusions.

In the model used to fit the data presented in this chapter, the parameter *A* corresponds to the scattering contribution from the nanotubes, and is expected to be proportional to the volume fraction of nanotubes. The variation of *A* with filler volume fraction is shown in Figure 43. While the data in these plots are rather scattered, in general a large increase in nanotube scattering is occurring with increasing nanotube concentration. Sen *et al*. identified an excess increase in scattering intensity with increasing silica loading at filler loading levels lower than 10 vol%, with scattering from the silica was being counted alongside that from single deuterated chains.[53] Nusser *et al*. found that core–shell nanoparticles (a hydrophobically-modified silica nanofiller) in a polymer matrix [poly(ethylene-*alt*-propylene)] scattered strongly independent of incorporation into the matrix, as the core and shell have different scattering length densities, leading to increased scattering with increasing loading, which may mask underlying effects.[54] Based on these works it is believed that the scale of the increase in the value of *A* is likely to be a consequence of the lack of contrast-matching in the systems presented here.

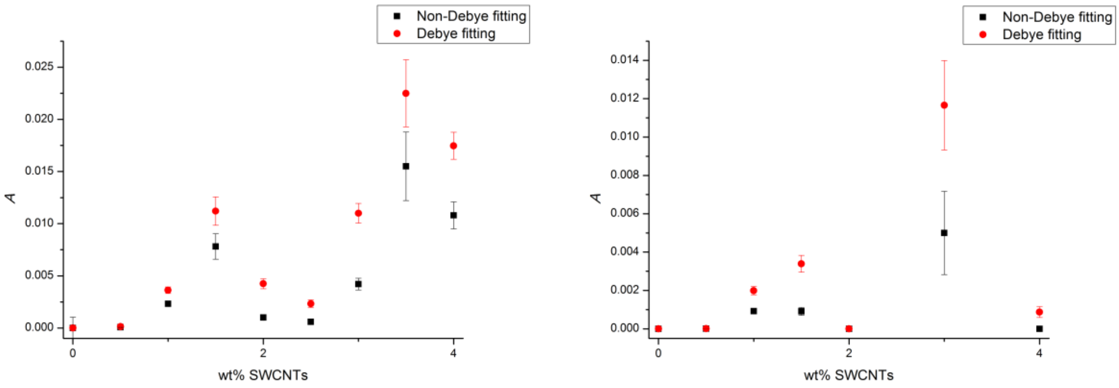

Figure 43: Plots of parameter *A* extracted from both the Zimm and Debye fittings of dΣ/dΩ *vs*. SWCNT concentration for (left) the 110k PS and (right) 230k series of PS/SWCNT nanocomposites.

One notable feature about the increase in *A* with increasing nanotube concentration is that the increase is not linear. If the increase in the value of *A* was simply a consequence of the lack of contrast-matching, a linear trend would be expected. Instead *A* appears to peak at around 1.5% before rising again at higher concentrations. The nanotube dispersion in the samples used for QENS (which are analogous to the samples used for SANS) was examined using SAXS (Figure 40), and it was identified that the dispersion of the nanotubes changed at around 1 wt%. It may be the values of *A* obtained from the fitting presented here are showing the effects of a combination of additional scattering arising from contrast scattering issues and aggregation effects.

As a result of this analysis, it was discovered that it was essential to repeat the SANS experiments on more accurately contrast-matched samples to minimise the contribution to the scattering from the CNTs, although perfect contrast-matching is not possible with carbon nanotubes as there is discernible variation in scattering length density with radius on a length scale commensurate with neutron wavelength, leading to similar additional scattering issues to those experienced by Nusser *et al*. with core–shell nanoparticles in a polymer matrix.[54] This second round of work was carried out in collaboration with colleagues at the University of Pennsylvania, using the small angle neutron scattering work presented in this thesis as the basis for further experiments, and resulted in the 2013 and 2015 papers by Tung *et al*.[86, 87]

The work by Tung *et al*. conducted for the paper published in 2013[86] undertook a full rigorous experimental contrast-matching of the samples before a full set of samples was made at the contrast-matched ratio (72.5/27.5 dPS/hPS) and small angle neutron scattering was conducted in a manner similar to that presented in this chapter, with the introduction of an additional term to independently take into account scattering from the rod network created by the CNTs in the sample ($B \times Q^{-2}$, Equation 34).

$$\frac{\mathrm{d}\Sigma}{\mathrm{d}\Omega}(Q) = A \times \mathrm{Debye}\left(Q, R_g\right) + B \times Q^{-2} + C \times Q^{-4} + D$$

Equation 34

where $A \times \mathrm{Debye}\left(Q, R_g\right)$ represents the single chain contribution from the Gaussian chains, $B \times Q^{-2}$ corresponds to the scattering from the CNTs, $C \times Q^{-4}$ represents the contribution from voids and defects in the sample and D takes into account the incoherent scattering from the hydrogen atoms in the sample (which was found to be very small and was omitted from the final fitting).

The work in Tung's 2013 paper concluded that for SWCNT/PS nanocomposites where the radius of the nanotubes was smaller than the radius of gyration of the polymer ($R_{\mathrm{gSWCNT}}/R_{\mathrm{g}} \approx 0.4$) and MWCNT/PS nanocomposites where $R_{\mathrm{gSWCNT}}/R_{\mathrm{g}} \approx 1$, no change in radius of gyration occurred relative to the bulk up to a filler loading level of 2 wt%. Above 2 wt% filler, the radius of gyration in the SWCNT/PS nanocomposites increased monotonically reaching an R_{g} increase of 36% at 10 wt% filler. For the MWCNT/PS nanocomposite, the radius of gyration fell slightly above 2 wt% nanotubes.

Tung *et al*.'s 2015 paper used SANS to investigate the effect of alignment on the radius of gyration of PS chains in a series of PS/SWCNT nanocomposites with increasing nanotube concentrations. Melt fibre spinning was used to align the nanotubes in the nanocomposites, then SANS was conducted, fitting the data as before, but the scattering parallel and perpendicular to the direction of alignment were fitted separately to determine the radii of gyration parallel and perpendicular to the direction of alignment ($R_{\mathrm{g}}^{\mathrm{par}}$ and $R_{\mathrm{g}}^{\mathrm{per}}$, respectively). Tung *et al*. found that $R_{\mathrm{g}}^{\mathrm{per}}$ was slightly higher than the $R_{\mathrm{g}}^{\mathrm{non}}$ (the radius of gyration from a non-aligned PS/SWCNT nanocomposite), while $R_{\mathrm{g}}^{\mathrm{par}}$ was found to be much lower, taking values close to those of the bulk, indicating that the polymer chains had expanded perpendicular to the direction of alignment.

The reason behind the results presented in each paper is the same: mesh size and the low interaction potential between PS and CNTs. As the nanotube loading is increased, the mesh created by the nanotubes becomes finer. If the mesh size is greater than the R_{g} of the polymer chains, the mesh does not impinge on the chains and the chains adopt their preferred conformation, leading to no change in R_g from that measured in the bulk. In a non-aligned sample, when the mesh size becomes smaller than the radius of gyration, the polymer chains expand isotropically to avoid the nanotubes. If a composite contains a fixed wt% CNTs, a sample containing SWCNTs will have a higher number density of CNTs than a sample containing MWCNTs, leading to the sample containing SWCNTs having a smaller mesh size. When the nanotubes in the PS/SWCNT nanocomposites are aligned, the mesh size decreases perpendicular to the direction of alignment, and the polymer chains expands perpendicular to the alignment direction to reduce the interaction with the naotubes; this effect is more pronounced at higher concentrations as the decrease in mesh size with increasing nanotube concentration is compounded with the decrease in mesh size caused by the alignment of the nanotubes.

The same result may not be found for other polymer/nanotube systems: PS has only a weak interaction potential with carbon nanotubes, so the polymer chains adopt a conformation that reduces the interfacial interaction. Other polymers, such as PMMA,[121, 146] have a positive interaction potential with carbon nanotubes, and therefore may expand parallel to the direction of alignment in a bid to increase the favourable interactions between the nanotubes and the polymer.

3.4 Conclusions

Small angle neutron scattering measurements were conducted on twenty samples: nine 110k samples, seven 230k samples and four 230k annealed samples, containing between 0 and 4 wt% SWCNTs, across a Q range of 0.00147 to 0.428 Å^{-1}.

The reduced data for the 110k and 230k PS samples were fitted using Zimm and Debye equations in order to extract the radius of gyration for each sample. The fitting was moderately successful for all samples, with both the Zimm and Debye equations, with the quality of the fits varying between samples. The fitting to the Zimm equation consistently produced higher values for R_g, with greater error in the values than was seen for the Debye fitting. The Debye fitting of the 0 wt% $I(Q)$ data returned R_g values for the neat polymers that were a good match with those from the literature[169] (Table 24).

Table 24: Summary of R_g values obtained for neat PS matrices from the literature, Zimm and Debye fits

Polymer	**Literature value for R_g/Å^a**	**Zimm value for R_g/Å**	**Debye value for R_g/Å**
110 kg mol^{-1} PS	89.2	101	87.4
230 kg mol^{-1} PS	129	143	124
^{a}Fetters *et al.*, Macromolecules, 1994.[169]			

In general the measured R_g values increased with increasing nanotube concentration, by up to ~450% for the 110k PS series of samples, and by up to ~500% for the 230k PS nanocomposites. These values are significantly higher than those reported for comparable systems containing spherical nanoparticles, and calculating the energy cost of such stretching at 4.5 k_BT and 5 k_BT per chain, respectively,[170] suggests that the energetic cost for this would be prohibitively high and the system would agglomerate rather than mix under these conditions. An alternative explanation is that the apparent increase in R_g is an artefact from the CNT loading which contributes a Q^{-2} dependence to the scattering, an effect that is most likely attributable to the system being investigated not being contrast-matched.[53, 54, 68, 69] Based on this second conclusion, an improved version of the experiment was conducted by Tung *et al.*,[86] who published the result that the polymer R_g increases with increasing SWCNT concentration relative to that of the bulk, when $R_{SWCNT}/R_g \approx 0.4$, but only above 2 wt% filler, and at 10 wt% the increase in R_g was 36%.

Chapter 4: Quasielastic neutron scattering

4.1 Introduction

The primary aim of this thesis is to provide an explanation from the minimum in the diffusion coefficient at the percolation threshold when the polymer radius of gyration is greater than the nanotube radius, as identified by Mu *et al*.[129, 130] In the previous chapter, the polymer radius of gyration, which, based on Equation 26, was expected to exhibit a similar minimum, was found to increase with nanotube concentration. This result was expanded on by Tung *et al*., who identified that at nanotube concentrations below 2 wt%, the R_g remained approximately constant for both PS/SWCNT and PS/MWCNT nanocomposites; at nanotube concentrations above 2 wt%, the R_g in PS/MWCNT nanocomposites decreased slightly, while that of PS/SWCNT nanocomposites increased significantly, with an increase of 36% being identified at 10 wt% SWCNTs.[86] Tung *et al*. also found that the R_g increased more perpendicular to the alignment direction than parallel to it.[87] This means that the minimum in polymer diffusion in PS/CNT nanocomposites cannot be attributed to the effect of the nanotubes on the radius of gyration, and might instead be caused by the effect of the nanotubes on the fast dynamics of the polystyrene matrix.

Chapter 4 presents the findings from the quasielastic neutron scattering (QENS) experiments on polystyrene/SWCNT nanocomposites. The chapter begins with analysis of the static structure factor, followed by examination of the elastic scan, including extraction of the mean squared displacement, polymer stiffness and glass transition temperature. The second half of the chapter covers the Fourier transform of the QENS peaks and Kohlrausch–Williams–Watts fitting of resulting the $I(Q,t)$ curves.

4.2 Static structure factor

4.2.1 Introduction

The static structure factor obtained from neutron scattering records the elastic scattering of a sample and provides information on how a material scatters neutrons without resolving the energy of the scattered neutrons; it parallels the SSF obtained from X-ray scattering data, which, for PS, is discussed in Chapter 2, and can be used to provide information about the interactions between structural groups within a system. The SSF records the coherent scattering, which in polystyrene is dominated by the scattering from the carbon and deuterium nuclei within the polymer chain. Experimentally, the static structure factor is obtained by integrating the elastic intensity with respect to change in energy, *i.e.* the elastic portion of the quasielastic peak, at a given T and Q, without resolving the energy of the scattered neutrons.

As the SSF is dominated by the scattering from the deuterium and carbon atoms within the polymer chain, the SSF of chain-deuterated PS provides information on the polymer chain interactions, while the SSF of ring-deuterated PS focuses on the phenyl ring interactions (Table 25). For clarity, in this section chain-deuterated PS will be referred to as d3 PS, and ring-deuterated PS as d5 PS.

Table 25: Coherent scattering cross section of hydrogen, carbon and PS

Species	**Coherent scattering cross section (10^{-24} cm^2)[162]**
Hydrogen	1.7583
Deuterium	5.592
Carbon	5.551[a]
d3 PS ($(C_8H_5D_3)_n$)	69.9755
d5 PS ($(C_8H_3D_5)_n$)	77.6429
[a]Average C value based on the natural abundances of C12 and C13.	

4.2.2 Results and analysis

4.2.2.1 Data reduction

Raw data obtained on the IRIS beamline at ISIS for d3 and d5 PS containing between 0 and 4 wt% single-walled carbon nanotubes (SWCNTs) were reduced using the computer programme MANTID.[171] The SSF was extracted from the QENS runs at each temperature (T) by first adding all equivalent runs (the data at each temperature were recorded in small blocks rather than as one long run as a precaution against data loss and issues that could arise from instrument failure), then evaluating the quasielastic peak. The quasielastic peak was integrated between the limits -0.01 to 0.01 meV (*i.e.* the FWHM of the resolution peak,[172] 0.0175 meV, plus a bit to encompass the majority of the peak, but not the background), to give the elastic intensity, $I(Q)$, at a given T and scattering vector (Q). Data from each detector was kept separate; no binning of the data in terms of Q was conducted during the analysis.

4.2.2.2 Data normalisation

For an initial evaluation, data were normalised such that the maximum value of $I(Q)$ *vs*. Q was equal to one; all other data points in a given set were divided through by the same normalisation factor. For secondary evaluation, some data sets were also normalised such that the maximum value in a secondary peak had a value of $I(Q) = 1$; where this is the case a note has been made to this effect.

4.2.2.3 Results and discussion

4.2.2.3.1 d3 PS SSF: effect of temperature

The SSF plots for d3 PS as a function of temperature recorded on IRIS at ISIS are shown in Figure 44, while Figure 45 shows the same data, but normalised to the second (polymerisation) peak. These data are analogous to the wide-angle X-ray scattering (WAXS) data obtained by Ayyagari and co-workers on fully-hydrogenated PS (Figure 46),[116] except that X-rays are scattered by the electrons in the system rather than the nuclei. In addition, as the data presented here are from d3 PS, they are dominated by the chain interactions and have a smaller contribution from any phenyl–chain and phenyl–phenyl correlations, which arise from coherent scattering from the carbon atoms in the sample. In the Q-range under examination here (Q = 0.44–1.86 Å^{-1}), the WAXS data presented by Ayyagari and co-workers[116] exhibits two peaks: one at $Q \approx 0.8$ Å^{-1} and a second at $Q \approx 1.4$ Å^{-1}, corresponding to distances of 7.9 and 4.5 Å, respectively. The peak at low-Q is termed the 'polymerisation peak' as it is not present in the scattering of the monomer; the peak at high-Q is called the 'amorphous peak' and is present in the scattering of both the monomer and the polymer. The low-Q polymerisation peak in the WAXS spectra of PS exhibits unusual temperature-dependence, increasing in intensity with increasing temperature (reported by Mitchell and Windle[173] between 20 and 250 °C). As for the WAXS data presented by Ayyagari and co-workers, the neutron data presented here have peaks at the same positions as those found in the WAXS spectra of PS, and the low-Q peak exhibits the same anomalous temperature-dependence [Figure 45(a)], leading to the conclusion that the neutron data exhibit a low-Q polymerisation peak and a high-Q amorphous peak; however, the intensities of the peaks in the d3 PS neutron data are reversed compared to the WAXS data for fully hydrogenated PS, with the low-Q polymerisation peak ($Q \approx 0.75$ Å^{-1}) having a much higher intensity than the high-Q amorphous peak ($Q \approx 1.4$ Å^{-1}); this is consistent with the additional weighting to the backbone contribution arising from the deuteration, and the WAXS being dominated by the carbon atoms, of which 5/8 are found in the phenyl rings in PS.

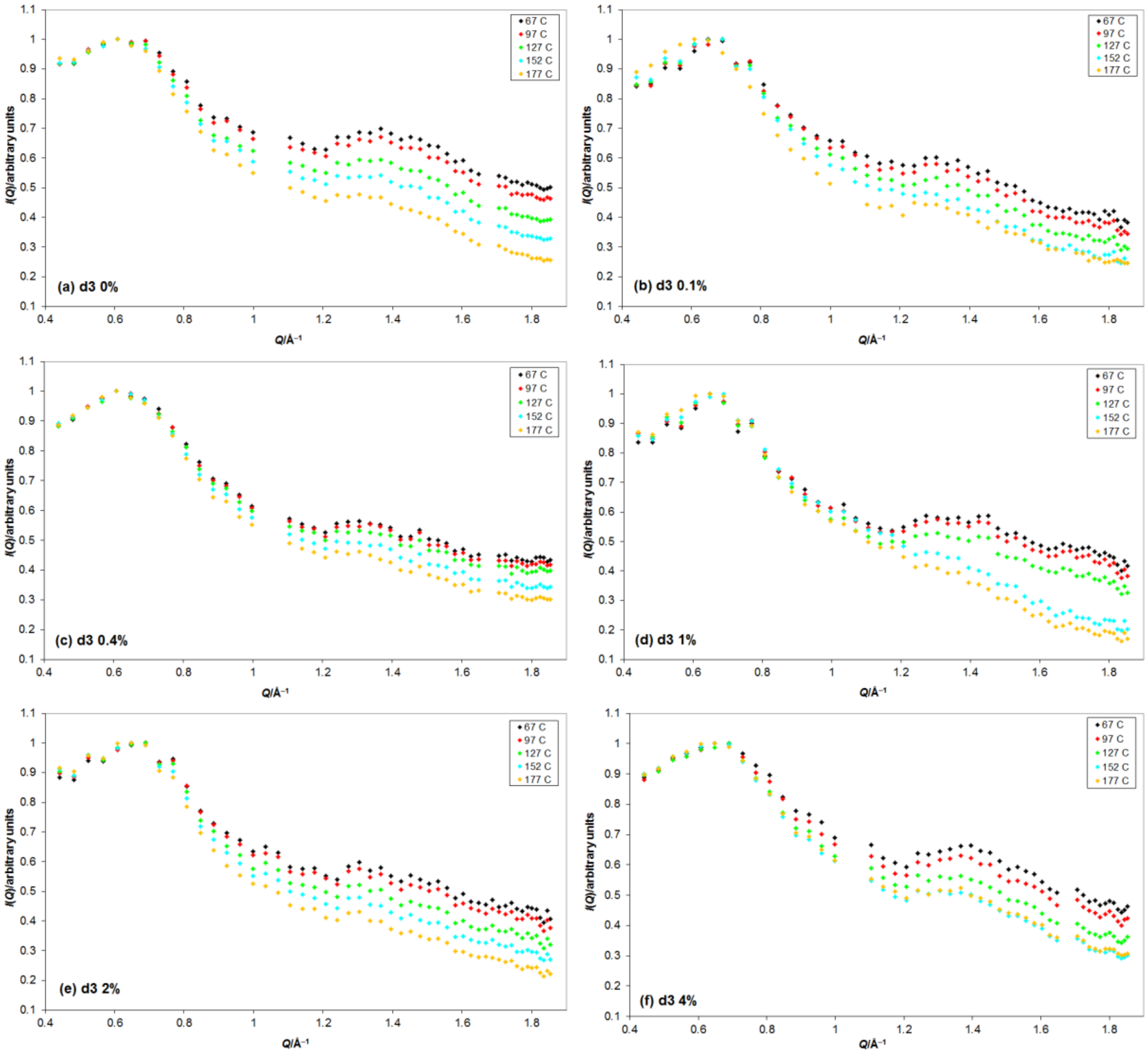

Figure 44: SSF for d3 (chain-deuterated) PS with 0–4 wt% SWCNTs recorded on IRIS at ISIS: (a) 0 wt%, (b) 0.1 wt%, (c) 0.4 wt%, (d) 1 wt%, (e) 2 wt%, (f) 4 wt%. All data are normalised such that the maximum value has an *I*(*Q*) value of 1. Error values on the *I*(*Q*) values are ±0.5%, which is smaller than the size of the data points, therefore error bars have been omitted.

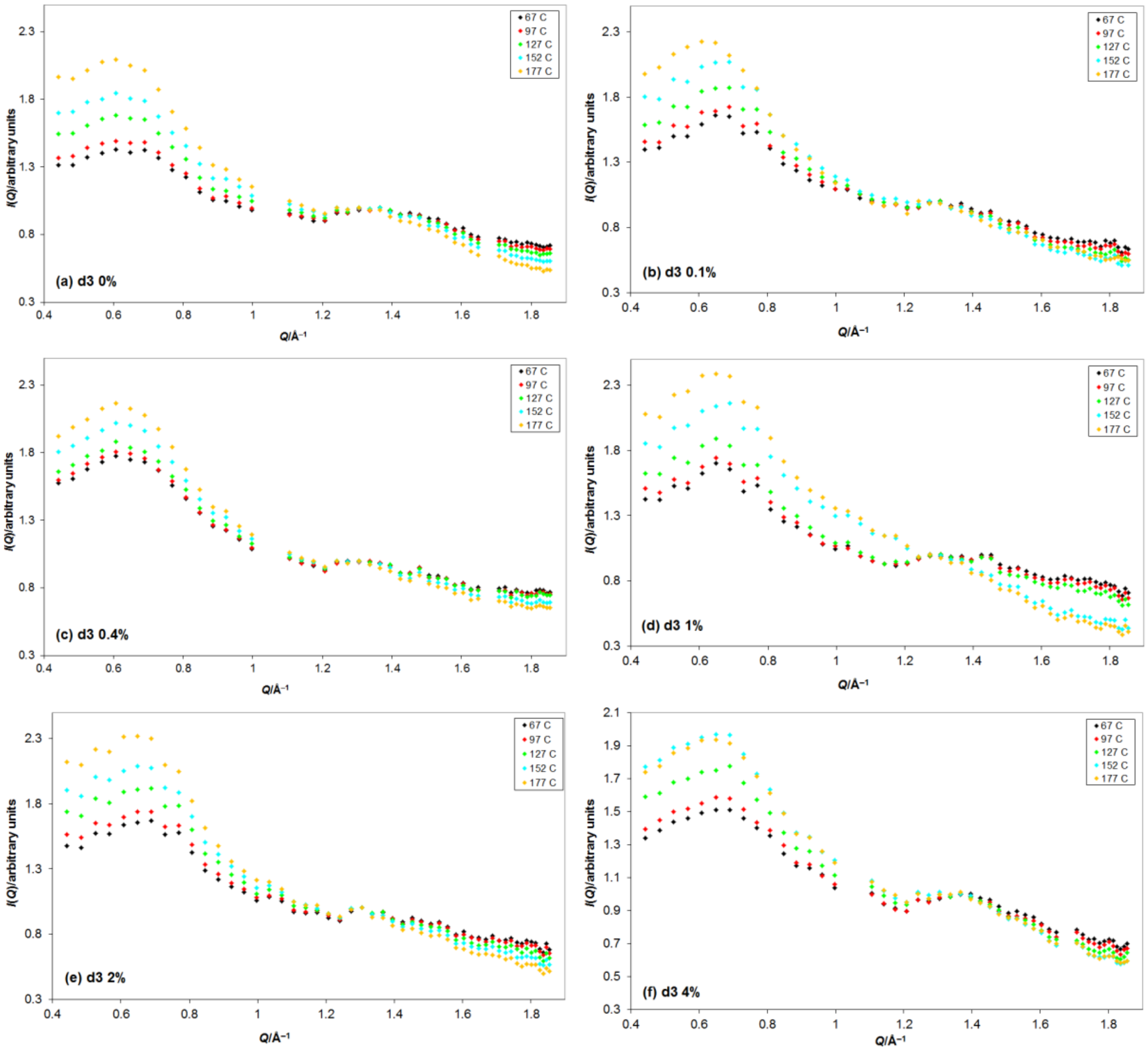

Figure 45: SSF for d3 (chain-deuterated) PS with 0–4 wt% SWCNTs recorded on IRIS at ISIS: (a) 0 wt%, (b) 0.1 wt%, (c) 0.4 wt%, (d) 1 wt%, (e) 2 wt%, (f) 4 wt%. All data are normalised such that the maximum value in the secondary (amorphous) peak has an *I*(*Q*) value of 1. Error values on the *I*(*Q*) values are ±0.5%, which is smaller than the size of the data points, therefore error bars have been omitted.

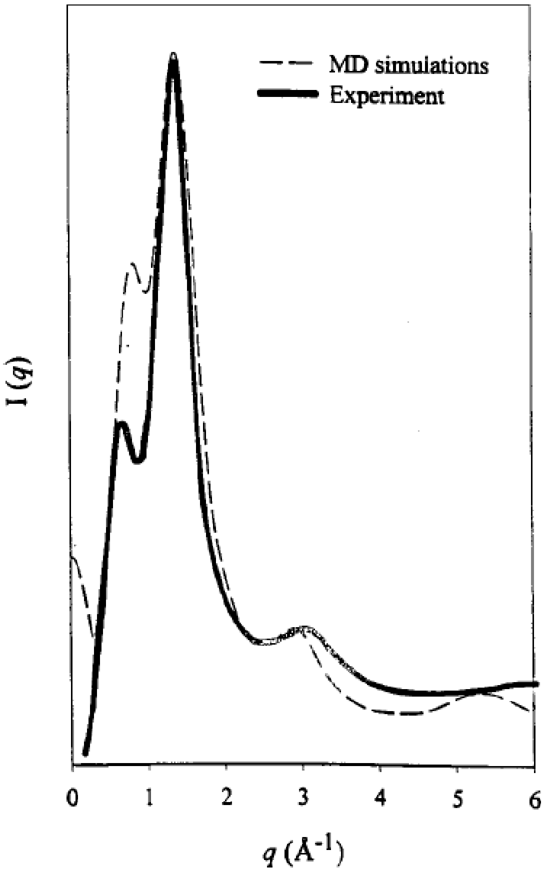

Figure 46: X-Ray scattering intensity for atactic polystyrene from experiment (293 K, solid line) and molecular dynamics simulation (298 K, dashed line). Ayyagari and co-workers,[116] reproduced with permission from ACS © 2000.

The temperature-dependence of the high-*Q* amorphous peak is as expected for a polymer (Figure 44): the intensity decreases with increasing temperature as the polymer expands and there is less correlation between the positions of non-connected individual atoms. Ayyagari and co-workers attributed this peak to intermolecular phenyl–phenyl and phenyl–chain correlations,[116] therefore in the neutron scattering SSF of d3 PS the high-*Q* peak must arise from correlations between the phenyl–phenyl and phenyl–chain *carbon* atoms. As the temperature increases it is expected that these interactions would weaken as the polymer chains become more mobile and the polymer undergoes thermal expansion.

The low-*Q* polymerisation peak of PS primarily arises from intermolecular chain–chain correlations, but also has a contribution from phenyl–chain and phenyl–phenyl intermolecular interactions.[116] Here (Figure 45) the scattering of the deuterons in the chain are being recorded alongside scattering from the carbon atoms in the sample, so while the intermolecular chain–chain contribution is primarily being observed, contributions from the whole molecule are also being detected. As has been recorded in the WAXS literature,[116, 173] this polymerisation peak displays an unusual temperature-dependence, increasing in intensity with increasing temperature. Ayyagari *et al.*[116] suggested that this anomalous behaviour arose from the phenyl–phenyl and phenyl–chain contributions to the peak, which is likely to be the case here as the scattering from the carbon atoms in the whole molecule are being observed alongside the more localised scattering from the deuterium atoms in the polymer chains.

There is an exception to the trends described in the previous discussion: the SSF for the 4% sample at 152 °C is almost identical to that at 177 °C [Figure 44(f) and Figure 45(f)]. Intuitively, one would expect these higher temperatures to follow the same trends as seen for the lower temperatures: an increase in intensity of the polymerisation peak and a decrease in intensity of the amorphous peak at 177 °C compared to 152 °C, but this is not the case. The scattering data presented here arises from both the deuterium and carbon atoms in the sample. When carbon nanotubes are added to the system, their carbon atoms will also make a contribution to the scattering of the sample as a whole. It may be that there is a background contribution arising from something that is very strongly correlated at low concentrations, but that at the higher temperatures under investigation the CNTs may have long enough to aggregate, changing the contribution the nanotubes make to the SSF. However, the d3 PS + 4 wt% SWCNT was run at 177 °C before it was run at 152 °C, so when the sample was run at 152 °C it is likely to have already undergone aggregation if it were going to occur. Another possible explanation is that the phenyl rings on the polymer exhibit a temperature-dependent interaction with the carbon atoms in the CNTs, although the exact nature of this interaction is unclear.

4.2.2.3.2 d3 PS SSF: effect of CNT concentration

The SSF plots of d3 PS as a function of concentration at 67 and 177 °C normalised to the maximum value in the first and second peaks are shown in Figure 47 and Figure 48, respectively.

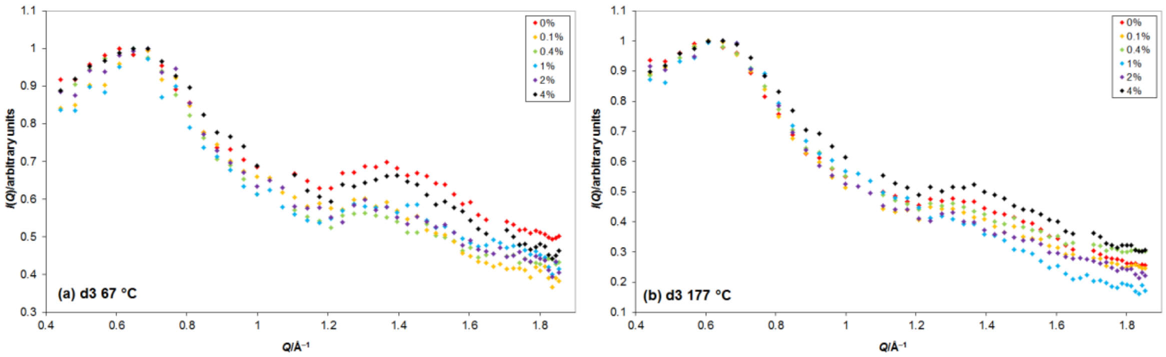

Figure 47: SSF for d3 (chain-deuterated) PS at (a) 67 and (b) 177 °C. All data are normalised such that the maximum value has an *I*(*Q*) value of 1. Error values on the *I*(*Q*) values are ±0.5%, which is smaller than the size of the data points, therefore error bars have been omitted.

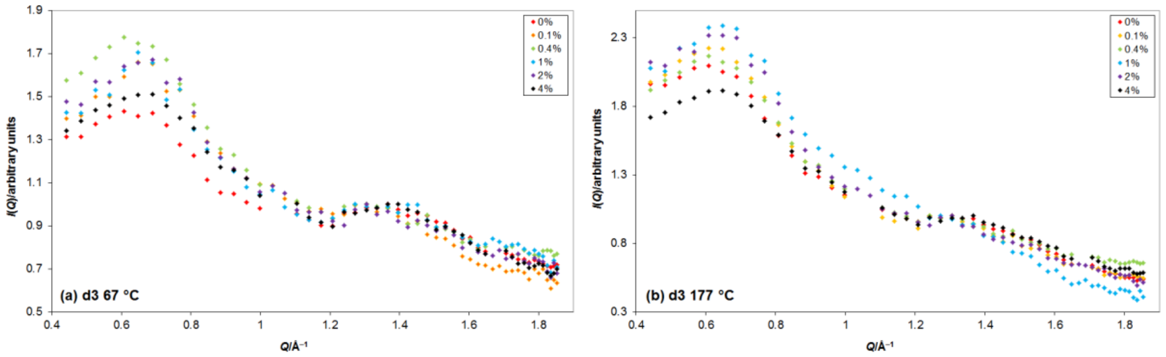

Figure 48: SSF for d3 (chain-deuterated) PS at (a) 67 and (b) 177 °C. All data are normalised such that the maximum value in the amorphous (high-*Q*) peak has an *I*(*Q*) value of 1. Error values on the *I*(*Q*) values are ±0.5%, which is smaller than the size of the data points, therefore error bars have been omitted.

Increasing the concentration of nanotubes in the composite results in a reduction in the intensity of the amorphous peak across all values of *Q* at both 67 and 177 °C for all concentrations between 0.1 and 3 wt% SWCNTs, but the peak intensity recovers when the nanocomposite contains 4 wt% SWCNTs (Figure 47). It would be expected that the nanotubes would expand the network of polymer chains, providing more than one possible environment to the polymer chains and disrupting some of the chain–chain correlations, broadening the peak and decreasing the peak intensity. The gradual recovery in peak intensity when the nanocomposites contain between 1 and 4 wt% nanotubes is probably due to the nanotubes displaying increasing levels of aggregation with concentration, and the nanotubes and polymer existing in segregated pockets, thus increasing levels of polymer chains exhibit the same level of interaction as in the pure polymer. This agglomeration is confirmed by the SAXS results from the h3 PS samples, which show a change in line shape at SWCNT concentrations higher than 1 wt% (Figure 42), indicating at least an increase in polydispersity at higher loading levels, if not full aggregation. It may be that changes in the amorphous peak in the presence of CNTs can be used as a measure of the extent to which the CNTs are dispersed in the polymer matrix.

Adding nanotubes to the composite has the reverse effect on the intensity of the polymerisation peak (Figure 48): when between 0.1 and 3 wt% SWCNTs are included in the composite, the polymerisation peak increases in intensity, then returns to the intensity of the neat polystyrene when the composite contains 4 wt% nanotubes. The reason for this is not obvious; it might be that the CNTs tend to cause some alignment of the backbones near their interface with the polymer, which happens to be on the same length scale as the polymerisation peak.

4.2.2.3.3 d5 PS SSF: effect of temperature and concentration

The d5 PS data shown in Figure 49 and Figure 50 are dominated by scattering from the polystyrene phenyl ring and therefore provides information about the phenyl–phenyl interactions; however, as for the scattering from d3 PS, scattering from carbon atoms in the molecule also contributes. These plots have far fewer features than the d3 PS scattering, with no definitive polymerisation peak at any temperature or concentration, and no amorphous peak in the scattering from the neat polymer. The absence of the polymerisation peak is not surprising as Ayyagari and co-workers[116] attributed this peak primarily to scattering from sources other than phenyl–phenyl correlations, with only a weak intermolecular phenyl–phenyl contribution. The lack of high-*Q* amorphous peak in the SSF of pure d5 PS is unexpected as Ayyagari and co-workers[116] ascribed this peak primarily to intermolecular and intramolecular phenyl–phenyl correlations, with an additional contribution from intramolecular phenyl–chain interactions.

As the nanotube concentration is increased, a strongly temperature-dependent high-*Q* peak emerges in the same position as the amorphous peak in the WAXS of neat PS; this peak displays standard temperature-dependence, decreasing in intensity with increasing temperature. The amorphous peak disappears at 4 wt% SWCNTs; this sample exhibits very similar scattering to that of the nanotube-free sample. As the scattering shows no definitive polymerisation peak, the data has not been normalised to the maximum value in the amorphous peak. It is not obvious why the amorphous peak should increase with CNT concentration, but it must be due to the CNTs. The SSF from the d3 PS suggests that agglomeration is seen with increased loading, and the similarity of the amorphous peaks for d5 PS with 0 and 4 wt% SWCNTs suggests that the appearance of the amorphous peak for the intermediate concentrations is related to the available surface area and CNT/polymer interactions.

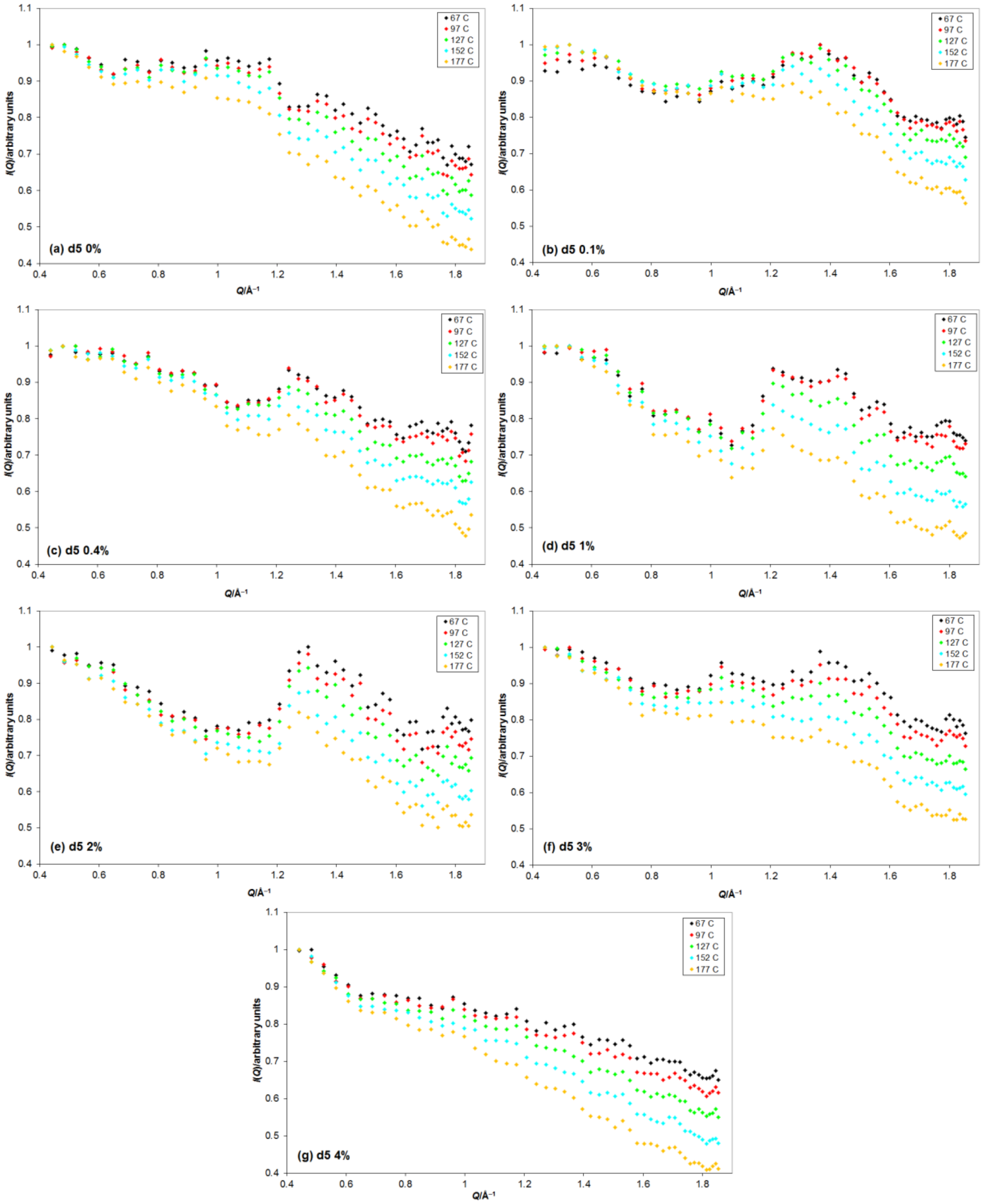

Figure 49: SSF for d5 (ring-deuterated) PS with 0–4 wt% SWCNTs: (a) 0 wt%, (b) 0.1 wt%, (c) 0.4 wt%, (d) 1 wt%, (e) 2 wt%, (f) 3 wt%, (g) 4 wt%. All data are normalised such that the maximum value has an *I*(*Q*) value of 1. Error values on the *I*(*Q*) values are ±0.5%, which is smaller than the size of the data points, therefore error bars have been omitted.

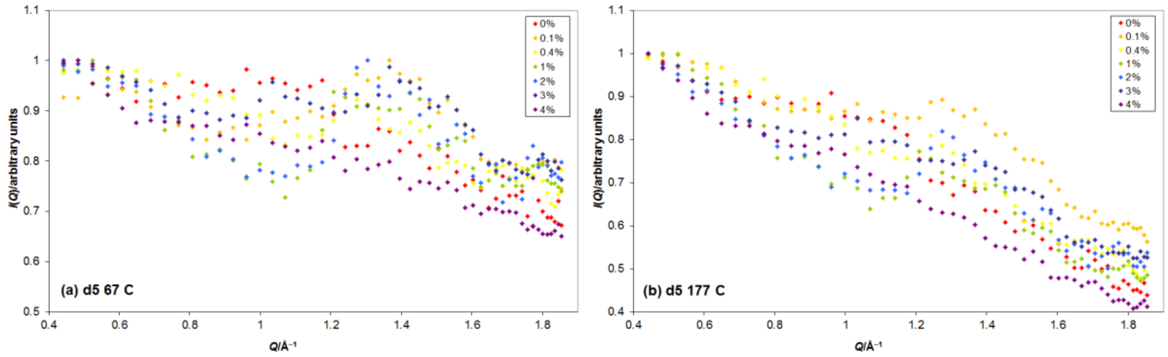

Figure 50: SSF for d5 (ring-deuterated) PS at (a) 67 °C and (b) 177 °C. All data are normalised such that the maximum value has an *I*(*Q*) value of 1. Error values on the *I*(*Q*) values are ±0.5%, which is smaller than the size of the data points, therefore error bars have been omitted.

The data in Figure 50 corroborate that from Figure 49; while the data is very scattered, possibly owing to some variation in CNT dispersion, all nanotube concentrations between 0.1 and 3 wt% display increased intensity compared to neat PS at both 67 and 177 °C, while at 4 wt% SWCNTs, the intensity returns to that of neat PS.

The amorphous peak in PS is due to intra and intermolecular phenyl ring correlations.[116] Below 4 wt% the small nanotube bundles will be sitting between the polymer chains, altering the intermolecular phenyl ring correlations, and causing the amorphous peak to emerge. Conversely, the nanotubes are unlikely to have an effect on the intramolecular correlations as sterically the nanotube bundles will not easily be able to fit between the phenyl rings on the polymer chain, with adjacent phenyl rings on the same side of the polymer chain having a maximum separation of 2.28 Å, while the nanoparticle bundles have an average diameter of 4 nm (s.d. 2.55 nm) and average bundle length of 410 nm (s.d. 280 nm). Once a nanotube loading of 4 wt% has been achieved, the nanotubes and polymer chains are likely to exist in localised pockets, as was inferred from the d3 PS SSF scattering, and the scattering will return to that of the neat polymer as the polymer and nanotubes scatter independently.

In the d3 scattering, the samples displayed the same scattering at 152 and 177 °C; the same thing does not occur for the d5 scattering, instead the intensity of the amorphous peak continues to decrease between 152 and 177 °C. The reason for this difference is not clear, however, it may be that the behaviour displayed by the d3 PS sample is an effect arising from sample history rather than an effect inherent to the material itself; each sample was pressed until it was the correct size and shape for the scattering experiment, so some samples were pressed for longer than others. During sample preparation, the samples were hot-pressed at 150 °C, for a minimum of 1.63 h, sufficient temperature and time for the polymer chains to flow (the reptation time for the polymers in these experiments is 6 min or less,[154] but the SWCNT relaxation and agglomeration times may be longer), annealing the sample and removing stresses arising from processing; then, during the scattering experiments, the samples were further exposed to temperatures well above the glass transition temperature for a minimum of 4 h, allowing further annealing to occur. It may be that the d5 PS sample had been exposed to longer heating periods prior to conducting the scattering experiments, and was thus less susceptible to further change upon heating during the scattering experiments. In addition, the downward trend in $I(Q)$ is more pronounced at higher temperatures and flatter at lower temperatures (Figure 50). It may be that the shape of $I(Q)$ reflects that some relaxations at high temperature/loading become possible but only over shorter length scales shorter than those previously explored *via* SAXS.

4.2.2.3.4 XRD of SWCNTs

In discussing the results from the static structure factor, the neutron SSF has been compared to the XRD of pure polystyrene, but not that of pure carbon nanotubes. An isolated single walled carbon nanotube should not be expected to exhibit sharp Bragg peaks as there are no planes available for diffraction to occur from. However, SWCNTs typically exist as aggregated bundles composed of tens to hundreds of tubes. The nanotubes self-assemble into a hexagonal lattice held together with van der Waals forces; this structure then has a diffraction pattern primarily arising from characteristic (1 0) planes, with a shoulder at Q = 0.44 Å^{-1} (corresponding to d = 14 Å). Additional broad maxima at higher Q values are present [$Q \approx 0.9$ and 1.5 Å^{-1} (corresponding to d = 7 and 4.2 Å, respectively)]; these correspond to other reflections from the hexagonal packing. If the SWCNTs are contaminated by MWCNTs, a signal would also arise from the 002 reflection of graphite-like arrangement of the nested walls.[174] While the signals from the SWCNTs may be present in the spectra from the nanocomposites, the nanotubes are present only at low concentrations, and the scattering signal will be dominated by that from the polymer matrix. Some effect may be anticipated at the higher nanotube concentrations under examination, as above 1 wt% the SAXS data for these samples suggests that the distribution of the nanotubes changes, possibly agglomerating and increasing the degree of hexagonal packing of the nanotubes in the samples. However, the SSFs for the nanocomposites containing 0 and 4 wt% SWCNTs are very similar (Figure 48 and Figure 50); if pronounced scattering from aggregated SWCNTs was present, the SSF for the 4 wt% samples would be expected to be different to that of the 0 wt% sample, therefore it can be assumed that any nanotube contribution to the SSF is small.

4.2.2.3.5 Consideration of error

While the statistical error of the individual data points is small both here for the static structure factor and later in the elastic scan data, the scatter is large. There are several potential sources for this scatter. First, the error in the nanotube concentration is large as the method used to produce the nanocomposites requires the nanotubes to be transferred between containers many times, and even with repeated careful rinsing it is inevitable that this, combined with solvent evaporation, will lead to errors in the stated nanotube concentration. The error in nanotube concentration in an individual sample may be up to *ca*. 12% of the stated wt%, *e.g.* 4 ± 0.48 wt%. Secondly, the samples are held at temperatures above the glass transition temperature for long periods during many of the measurements; at such temperatures, the polymer is in its viscoelastic state and can flow, leading to alteration of the distribution of the nanotubes. Thirdly, multiple scattering has not been taken into account during the analysis. The samples were pressed to a thickness corresponding to a sample transmission of between 90 and 95%, thus reducing the chances of multiple scattering occurring, but the nature of the pressing process used to prepare the samples is such that the samples were not fully even, and some regions may have contributed multiple scattering.

4.3 Elastic scan

4.3.1 Introduction

Elastic scans record the integrated intensity within a narrow energy window as a function of T and Q. At very low temperatures a QENS peak is very sharp and well defined; as the temperature increases, the peak broadens because of additional rotational and translational motions within the polymer chain, resulting in a drop in the intensity of the peak. By plotting the intensity as a function of Q and T, information about the dynamics within a polymer sample can be obtained.

4.3.2 Results and analysis

The elastic scan analysis presented here is based on the analysis conducted by Sanz *et al.*[120] on QENS from polystyrene and poly(4-methyl styrene) with C_{60} (on spectrometer IN16 at ILL, $0.2 \leq Q \leq 1.9$ Å^{-1}), a system that is, in many ways, analogous to that investigated here. Following reduction and normalisation, the mean squared displacement, neutron glass transition temperature and stiffness were calculated from the data recorded.

4.3.2.1 Data reduction

4.3.2.1.1 ISIS data

As for the static structure factor data, the elastic scan data from ISIS were reduced using the computer programme MANTID.[171] The fixed window scan for each sample was calculated from elastic peaks recorded every 5–10 °C between –230 and 180 °C.

4.3.2.1.2 NIST data

The data recorded on HFBS at NIST were reduced by Madhusudan Tyagi, a beam scientist at NIST. Rather than being recorded at fixed temperatures, the data recorded on HFBS were taken as the sample was being heated, and the elastic peaks were recorded at fixed times rather than temperatures; consequently the elastic peaks from the HFBS data are of lower intensity than those from the IRIS data. Elastic peaks were recorded at intervals of approximately 1 K between 41 and 453 K.

4.3.2.1.3 All data

For the data recorded on IRIS, the elastic peak at each temperature was integrated between –0.01 and 0.01 meV, to give the elastic intensity, $I(Q)$, at a given T and Q. This integration range was chosen to span the energy resolution of IRIS (17.5 μeV).[172] The data recorded on HFBS does not need integrating as the Doppler that creates the energy transfer window is switched off for the elastic scan. No binning of the data in terms of T or Q was conducted at this point in the analysis.

4.3.2.2 Data normalisation

The elastic neutron intensity was normalised by dividing the intensity at a given temperature by the intensity extrapolated to $T = 0$ K, an approach introduced by Sanz *et al.*[120] The extrapolation was conducted using the data from 43–263 K (ISIS) and 41–273 K (NIST). Sample plots recorded at ISIS are shown in Figure 51 and Figure 52. Sample data sets recorded on HFBS at NIST are shown in Figure 53 and Figure 54. This approach worked well for the majority of the NIST data, but has obvious failings for the ISIS data (Figure 52) and some of the NIST data (not shown), with many of the normalised data points having values greater than 1; this failing is most common for the low-Q and low-T data and is a consequence of the measured scattering being very close to the instrumental resolution. As the Q values and the temperature are increased, the peaks that are being measured become broader and more distinct from the instrumental resolution, allowing greater confidence in the reliability of measurements recorded.

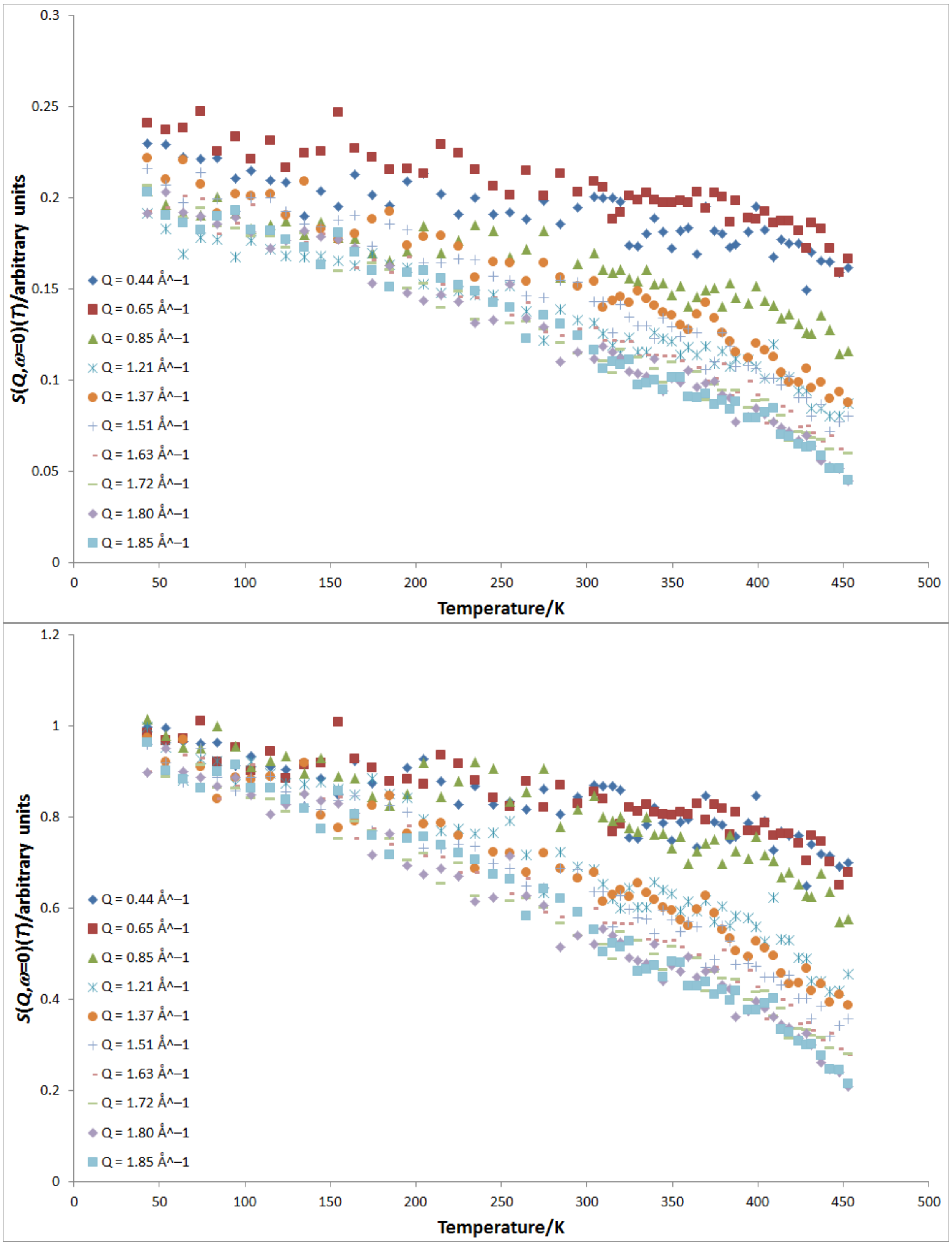

Figure 51: Elastic scan of neat ring-hydrogenated polystyrene (h5 PS) from 43 to 454 K at selected values of *Q* from 0.44 to 1.85 Å^{-1}, recorded on IRIS at ISIS. The plot at the top shows the data after reduction; the plot at the bottom shows the reduced data after normalisation by the elastic intensity extrapolated to *T* = 0 K.

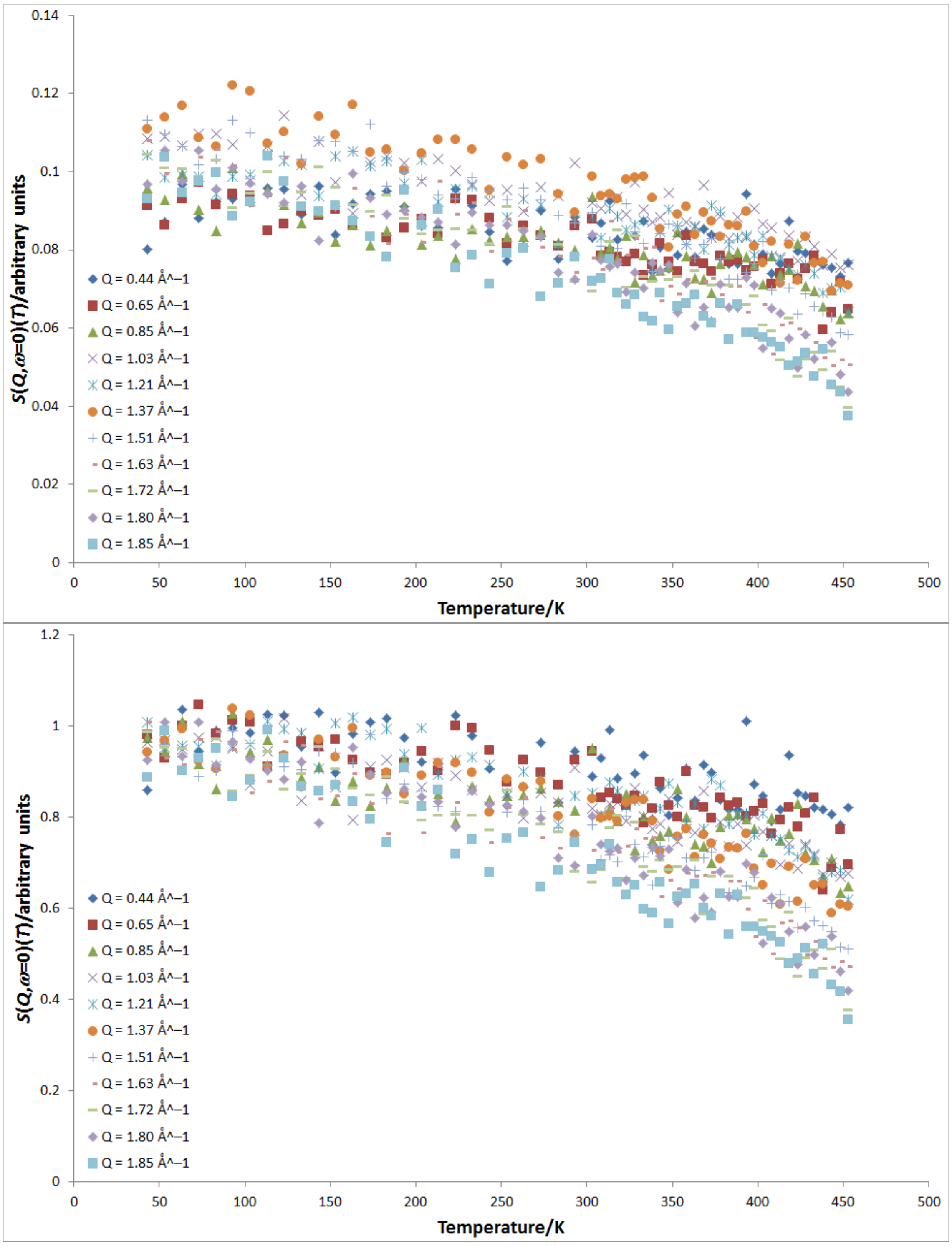

Figure 52: Elastic scan of neat chain-hydrogenated polystyrene (h3 PS) from 43 to 454 K at selected values of *Q* from 0.44 to 1.85 Å^{-1}, recorded on IRIS at ISIS. The plot at the top shows the data after reduction; the plot at the bottom shows the reduced data after normalisation by the elastic intensity extrapolated to *T* = 0 K.

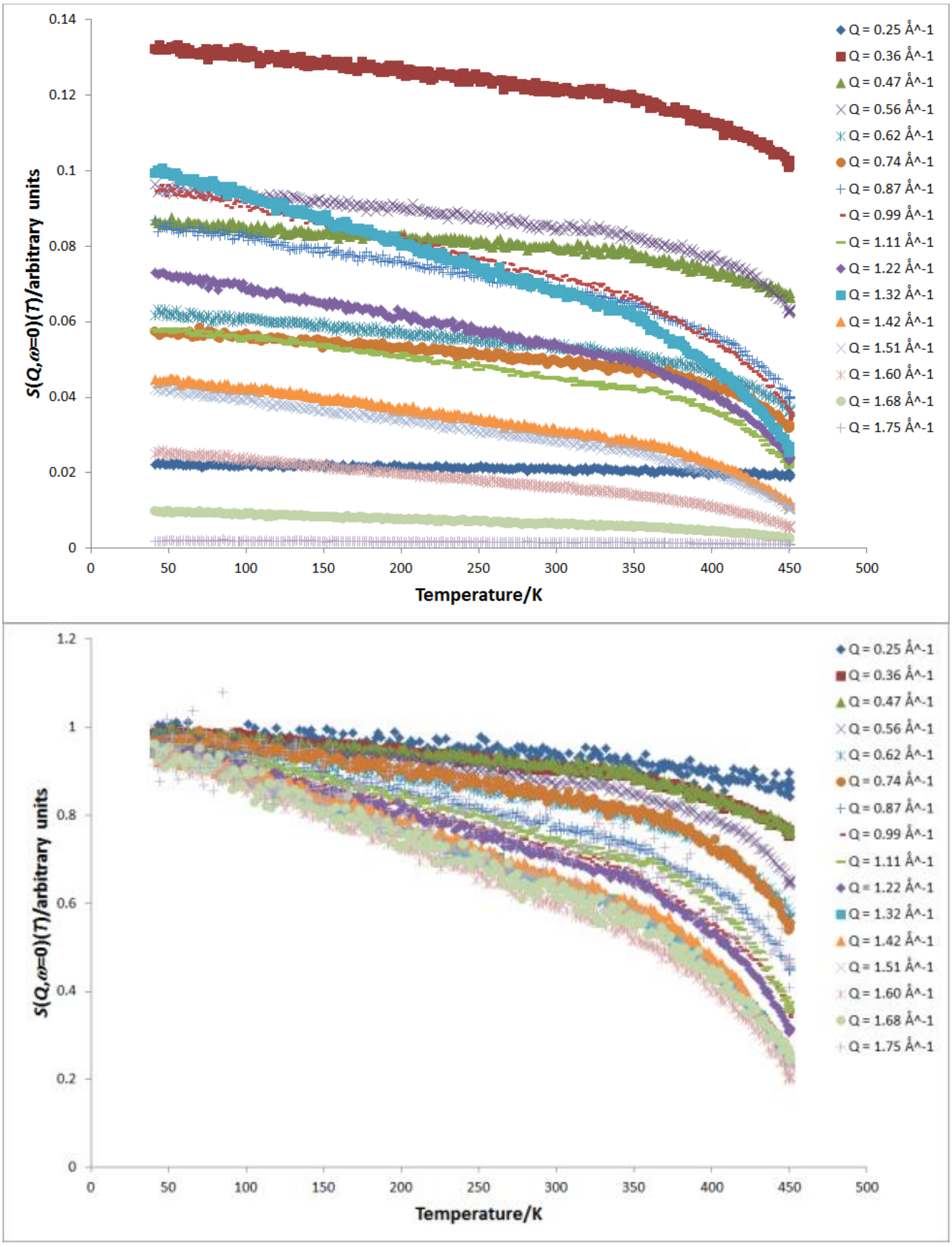

Figure 53: Elastic scan of neat ring-hydrogenated polystyrene (h5 PS) from 44 to 450 K at all recorded values of *Q* (0.25 to 1.75 $Å^{-1}$), recorded on HFBS at NIST. The plot at the top shows the data after reduction; the plot at the bottom shows the reduced data after normalisation by the elastic intensity extrapolated to *T* = 0 K.

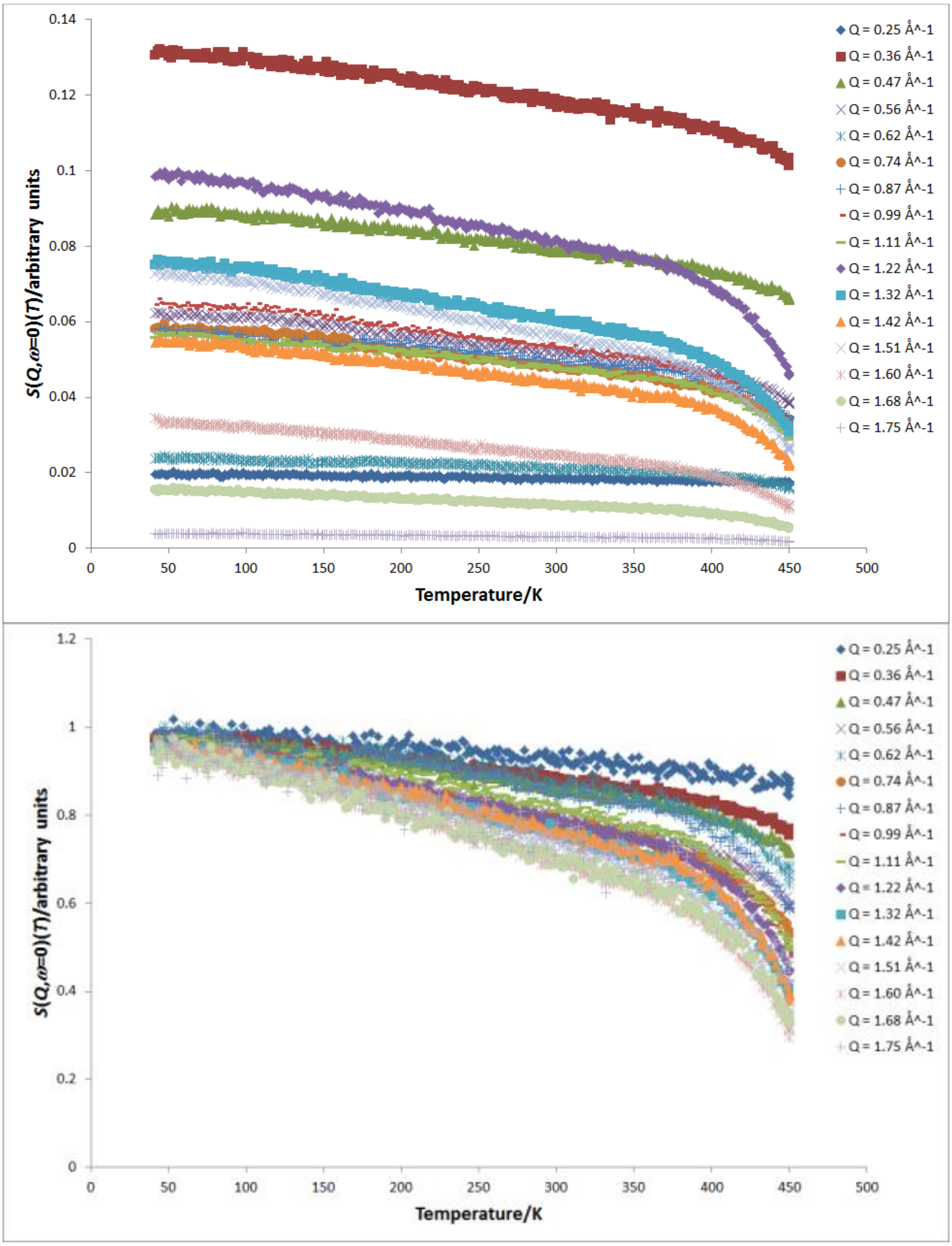

Figure 54: Elastic scan of neat chain-hydrogenated polystyrene (h3 PS) from 44 to 450 K at all recorded values of *Q* (0.25 to 1.75 Å^{-1}), recorded on HFBS at NIST. The plot at the top shows the data after reduction; the plot at the bottom shows the reduced data after normalisation by the elastic intensity extrapolated to *T* = 0 K.

4.3.2.3 Fixed window scan

The normalised fixed window scans for all samples are shown in Figure 55 (h5 PS, IRIS), Figure 56 (h5 PS, HFBS), Figure 57 (h3 PS, IRIS) and Figure 58 (h3 PS, HFBS).

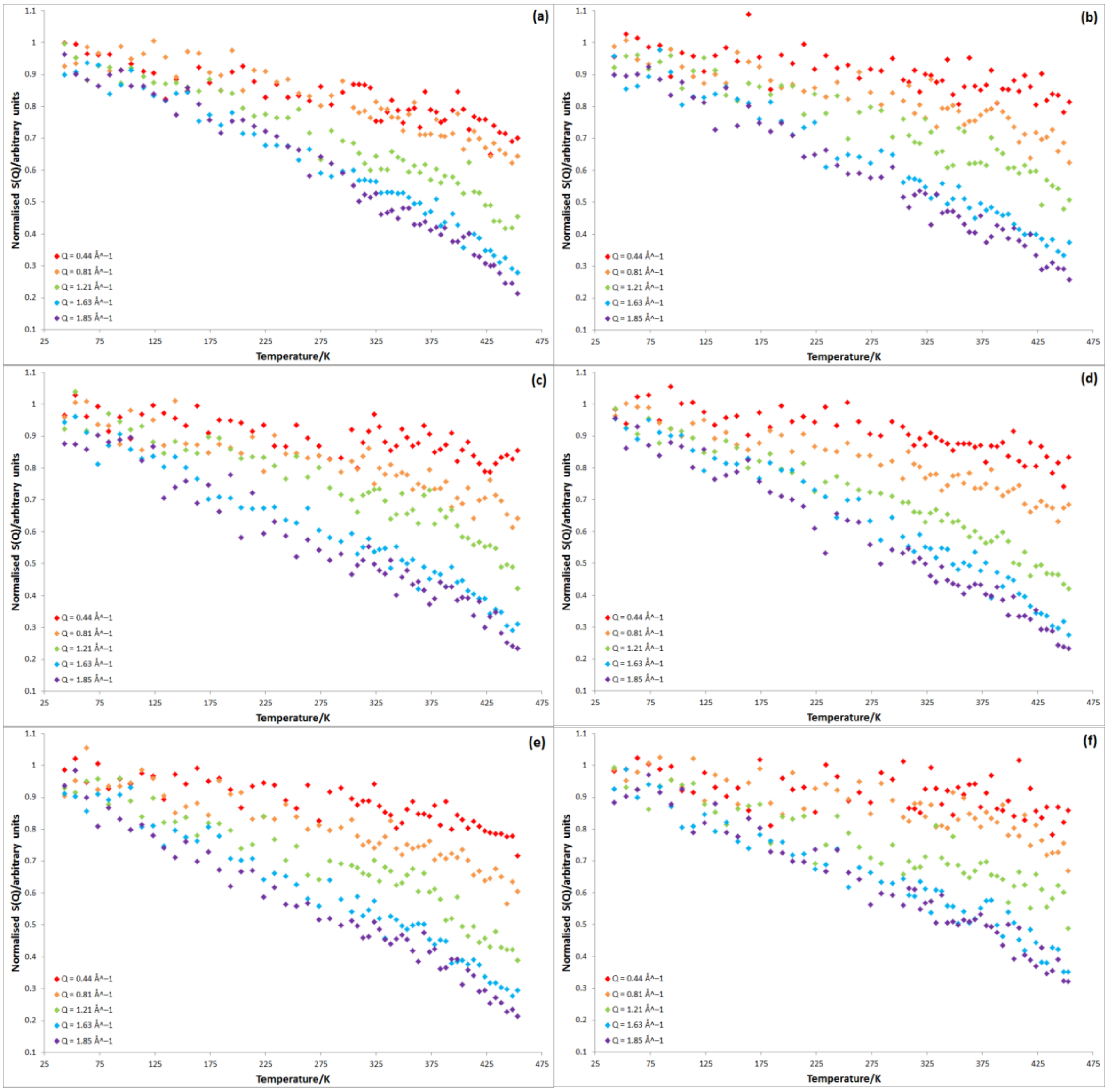

Figure 55: Normalised elastic scans for h5 (ring-hydrogenated) PS with (a) 0, (b) 0.1, (c) 0.4, (d) 1, (e) 2 and (f) 4 wt% SWCNTs recorded on IRIS at ISIS.

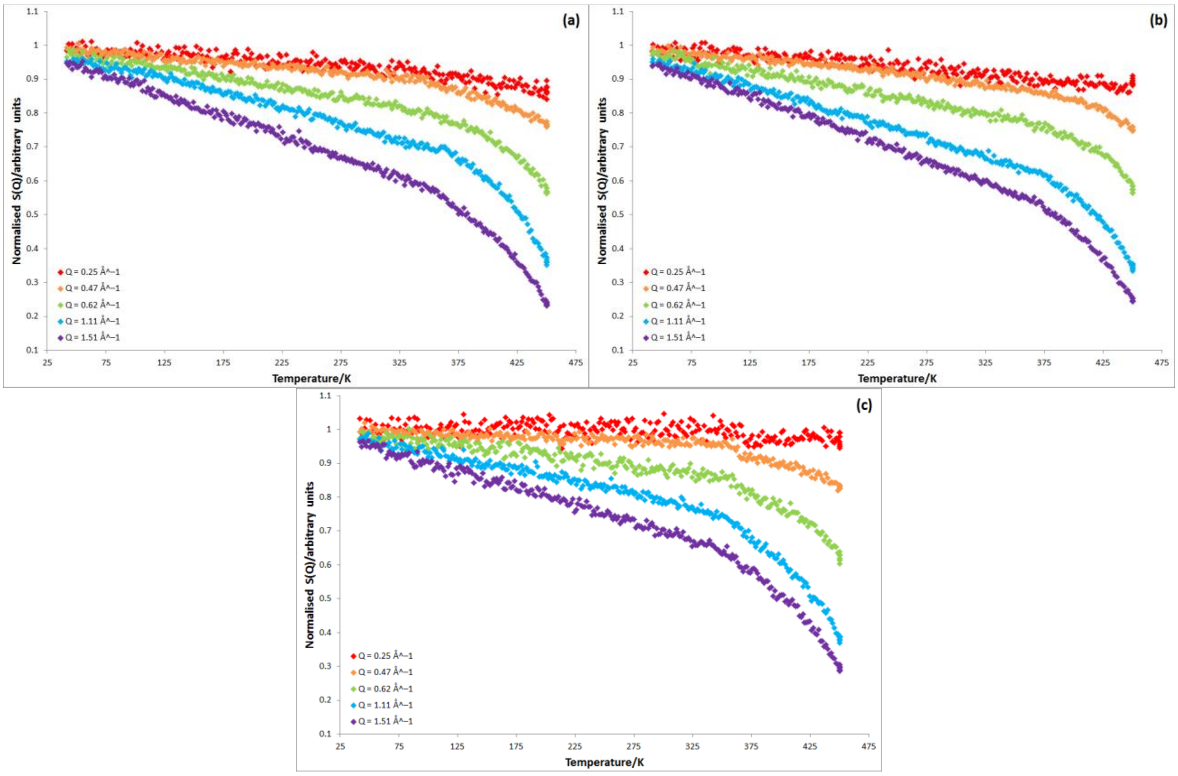

Figure 56: Normalised elastic scans for h5 (ring-hydrogenated) PS with (a) 0, (b) 0.4 and (c) 4 wt% SWCNTs recorded on HFBS at NIST.

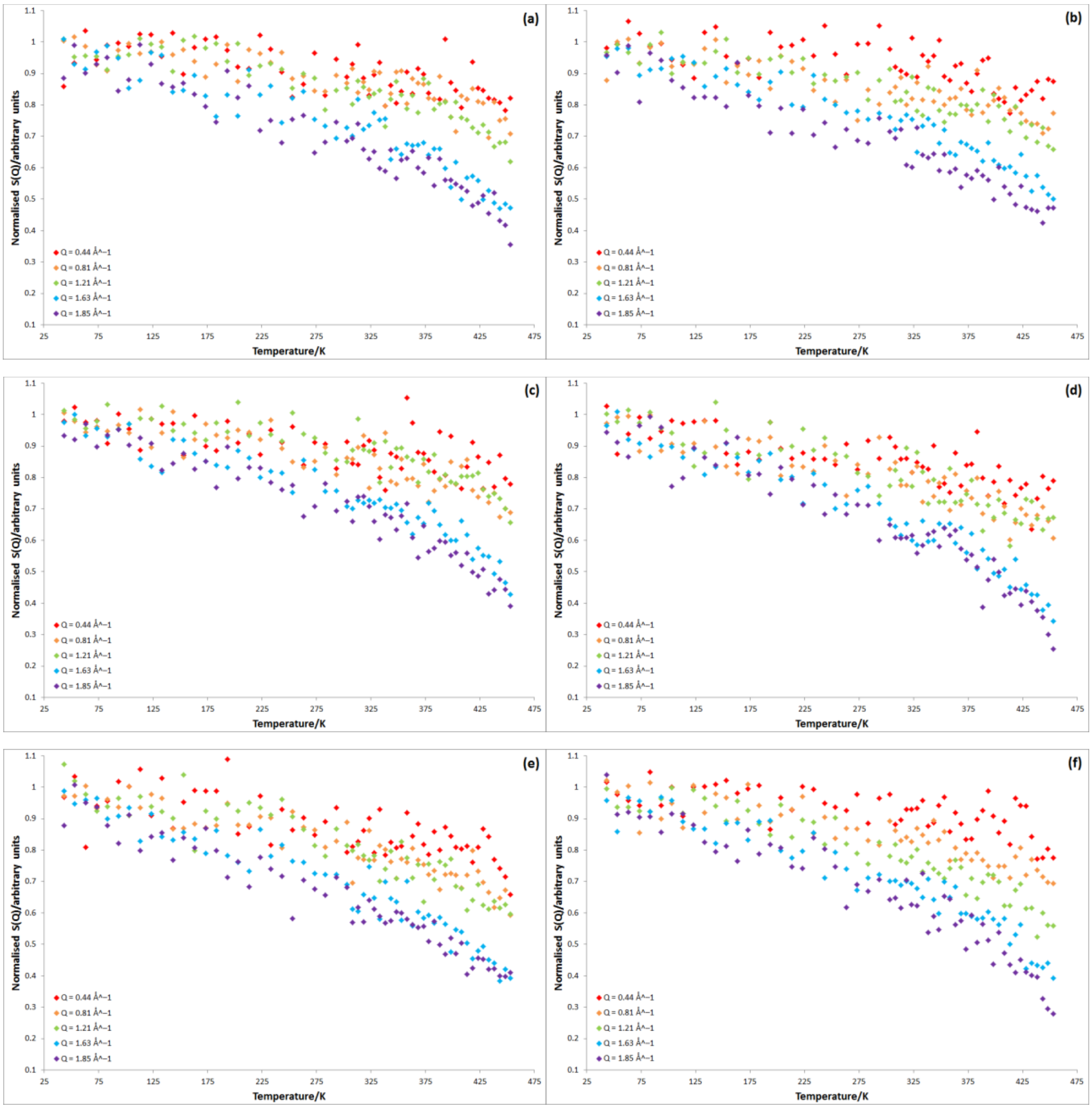

Figure 57: Normalised elastic scans for h3 (chain-hydrogenated) PS with (a) 0, (b) 0.1, (c) 0.4, (d) 1, (e) 2 and (f) 4 wt% SWCNTs recorded on IRIS at ISIS.

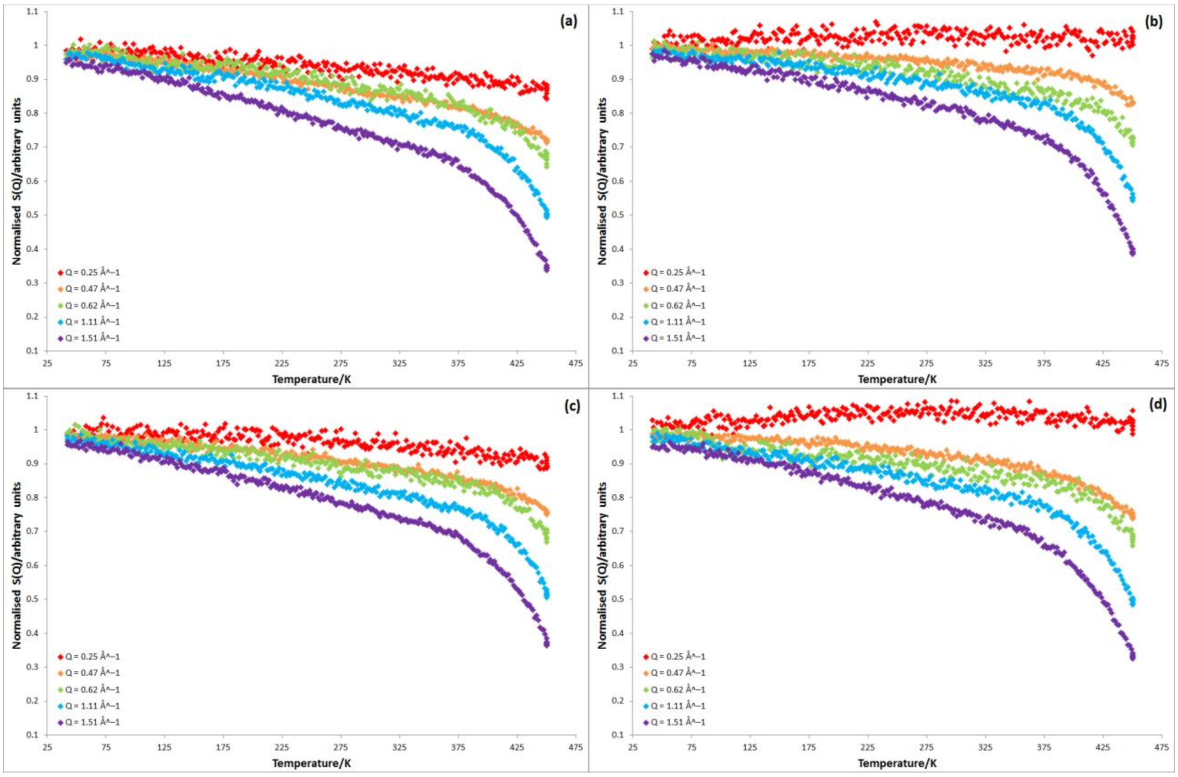

Figure 58: Normalised elastic scans for h3 (chain-hydrogenated) PS with (a) 0, (b) 0.1, (c) 0.4 and (d) 4 wt% SWCNTs recorded on HFBS at NIST.

In the elastic scan, because the data are normalised with respect to the 0 K data, the focus is on the motions of the hydrogen atoms within the polymer, so for chain-hydrogenated PS (h3 PS) chain motion is being explored, and for ring-hydrogenated PS (h5 PS) the emphasis is on ring motion. On first inspection, it is obvious that the elastic scan for the ring (Figure 55 and Figure 56) drops in intensity faster than that of the chain (Figure 57 and Figure 58), this happens because an individual styrene ring is less constrained than the polymer chain as a whole as it is only bonded at one end of the moiety and thus requires less energy to become mobile.

The ISIS data (Figure 55 and Figure 57) is more scattered than the NIST data (Figure 56 and Figure 58), and includes far fewer data points; this is because IRIS has a larger number of smaller detectors, so greater *Q* resolution is possible at the expense of the statistical quality of data.

In general the elastic intensity decreases with increasing *T* and increasing *Q*,[117, 120, 121, 134] which is expected because as the temperature of the system increases there is more energy available for the polymer to move, which results in fewer elastic scattering events. An increase in *Q* results in the same decrease in elastic intensity: an increase in *Q* corresponds to a reduction in the length scale under examination, and smaller length scales require less energy to become mobile. At temperatures below ~75 K, all decreases in intensity with temperature arise solely from the Debye–Waller factor, *i.e.* all motion in this region is purely vibrational, arising from residual quantum energy.[31] As the temperature increases beyond this region, larger scale motions start to occur, *e.g.* phenyl ring reorientation, and the drop in elastic intensity is steeper. At T_g

(approximately 100 °C for PS), an increase in the gradient of elastic intensity *vs.* Q is exhibited as the polymer chains have enough energy to freely reorient; gradient change at T_g is more apparent for the data recorded on HFBS at NIST than for that recorded on IRIS at ISIS. The sharper gradient change at T_g is a characteristic of the spectrometer; HFBS and IRIS measure different time scales, with IRIS recording scattering from 2 to 200 ps,[175] and HFBS recording data from 100 ps to 10 ns,[176] therefore HFBS records slower motions than IRIS.

4.3.2.4 Mean squared displacement

The elastic scattering of a sample is related to the mean squared displacement *via* the Debye–Waller factor (Equation 19).[31] Equation 19 can be rearranged to give Equation 35, and a linear plot of $\ln(I_{\mathrm{elastic}})$ *vs.* Q^2 will have a slope of $-\langle u^2\rangle/3$, allowing $\langle u^2\rangle$ to be extracted (sample linear plots are shown in Figure 59).

$$ln(I_{elastic}) = -\frac{\langle u^2\rangle}{3}Q^2$$

Equation 35

Plots of the mean squared displacement *vs.* T recorded at ISIS and NIST are shown in Figure 60 and Figure 61, respectively. The plots have been separated out according to spectrometer as IRIS and HFBS records motions on different time scales, therefore the data are not directly comparable.

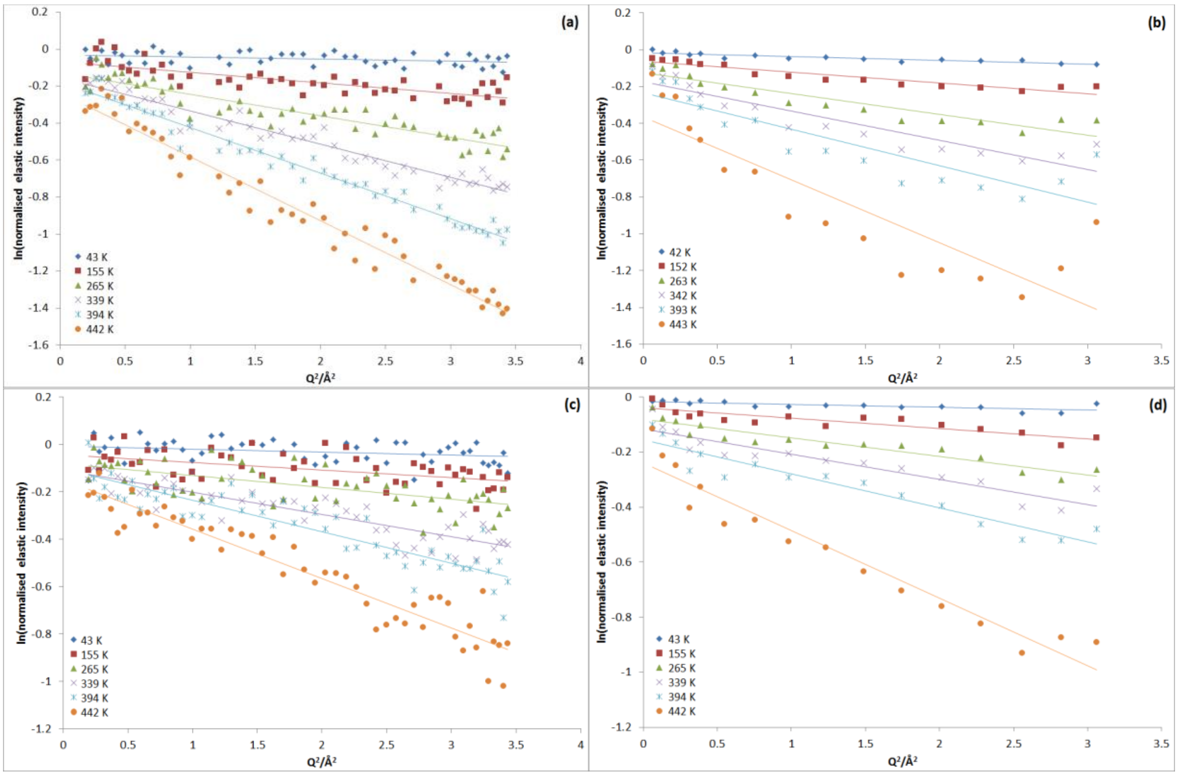

Figure 59: Natural logarithm of the normalized elastic intensity of (a) neat h5 PS, (b) h5 PS with 0.4 wt% SWCNTs, (c) neat h3 PS, and (d) h3 PS with 0.4 wt% SWCNTs as a function of Q^2 for selected temperatures. (a) and (c) are from data recorded on IRIS at ISIS, while (b) and (d) are from data recorded on HFBS at NIST. The Debye–Waller factor can be extracted from these plots by evaluating the slope: the slope has a value of $-\frac{\langle u^2\rangle}{3}$.

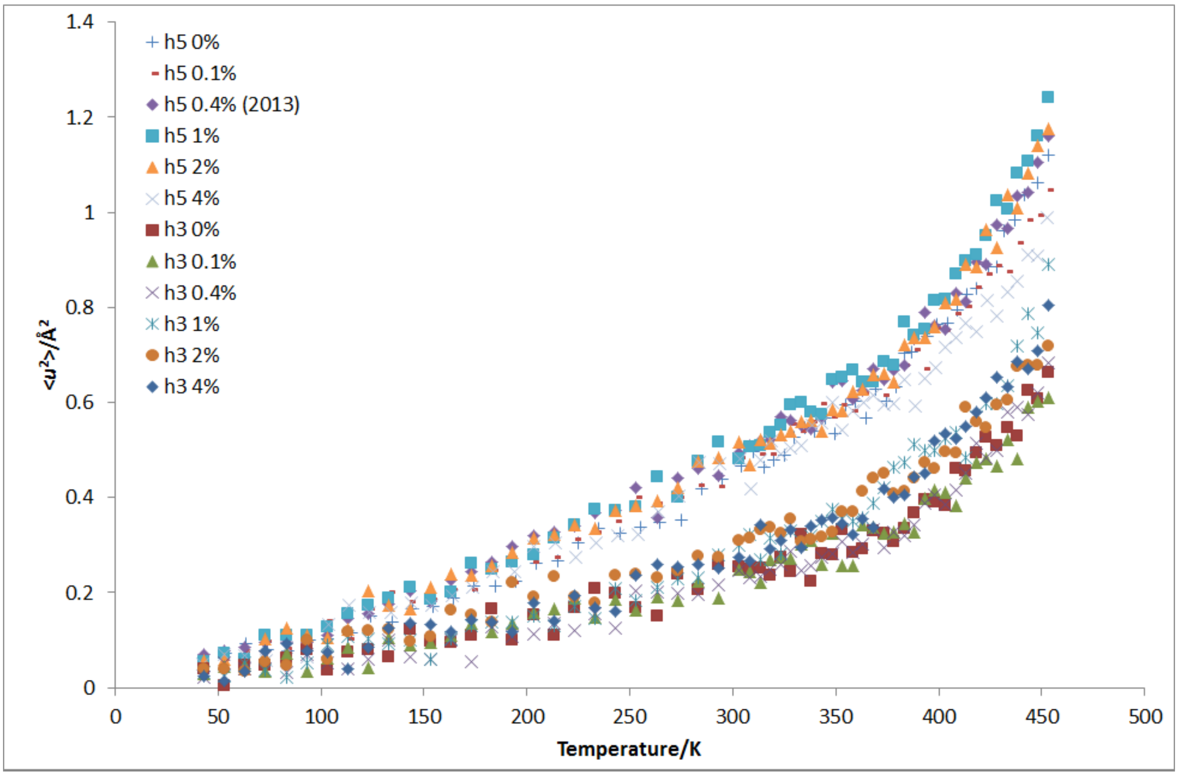

Figure 60: Mean-square displacement $\langle u^2\rangle$ as a function of temperature for h5 (ring-hydrogenated) and h3 (chain-hydrogenated) PS with between 0 and 4 wt% SWCNTs (see legend for sample composition details) from data recorded on IRIS at ISIS.

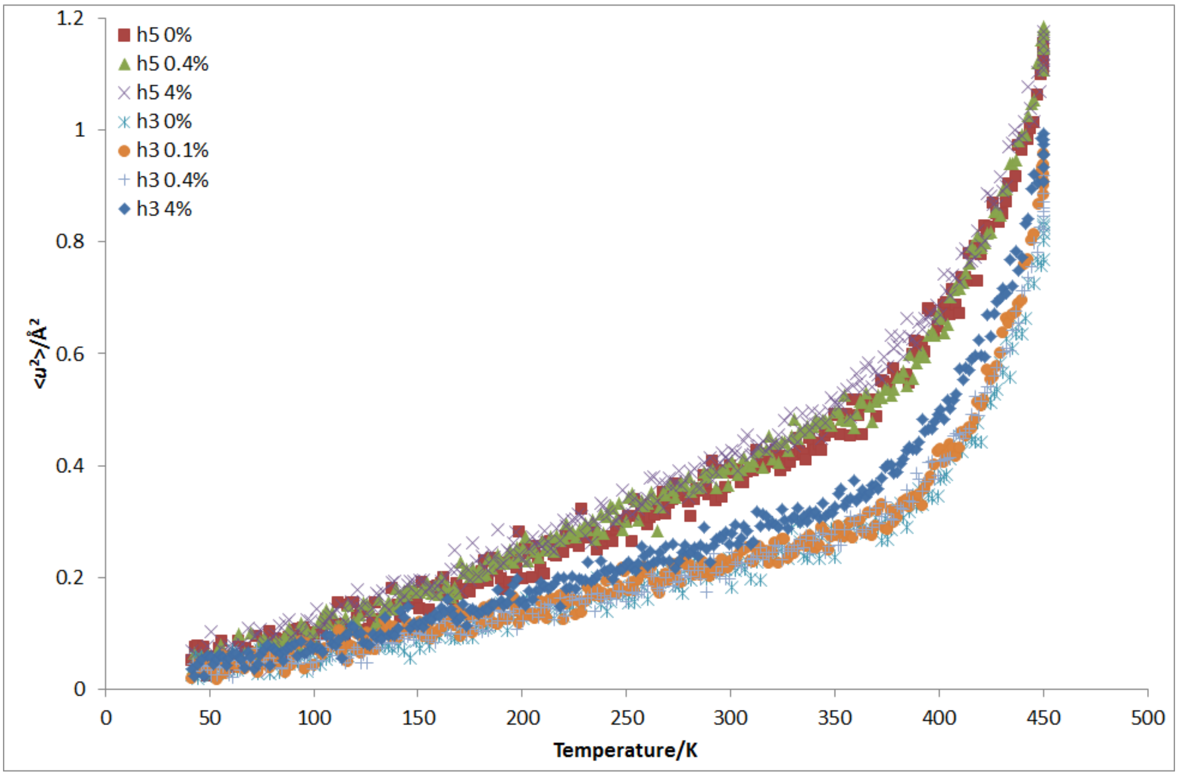

Figure 61: Mean-square displacement $\langle u^2 \rangle$ as a function of temperature for h5 (ring-hydrogenated) and h3 (chain-hydrogenated) PS with between 0 and 4 wt% SWCNTs (see legend for sample composition details) from data recorded on HFBS at NIST.

4.3.2.4.1 Ring motion *vs.* chain motion

From both Figure 60 and Figure 61 it is clear that the ring displays higher values of $\langle u^2 \rangle$ than the chain across all concentrations, consistent with the SSF; as a result, ring motion starts earlier than chain motion, and continues to be faster than the chain motion as the temperature is increased. Both plots indicate a change in gradient at between 350 and 400 K, corresponding to the glass transition temperature of polystyrene. The change in gradient associated with T_g is sharper in the data recorded on HFBS at NIST (Figure 61), with $\langle u^2 \rangle$ for the chain increasing more rapidly than that of the ring; this is not apparent in the data recorded on IRIS at ISIS (Figure 60), but both the chain and the ring show a minor change in gradient, indicative of the T_g. Chain motion is inherently on the slower end of polymer relaxations, therefore HFBS is more sensitive to T_g as this spectrometer resolves motions on longer timescales than IRIS.

4.3.2.4.2 Effect of concentration

Looking at the h3 PS (chain-hydrogenated PS) data from ISIS in Figure 60, the chain motion data fall into two groups: samples with nanotube concentrations below 1 wt%, and samples with nanotube concentrations of 1 wt% or above. Those samples with lower nanotube concentrations show lower $\langle u^2 \rangle$ values than those with higher nanotube concentrations. The data broadens into two sets long before T_g, and the difference between the two groups is most apparent in the region of the glass transition temperature. This grouping of the data is also apparent in the data recorded at NIST (Figure 61), with the data from the 0, 0.1 and 0.4 wt% samples clustering and the 4 wt% sample showing much higher $\langle u^2 \rangle$ values, across all temperatures. This result indicates that the chain motion becomes less hindered on addition of the CNTs, *i.e.* the CNTs plasticise the PS chains, a result previously encountered by Sanz *et al.*[120] in PS-related polymer matrices containing C_{60}. Sanz *et al*. attributed the local plasticisation of the fast proton dynamics in their system to an increase in free volume arising from restricted packing on addition of the nanoparticles, which could also be happening in the system under examination here. This local plasticisation could also be explained by a localised region of lower polymer density at the PS/SWCNT interface, an idea proposed by Picu and Ozmusul,[80] and Termonia *et al.*[78] *via* Monte Carlo simulations. A region of this type would allow additional freedom of movement in this interfacial region, which could register as increased chain proton mobility, and is consistent with the diffusion behaviour identified by Mu *et al.*[129, 130]

The ring data (h5 PS) shows different trends depending on the spectrometer used. The data recorded on IRIS at ISIS (Figure 60) shows all the data clustering quite tightly below T_g, although it could be argued that the 0 and 4 wt% data are always slightly lower than those from the other samples. Above the T_g, the 4 wt% data clearly drops below the other data sets, indicative of lower mobility, so the sample is less mobile in the experimental window. The data from HFBS (Figure 61) shows a different picture: as before, the 0 and 0.4 wt% data show very similar values, with the data sets crossing over one another at several points below T_g, however, the data from the 4 wt% sample is consistently higher than that of the other data sets, especially around the T_g. One possible explanation for the discrepancy between the data recorded at NIST and that recorded at ISIS is the different recording time scales of the two spectrometers. It may be that the motion is occurring on a time scale that occurs on the borderline between what each spectrometer can detect: when the sample is examined using IRIS, the spectrometer detects reduced mobility in the 4 wt% sample as any motion occurring is *just* too slow to be picked up by the spectrometer, and therefore HFBS detects enhanced motion as the time scales of the motion are on the borderline between the picosecond region and the nanosecond region, *i.e.* the ring motion is too slow to be recorded by IRIS, but is the right speed to be logged by HFBS. Another possible cause of the different mobilities seen for the samples on the two spectrometers is the inevitable differences in sample history which, although slow compared to the relaxation time of the polymer, could result in slightly differing levels of dispersion of the CNTS.

4.3.2.5 Stiffness

Through the idealised harmonic solid model, the mean squared displacement of a material can be related to its stiffness:

$$\kappa = \frac{3k_B T}{\langle u^2 \rangle}$$

Equation 36

where κ is the stiffness of the material and k_B is Boltzmann's constant. This idea originated in protein science,[109] but can easily be applied to synthetic polymers. Plotting $\langle u^2 \rangle$ *vs*. $1/T$ gives a straight line with the slope $\frac{3k_B}{\kappa}$ allowing κ to be extracted. At temperatures below 80 K motion is purely harmonic, at higher temperatures application of Equation 36 is heuristic as the harmonic approximation is only valid before activated processes such as side-group rotations and chain motion start to dominate the loss in elastic intensity. In this work, Equation 36 was applied to the data up to 160 K as the plots of $\langle u^2 \rangle$ vs. $1/T$ are consistently linear up to this temperature (Figure 60 and Figure 61). The stiffness data is displayed in Figure 62.

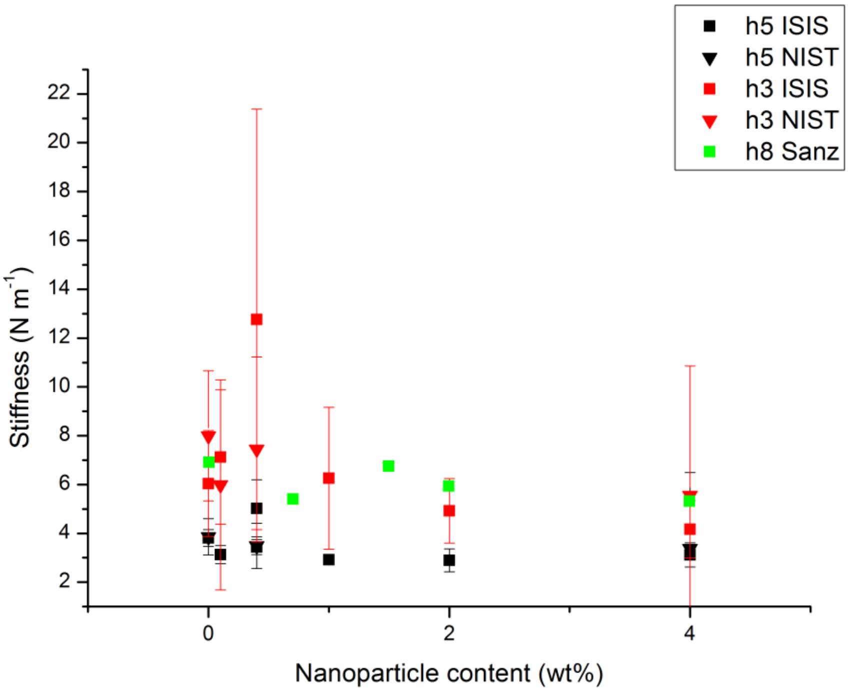

Figure 62: Polymer stiffness for ring- and chain-hydrogenated polystyrene–SWCNT nanocomposites as a function of nanoparticle concentration (SWCNTs for the data presented in this chapter). Additional stiffness data from Sanz *et al.*'s 2008 paper[120] on PS–C_{60} nanocomposites, recorded on spectrometer IN16 at ILL, are also included (in this case the nanoparticles are C_{60}).

The stiffness model allows an imprecise quantitative assessment of the mean squared displacement data: here a very slight decrease in chain stiffness is observed with the addition of

SWCNTs; this is the same effect as seen by Sanz *et al.*[120] on addition of C_{60} to polystyrene (green data points in Figure 62). This softening effect is caused by the increase in free volume that arises because of the packing frustrations encountered with the addition of the nanotubes. In contrast, the nanotubes have no significant effect on the stiffness of the ring. This difference in behaviour is most likely because the nanotubes are unable to penetrate the small spaces between the polymer rings, as discussed in relation to the SSF, and therefore the rings are not influenced by the presence of the nanotubes.

4.3.2.6 Glass transition temperature

4.3.2.6.1 Neutron glass transition temperatures

The neutron glass transition temperatures for each of the samples used in this work were calculated from the plots of $\langle u^2 \rangle$ *vs*. *T*. Excel was used to plot a line of best fit through the data between 250 and 325 K (below the T_g) and 390 and 420 K (after the T_g, but before the $\langle u^2 \rangle$ values started to increase exponentially), then the two line equations were solved simultaneously to give the mutual value for *T*, *i.e.* the intercept of the two lines and the temperature corresponding to the glass transition temperature (Equation 37). The values extracted from the neutron data are listed in Table 26 and Table 27 and plotted in Figure 63. The error values included in Table 26 and Table 27 were calculated based on the least squares fit error values for the intercept and slope values. No T_g value could be extracted from the data recorded on IRIS at ISIS for the h3 PS sample with 1 wt% SWCNTs as the discontinuity was not sharp enough to plot two lines with significantly different gradients.

$$\left(\frac{d\langle u^2\rangle}{dT}\right)_1 T_g + \langle u^2\rangle_1 = \left(\frac{d\langle u^2\rangle}{dT}\right)_2 T_g + \langle u^2\rangle_2$$

$$T_g = \frac{[\langle u^2\rangle_2 - \langle u^2\rangle_1]}{\left[\left(\frac{d\langle u^2\rangle}{dT}\right)_1 - \left(\frac{d\langle u^2\rangle}{dT}\right)_2\right]}$$

Equation 37

Table 26: Neutron T_g values extracted from the $\langle u^2 \rangle$ *vs. T* data recorded on IRIS at ISIS

Polymer matrix	**Wt% SWCNTs**	**Neutron T_g/K**	**Error/K**
h5 PS	0	357.5	1.57
h5 PS	0.1	384.9	0.93
h5 PS	0.4	367.9	9.59
h5 PS	1	375.0	1.02
h5 PS	2	381.7	0.59
h5 PS	4	396.4	11.0

h3 PS	0	391.3	3.49
h3 PS	0.1	362.8	14.4
h3 PS	0.4	377.3	4.56
h3 PS	2	391.8	0.92
h3 PS	4	360.4	5.72

Table 27: Neutron T_g values extracted from the $\langle u^2 \rangle$ *vs. T* data recorded on HFBS at NIST

Polymer matrix	**Wt% SWCNTs**	**Neutron T_g/K**	**Error/K**
h5 PS	0	364.2	4.08
h5 PS	0.4	380.6	0.04
h5 PS	4	369.3	1.81
h3 PS	0	380.4	0.49
h3 PS	0.1	380.1	0.38
h3 PS	0.4	379.2	0.58
h3 PS	4	376.9	0.45

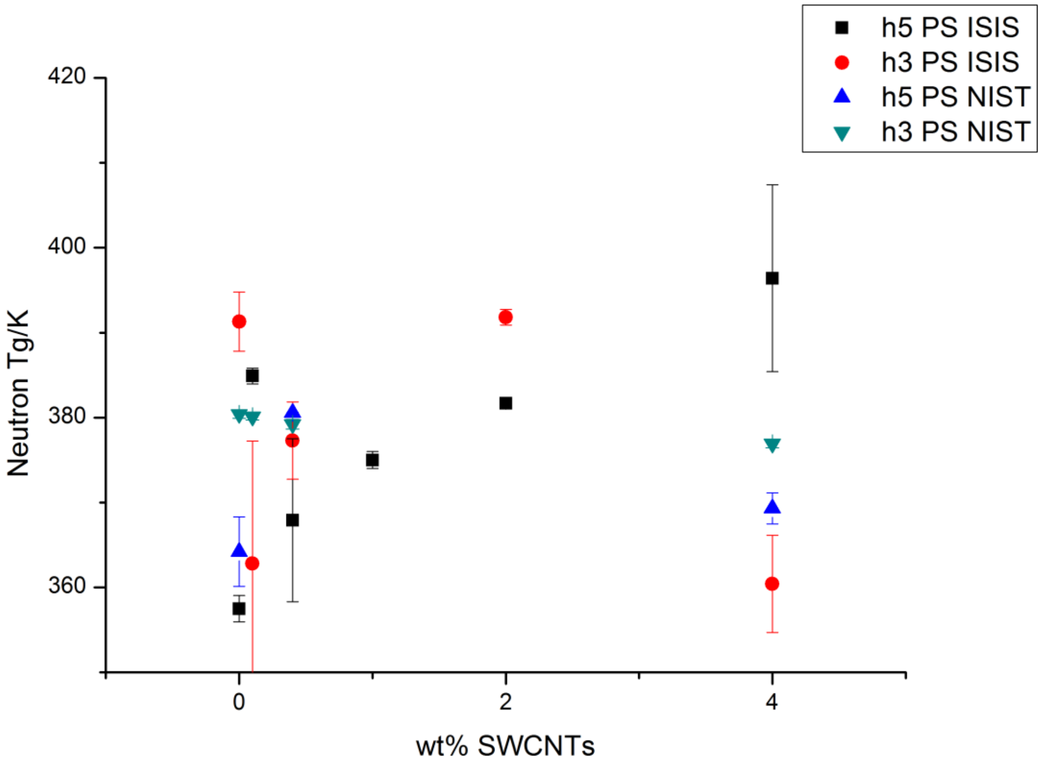

Figure 63: Neutron glass transition temperature values extracted from measuring the temperature of the discontinuity in the $\langle u^2 \rangle$ *vs. T* plots.

While the numerical values for the T_g values extracted from the data recorded at the two beamlines do not match, they do display the same trend, with higher T_g values for the chain (h3

PS data) than the ring (h5 PS data). This observation correlates well with the $\langle u^2 \rangle$ data, which indicated greater mobility of the ring than the chain at all temperatures (Figure 60 and Figure 61).

The filled samples display different trends depending which part of the polymer is under examination, and which spectrometer was used to collect the data. The $\langle u^2 \rangle$ *vs*. *T* data recorded at ISIS is more scattered than that recorded at NIST; this results in the error in the line of best fit being greater, and a corresponding larger error in the T_g values extracted from these fits. In addition, the discontinuities in the $\langle u^2 \rangle$ *vs*. *T* data were more pronounced in the data recorded on HFBS than on IRIS, leading to a greater uncertainty in the T_g values extracted from the data from IRIS. Based on the scatter and the lack of continuity between the T_g values from the two spectrometers, the results will be discussed separately.

The h3 PS data recorded on ISIS provides information on the mobility of the chain. The T_g values extracted from the $\langle u^2 \rangle$ *vs*. *T* data go up and down with increasing nanotube concentration, and the large error bars associated with the data make it impossible to discern a trend. The data from h5 PS, associated with the phenyl rings in the polystyrene are less scattered than those from the chain, and indicate an increase in T_g with increasing SWCNT concentration, except for the 0.1 wt% sample, which has an anomalously higher value than all other concentrations examined. The increase in T_g with increasing CNT concentration indicates that the nanotubes are hindering the ring motion, in contrast to the stiffness data. The larger increase for the 0.1 wt% sample could be due to this sample having better dispersed nanotubes than the samples containing higher concentrations; this would allow a larger SWCNT/polymer interface, enhancing any effect.

The T_g data from h3 PS recorded on HFBS have very small error bars, and provide the most reliable $\underline{T}_g$ data recorded from the experiments presented here as they are based on a sharp change in slope and the line of best fit was calculated from a large number of values; these factors suggest that any trend seen is real. The data indicate a very small lowering in T_g (3.5 K between 0 and 4 wt% SWCNTs), indicating that the nanotubes make it easier for the chain to gain enough energy to move freely, consistent with increased mobility.

The T_g data from the h5 PS samples are much more scattered with larger error bars than those from h3 PS. The data display an increase in T_g followed by a decrease. However, as there are only three data points for this polymer it is difficult to elucidate any trend.

Comparing the data from the two spectrometers, it looks like the faster relaxations of the h5 PS nanocomposites are better captured on IRIS, which has the faster time window, and the slower chain motions are better captured on HFBS. Although the absolute values cannot be compared between the sets, the trends are interesting: the results on h3 PS from HFBS suggest that not much happens to the backbone motion with increasing SWCNTs, and the data from IRIS data does not contradict this. The IRIS data shows a clear increase in T_g for h5 PS with increasing CNT concentration, which HFBS in unable to measure.

4.3.2.6.2 Calorimetric glass transition temperatures

The calorimetric glass transition temperatures of the nanocomposites are shown in Figure 64 and are the average of the two runs, with error bars corresponding to the standard deviations of these averages. The first feature of note about these values is that they are significantly higher than the literature value for the T_g of PS, ~100 °C;[110] the calorimetric T_g values were obtained from heating ramps at 300 °C min^{-1}, which are much higher than those usually used, and this accounts for this increase in the measured value. The values obtained here are self-consistent as all samples were tested under the same conditions, and allow the relative change in T_g between samples with different nanotube concentrations to be compared. Figure 64 suggests that significant variations in T_g can occur as a result of CNT loading, and that there may be a decrease at intermediate concentrations before recovery at higher concentrations. The trends seen are the same for h3 and h5 PS matrix SWCNT nanocomposites; this is expected as the calorimetric T_g is a measure of whole chain motion on long length scales, therefore the small localised differences arising from ring and chain deuteration are not significant.

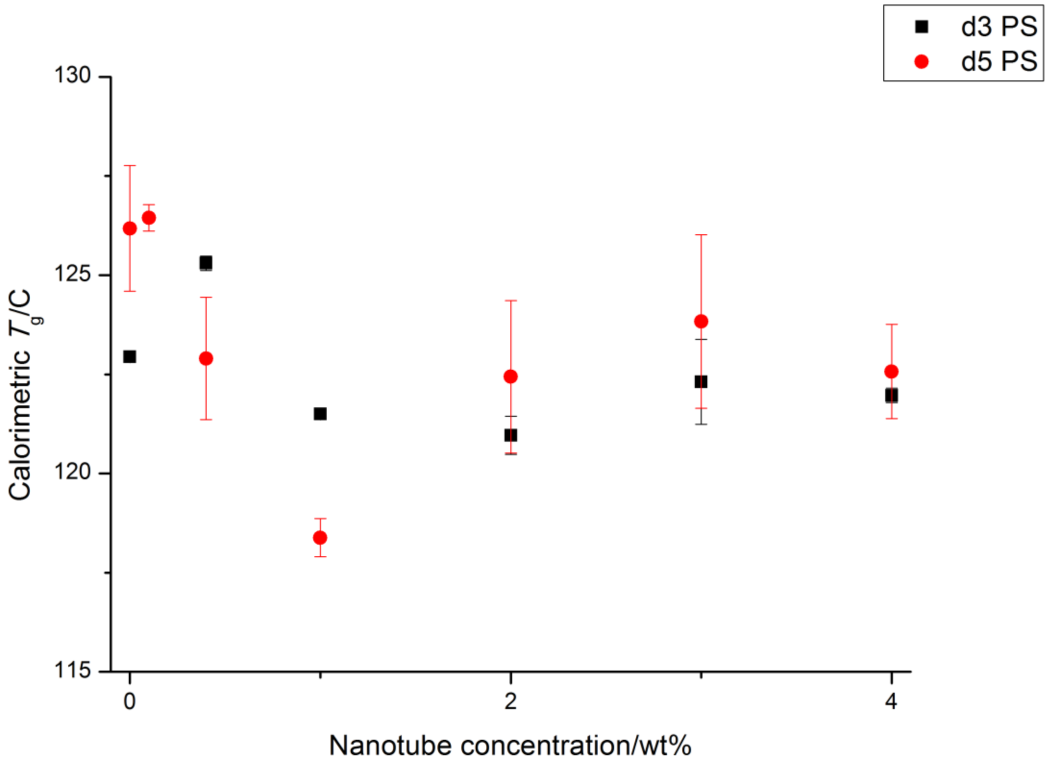

Figure 64: Calorimetric T_g values for the d3 (black squares) and d5 PS (red circles) SWCNT nanocomposites used in the QENS experiments. The error bars correspond to the standard deviations of the average values from two heating runs.

4.3.2.6.3 Discussion of T_g values

While the variations in T_g with nanotube loading are small compared to instrumental resolution, at the temperature at which the minimum in the diffusion coefficient was identified (150 °C for SWCNTs[129] and 170 °C for MWCNTs[130]), a 10 °C shift in temperature can lead to an order of magnitude change in diffusion coefficient,[177] so these small perturbations in T_g with nanotube concentration are large enough to have an large influence on the dynamics at higher temperatures.

4.4 KWW fitting

4.4.1 Introduction

Following reduction, the data recorded in a QENS experiment takes the form of a dynamic incoherent structure factor, $S(Q,\omega)$. $S(Q,\omega)$ is related to the intermediate scattering function $I(Q,\omega)$ *via* convolution with the resolution function of the spectrometer (Equation 38).

$$I(Q,\omega) = S(Q,\omega) \otimes R(Q,\omega)$$

Equation 38

On Fourier transform, this relationship is transferred from the energy domain to the time domain and the convolution with the resolution function becomes a simple multiplication (Equation 39).

$$I(Q,t) = S(Q,t) \times R(Q,t)$$

Equation 39

Transforming the data in this way has the advantage of removing resolution effects and allows direct comparison of data recorded on different instruments or at different times on the same instrument.

$I(Q,t)$ often takes the form of a stretched exponential, which can be fitted with the empirical Kohlrausch–Williams–Watts stretched exponential function (KWW),[178, 179] Equation 40, where β is a stretching parameter ($0 < \beta \leq 1$) that measures the deviation of the curve from a non-stretched exponential (when $\beta = 1$, the exponential is non-stretched, and the all the molecules in the system behave in the same manner, relaxing homogenously[152]), and τ_{KWW} is a decay constant that represents the relaxation time of the polymer. This function has frequently been used to analyse relaxation processes in polymeric materials.[180-184]

$$\mathrm{KWW}(t;\ \tau_{\mathrm{KWW}}, \beta) = \exp\left[-\left(\frac{t}{\tau_{\mathrm{KWW}}}\right)^{\beta}\right]$$

Equation 40

The Origin files for all data sets fitted with the KWW function are provided as electronic supplementary information.[185]

4.4.2 Data reduction

No QENS data were recorded on HFBS at NIST. All work relating to KWW fitting refers to data collected at ISIS.

Data were reduced using the 'Indirect: Convert to Energy' algorithm in MANTID[171] against a calibration file recorded at during the same session as the experimental data. Data were binned into 17 groups, with each group containing data from three detectors. This binning of data reduces the data resolution in terms of *Q*, but also reduces the noise associated with the data, thus increasing their reliability.

For those data sets recorded on IRIS in 2010, both the QENS and resolution files were recorded with four of the standard 51 detectors not in use. The missing detectors were in pairs: detectors 16 and 17, and 38 and 39, corresponding to *Q* values of 1.034, 1.070, 1.668 and 1.688. For these samples, the data were grouped into 17 groups as before, but the data from the two groupings containing the data from only one detector (*i.e.* groups 6 and 17) were discarded.

4.4.3 Fourier transform

Data were Fourier transformed using the 'TransformToIqt' algorithm in MANTID.[171] This algorithm requires a resolution file for the deconvolution process; in cases where a full resolution file had been recorded during the same session as the experimental data, this resolution file was used in the Fourier transform. Sample decay curves from a data set with a dedicated resolution file are shown in Figure 65.

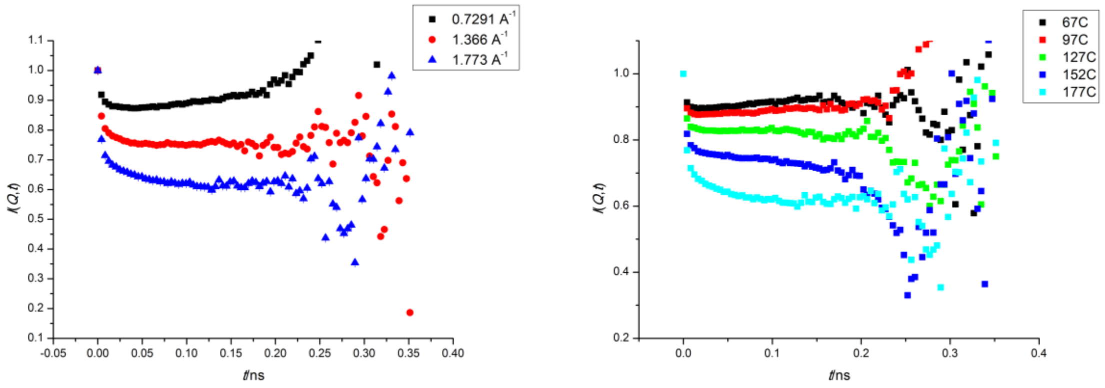

Figure 65: Sample *I*(*Q*,*t*) decay curves created *via* Fourier transform of the *S*(*Q*,*ω*) QENS peaks deconvolved with a dedicated instrument resolution peak, *R*(*Q*,*ω*) recorded during the same neutron scattering session. The curves shown are from the neat h3 PS sample at: 177 °C and three *Q* values (detailed in the legend, left), and *Q* = 1.773 Å^{-1} at five temperatures (detailed in the legend, right)

The experimental data recorded on IRIS in 2011 do not have a resolution file associated with them owing to an oversight during the experiment; for these data sets, where an elastic scan was recorded during the session, resolution files were created by summing the data from the first five temperatures in the elastic scan. These data points were recorded at very low temperatures, so only a negligible amount of motion outside the elastic window was occurring; therefore these 'resolution' files can be confidently taken as truly representing the resolution of the instrument. However, it must be taken into consideration that these 'resolution' files are noisier than an independently recorded resolution file would be. One sample from 2011 (h5 PS + 0.1 wt% SWCNTs) does not have an elastic scan associated with it recorded in 2011 as its elastic scan was recorded in 2010; for this data set, the 'resolution' file from the elastic scan of the h5 PS + 1 wt% SWCNTs sample was used instead. Examples of decay curves from a sample where the first five data points of the elastic scan were used in lieu of a dedicated resolution file are shown in Figure 66.

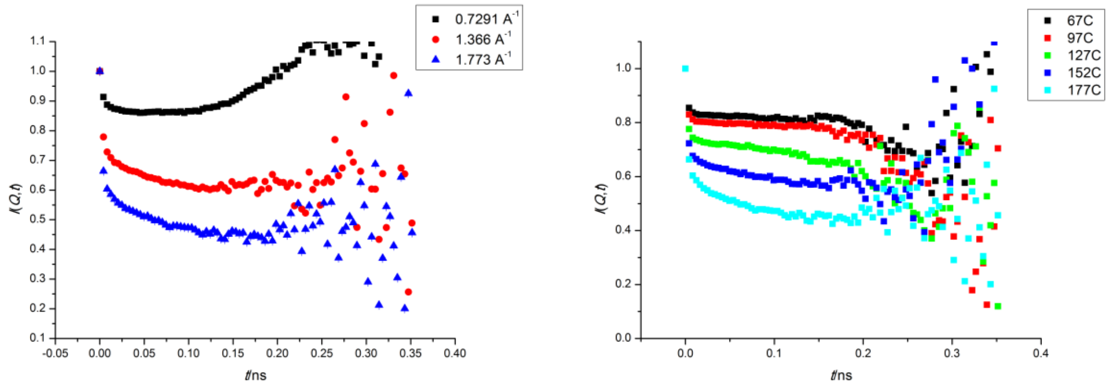

Figure 66: Sample $I(Q,t)$ decay curves created *via* Fourier transform of the $S(Q,\omega)$ QENS peaks deconvolved with an instrument resolution peak, $R(Q,\omega)$, improvised by adding the peaks recorded from the first five temperatures of the elastic scan of the same sample. The curves shown are from the h5 PS sample with 2 wt% SWCNTs at: 177 °C and three Q values (detailed in the legend, left), and Q = 1.773 Å^{-1} at five temperatures (detailed in the legend, right).

Following Fourier transform, the $I(Q,t)$ data for all samples take the form of a decay curve, with the curve dropping sharply down to a flat background, and the background dropping as the temperature and Q value increase. In all cases, the data becomes noisy after *ca*. 0.15 ns, because $\tau \propto h/\Delta E$, where ΔE is the full width at half maximum of the QENS peak. In many cases the data becomes noisy long before this, especially at low-T and Q, where the QENS peaks have very similar widths to the resolution peak, therefore each data set was considered individually and truncated at or before this time. Sample curves indicating the point at which the data were truncated are shown in Figure 67; these curves and their truncation times are representative of all data sets. Full details of the times at which each data set was truncated are given in Appendix 2; in all cases, the longest time considered was 0.15 ns.

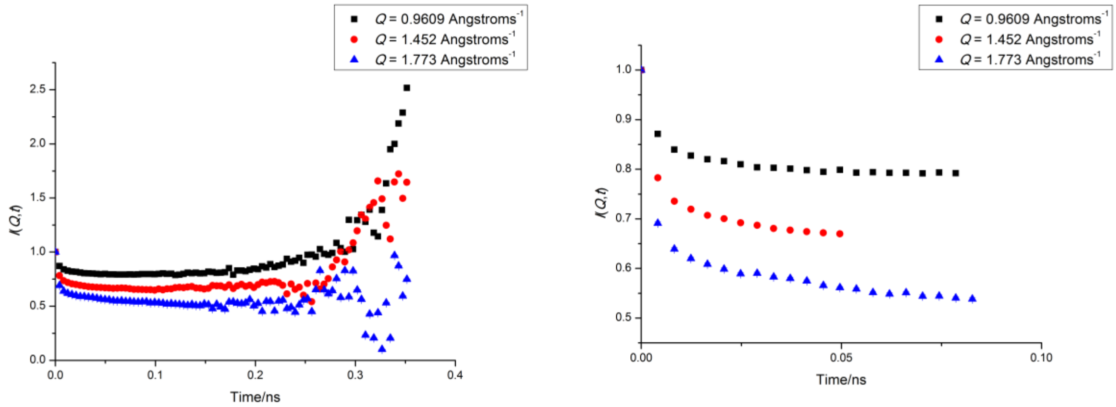

Figure 67: Sample I(Q,t) decay curves (left) before and (right) after truncation at the point at which the data displays an upturn or becomes noisy. These curves display data obtained from h5 PS + 0.4 wt% SWCNTs samples at 177 °C, and are representative of all samples. Details of the Q values of each data set are given in the legends of each plot.

4.4.4 Data fitting

4.4.4.1 Introduction

The KWW stretched exponential function (Equation 41) has frequently been fitted to intermediate scattering function decay curves to extract the relaxation times within polymer systems.[180-184]

$$f(t; A, \tau_{\mathrm{KWW}}, \beta) = A + (1 - A)\exp\left(\frac{t}{\tau_{\mathrm{KWW}}}\right)^{\beta}$$

Equation 41

A is a Q- and T-dependent background ($0 \leq A \leq 1$), which represents the amount of material that is stationary within the sample over the range of instrumental sensitivity; the related amplitude term, $(1 - A)$, represents the amount of material that is mobile within the sample. τ_{KWW} is the decay constant ($\tau_{\mathrm{KWW}} > 0$), and β is the stretching exponent ($0 < \beta \leq 1$). The parameter β is a shape parameter that characterises the breadth of the distribution of relaxation times exhibited by the system, and is generally, although not always,[180, 183] Q and T-independent. For polymers above their glass transition temperature that exhibit Rouse dynamics, β takes a value of 0.5.[182, 186] For polymers in their glassy state, *i.e.* below the T_g, $I(Q,t)$ data may still be fitted using a KWW function if side group motion is detected, which is the case for polystyrene, which exhibits side group motion in the form of libration of phenyl rings at temperatures as low as 200 K.[89, 91, 92]

4.4.4.2 Fitting round one: establishing β(T, Q, [SWCNT])

In order to determine an appropriate value of β for fitting the data presented in this chapter, an initial round of fitting was conducted only on the data from the h3 samples as all of these samples had a full dedicated resolution file and no missing detectors. The intention of this round of fitting was to obtain an average value of β to use for all future fittings. In this initial round of fitting, all the parameters were allowed to vary within the limits displayed in Table 28. Fitting was conducted up to the time values indicated in Table 34–Table 46. All fitting was conducted in Origin.[168]

Table 28: Starting values and limits for the initial of the KWW function to *I*(*Q*,*t*)

Parameter	Units	Lower limit	Upper limit	Initial value
A	—	0	1	0.5
τ_{KWW}	ns	0	—	5
β	—	0	1	0.5

Under this fitting regime, all of the data sets were fitted well by the KWW function (Figure 68–Figure 71). The average value of β obtained from this round of fitting is 0.61 (s.d. 0.26; 595 individual values of β; 7 samples, 17 Q values, 5 temperatures). Figure 71 indicates that for this data series, the value of β does show some Q-dependence, with β decreasing with increasing Q; the shape of this Q-dependence suggests that a background from the underlying static structure factor is being observed. In addition the value of β shows a clear T-dependence, generally decreasing with increasing T.

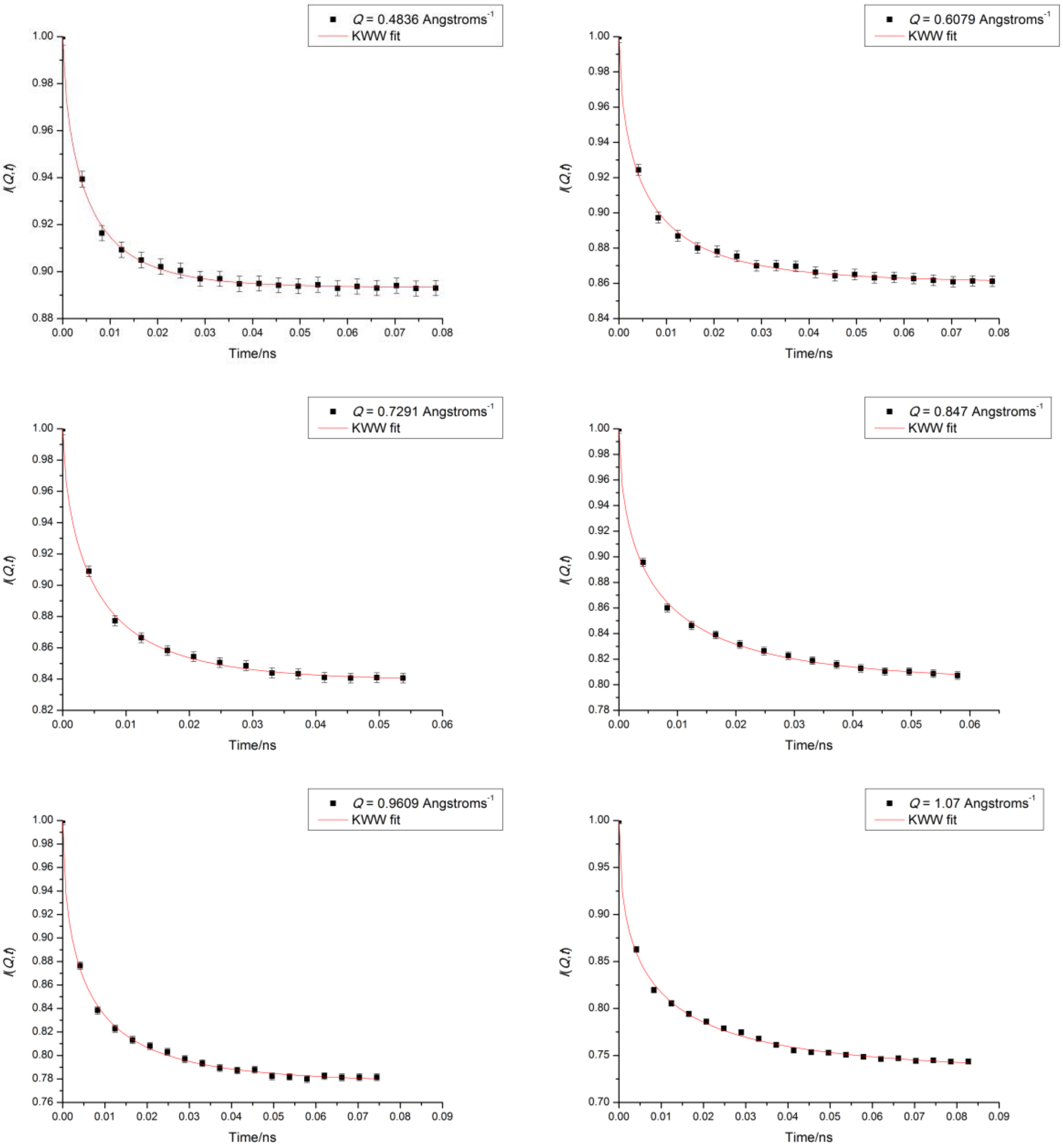

Figure 68: Fits of the KWW function with freely varying β to the $I(Q,t)$ curves of h3 PS + 4 wt% SWCNTs at 177 °C. Details of the Q values of the data are given in the legends of each individual plot.

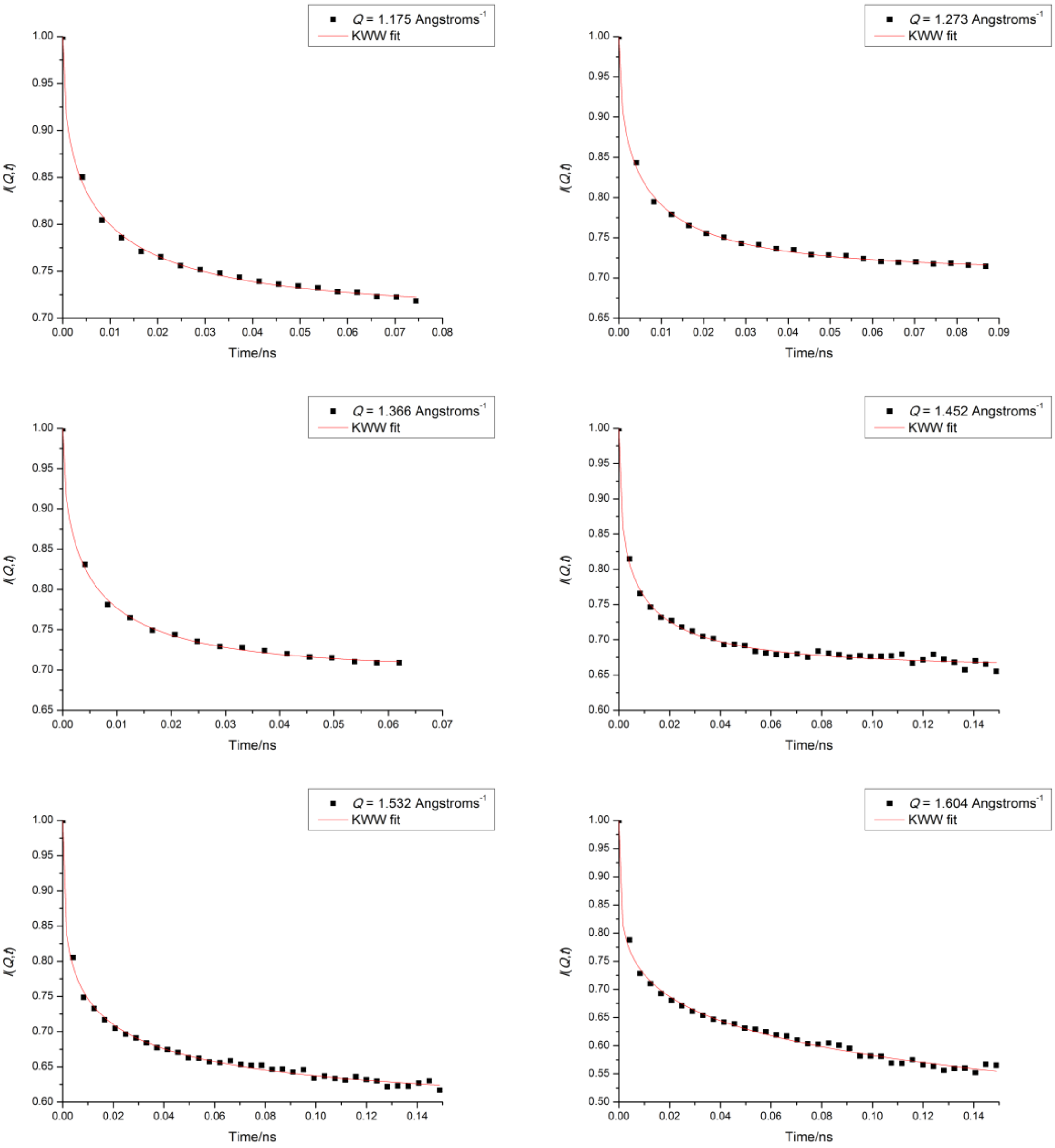

Figure 69: Fits of the KWW function with freely varying β to the $I(Q,t)$ curves of h3 PS + 4 wt% SWCNTs at 177 °C. Details of the Q values of the data are given in the legends of each individual plot. Continuation of Figure 69.

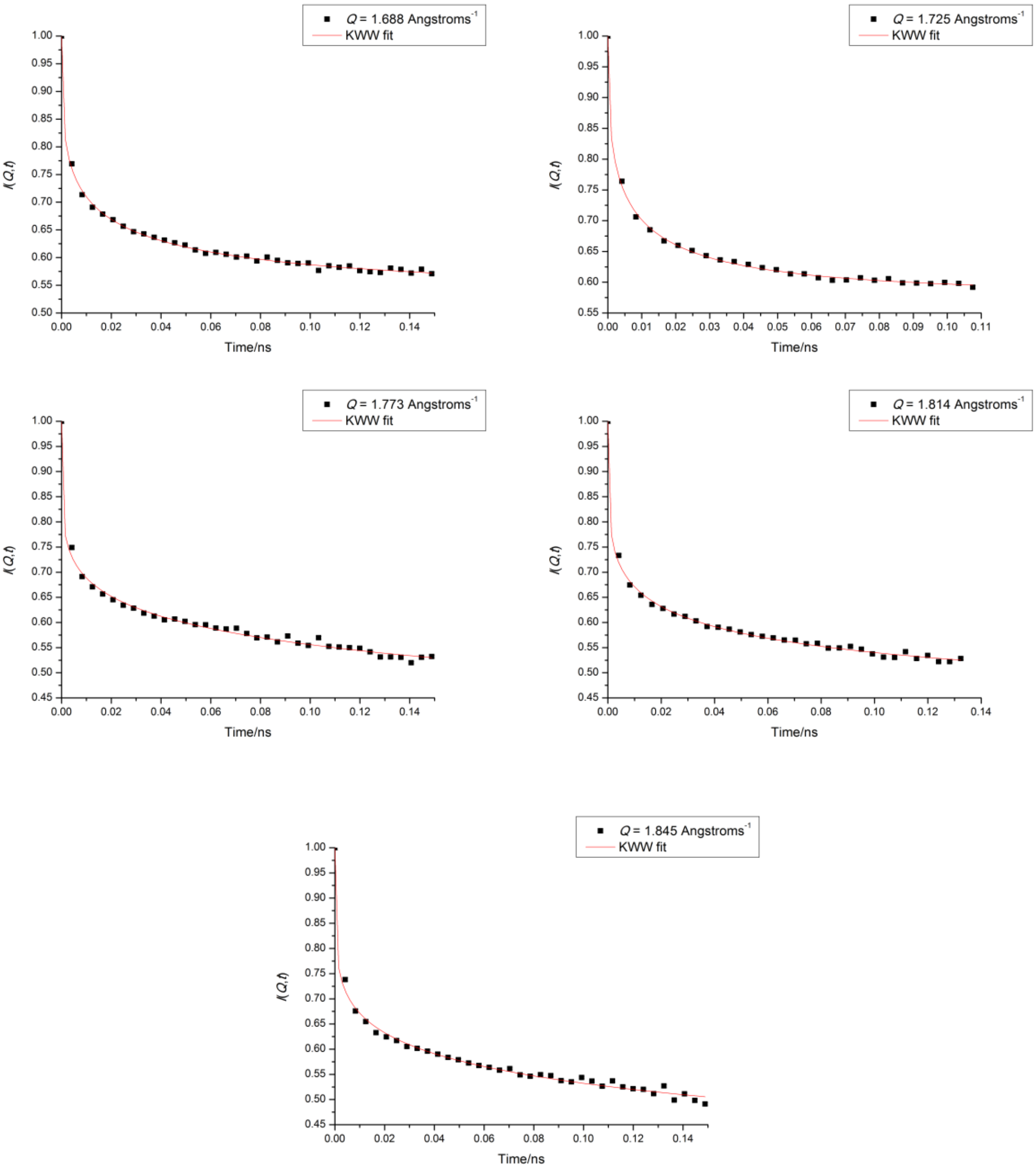

Figure 70: Fits of the KWW function with freely varying β to the *I*(*Q*,*t*) curves of h3 PS + 4 wt% SWCNTs at 177 °C. Details of the *Q* values of the data are given in the legends of each individual plot. Continuation of Figure 69.

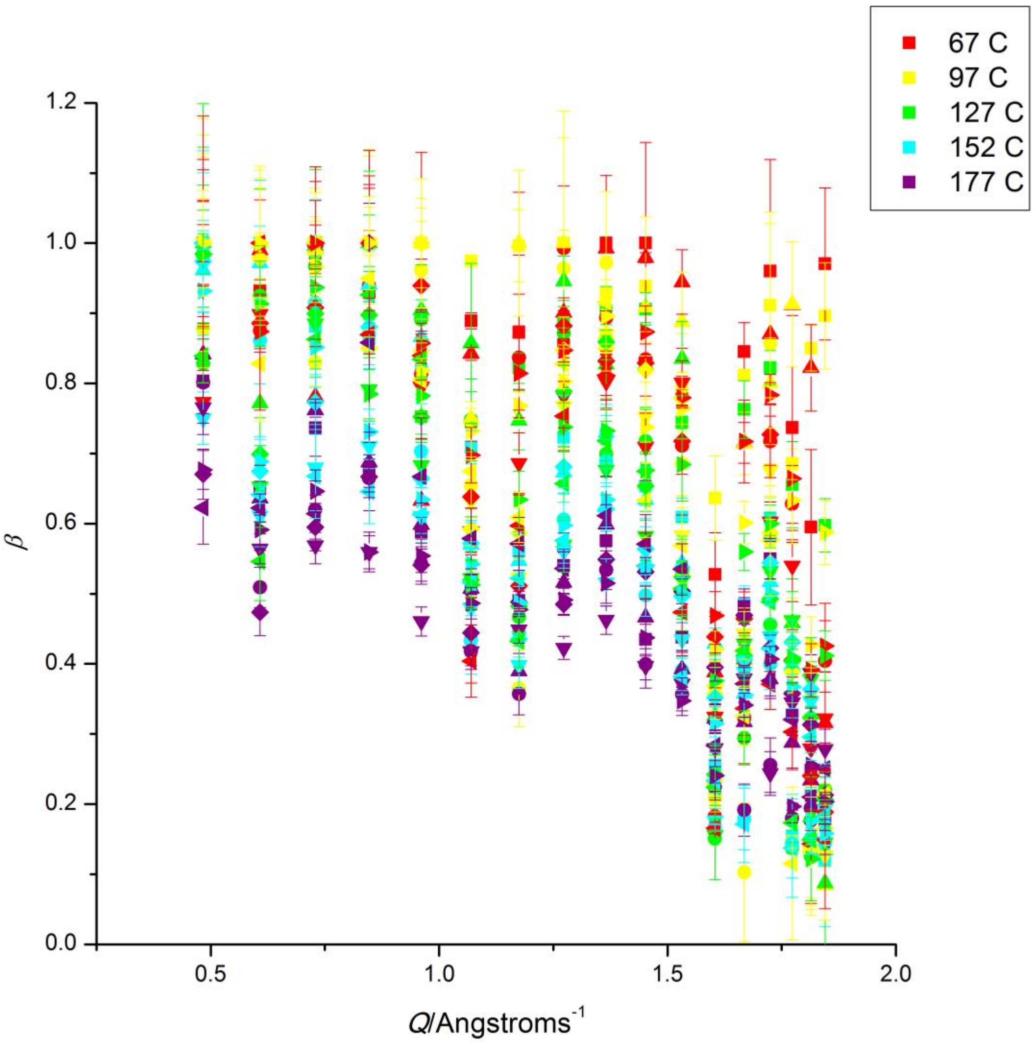

Figure 71: β values obtained from fitting all 595 curves from the h3 PS series of samples. Samples containing 0 wt% SWCNTs are squares; 0.1 wt%, circles; 0.4 wt%, point-up triangles; 1 wt%, point-down triangles; 2 wt%, diamonds; 3 wt%, left-pointing triangles; and 4 wt%, right-pointing triangles. Beta values extracted from data recorded at 67 °C are indicated in red; 97 °C, yellow; 127 °C, green; 152 °C, blue; and 177 °C, purple.

The values of β obtained from the initial fitting of the h3 PS samples suggests three possible routes for the final fitting of the data: (i) allowing β to float to any value; (ii) fit the data fixing the value of β at 0.61; and (iii) using a *Q*-dependent value of β obtained by fitting a straight line through all the beta values and using the *Q*-dependence of this line to calculate a different value of β for each *Q* value. The first approach was rejected as, while the fits are visually good across all *Q* values, the parameters extracted from the fits at the high-*Q* end had large error bars associated with them, suggesting that the fits were not as good as they first appeared (Figure 72).

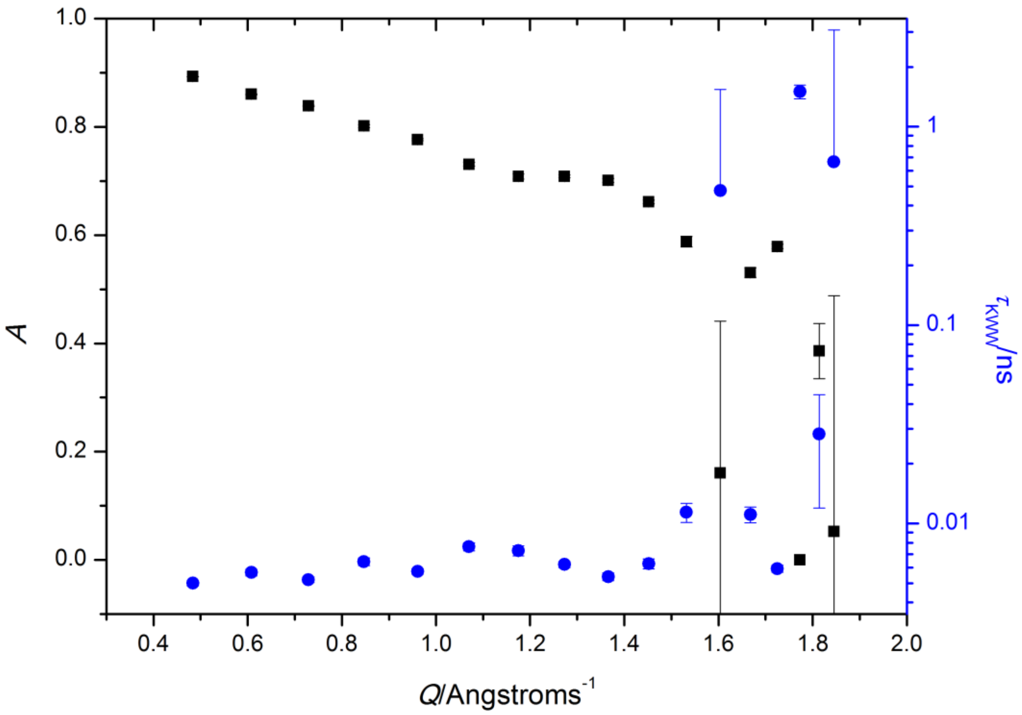

Figure 72: Plot of *A* (black, left-hand *y*-axis) and τ_{KWW} (blue, right-hand *y*-axis) extracted from the KWW fits using variable β for h3 PS + 4 wt% SWCNTs at 177 °C.

4.4.4.3 Fitting round two, (i) β *= 0.61*

For the first approach in the second round of fitting, the intermediate scattering function decay curves for the h3 PS nanocomposites were fitted with the KWW stretched exponential function with $\beta = 0.61$ (Equation 42).

$$f(t; A, \tau_{\mathrm{KWW}}) = A + (1 - A)\exp\left(\frac{t}{\tau_{\mathrm{KWW}}}\right)^{0.61}$$

Equation 42

A and τ_{KWW} were allowed to vary as for the first fitting; full details are given in Table 29. This fitting procedure was conducted on all h3 PS nanocomposite *I*(*Q*,*t*) curves; fitting was conducted in Origin.[168] The fits for h3 PS + 4 wt% SWCNTs at 177 °C are shown in Figure 73–Figure 76.

Table 29: Starting values and limits for the secondary fitting of the KWW function to $I(Q,t)$

Parameter	**Units**	**Lower limit**	**Upper limit**	**Initial value**
$\boldsymbol{A}$	—	0	1	0.5
$\boldsymbol{\tau_{\mathrm{KWW}}}$	ns	0	—	5
β	—	—	—	0.61[a]

[a] Fixed value obtained from a preliminary round of fitting the KWW function to the $I(Q,t)$ curves of the h3 PS series of samples with 0–4 wt% SWCNTs

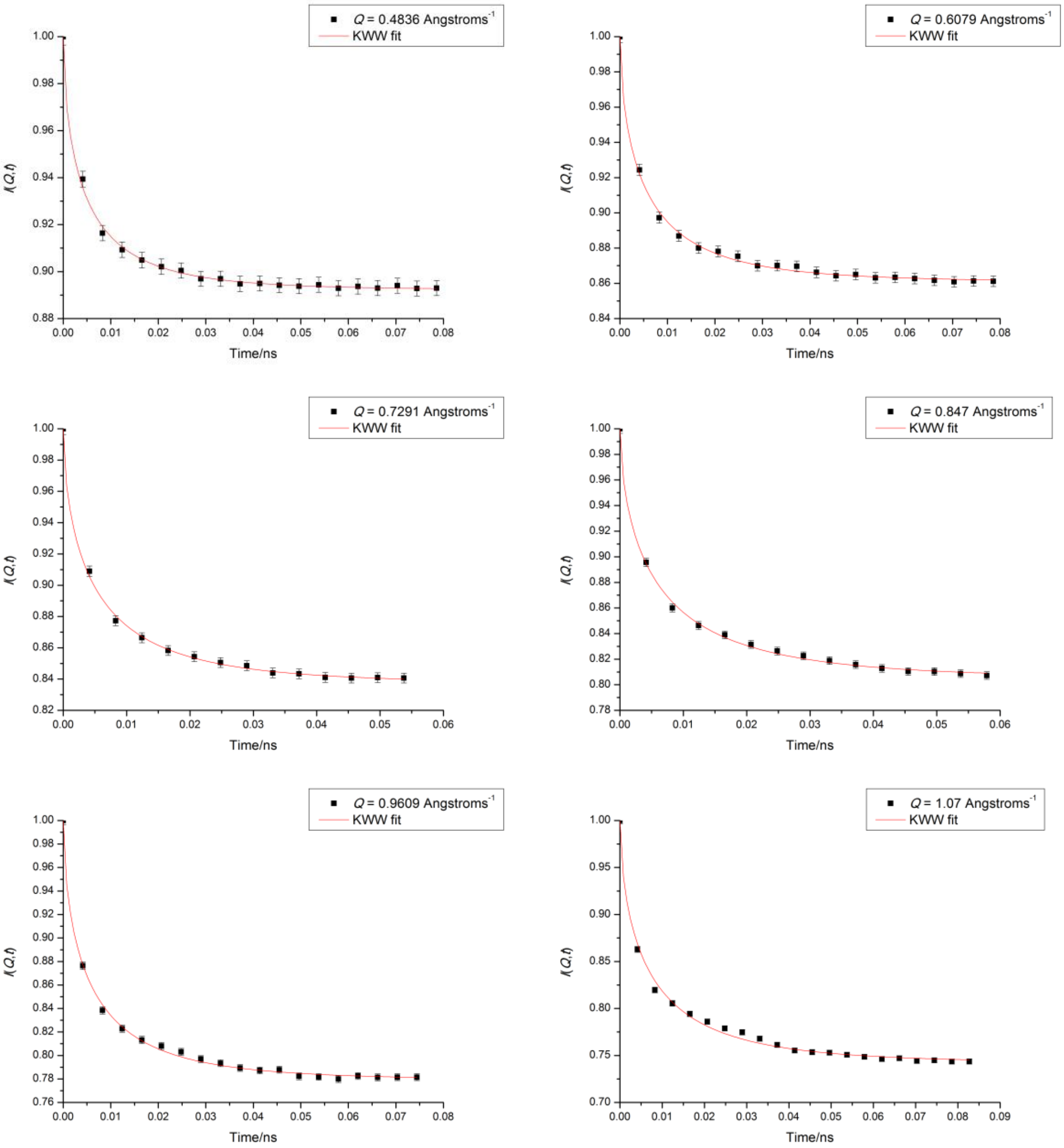

Figure 73: Fits of the KWW function with β = 0.61 to the $I(Q,t)$ curves of h3 PS + 4 wt% SWCNTs at 177 °C. Details of the Q values of the data are given in the legends of each individual plot.

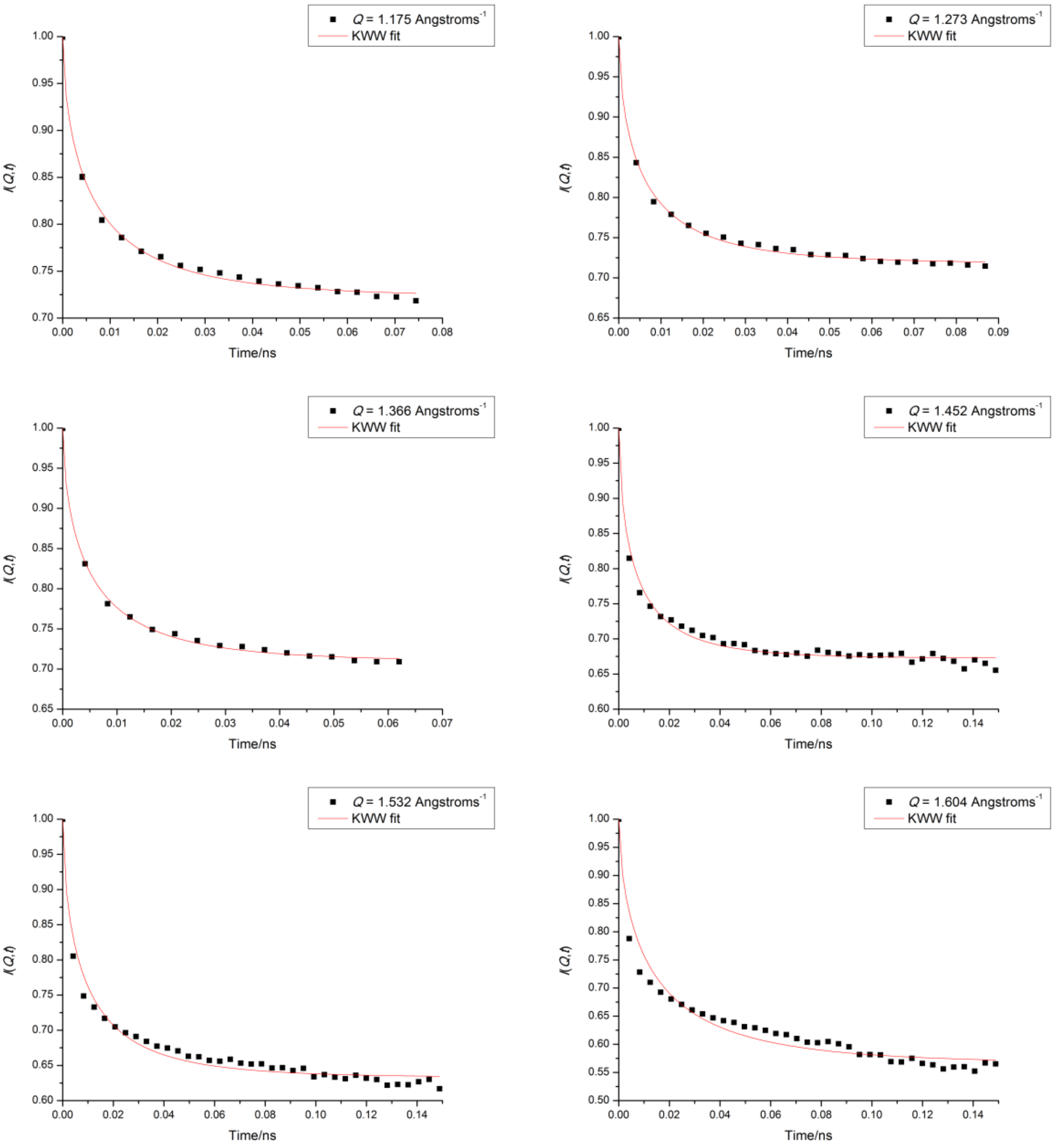

Figure 74: Fits of the KWW function with β = 0.61 to the *I*(*Q*,*t*) curves of h3 PS + 4 wt% SWCNTs at 177 °C. Details of the *Q* values of the data are given in the legends of each individual plot. Continuation of Figure 74.

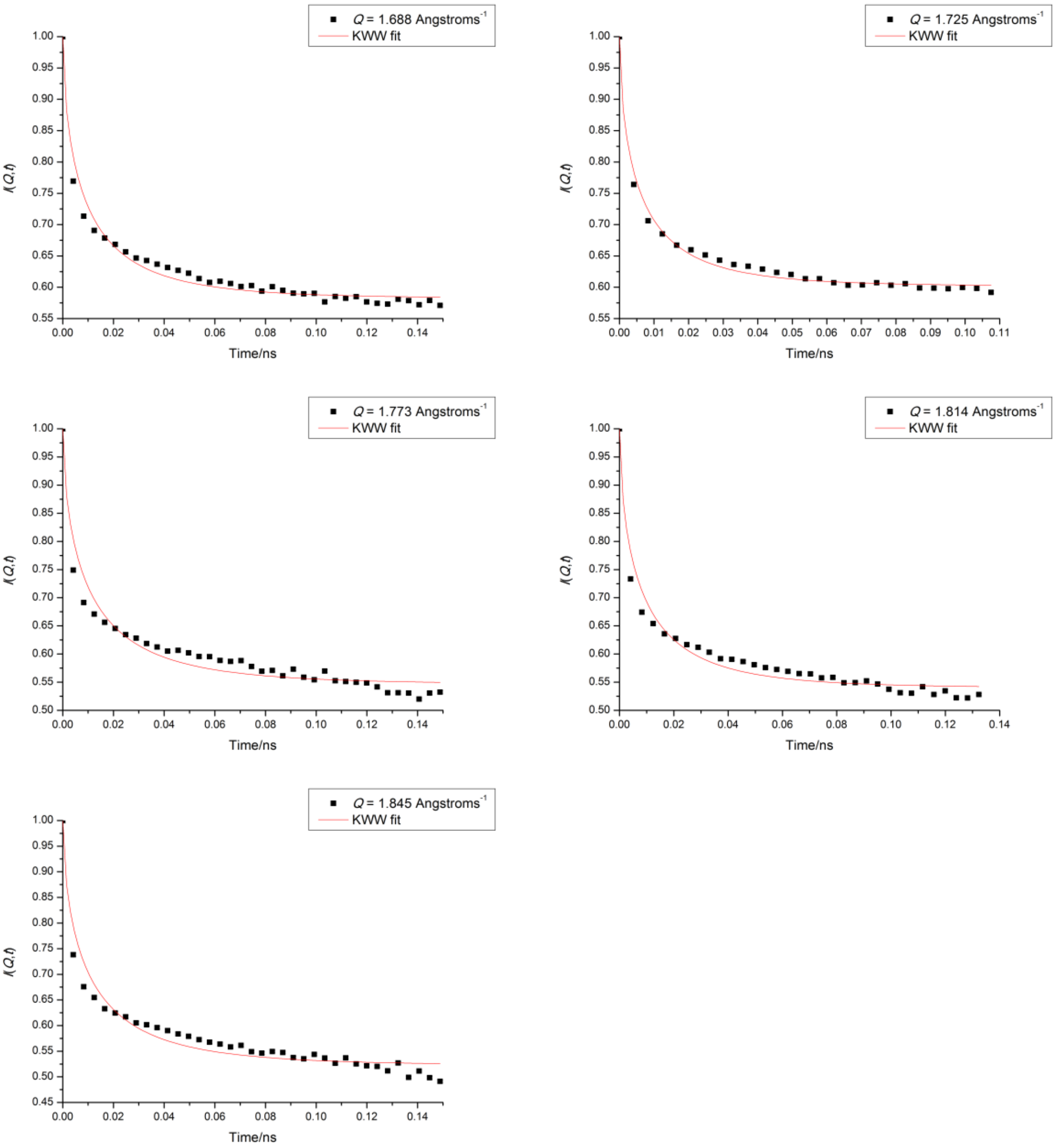

Figure 75: Fits of the KWW function with β = 0.61 to the *I*(*Q*,*t*) curves of h3 PS + 4 wt% SWCNTs at 177 °C. Details of the *Q* values of the data are given in the legends of each individual plot. Continuation of Figure 74.

4.4.4.4 Fitting round two: (ii) Q-dependent β

For the second approach in the second round of fitting, *Q*-dependent values of β were determined by plotting a straight line through the β data and using Excel to calculate the equation of this line (Figure 76 and Equation 43).

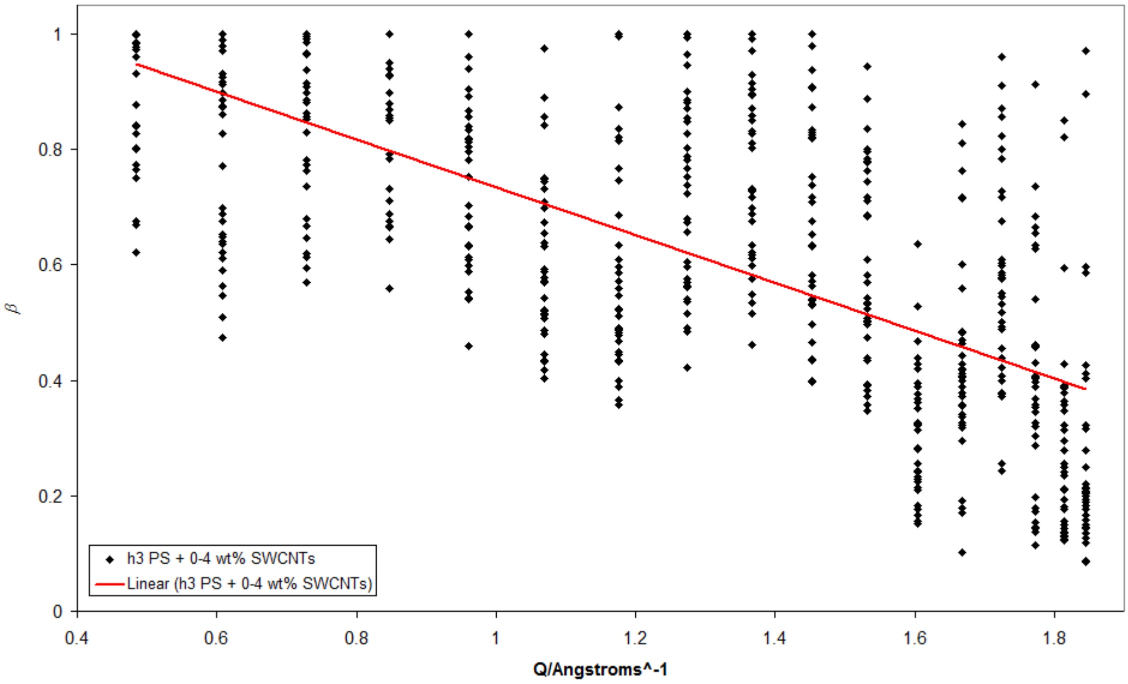

Figure 76: All β values extracted from the KWW fits to the *I*(*Q*,*t*) curves for the h3 PS nanocomposite series, fitted with a straight line.

$$\beta = -0.4133Q + 1.147$$

Equation 43

Equation 43 was then used to calculate β values for the values of *Q* for which data had been collected (Table 30). These values of β were used in the KWW equation (Equation 41), and each *I*(*Q*,*t*) curve was fitted. As before, *A* and τ_{KWW} were allowed to vary freely within limits; full details are given in Table 30 and Table 31. This fitting procedure was conducted in Origin[168] on the *I*(*Q*,*t*) curves for a single sample: h3 PS + 4 wt% SWCNTs at 177 °C; the fits are shown in Figure 77–Figure 80.

Table 30: *Q*-dependent values of β obtained from the straight line fit through the β values from the preliminary fits of the KWW function to the I(*Q*,t) curves from the h3 PS series of nanocomposites

Q/Angstroms^{-1}	β^{a}
0.4836	0.9476
0.6079	0.8962
0.7291	0.8461
0.8470	0.7974
0.9609	0.7503
1.0700	0.7053
1.1750	0.6619
1.2730	0.6214
1.3660	0.5829
1.4520	0.5474
1.5320	0.5143
1.6040	0.4846
1.6680	0.4581
1.7250	0.4346
1.7730	0.4147
1.8140	0.3978
1.8450	0.3850

[a] β calculated from the straight line equation plotted through all the β values obtained from the fitting of KWW to the *I*(*Q*,*t*) curves of the h3 PS series of nanocomposites containing between 0 and 4 wt% SWCNTs.

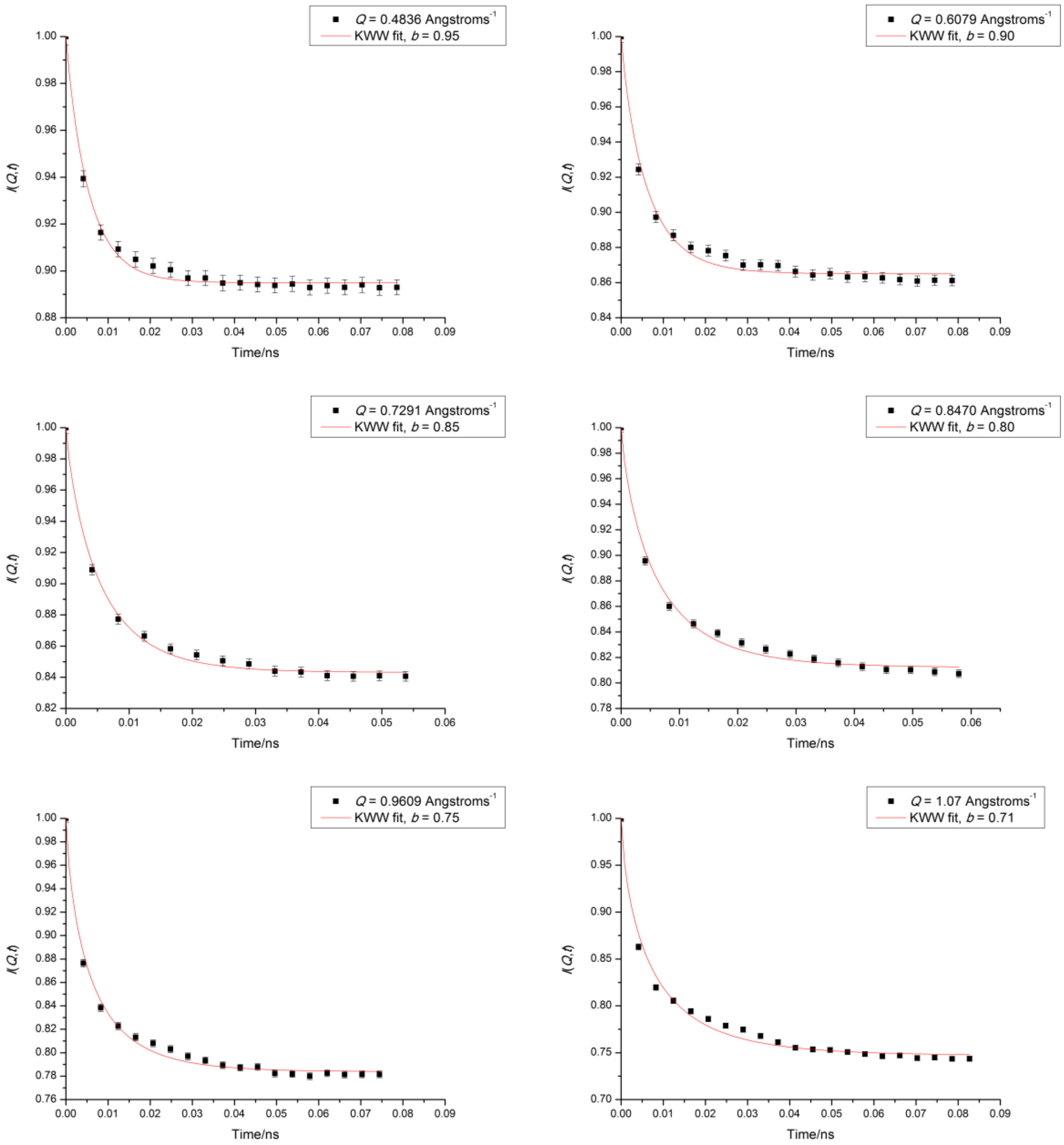

Figure 77: Fits of the KWW function with *Q*-dependent *β* to the *I*(*Q*,*t*) curves of h3 PS + 4 wt% SWCNTs at 177 °C. Details of the *Q* and *β* values of the data are given in the legends of each individual plot.

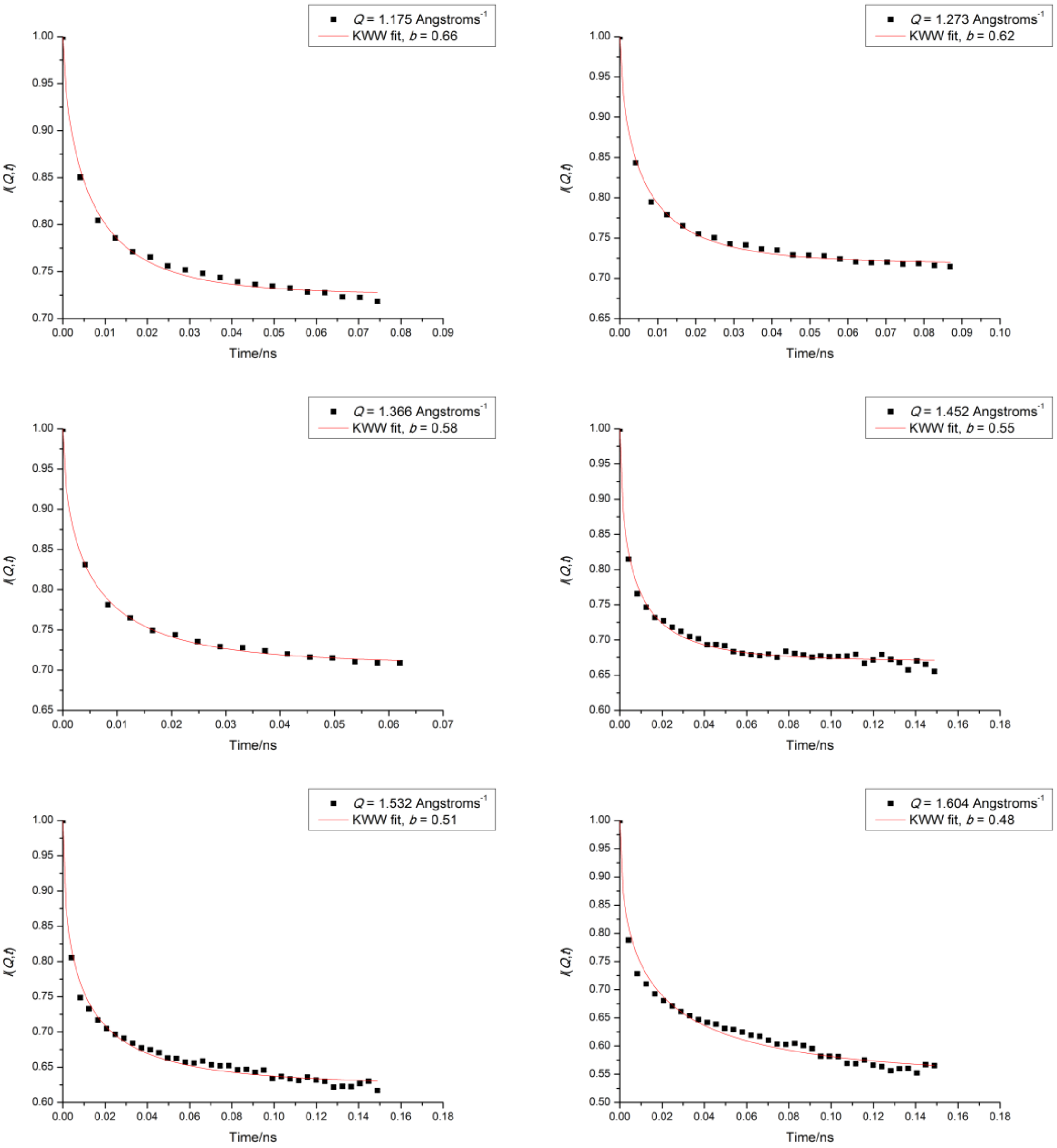

Figure 78: Fits of the KWW function with *Q*-dependent β to the *I*(*Q*,*t*) curves of h3 PS + 4 wt% SWCNTs at 177 °C. Details of the *Q* and β values of the data are given in the legends of each individual plot. Continuation of Figure 78.

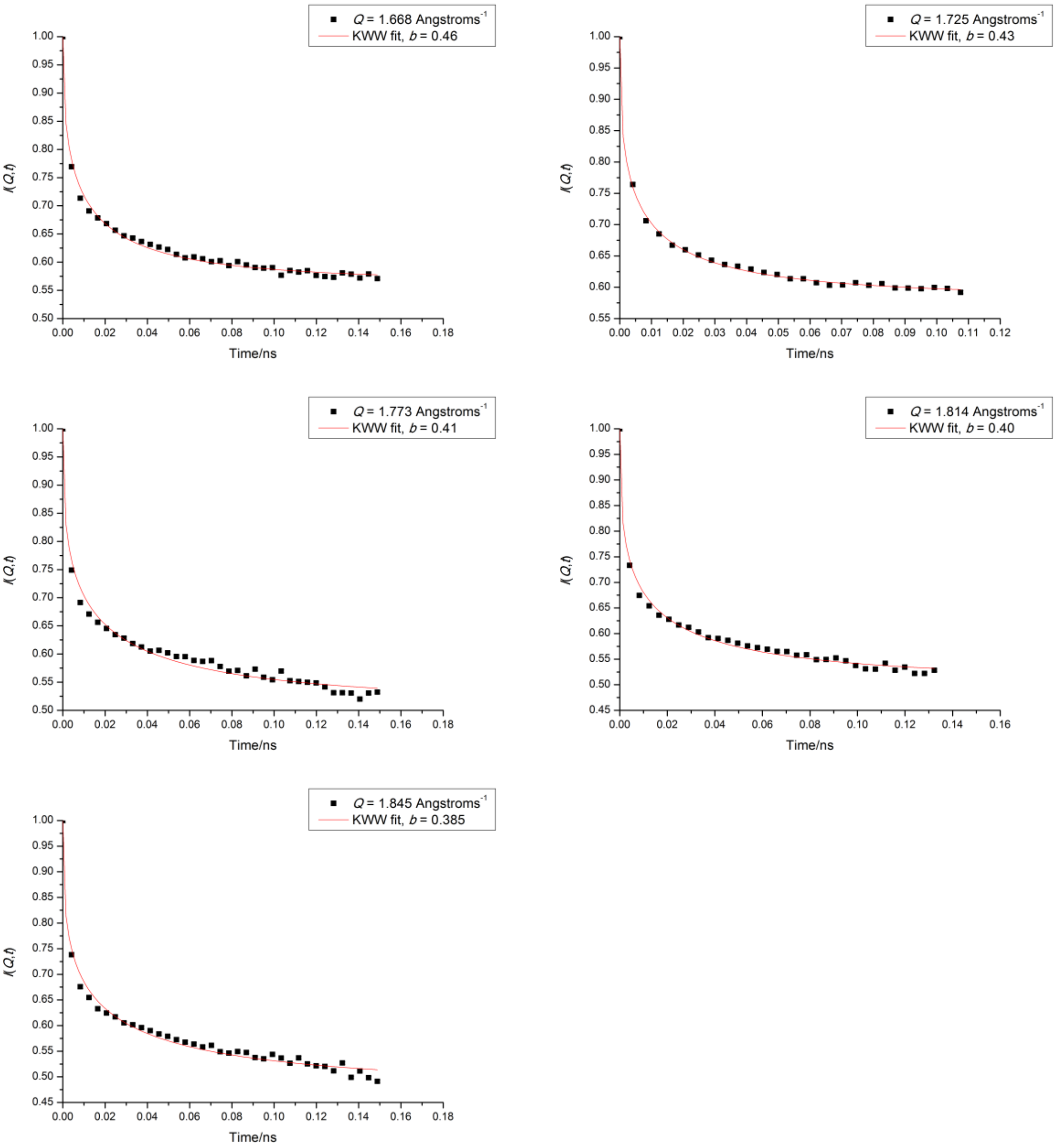

Figure 79: Fits of the KWW function with Q-dependent β to the $I(Q,t)$ curves of h3 PS + 4 wt% SWCNTs at 177 °C. Details of the Q and β values of the data are given in the legends of each individual plot. Continuation of Figure 78.

Table 31: Starting values and limits for the secondary fitting of the KWW function to *I*(*Q*,*t*)

Parameter	Units	Lower limit	Upper limit	Initial value
A	—	0	1	0.5
$\boldsymbol{\tau_{\mathrm{KWW}}}$	ns	0	—	5
$\boldsymbol{\beta}$	—	—	—	Fixed, *Q*-dependent[a]
[a]Fixed values obtained from the equation of the straight line through all the beta values from the preliminary fitting of the KWW function to the *I*(*Q*,*t*) curves of the h3 PS series of samples with 0–4 wt% SWCNTs; for full details, see Table 30.				

4.4.4.5 Comparing the approaches to fitting

The three different approaches to the evaluation of β produced different levels of fit, with the fits that were obtained by allowing β to vary freely (Figure 68–Figure 71) being generally better than those obtained when β was either fixed at 0.61 (Figure 73–Figure 76) or *Q*-dependent (Figure 77–Figure 80). At low-*Q*, the fitting with β fixed at 0.61 worked reasonably well for all data sets, however at higher values of *Q*, and especially for $Q \geq 1.45$ Å^{-1} (corresponding to $d = 4.3$ Å), the fits become markedly poorer (Figure 73–Figure 76). Across the *Q*-range under examination, the fits when a *Q*-dependent value of β was used are less good than those obtained from either fitting whilst allowing β to vary freely, or from the low-*Q* fits to the *I*(*Q*,*t*) curves when using $\beta = 0.61$ (Figure 68–Figure 71 and Figure 73–Figure 76). However, at high-*Q* ($Q > 1.45$ Å^{-1}) the fits achieved using *Q*-dependent values of β are better than those obtained when using $\beta = 0.61$ (Figure 73–Figure 76 *vs*. Figure 77–Figure 80).

Figure 80 shows the *A* and τ_{KWW} parameters extracted from the KWW fits for the three different approaches used. The three different approaches produced very similar values for both *A* and τ_{KWW} up to $Q \approx 1.45$ Å^{-1}, but for *Q* values greater than this the parameters extracted from the fittings with variable β diverge, with large associated error bars. Since there is no *a priori* reason for the fraction of immobile polymer to have such a widely scattered dependence on *Q*, it appears that allowing beta to vary freely gives erroneous values for *A* and perhaps τ.

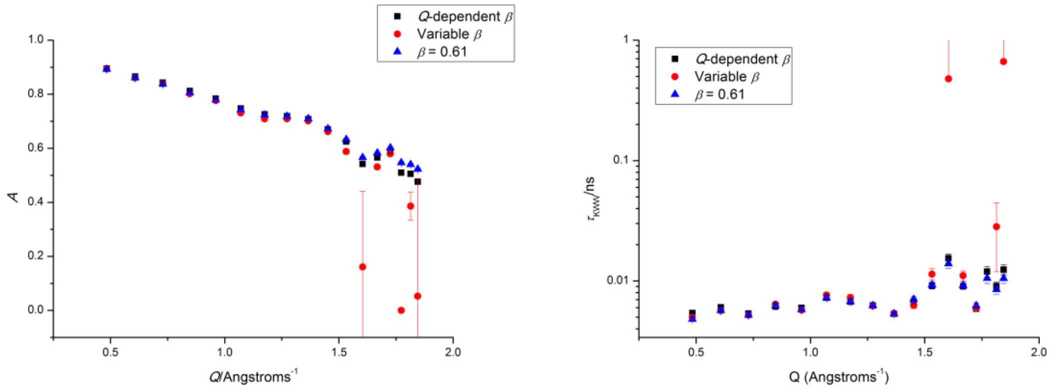

Figure 80: Plots of (left) *A* and (right) τ_{KWW} extracted from the KWW fits using three different forms for β: variable, fixed and *Q*-dependent; for h3 PS + 4 wt% SWCNTs at 177 °C.

Surprisingly, the *A* and τ_{KWW} parameters extracted from those fits where β was fixed at 0.61 and where β was *Q*-dependent are very similar, in spite of the fits generally appearing poorer for the *Q*-dependent β fits at low-*Q* values and poorer for the fixed-β fits at high *Q* values. This suggests that there is no need to complicate the analysis by fitting every data set with the *Q*-dependent values of β.

4.4.4.6 Fitting round three: two Q regimes

As was noted in the previous section, the data presented in this chapter appears to fall into two regimes: one below $Q \approx 1.45$ Å^{-1} ($d > 4.3$ Å) where the data is well fitted by fixing β at 0.61; and a second regime above $Q \approx 1.45$ Å^{-1} ($d < 4.3$ Å), where the data requires a significantly lower value of β to be well fitted and for meaningful values of *A* and τ_{KWW} to be extracted from the fits. Based on this assessment of the data, the analysis going forward requires the data to be divided into two *Q* regions, with the two regions using a different β value in the KWW fitting.

The low-*Q* data is well fitted by the KWW function when $\beta = 0.61$; this value of β will be used for the data up to $Q = 1.45$ Å^{-1}. For the higher *Q* data, a lower value of β was determined by taking the average β value from all the $I(Q,t)$ curves where $Q \geq 1.45$ Å^{-1} fitted with the KWW function when β was allowed to vary freely. This gave an average of 0.44 (s.d. 0.23).

Sample fits of the high-*Q* data to KWW with this value of β are shown in Figure 81. The fits are significantly better than those fitted to the KWW function with $\beta = 0.61$ over the same range of *Q* values (Figure 73–Figure 76). The *A* and τ_{KWW} values extracted from these fits are shown in Figure 82, in comparison to the values obtained from the KWW fits using *Q*-dependent values of β and β = 0.61. The three different fitting approaches all lead to *A* and τ_{KWW} values with small error bars, and the three approaches return values displaying the same trends and variation with *Q*. Especially for parameter *A*, fits conducted with $\beta = 0.44$ returned values closer to those obtained from the fits conducted with *Q*-dependent β than those fits conducted with $\beta = 0.61$.

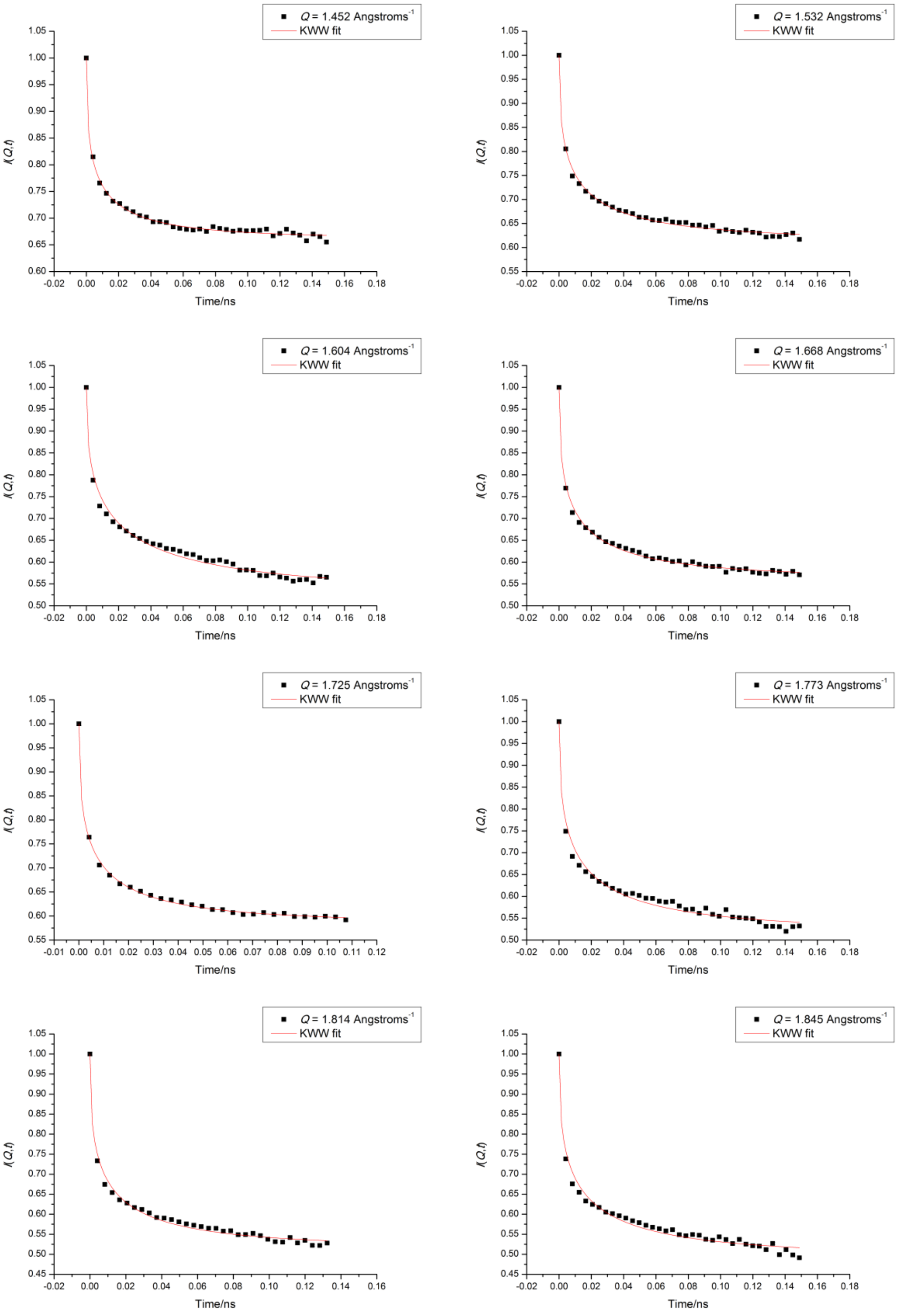

Figure 81: Fits of the KWW function with β = 0.44 to the high-Q $I(Q,t)$ curves of h3 PS + 4 wt% SWCNTs at 177 °C. Details of the Q values of the data are given in the legends of each individual plot.

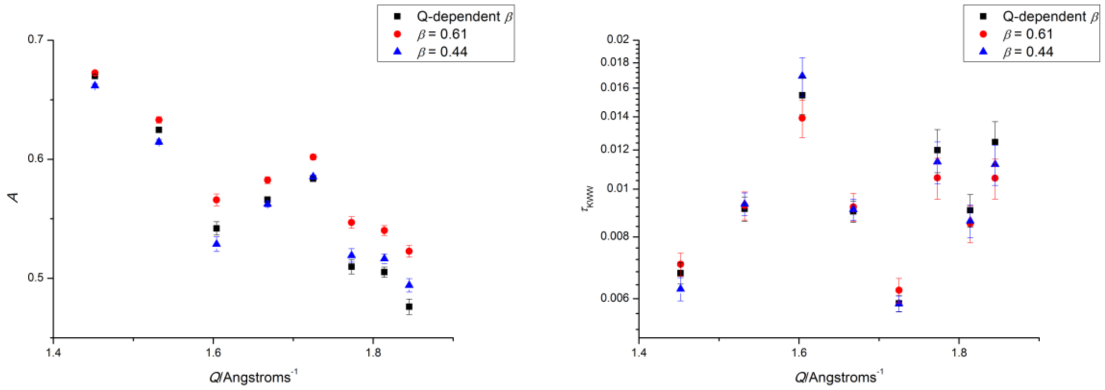

Figure 82: Plots of (left) A and (right) τ_{KWW} extracted from the KWW fits using three different approaches to β: Q-dependent, $\beta = 0.61$ and $\beta = 0.44$; for h3 PS + 4 wt% SWCNTs.

4.4.5 Results and discussion

4.4.5.1 KWW fitting: the value of β

When the value of the KWW fitting parameter β is allowed to vary freely, the values returned exhibit a distinct downward trend with increasing Q (Figure 71 and Equation 43). A β value of 1 is indicative of the system exhibiting a single relaxation time, *i.e.* the diffusion of small molecules (which does not apply here as the polymers under examination are long chain molecules), while a β value closer to 0 corresponds to a broad spectrum of relaxation times, *i.e.* a heterogeneous state.[187] The β *vs.* Q behaviour presented here suggests that at longer length scales the system exhibits a narrower range of relaxation times than at higher Q, *i.e.* shorter length scales. This is in agreement with Ganazzoli *et al*., whose work suggests that at longer length scales, the diffusive regime sets in and β approaches 1.[182] The Q-dependence of β is, however, contrary to the work of Arialdi *et al*., which identified a slight upward trend in β with Q for polyethylene,[184] and the work of Swenson *et al*. whose comparison of β values obtained from photocorrelation spectroscopy (a technique that measures global density fluctuations, $Q < 0.01$ Å^{-1}) and dielectric spectroscopy (which measures more local length scales, $Q \approx 1$ Å^{-1}) suggested that longer range measurements resulted in lower values of β.[183]

As a value of $\beta = 0.44$, a value similar to that found for other polymer systems,[180, 184, 188, 189] fitted the high-Q data well, and this is the region in which there is most confidence, the decision was taken to concentrate on fitting only the high Q region data ($Q \geq 1.45$ Å^{-1}; $d \leq 4.3$ Å), and only fitting using $\beta = 0.44$. The length scales under examination in this Q-region are much smaller than the radii of gyration of the polystyrene matrices [R_g (229 kg mol^{-1}) = 128 Å; R_g (397 kg mol^{-1}) = 169 Å], therefore these neutron measurements are examining individual bonds and small collections of atoms, rather than whole molecule or diffusive motions.

4.4.5.1.1 h3 vs. h5

In this work, scattering data from both ring and chain-hydrogenated samples was examined. The value of β to be used in the KWW fitting was obtained by taking the average β values from the KWW fittings of only the chain-hydrogenated samples, as these were the data sets for which full, independent resolution files existed, allowing greater confidence in the data presented. In doing this, it was assumed that the same value of β is also appropriate for the fitting of the ring hydrogenated samples. In order to test this assumption, the data sets recorded for the h5 PS nanocomposites with a full resolution file [h5 PS + 0, 0.1 (177 °C only), 0.4 and 4 wt% SWCNTs] were fitted with the KWW function (Equation 41) using the parameters given in Table 28 and the average β value calculated; of these data sets, only one had no missing detectors, so two averages were taken, one with just the β values from the h5 PS + 0.4 wt% SWCNTs, the other with the β values from all four samples. The averages are given in Table 32.

Table 32: Values of β obtained from the fitting the KWW function to $I(Q,t)$ for the h5 PS nanocomposites with full resolution files[a]

Sample	**Q range under examination/Å^{-1}**	**Average β value from first round of KWW fitting**	**Standard deviation**
h5 PS + 0.4 wt% SWCNTs	All Q: 0.44–1.86	0.56[a]	0.29
h5 PS + 0.1[b], 0.4, 1 and 4 wt% SWCNTs	All Q: 0.44–1.86	0.56[a]	0.30
h5 PS + 0.1[b], 0.4, 1 and 4 wt% SWCNTs	1.45–1.86	0.37	0.22

[a] Average recorded across all Q values for which data were recorded.

[b] Data were included for the h5 PS + 0.1 wt% sample at 177 °C only. The other data recorded for this sample did not have an independent resolution file.

[c] Average β value obtained for data where $Q \geq 1.45\ \text{Å}^{-1}$.

The average values of β obtained from fitting the h5 PS nanocomposites are broadly distributed, as indicated by the standard deviation values in Table 32, but are well within the standard deviations of the values obtained for the h3 PS nanocomposite series. The equation of the line through all the β values for the h5 PS samples (Figure 83 and Equation 44) is also similar to that obtained for the h3 PS samples (Equation 43), leading to the conclusion that it is appropriate to use the same value of β to fit the $I(Q,t)$ curves from both the h3 PS and h5 PS samples; this is confirmed on seeing the two lines plotted on the same axes (Figure 84).

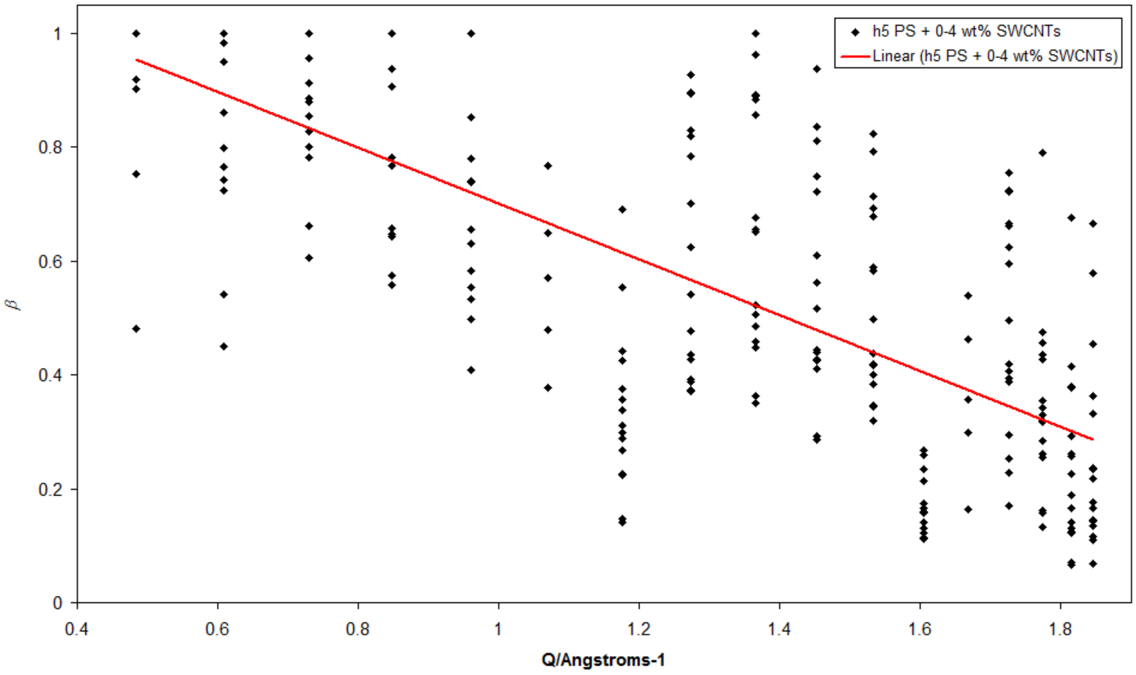

Figure 83: All β values extracted from the KWW fits to the $I(Q,t)$ curves for the h5 PS nanocomposite series, fitted with a straight line.

$$-0.4899Q + 1.1908$$

Equation 44

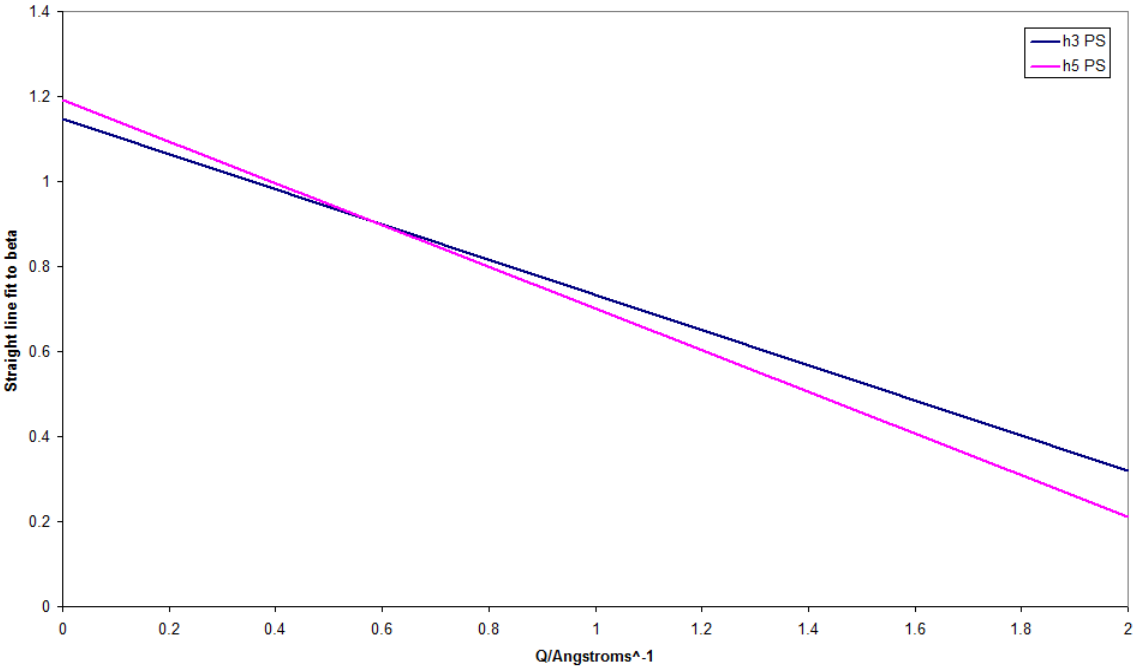

Figure 84: Straight line fits to h3 (blue) and h5 (pink) PS.

4.4.5.2 Variation of A with temperature

The parameter *A*, or amplitude, from the KWW function corresponds to the background, and measures the amount of material that is stationary within a sample. This parameter is expected to decrease with increasing temperature and *Q*, which is the case for the vast majority of both the h3 and h5 nanocomposite samples investigated (Figure 85 and Figure 86).

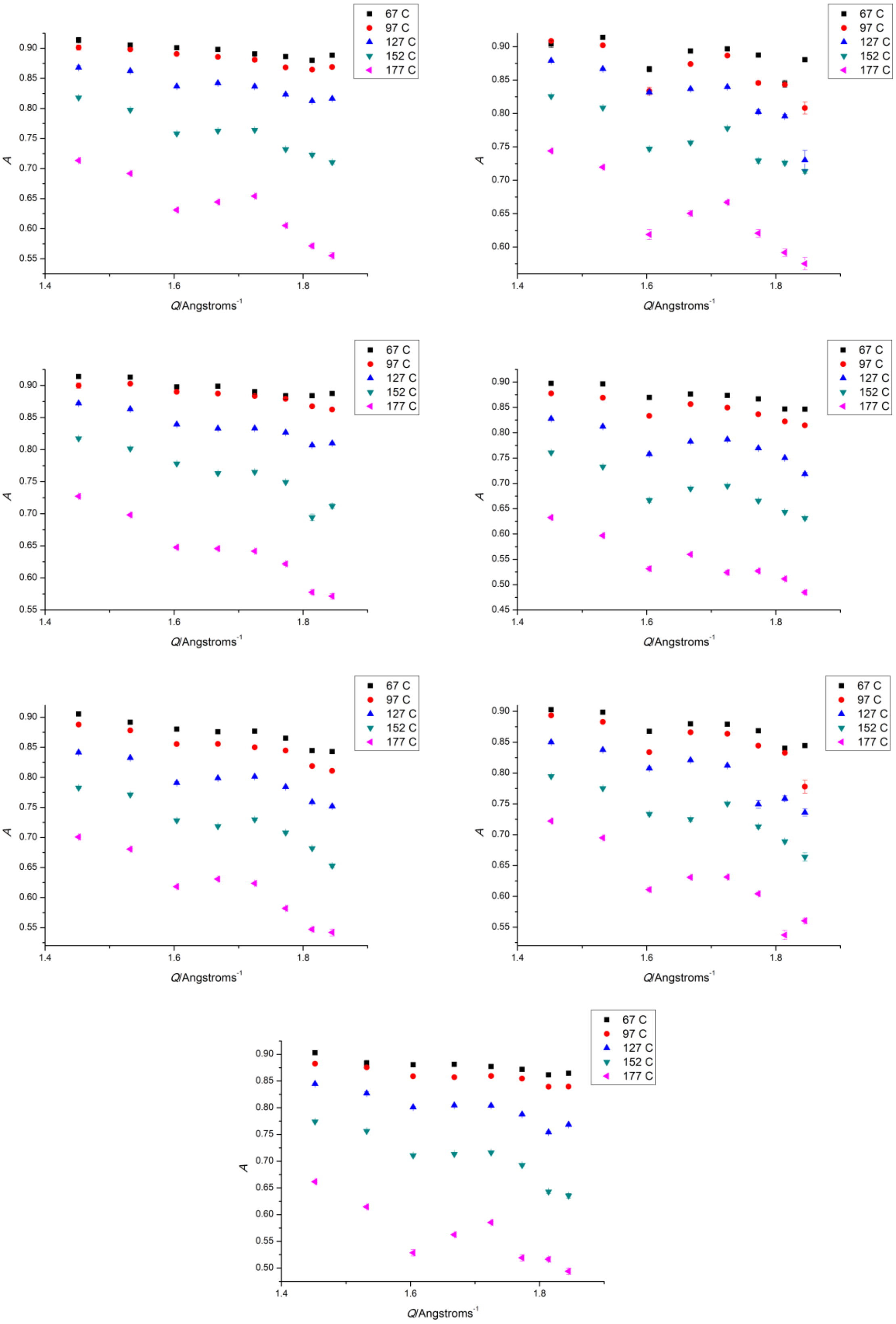

Figure 85: The KWW background parameter, *A*, *vs*. *Q* as a function of temperature for the h3 PS series of nanocomposites. Each plot corresponds to a different nanotube concentration: top row, left: 0 wt% SWCNTs; top row, right: 0.1 wt% SWCNTs; row two, left: 0.4 wt% SWCNTs; row two, right: 1 wt% SWCNTs; row three, left: 2 wt% SWCNTs; row three, right: 3 wt% SWCNTs; bottom row: 4 wt% SWCNTs.

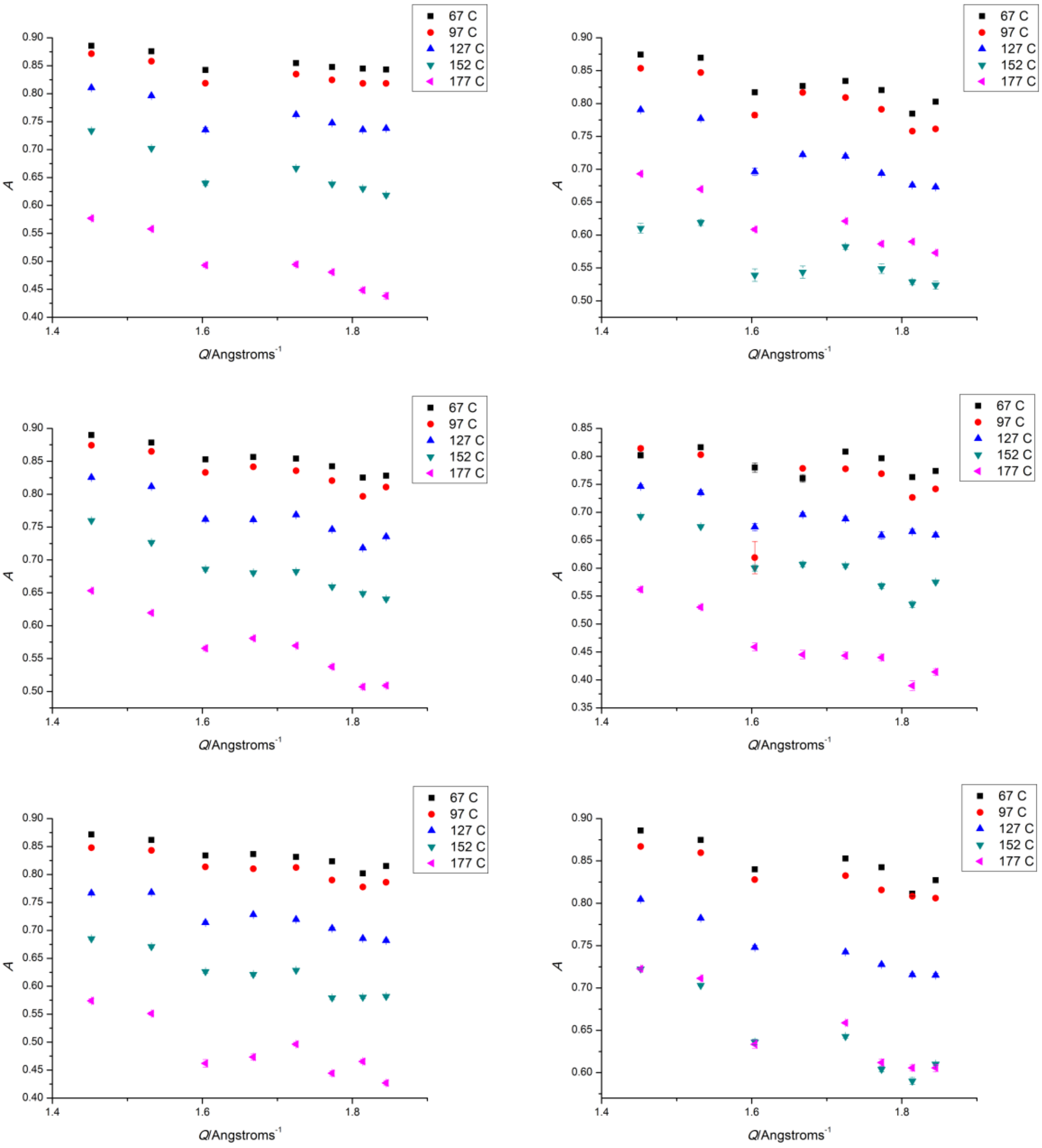

Figure 86: The KWW background parameter, *A*, *vs*. *Q* as a function of temperature for the h5 PS series of nanocomposites. Each plot corresponds to a different nanotube concentration: top row, left: 0 wt% SWCNTs; top row, right: 0.1 wt% SWCNTs; row two, left: 0.4 wt% SWCNTs; row two, right: 1 wt% SWCNTs; row three, left: 2 wt% SWCNTs; row three, right: 4 wt% SWCNTs.

The major exception to the temperature-dependence trend outlined earlier is the h5 PS nanocomposite with 0.1 wt% SWCNTs (Figure 86, top right), whose values of *A* at 152 °C consistently fall below those of the data recorded at 177 °C at all *Q*. While this anomalous result may be a characteristic of the particular sample, this seems rather counterintuitive and the result may in fact be attributed to the 177 °C data being recorded during a different experimental session to the 67–152 °C data, and the 67–152 °C datasets not having their own independent resolution file. For the other samples that did not have a resolution file associated with them, the first few points from the elastic scan were used to improvise a resolution file; for the h5 + 0.1 wt% sample, the elastic scan was recorded during the earlier experiment, so the first few points of the elastic scan from the h5 PS + 1 wt% SWCNTs sample were used, which may introduce an additional source of error that would be most apparent at low-*Q* and low-*T* where the dynamics are slow compared to the instrumental range, and is certainly plausible as the root of the anomalous behaviour exhibited by this sample.

The h5 PS + 4 wt% SWCNTs sample also displays an exception to the trend observed for the other samples: the *A* values extracted from the KWW fits at 152 and 177 °C are very similar for this sample, with the data recorded at 152 °C occasionally falling below that recorded at 177 °C. The cause of this anomaly is less apparent, as all data for this sample was recorded during a single experimental session, and with a dedicated resolution file, suggesting that this may be an effect characteristic of the material, rather than a consequence of an error in the experiment. However, this result is consistent with the SSF of the d5 PS + 4 wt% SWCNTs (corresponding to h3 PS + 4 wt%), where the data at 152 °C were almost identical to those at 177 °C; this did not occur for the sample composed of d3 PS + 4 wt% SWCNTs (which corresponds to the h5 PS + 4 wt% sample presented here). All the data presented so far suggest that the nanotubes have agglomerated at loading levels as high as 4 wt%; this agglomeration affects the amount of surface area available for the polymer chains to interact with, consistent with Weir *et al.*'s findings for graphene oxide/polymer nanocomposites,[190] and heating a sample is likely to change the distribution of the nanotubes in a sample as the nanotubes are mobile, and may lead to these structural and dynamic anomalies at the highest loading levels, as confirmed by SAXS (Figure 40).

It is of note that the *A* parameters extracted from the KWW fits shown in Figure 85 and Figure 86 generally display very low error values, indicating that there can be confidence in the fits of the KWW function to the $I(Q,t)$ curves. In addition, the small peaks and troughs in the data as a function of *Q* match well between samples, suggesting that the undulations in the data are characteristic of the samples. During a QENS experiment, both the coherent and incoherent contributions to the scattering are recorded, but through proton labelling the amount of coherent scattering, which provides information on the structure of the sample, is minimised, allowing us to focus on the incoherent scattering, which provides information on the dynamics within a sample. However, for polystyrene there is still a small *Q*-dependent coherent scattering contribution arising from the hydrogen, deuterium and carbon atoms in the sample that cannot be removed through selective labelling and forms a background that sits underneath the incoherent scattering (Table 33), and is described by the static structure factor; this is more significant for the h5 PS samples that probe ring motion. Here one of the data sets with the most pronounced step-wise shape in the plot of *A* *vs*. *Q* is examined in further detail to confirm whether this shape arises from a coherent background contribution.

Table 33: Coherent and incoherent scattering cross sections for polystyrene

Species	**Coherent scattering cross section[a]/1e–24 cm^2**	**Incoherent scattering cross section[a]/1e–24 cm^2**	**Proportion of scattering that is incoherent**
PS, $[C_8H_8]_n$	58.4624	642.088	91.7%
d3/h5 PS, $[C_8H_5D_3]_n$	69.9755	407.508	85.3%
d5/h3 PS, $[C_8H_3D_5]_n$	77.6429	251.068	76.4%

[a] Calculated using coherent and incoherent cross section values for individual atoms given on the NIST Centre for Neutron Research website.[162]

Figure 87 shows the KWW parameter *A* as a function of *Q* for h5 PS with 2 wt% SWCNTs at 177 °C (fitted with β = 0.61, the value of β obtained when averaging over the whole *Q* range for h3 PS, which provides a good fit in the regions where the characteristic peaks in the static structure factor occur), data that provides information on the incoherent scattering from the phenyl rings in the polymer. The plot is overlaid with the static structure factor for d5 PS, also with 2 wt% SWCNTs at 177 °C, which provides information on the small coherent contribution to the scattering from the phenyl rings in the polymer. The peaks and troughs in the fitted parameter *A* mirror those in the static structure factor, suggesting that there is a minor background from the coherent contribution.

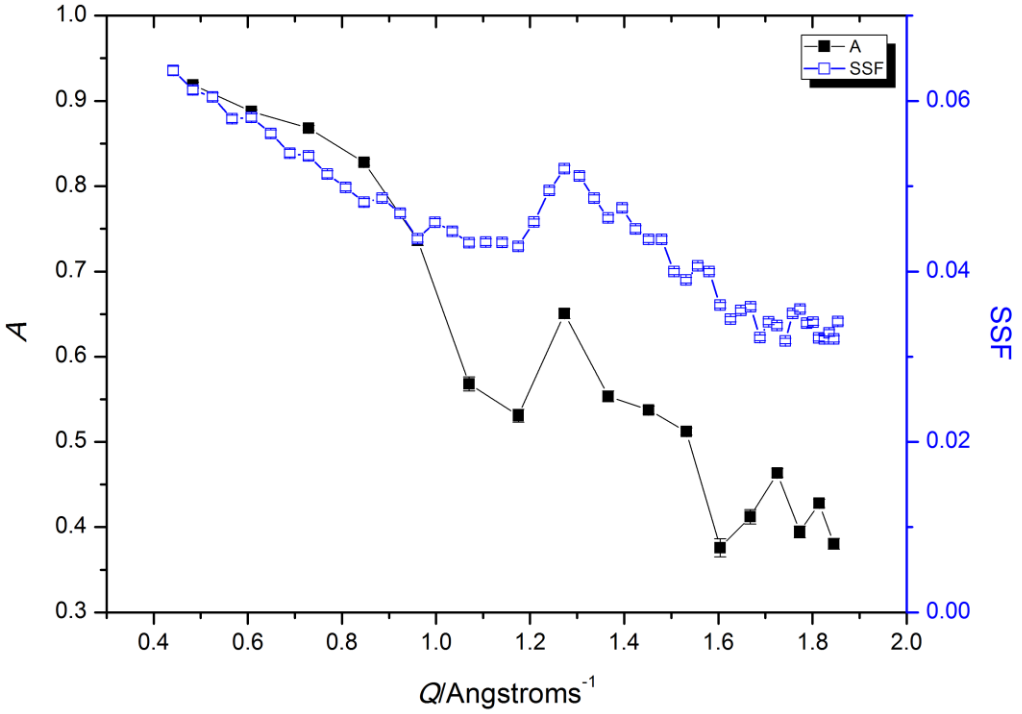

Figure 87: The KWW parameter A from h5 PS with 2 wt% SWCNTs, overlaid with the static structure factor from d5 PS with 2 wt% SWCNTs, both from data recorded at 177 °C. The lines joining the data points are provided as a guide to the eye.

Figure 88 overlays the incoherent scattering from the h3 PS sample incorporating 2 wt% SWCNTs at 177 °C with the static structure factor from the d3 PS sample containing 2 wt% SWCNTs. Again peaks and troughs from the SSF are echoed in the KWW parameter *A*, though not to the same extent as for the ring data shown in Figure 87.

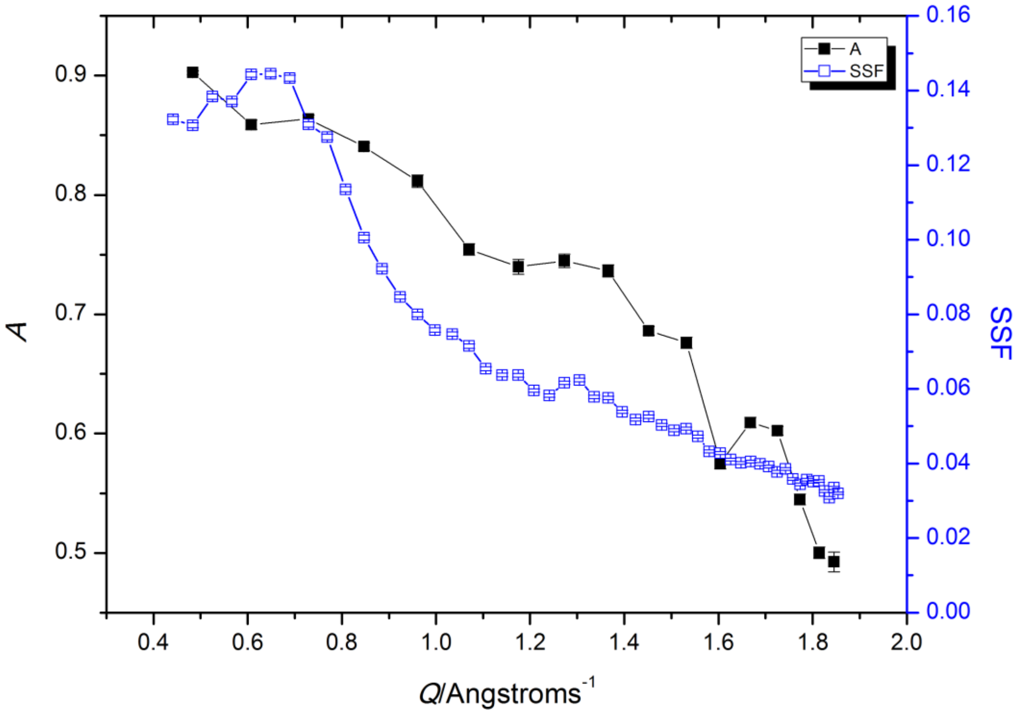

Figure 88: The KWW parameter A from h3 with 2 wt% SWCNTs, overlaid with the static structure factor from d3 PS with 2 wt% SWCNTs, both from data recorded at 177 °C. The lines joining the data points are provided as a guide to the eye.

4.4.5.3 Variation of τ_{KWW} with temperature

The parameter τ_{KWW} extracted from the KWW function measures the time scale of the motions the neutrons are interacting with. The τ_{KWW} values from fitting the KWW function to the $I(Q,t)$ curves from the h5 PS nanocomposites series are shown in Figure 89. The time resolution on IRIS at ISIS is 2–200 ps based on the energy range and resolution of the detectors.[175] Here the lower time limit of the resolution is taken as 4 ps (0.004 ns), to avoid experimental error; the lower time limit is indicated on each plot by a red horizontal line. On each plot (apart from the top right plot corresponding to 0.1 wt% SWCNTs) the only temperature for which all the τ_{KWW} values for a given sample are greater than the instrumental time resolution is 177 °C; this suggests that while the background parameter *A* extracted from the KWW fits provides some information about the amount of motion exhibited by the samples, the time scales of the motions are too close to the lower limit of the instrumental resolution for the time scale of the motion to be extracted on this instrument, with the motions appearing to be faster than the spectrometer is able to measure; this is counterintuitive, as it would generally be expected for motion to become faster with increasing temperature. The same is true for the data obtained for the h5 PS samples (Figure 90).

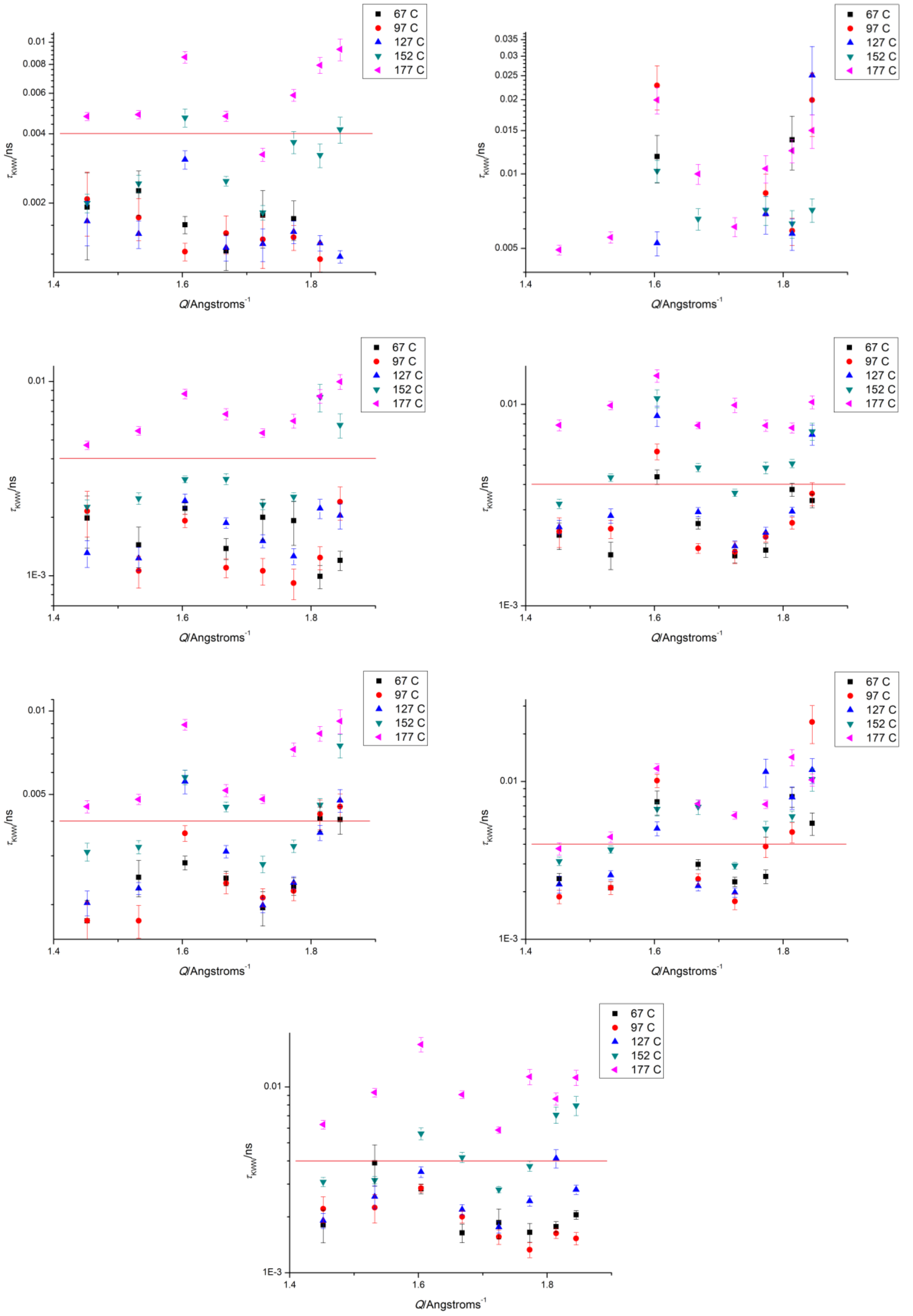

Figure 89: The KWW τ_{KWW} parameter, *vs*. *Q* as a function of temperature for the h3 PS series of nanocomposites. Each plot corresponds to a different nanotube concentration: top row, left: 0 wt% SWCNTs; top row, right: 0.1 wt% SWCNTs; row two, left: 0.4 wt% SWCNTs; row two, right: 1 wt% SWCNTs; row three, left: 2 wt% SWCNTs; row three, right: 3 wt% SWCNTs; bottom row: 4 wt% SWCNTs. The horizontal red line corresponds to the lower limit of the instrumental resolution.

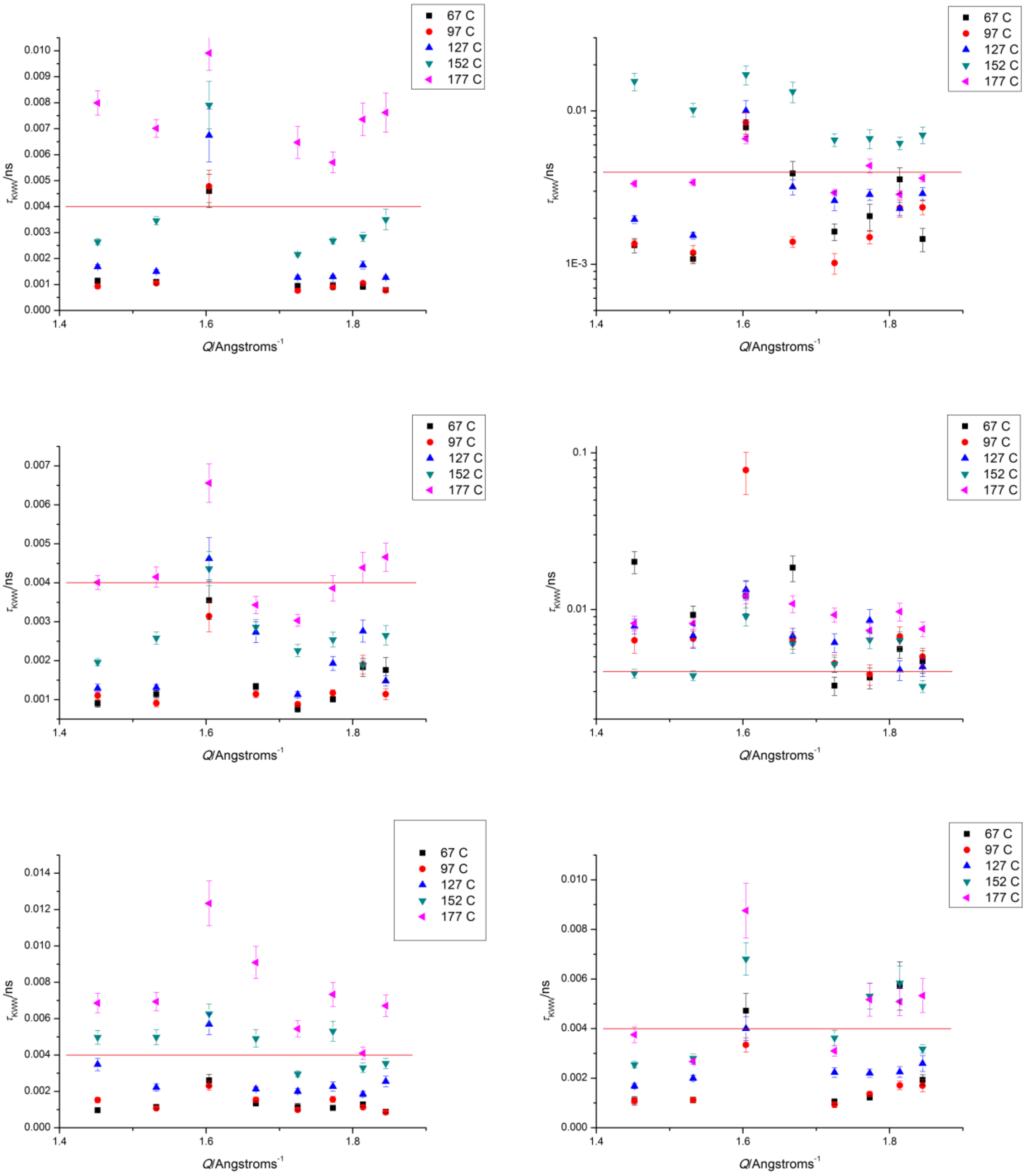

Figure 90: The KWW τ_{KWW} parameter, *vs.* Q as a function of temperature for the h5 PS series of nanocomposites. Each plot corresponds to a different nanotube concentration: top row, left: 0 wt% SWCNTs; top row, right: 0.1 wt% SWCNTs; middle row, left: 0.4 wt% SWCNTs; middle row, right: 1 wt% SWCNTs; bottom row, left: 2 wt% SWCNTs; bottom row, right: 4 wt% SWCNTs. The horizontal red line corresponds to the lower limit of the instrumental resolution.

The scattering data obtained for the h5 + 0.1 wt% SWCNTs sample at 177 °C falls below the instrumental resolution, suggesting that the hydrogen atoms in these samples are more mobile than the hydrogen atoms in the other samples. This is not confirmed by the mean squared displacement values extracted from the elastic scan of this sample, which indicates that the h5 + 0.1 wt% SWCNTs sample has $\langle u^2 \rangle$ values at the lower end of the spectrum. These anomalous values may be due to the improvised resolution file used for these data.

4.4.5.4 Variation of τ_{KWW} with concentration

Figure 91 and Figure 92 show τ_{KWW} *vs*. *Q* as a function of concentration for the h3 and h5 series of nanocomposites, respectively, at 177 °C. The h3 PS data provides information about the chain dynamics, while the h5 PS scattering corresponds to the ring dynamics. Comparing Figure 91 and Figure 92 indicates that the ring dynamics are faster than the chain motions, but in both cases the time scales of the motion at 177 °C are very close to the lower end of the time resolution of the instrument.

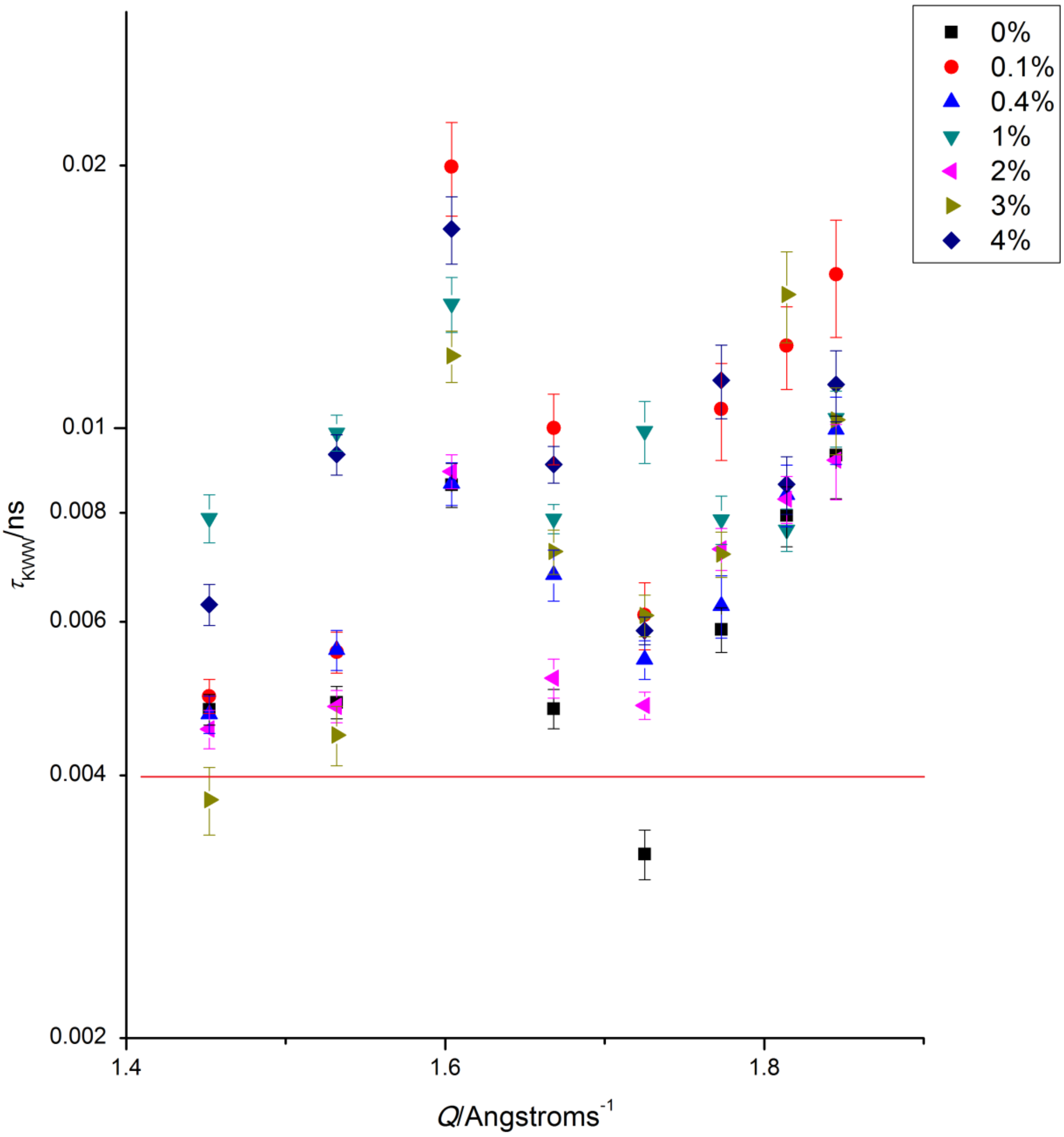

Figure 91: The KWW τ_{KWW} parameter, *vs*. *Q* as a function of concentration for the h3 PS series of nanocomposites at 177 °C. The red horizontal line indicates the lower limit of the instrumental resolution.

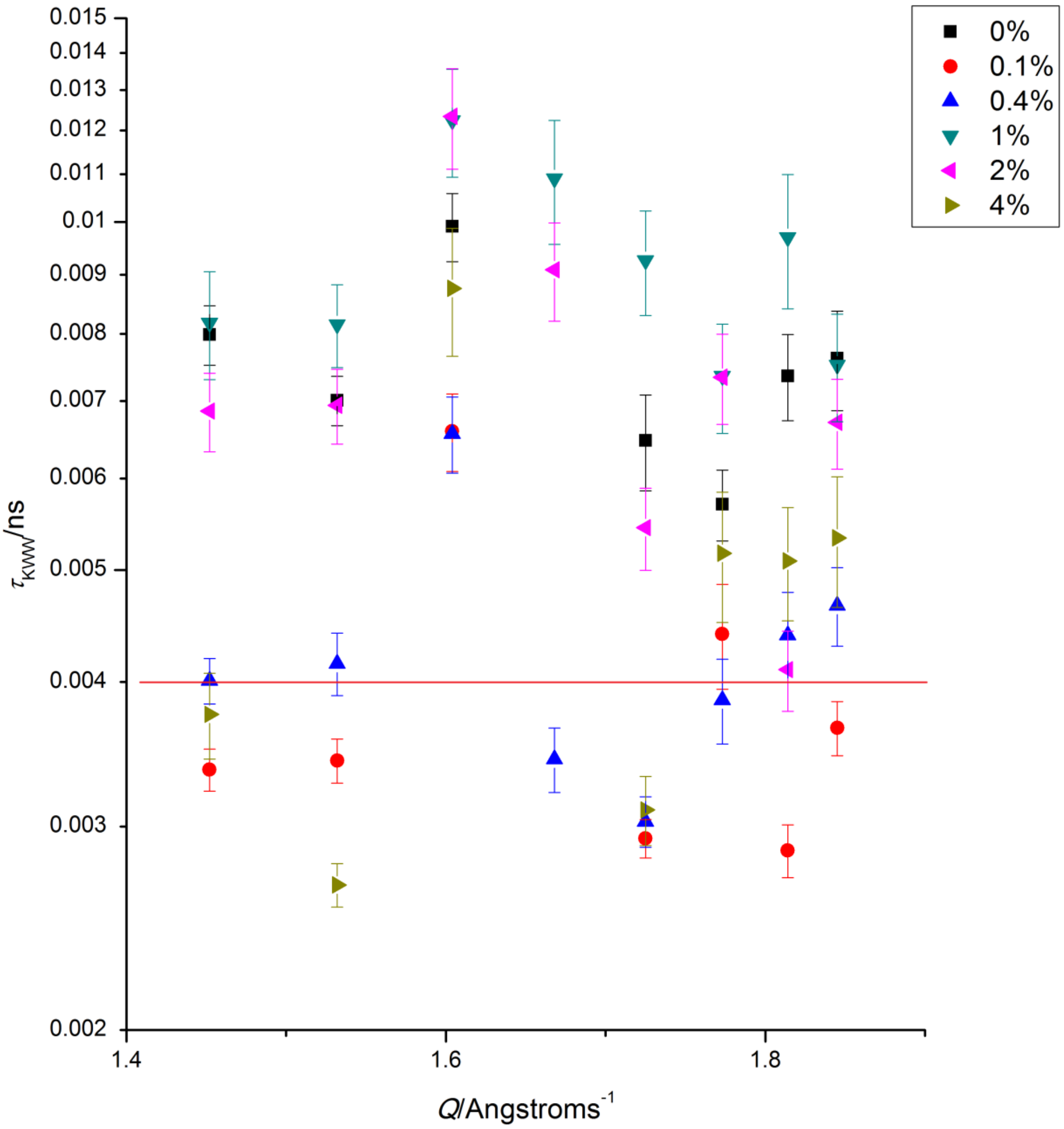

Figure 92: The KWW τ_{KWW} parameter, *vs.* Q as a function of concentration for the h5 PS series of nanocomposites at 177 °C. The red horizontal line indicates the lower limit of the instrumental resolution.

The τ_{KWW} values extracted from the chain scattering cover a time range from approximately 3.5 to 20 ps (Figure 91), and while it could be argued that the τ_{KWW} values of 0 and 2 wt% samples are lowest, and that those of the 1, 3 and 4 wt% samples are highest, overall there is no discernible trend in variation with concentration, within experimental error. The τ_{KWW} values for the ring hydrogenated samples fall between 3 and 12.5 ps (Figure 92), and again there is no consistent variation with concentration.

The observations in the previous paragraph lead to the conclusion that at the temperature for which meaningful values of τ_{KWW} can be extracted for the data recorded on IRIS at ISIS, adding SWCNTs to a PS matrix has no discernible effect on the relaxation times of the ring, while there is a marginal upward trend in τ_{KWW} with increasing Q for the chain data, except for the 1.6 Å data where A is anomalously low.

4.4.5.5 Relating S(Q,ω) to I(Q,t)

The fitting of KWW to the *I*(*Q*,*t*) curves indicated that the motions the system under examination were undergoing were not in the timeframe of the spectrometer. This is confirmed by comparing the *S*(*Q*,*ω*) curves for neat h5 PS to the resolution peak (Figure 93–Figure 97). Figure 93 compares the *S*(*Q*,*ω*) curves for neat h5 PS at 67 °C at four different *Q* values (*Q* = 0.48, 1.07, 1.53 and 1.77 $Å^{-1}$, corresponding to length scales of 13, 5.9, 4.1 and 3.5 Å, respectively). These curves a drop in intensity with increasing *Q*, but this drop is not accompanied by quasielastic broadening. The loss of intensity can be accounted for the by the motions being too fast for the spectrometer to pick up, so move from the elastic peak at very low *Q* to a flat background at higher *Q*. This scenario is exacerbated at 177 °C (Figure 94) as the nuclei have more thermal energy available than at 67 °C and the motions of the molecule are faster than at 67 °C [see also Figure 95 and Figure 97, which compare the *S*(*Q*,*ω*) peaks of h5 PS at a single Q value at 67 and 177 °C].

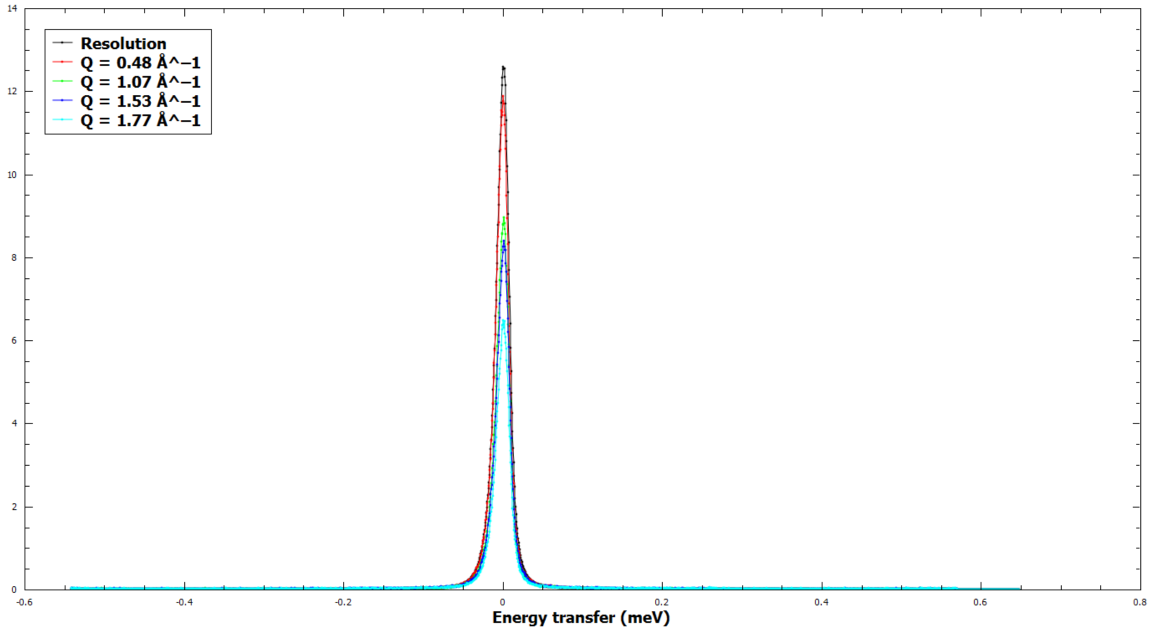

Figure 93: *S*(*Q*,*ω*) peaks for h5 PS with no SWCNTs at 67 °C for four different *Q*-values (details of the *Q*-values are given in the figure legend) compared to the resolution peak.

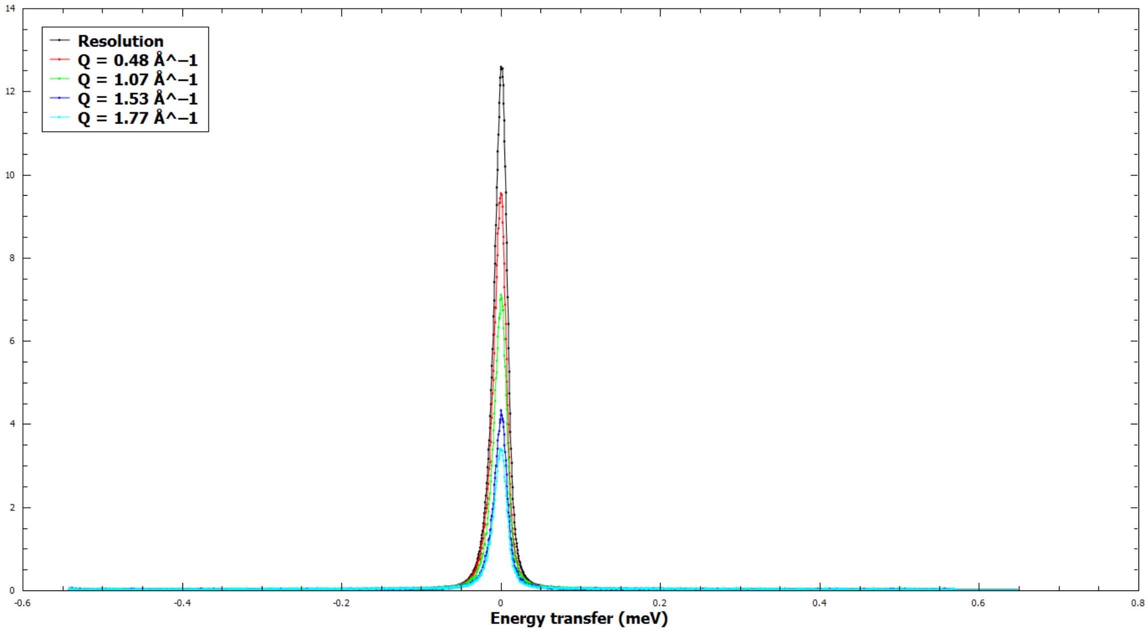

Figure 94: $S(Q,\omega)$ peaks for h5 PS with no SWCNTs at 177 °C for four different Q-values (details of the Q-values are given in the figure legend) compared to the resolution peak.

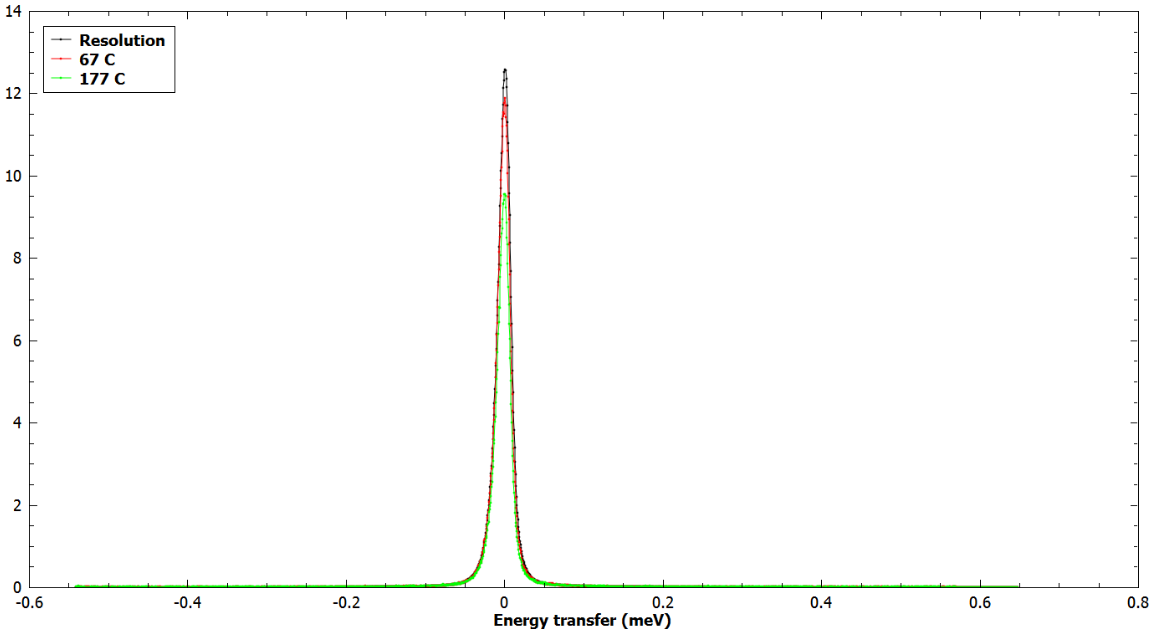

Figure 95: $S(Q,\omega)$ peaks for h5 PS with no SWCNTs at $Q = 0.48$ Å^{-1} at two temperatures (details of the temperatures are given in the figure legend) compared to the resolution peak.

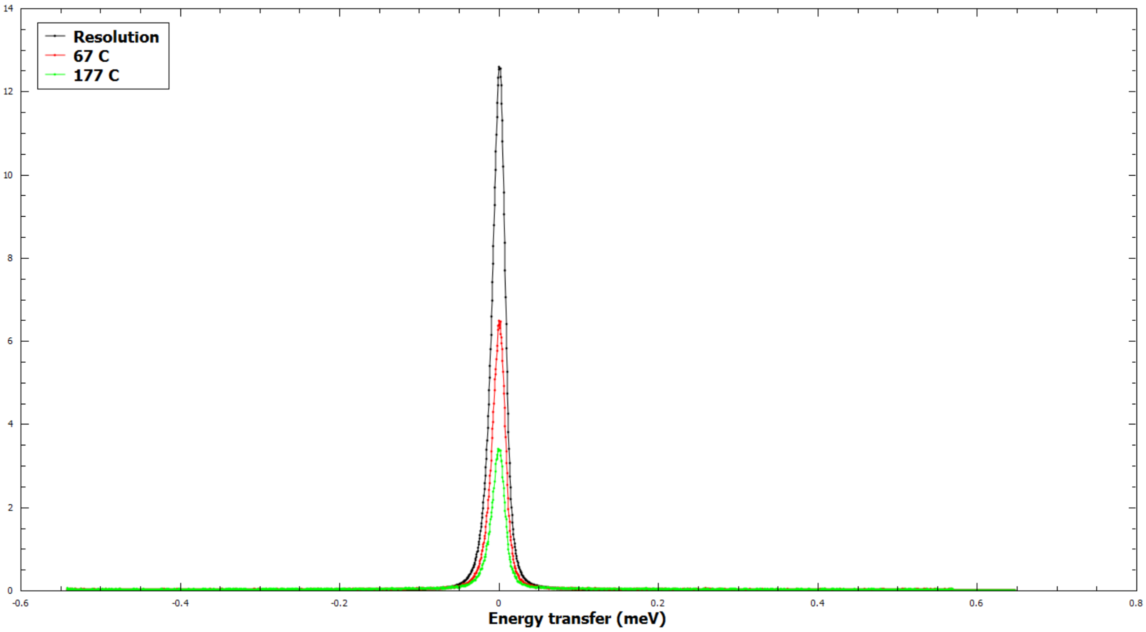

Figure 96: $S(Q,\omega)$ peaks for h5 PS with no SWCNTs at Q = 1.77 Å^{-1} at two temperatures (details of the temperatures are given in the figure legend) compared to the resolution peak.

Commensurate with the lack of broadening seen in the $S(Q,w)$ peaks, the $I(Q,t)$ curves decay very rapidly to the background level (Figure 97); indicating that most of the motion is occurring outside the measurement window.

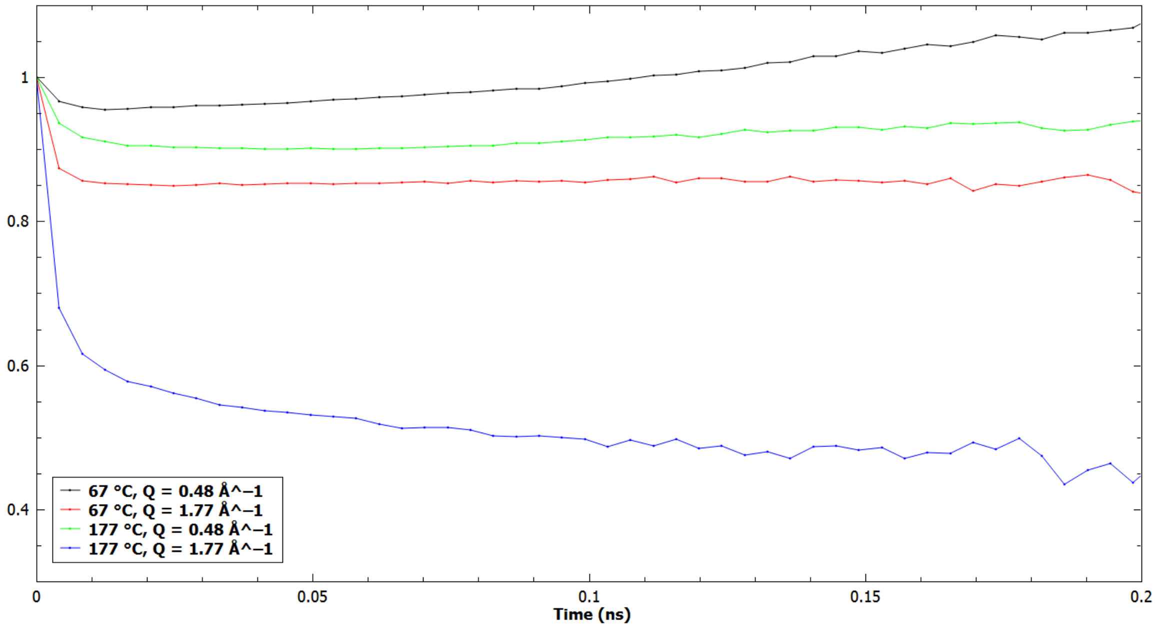

Figure 97: $I(Q,t)$ curves for h5 PS with no SWCNTs at two temperatures and two Q values. Black line: 67 °C, Q = 0.48 Å^{-1}; red line: 67 °C, Q = 1.77 Å^{-1}; green line: 177 °C, Q = 0.48 Å^{-1}; blue line: 177 °C, Q = 1.77 Å^{-1}.

Throughout the analysis presented in this chapter, the $I(Q,t)$ plots are shown with a data point at t = 0, $I(Q,t)$ = 1 (see, for example, Figure 97), this is an artefact from the Fourier transform and is inaccurate for the systems being studied. As outlined in 4.4.3 Fourier transform and Appendix 2: truncation times for $I(Q,t)$ data prior to KWW fitting, data were truncated prior to fitting, and in some cases, the KWW function was being fitted over only a very limited number of data points, leading to fitting that was not necessarily truly representative of the data set being fitted; this was exacerbated by including the data point at (0,1) as this data point falsely identifies a sharp drop in the curve that cannot be accounted for experimentally.

4.5 Conclusions

The work presented in this chapter clearly indicates that SWCNTs do influence the local, fast dynamics in PS/SWCNT nanocomposites. In addition the nanotubes have an effect on the static structure factor, indicating that they disrupt the local structure.

4.5.1 Short range dynamics

The elastic scan provided information about the local (d = 3.4–14 Å), fast dynamics in the nanocomposite system. This data clearly showed that the rings were more mobile than the chain in both the neat polymer and the nanocomposite, as expected. In terms of the chain, data obtained at both ISIS and NIST indicated that the addition of carbon nanotubes caused the polymer chains to become more mobile, exhibiting higher $\langle u^2 \rangle$ values, but only at concentrations greater than 1 wt%. This plasticisation of the polymer chains in nanocomposites has previously been observed in a PS/C_{60} nanocomposite by Sanz *et al*. who attributed the plasticisation to increased free volume in the nanocomposite arising from packing constraints introduced by the filler particles.[120] In the system presented here, the effect on the mean squared displacement is particularly pronounced in the region of the glass transition temperature.

The effect of nanotubes on $\langle u^2 \rangle$ values for the ring was less consistent, with no effect being seen in the data recorded at ISIS, but a clear increase in mean squared displacement on addition of 4 wt% SWCNTs for the data recorded at NIST. This could not be fully explained, but could arise from the different timescales of the two spectrometers, with HFBS at NIST probing slower motions than IRIS at ISIS, or may be due to the different thermal histories of the samples measured at the two beamlines.

This work isolated the ring and chain contributions to the polymer stiffness in PS/SWCNT nanocomposites for the first time. The stiffness data demonstrated reduced chain stiffness on addition of nanotubes to the PS, but had no discernible effect on the stiffness of the protons in the phenyl rings. Again, this plasticisation of the chain motion is consistent with Sanz *et al*.'s findings on PS/C_{60} nanocomposites, which examined the stiffness of the whole PS molecule.[120]

The QENS measurements and KWW fitting presented here indicated that, in this temperature region, the QENS data is outside the time-resolution of the instrument, therefore nothing can be extracted from the QENS data in this region, other than the proportion of material that is mobile or immobile in this time scale. However, this work did demonstrate that the KWW model is appropriate for this type of data, producing good fits with small error bars. It was also shown that it is appropriate in this case to use the same value of β for fitting both the ring and chain data.

In this work, no correction was made to the QENS data to compensate for the background arising from the static structure factor, however, comparing the static structure factor to the KWW parameter, A, *vs*. Q (Figure 87 and Figure 88) indicates that the KWW parameters clearly have a Q-dependent background that arises from the SSF of the PS. In addition, the SSF is also dependent on the concentration of nanotubes in the sample (Figure 44 and Figure 47). This could be an important consideration for future experiments.

4.5.2 Long range dynamics

4.5.2.1 Glass transition temperature

The neutron glass transition temperature, extracted from the plots of $\langle u^2 \rangle$ *vs*. T, suggest that the nanotubes may have some effect on the glass transition temperature of the composites, but the large error associated with these measurements made it hard to identify a discernible trend. The ring data recorded at ISIS identified an increase in T_g with increasing SWCNT concentration, but this change was not echoed in the data recorded on the same samples at NIST. The increase in T_g is not consistent with the nanotubes having no effect on the ring stiffness, unless it is taken into account that stiffness corresponds to very local motion, while the T_g corresponds to much larger, almost diffusive motions, and while these are related, they are different. Wong *et al*. found similar discrepancies between stiffness and T_g for PS with C_{60}.[125]

In contrast, the chain data recorded at NIST identified a decrease in T_g, but this was not found in the data recorded at ISIS. The reduction in T_g is consistent with the plasticisation effect identified by the chain stiffness both here and in Sanz *et al*.'s work on PS/C_{60} nanocomposites, however, these conflicting results suggest that the only chain motions slower than those that could be recorded on IRIS are affected by the addition of the nanotubes.

The calorimetric T_g, which corresponds to the energy required to mobilise long range, whole molecule motions, indicated a small minimum at around 1 wt% SWCNT loading. No difference was identified in the T_gs of the ring and chain-deuterated polymers, as expected as this technique does not differentiate between hydrogen and deuterium atoms.

4.5.2.2 Diffusion

This work was inspired by that of Mu *et al*.,[129, 130] who identified a minimum in the diffusion coefficient of a PS/CNT matrix at the percolation threshold; diffusion is related to the size of the matrix polymer chains and the relaxation time of the polymer *via* Equation 26. The work presented in Chapter 3, and the follow-up work conducted by Tung *et al*.,[86] identified that the presence of CNTs did not affect the polymer radius of gyration in the region of the minimum in the diffusion coefficient, suggesting that the minimum must instead have its origin in a change in the relaxation time of the matrix in the presence of the nanotubes. The work in this chapter indicates that while τ may be influenced by the presence of nanotubes, the precise nature of this change could not be identified. Fitting the $I(Q,t)$ data with the KWW model allowed relaxation times to be extracted from the QENS peaks recorded at 177 °C, but no discernible effect on the relaxation times of either the chain or the ring were identified.

That only relaxation times corresponding to motion at 177 °C could be resolved from the QENS measurements would indicate that the relaxation times for the lower temperature motions were too slow to be observed. Taking this into account, as well as the consideration that the plots of $\langle u^2 \rangle$ *vs*. T indicated that the primary differences in $\langle u^2 \rangle$ occurred at temperatures significantly lower than 177 °C, around the T_g, it would be worth considering conducting QENS on the samples at lower temperatures on a spectrometer with a slower time window, *e.g.* HFBS at NIST, which would allow the relaxation times of slower motions to be identified. This may shed further light on the origin of the minimum in the diffusion coefficient. It may also be using a lower molecular weight matrix for future experiments, as Mu *et al*. found that the minimum in the diffusion coefficient was more pronounced when tracers of lower molecular weights were used.[129]

4.5.3 Structure

In Chapter 4 it has been confirmed that the neutron static structure factor is analogous to the XRD, identifying both a low-Q polymerisation peak and a high-Q amorphous peak. This work has also identified that adding carbon nanotubes affects the intensities of the peaks at loading levels of between 0.1 and 3 wt%. The effect is more pronounced for the chain than the ring, which has been attributed to the size-incompatibility between the gap between phenyl rings and the size of the nanotube bundles.

4.5.4 Aggregation effects

One critical factor that has been identified through the static structure factor and small angle X-ray scattering is that there may be agglomeration occurring in the samples at concentrations greater than 1 wt%. At concentrations beyond this level the SSF amorphous and polymerisation peaks start to return to bulk values, and if it is assumed that the extent of property alteration is dictated by the surface area of the nanoparticle that is available for the polymer to interact with, a decrease in material properties with increasing nanoparticle concentration would indicate that the nanoparticle/polymer interface is becoming smaller rather than larger at greater loadings. This agglomeration effect is confirmed by the small angle X-ray scattering data collected on the samples, which indicates a fundamental change in dispersion at loading levels greater than 1 wt%. The dispersion issue is critical to optimising the properties of carbon nanotube nanocomposites, as has been widely cited in the literature,[2, 6, 7, 38] and is confirmed here. It is also worth noting that the diffusion experiments conducted by Mu *et al*. were carried out over annealing times that are large compared to the reptation time, since in the diffusion experiments the polymer had to diffuse a distance large compared to its own dimensions, therefore it is likely that the nanotubes underwent realignment during this diffusion process as well as in the experiments presented here.

Chapter 5: Conclusions

In 2009, Mu *et al*. published two papers regarding the diffusion of PS into a PS/CNT matrix, and identified that the diffusion coefficient exhibited a minimum at the percolation threshold.[129, 130] As the diffusion coefficient has contributions from both the size and relaxation time of the polymer chains in a system (Equation 26), this thesis has attempted to provide an explanation for this minimum, using small angle neutron scattering and quasielastic neutron scattering to investigate both the local structure and local dynamics in a series of PS/SWCNT nanocomposites.

SANS data were collected on 20 samples across two molecular weights, 110 kg mol^{-1} and 230 kg mol^{-1}, with SWCNT concentrations between 0 and 4 wt%. All data sets were fitted successfully with the Zimm and Debye equations (and Equation 32, respectively) to extract the polymer R_g. The Debye equation returned R_g values that were a good match with those reported in the literature for neat PS matrices of the appropriate molecular weights, while the Zimm fits had larger error bars and returned higher R_g values.

The R_g values were found to increase with CNT concentration by up to ~450% for the 110k PS series of samples, and by up to ~500% for the 230k PS nanocomposites. These values are significantly higher than those reported for comparable systems containing spherical nanoparticles, and calculating the energy cost of such stretching at 4.5 k_BT and 5 k_BT, respectively,[170] suggests that such a large increase in polymer R_g may be accounted for if the system has undergone agglomeration. Alternatively, the nanotubes may have been scattering in addition to the labelled chains in the polymer matrix, as the system was not contrast-matched.[53, 54, 68, 69] This result laid the foundation for Tung *et al.*'s 2013 work,[86] which found that at SWCNT concentrations greater than 2 wt% and when $R_{SWCNT}/R_g \approx 0.4$ the polymer R_g increased with increasing SWCNT concentration relative to that of the bulk, and at 10 wt% the increase in R_g was 36%.

While Tung *et al.*'s work resolved the question of whether nanotubes affected the polymer radius of gyration, the paper did not provide an explanation for the minimum in the diffusion coefficient, instead indicating that the minimum must have its origin in the dynamics of the nanocomposite system. In order to examine the small scale dynamics of the nanocomposite, quasielastic neutron scattering was conducted on samples in which the chain and ring had been labelled using selective deuteration/hydrogenation. The elastic scan data indicated that the rings were more mobile than the chain in both the polymer and the nanocomposite. Data recorded on IRIS at ISIS (2–200 ps) and HFBS at NIST (100 ps–10 ns) both indicated that adding nanotubes increased the mobility of the chain, but only at concentrations above 1 wt%, *i.e.* plasticisation. This effect was particularly pronounced at temperatures in the region of the T_g. The effect of the nanotubes on the mobility of the ring was less consistent, with no effect being found in the data recorded on

IRIS, but the slower motions recorded on HFBS indicated a clear increase in $\langle u^2 \rangle$ at a nanotube loading of 4 wt%.

The polymeric stiffness values extracted from the plots of $\langle u^2 \rangle$ *vs*. *T* isolated the ring and chain for the first time. The data indicated reduced chain stiffness on addition of SWCNTs, but no effect on the stiffness of the PS phenyl rings.

The QENS peaks recorded on IRIS at ISIS were Fourier transformed and the resultant $I(Q,t)$ *vs*. *t* curves were fitted successfully with the KWW function (Equation 40). While the fitting was successful, providing a useful indication of the proportion of material that is mobile or immobile within the timescale under investigation, only the data recorded at 177 °C returned τ_{KWW} values that fell within the instrumental resolution, suggesting that for the other temperatures investigated, the motions were too slow for meaningful relaxation times to be extracted. It was also noted that the KWW parameters extracted exhibited a clear *Q*-dependent background arising from the static structure factor. This may be an important consideration in future experiments.

The neutron T_g values, extracted from the plots of $\langle u^2 \rangle$ *vs*. *T* displayed different behaviour depending on which part of the molecule was labelled, and which spectrometer was used to record the data. The ring data recorded on IRIS showed an increase in T_g with increasing CNT concentration, while that recorded on HFBS was unchanged. The chain-labelled samples displayed a reduction in T_g when recorded on HFBS, but no change in the data from IRIS. This indicates that the faster ring motion is better captured on IRIS, while the slower chain motion is better captured by the slower time window of HFBS. These results suggest that the chains and rings are differently affected by the presence of nanotubes.

The calorimetric T_g obtained *via* DSC indicated a small minimum at ~1 wt% SWCNT loading. This indicates an earlier onset of motion around the percolation threshold, which would be expected to translate into faster diffusion at this concentration at slightly higher temperatures, however, this is contrary to the minimum in the diffusion coefficient, which indicates a slowing down in motion at the percolation threshold.

In addition to extract dynamic data from the QENS peaks, the static structure factor was obtained, and was confirmed to be analogous to the XRD SSF, with both a low-*Q* polymerisation peak and a high-*Q* amorphous peak. Adding nanotubes to the system affected the intensities of the peaks at loading levels between 0.1 and 3 wt%, with the effect being more pronounced for the chain than the ring.

Several of the results in this thesis indicate that agglomeration may have occurred in the samples at concentrations greater than 1 wt% SWCNTs. Dispersion of the nanoparticles is critical, as adding nanoparticles affect the polymer properties by introducing CNT/polymer interfaces. In systems where agglomeration has occurred, the surface area is not maximised, and the interfacial area decreases with increasing loading.

The dynamic results presented in this thesis clearly indicate the addition of nanoparticles to the polymer matrix affect the fast local dynamics, and disrupt the local structure. However, the work failed to identify the specific cause of the minimum in the diffusion coefficient as the motion of interest was too slow to be recorded in the QENS peaks recorded on IRIS. It would be interesting to repeat the dynamic experiments on a QENS spectrometer with a slower time window, *e.g.* HFBS, and see whether a wider range of relaxation times could be identified. It may also be worth using a lower molecular weight matrix for future experiments, as Mu *et al*. found that the minimum in the diffusion coefficient was more pronounced when tracers of lower molecular weights were used; this may make any trends easier to identify.[129]

In addition, this work identified issues with agglomeration at higher nanoparticle loadings. Therefore, prior to conducting any further dynamic studies, work should be conducted to improve the dispersion of the nanotubes in the matrix.

Appendices

Appendix 1: SANS 2D detector images

110 kg mol^{-1} samples

The SANS 2D detector images for the 110 kg mol^{-1} samples with 0–4 wt% SWCNTs are shown in Figure 36–Figure 37.

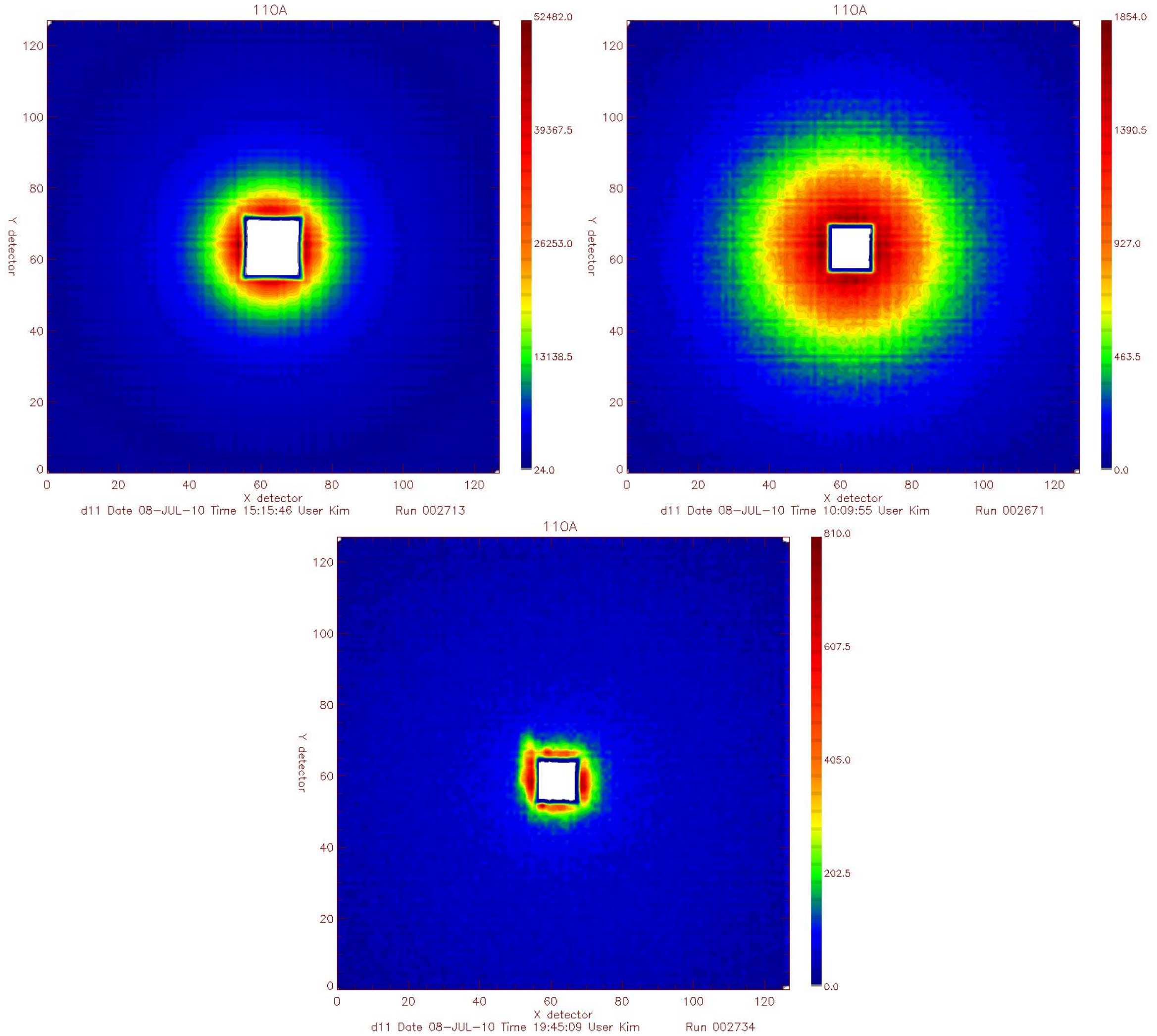

Figure 98: 2D SANS detector images for 110A (110 kg mol^{-1} with 0 wt% SWCNTs). Sample–detector distances: top left: 1.50 m; top right: 8.00 m; bottom: 39.0 m.

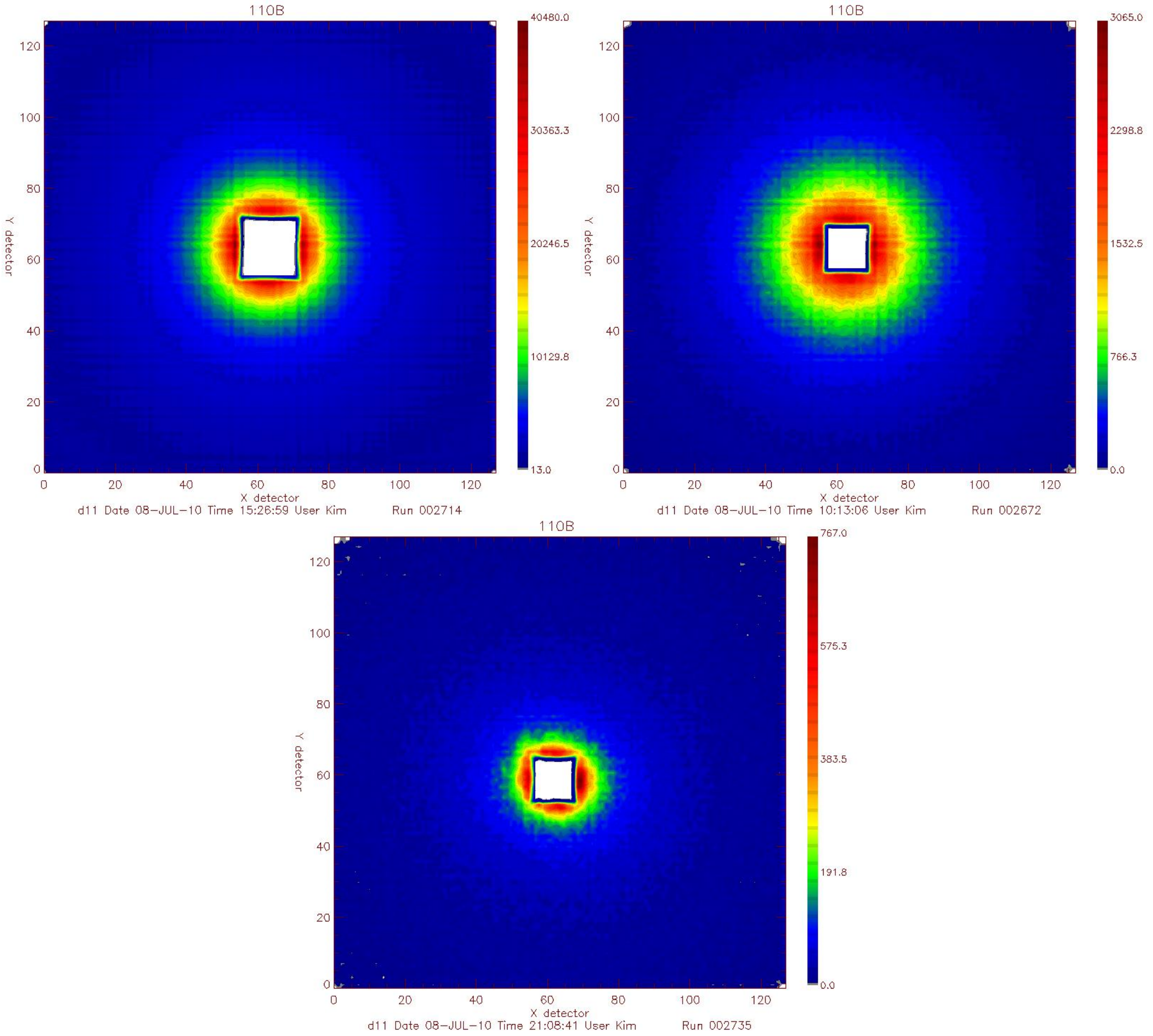

Figure 99: 2D SANS detector images for 110B (110 kg mol^{-1} with 0.5 wt% SWCNTs). Sample–detector distances: top left: 1.50 m; top right: 8.00 m; bottom: 39.0 m.

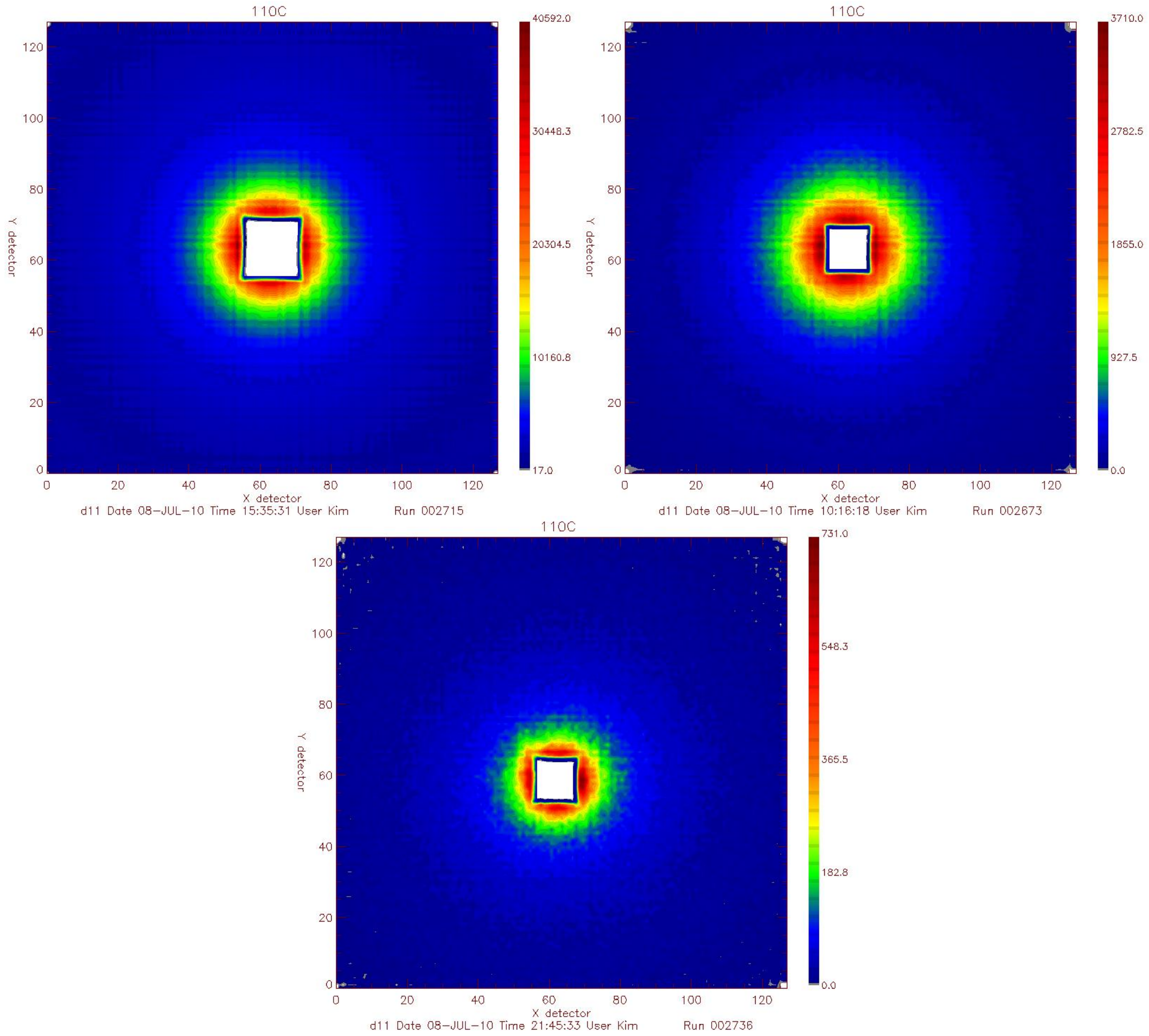

Figure 100: 2D SANS detector images for 110C (110 kg mol^{-1} with 1 wt% SWCNTs). Sample–detector distances: top left: 1.50 m; top right: 8.00 m; bottom: 39.0 m.

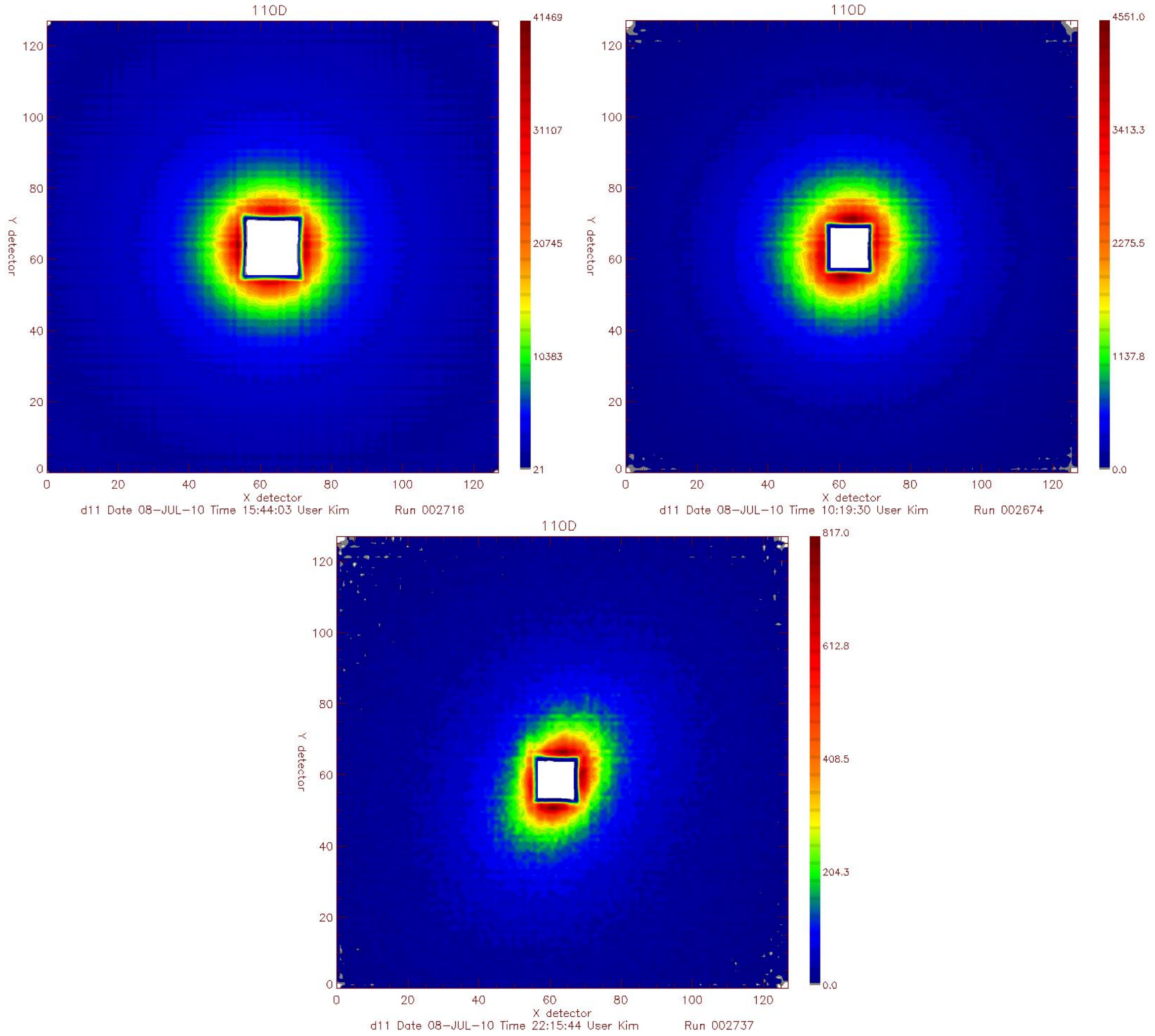

Figure 101: 2D SANS detector images for 110D (110 kg mol^{-1} with 1.5 wt% SWCNTs). Sample–detector distances: top left: 1.50 m; top right: 8.00 m; bottom: 39.0 m.

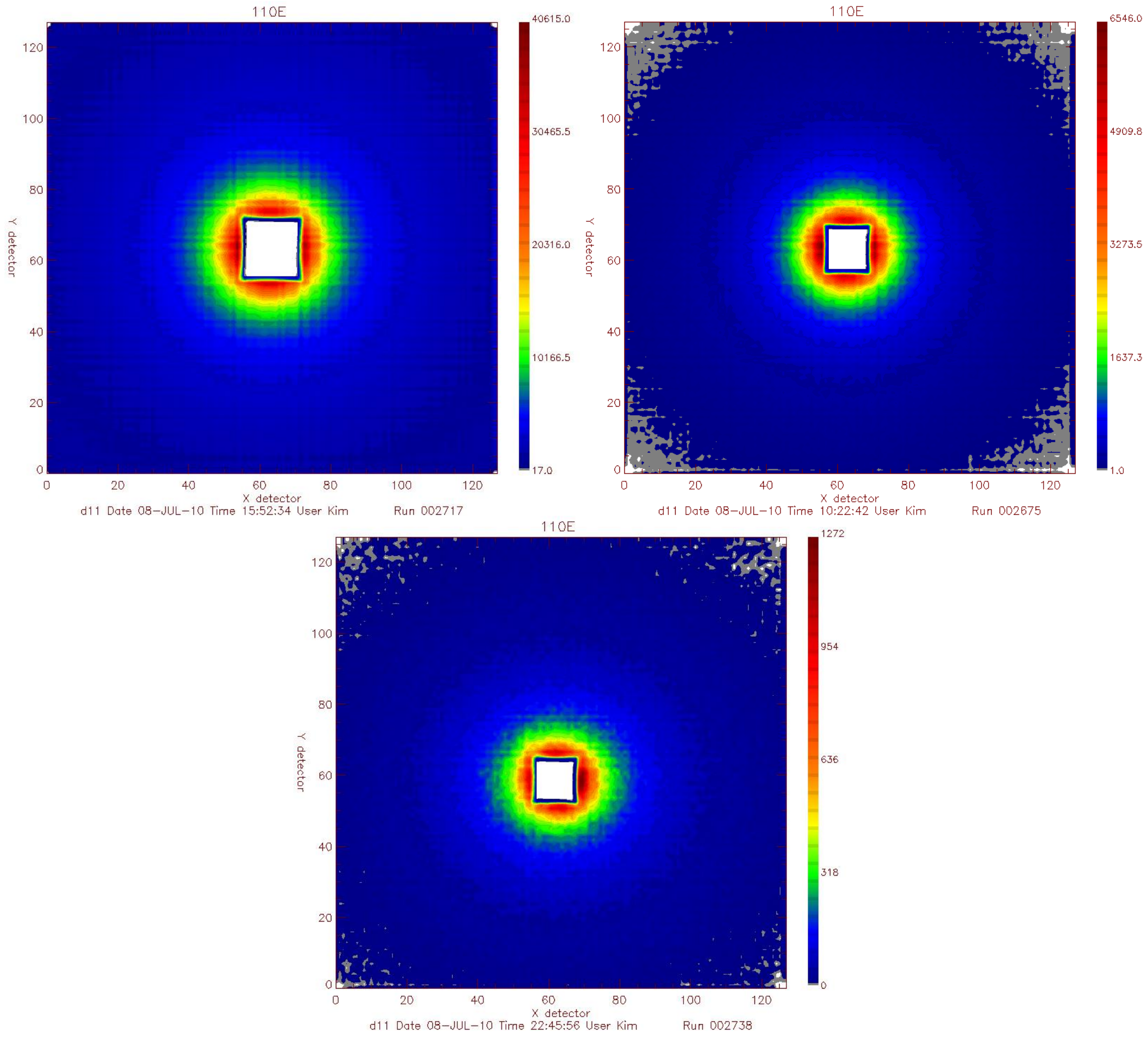

Figure 102: 2D SANS detector images for 110E (110 kg mol^{-1} with 2 wt% SWCNTs). Sample–detector distances: top left: 1.50 m; top right: 8.00 m; bottom: 39.0 m.

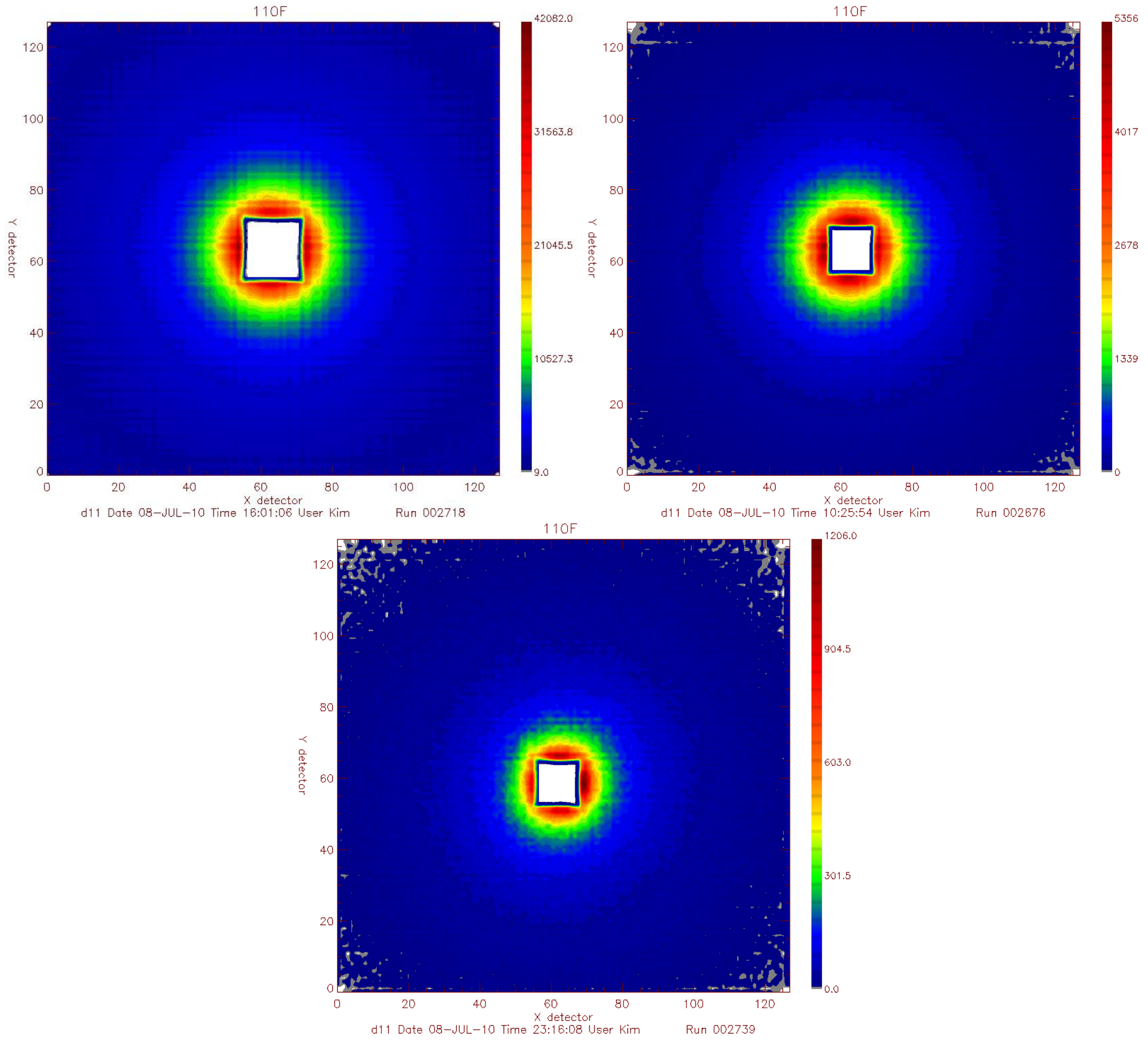

Figure 103: 2D SANS detector images for 110F (110 kg mol^{-1} with 2.5 wt% SWCNTs). Sample–detector distances: top left: 1.50 m; top right: 8.00 m; bottom: 39.0 m.

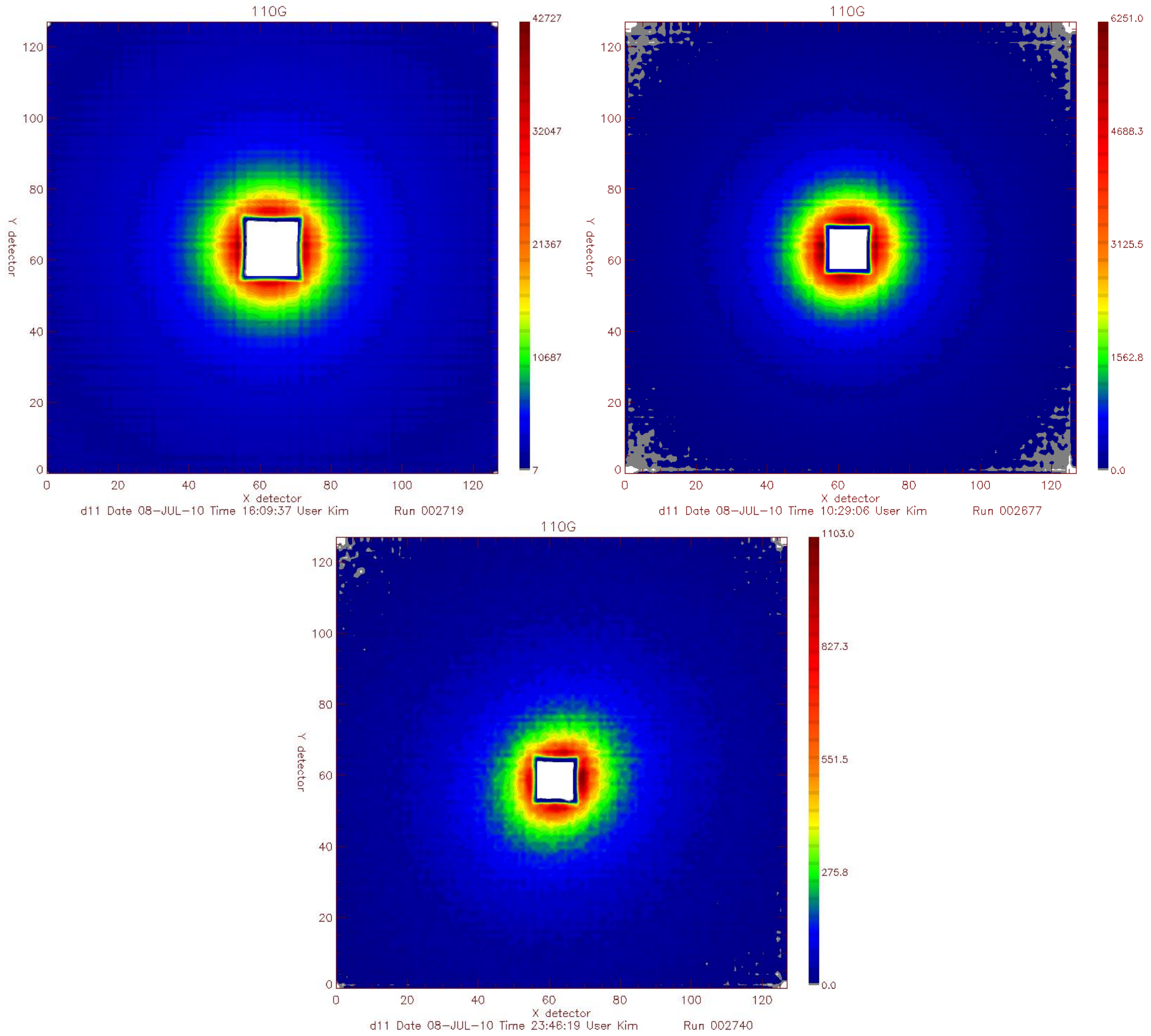

Figure 104: 2D SANS detector images for 110G (110 kg mol^{-1} with 3 wt% SWCNTs). Sample–detector distances: top left: 1.50 m; top right: 8.00 m; bottom: 39.0 m.

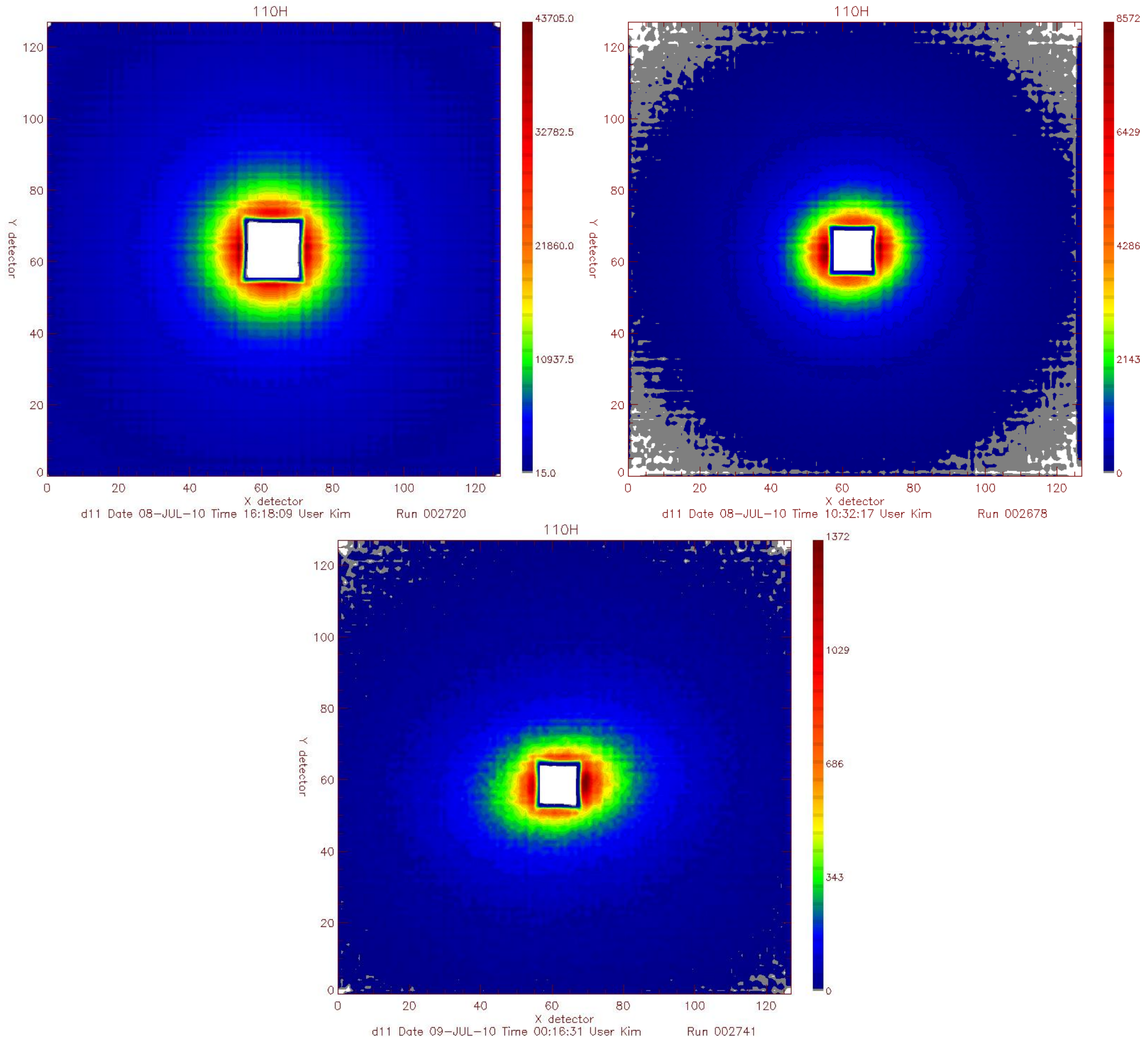

Figure 105: 2D SANS detector images for 110H (110 kg mol^{-1} with 3.5 wt% SWCNTs). Sample–detector distances: top left: 1.50 m; top right: 8.00 m; bottom: 39.0 m.

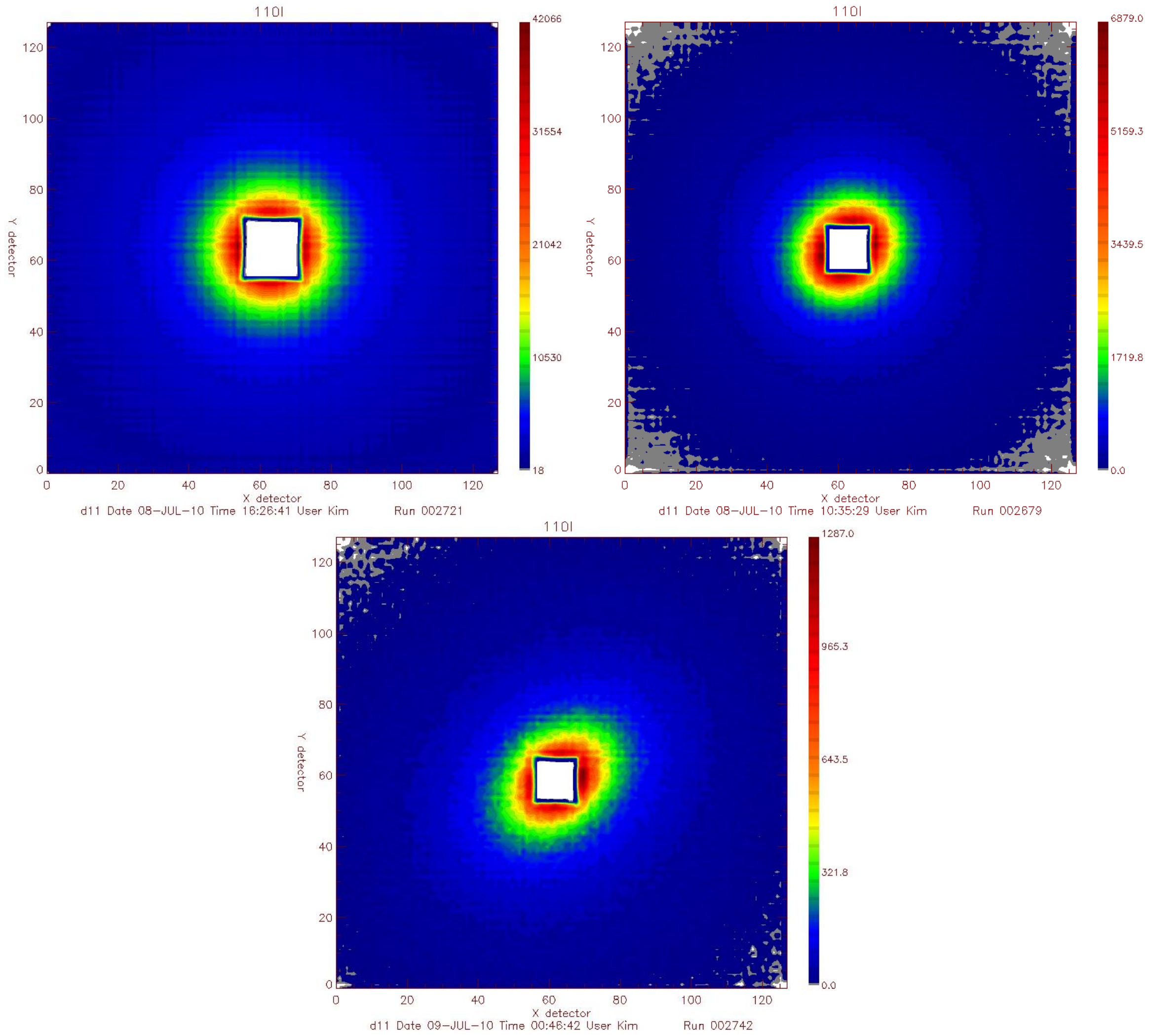

Figure 106: 2D SANS detector images for 110I (110 kg mol^{-1} with 4 wt% SWCNTs). Sample–detector distances: top left: 1.50 m; top right: 8.00 m; bottom: 39.0 m.

230 kg mol⁻¹ samples

The SANS 2D detector images for the 230 kg mol^{-1} samples with 0–4 wt% SWCNTs are shown in Figure 38–Figure 113.

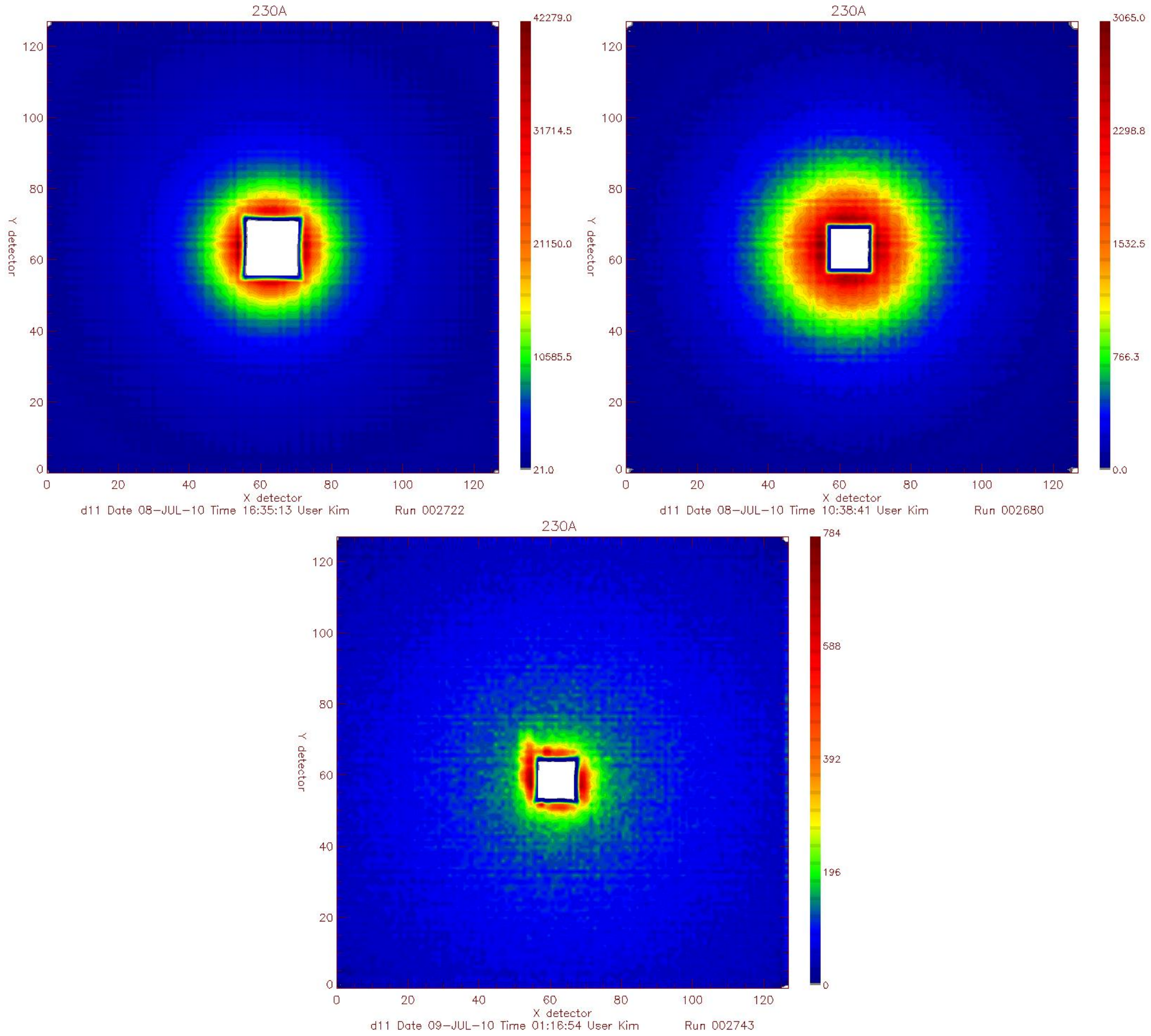

Figure 107: 2D SANS detector images for 230A (230 kg mol^{-1} with 0 wt% SWCNTs). Sample–detector distances: top left: 1.50 m; top right: 8.00 m; bottom: 39.0 m.

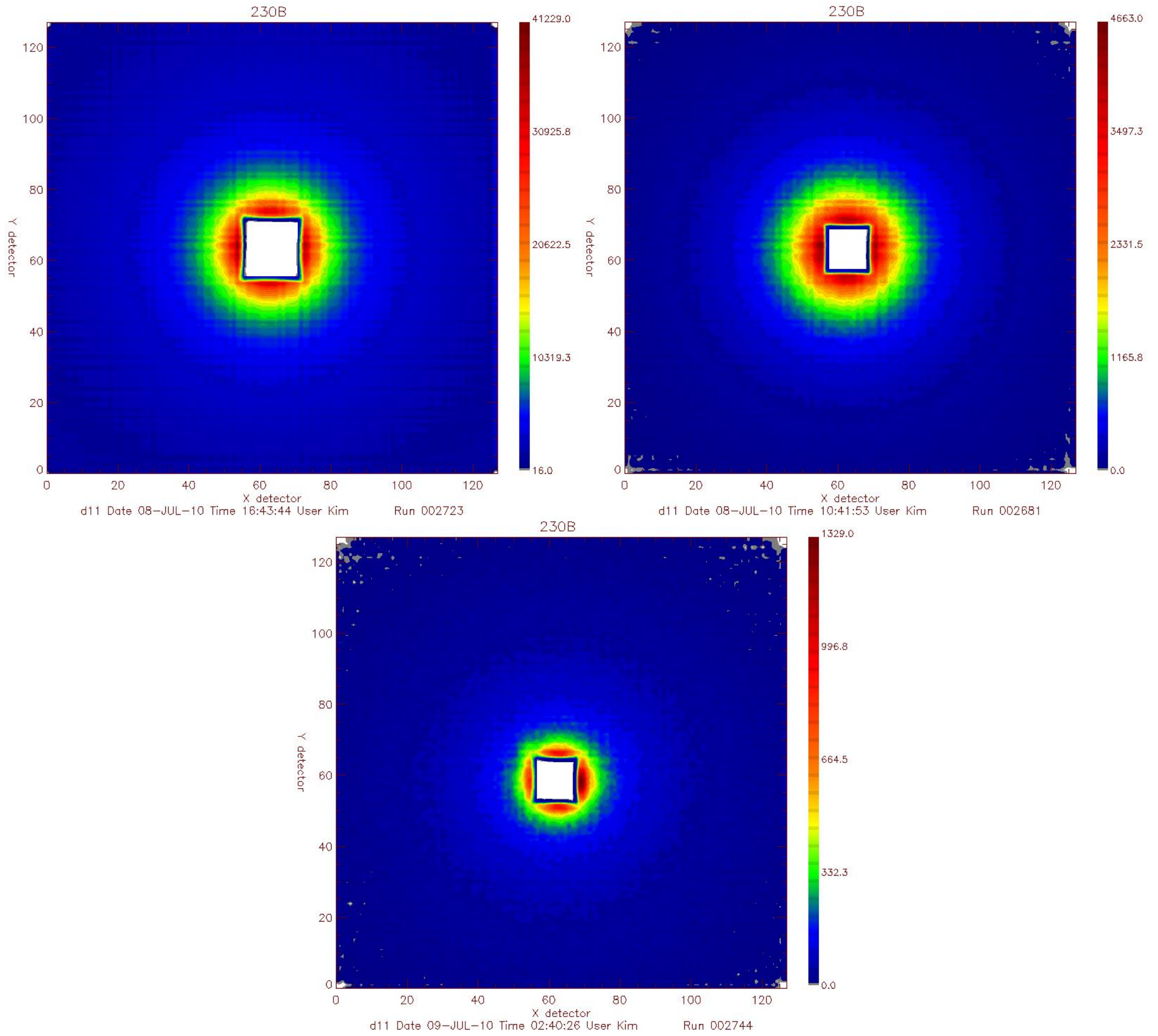

Figure 108: 2D SANS detector images for 230B (230 kg mol^{-1} with 0.5 wt% SWCNTs). Sample–detector distances: top left: 1.50 m; top right: 8.00 m; bottom: 39.0 m.

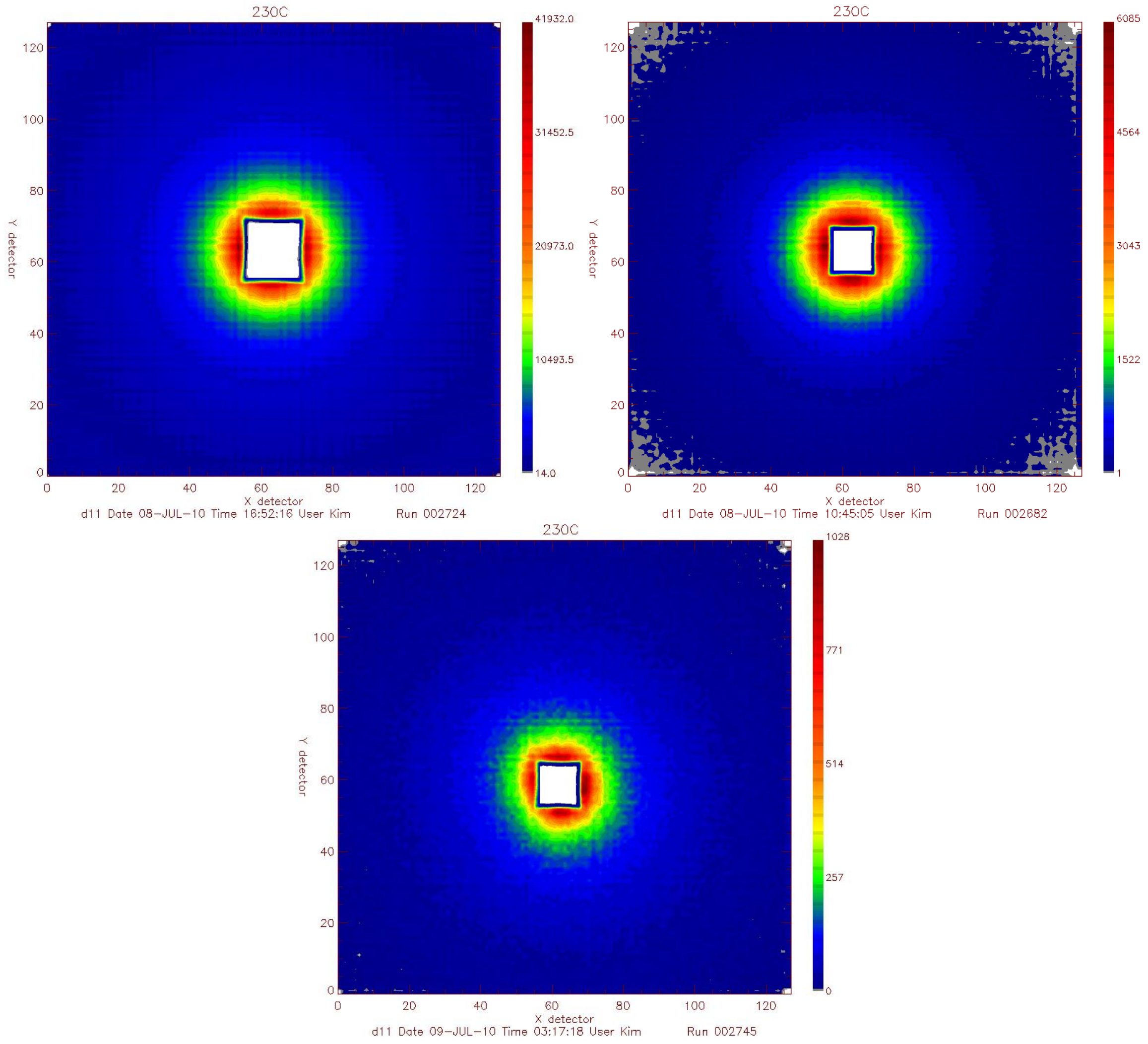

Figure 109: 2D SANS detector images for 230C (230 kg mol^{-1} with 1 wt% SWCNTs). Sample–detector distances: top left: 1.50 m; top right: 8.00 m; bottom: 39.0 m.

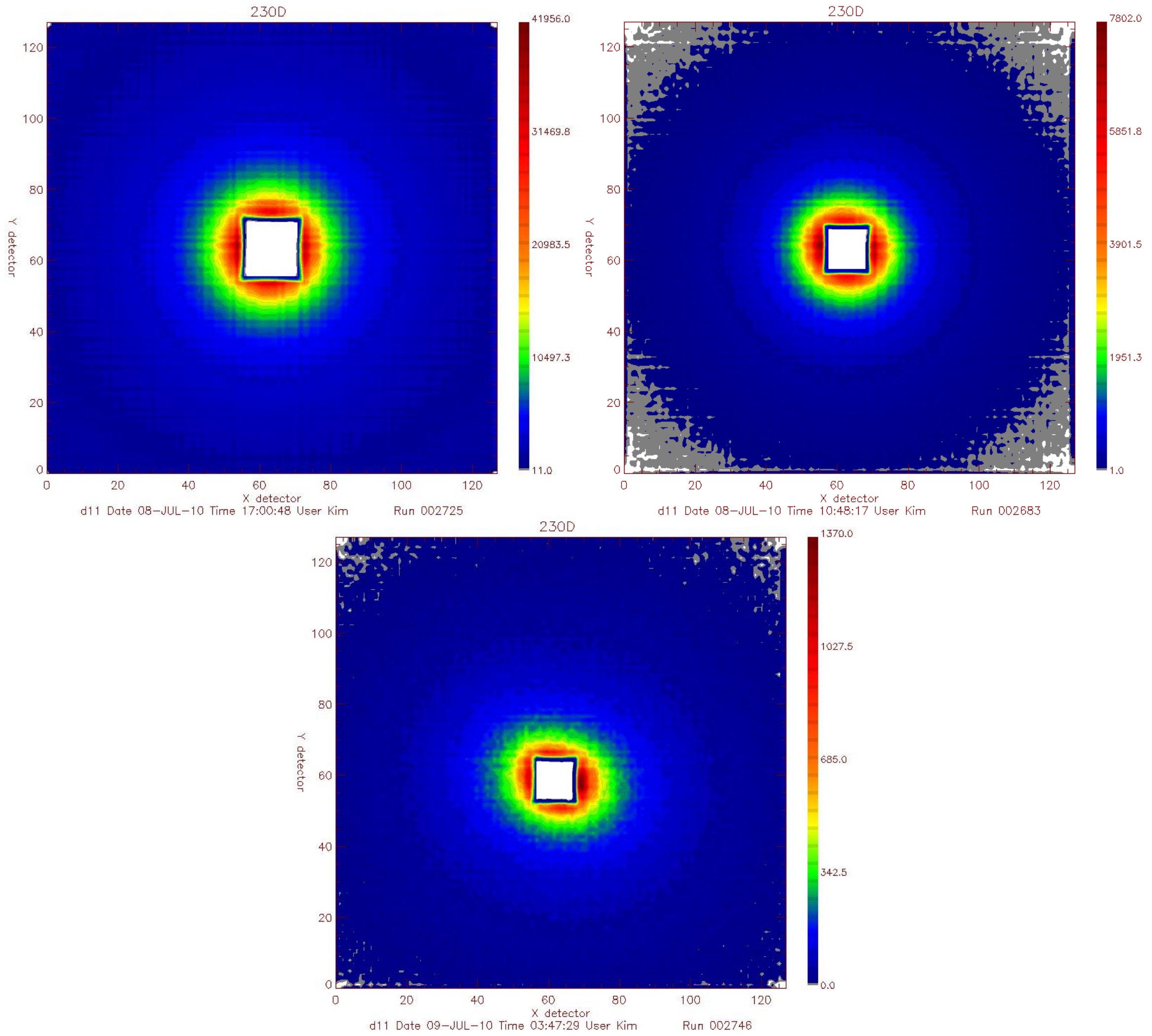

Figure 110: 2D SANS detector images for 230D (230 kg mol^{-1} with 1.5 wt% SWCNTs). Sample–detector distances: top left: 1.50 m; top right: 8.00 m; bottom: 39.0 m.

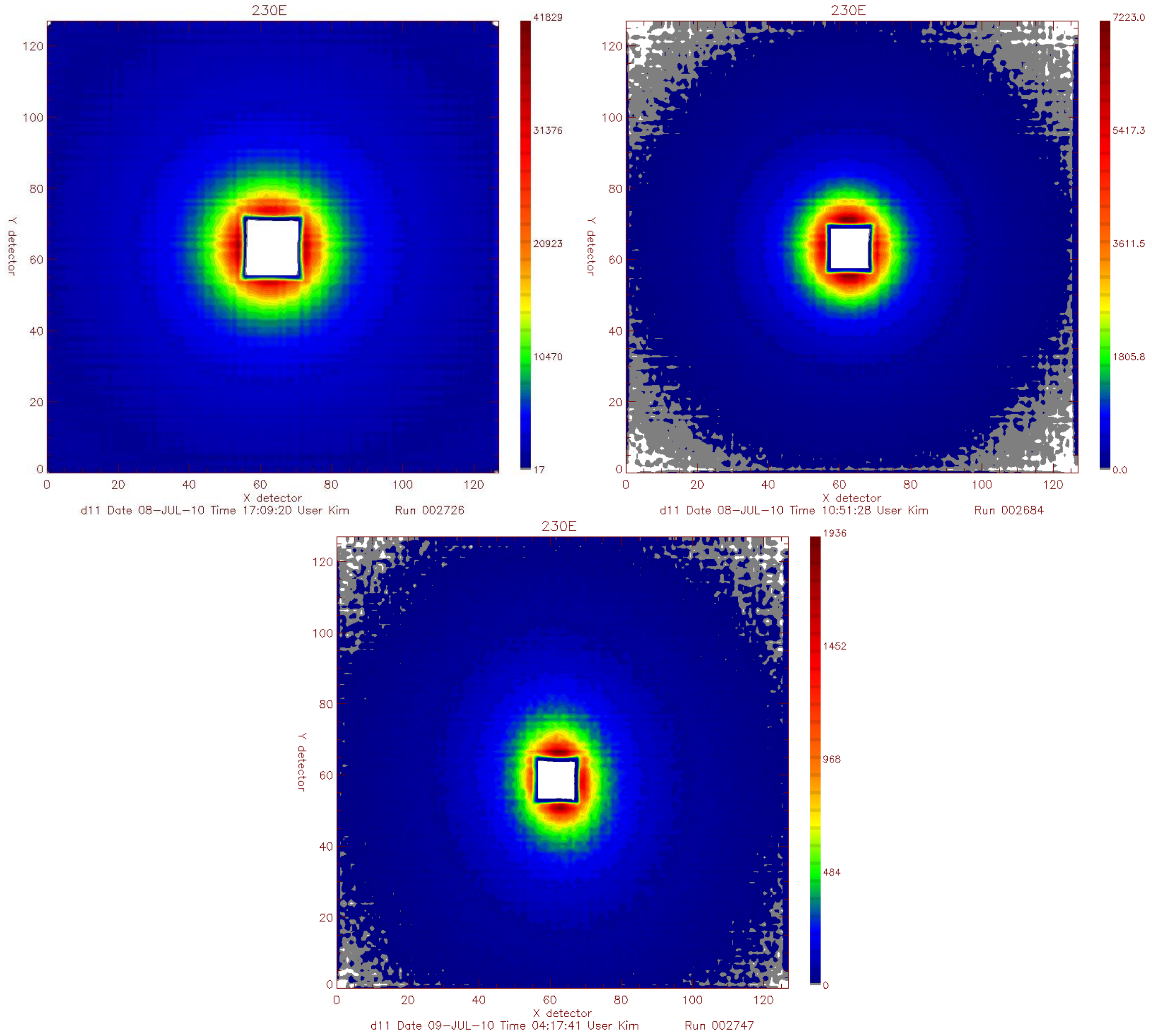
230E

230E

230E

Figure 111: 2D SANS detector images for 230E (230 kg mol^{-1} with 2 wt% SWCNTs). Sample–detector distances: top left: 1.50 m; top right: 8.00 m; bottom: 39.0 m.

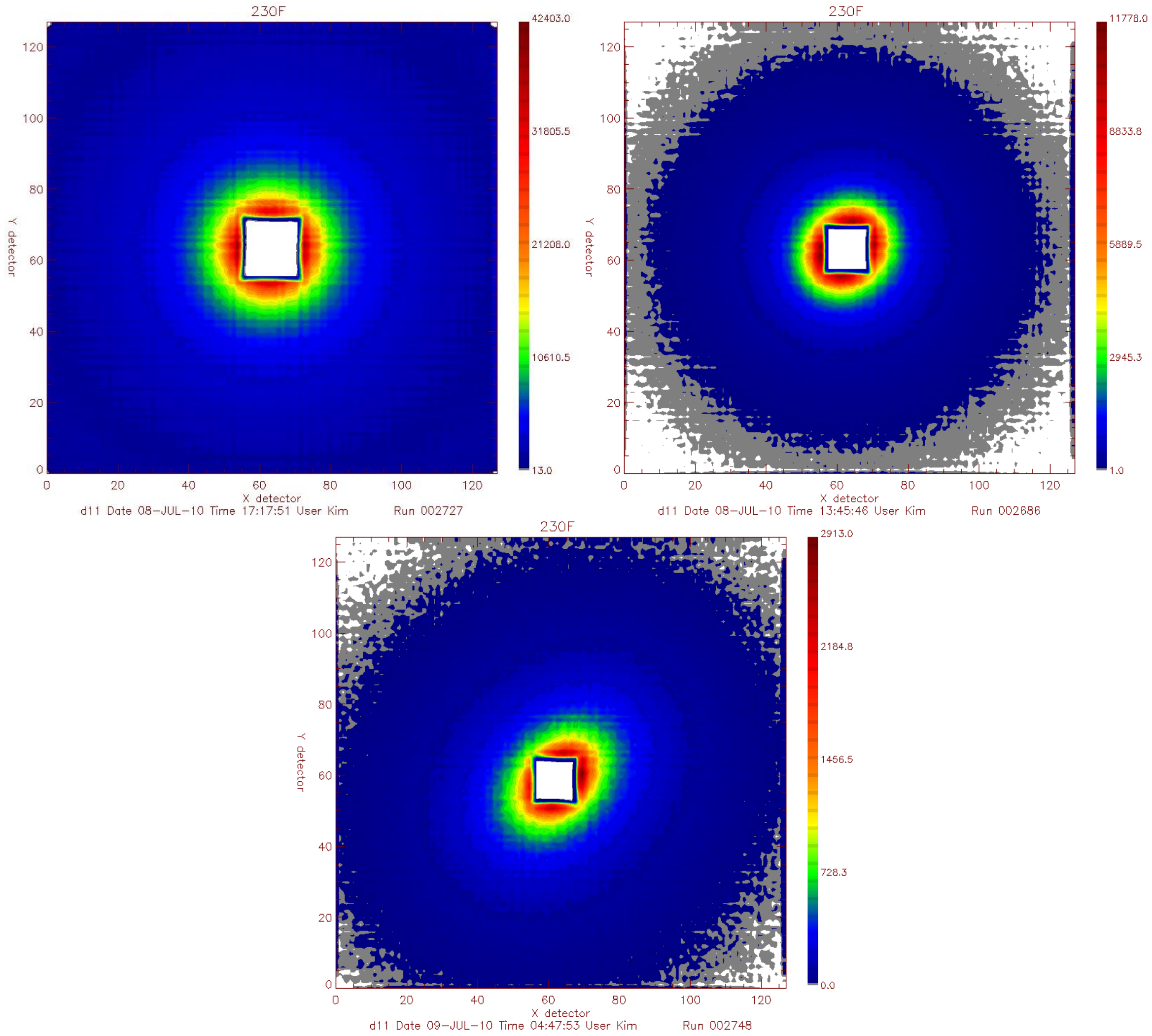

Figure 112: 2D SANS detector images for 230F (230 kg mol^{-1} with 3 wt% SWCNTs). Sample–detector distances: top left: 1.50 m; top right: 8.00 m; bottom: 39.0 m.

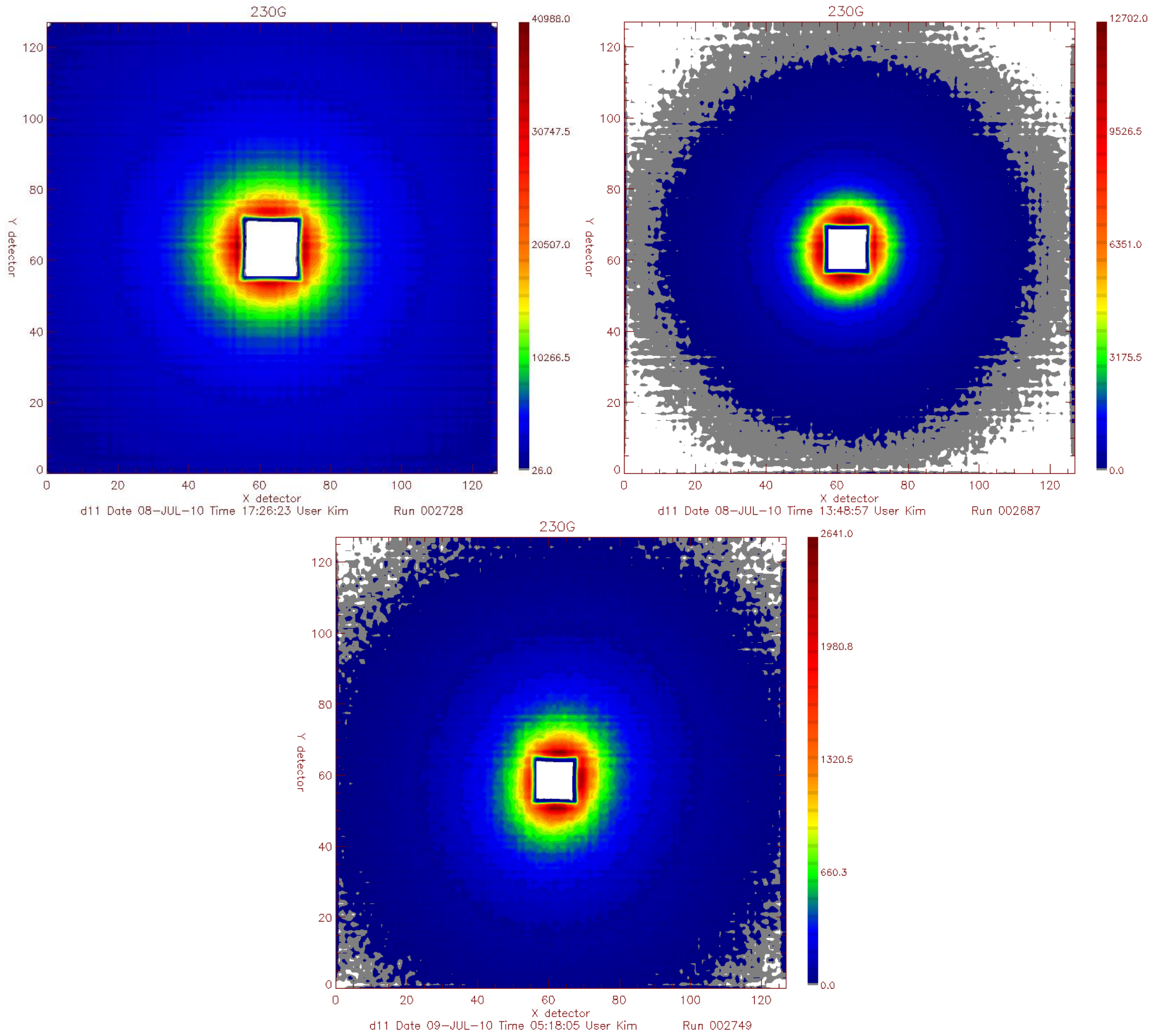

Figure 113: 2D SANS detector images for 230G (230 kg mol^{-1} with 4 wt% SWCNTs). Sample–detector distances: top left: 1.50 m; top right: 8.00 m; bottom: 39.0 m.

230 kg mol^{-1} annealed samples

The SANS 2D detector images for the annealed 230 kg mol^{-1} samples with 0–3 wt% SWCNTs are shown in Figure 32–Figure 35.

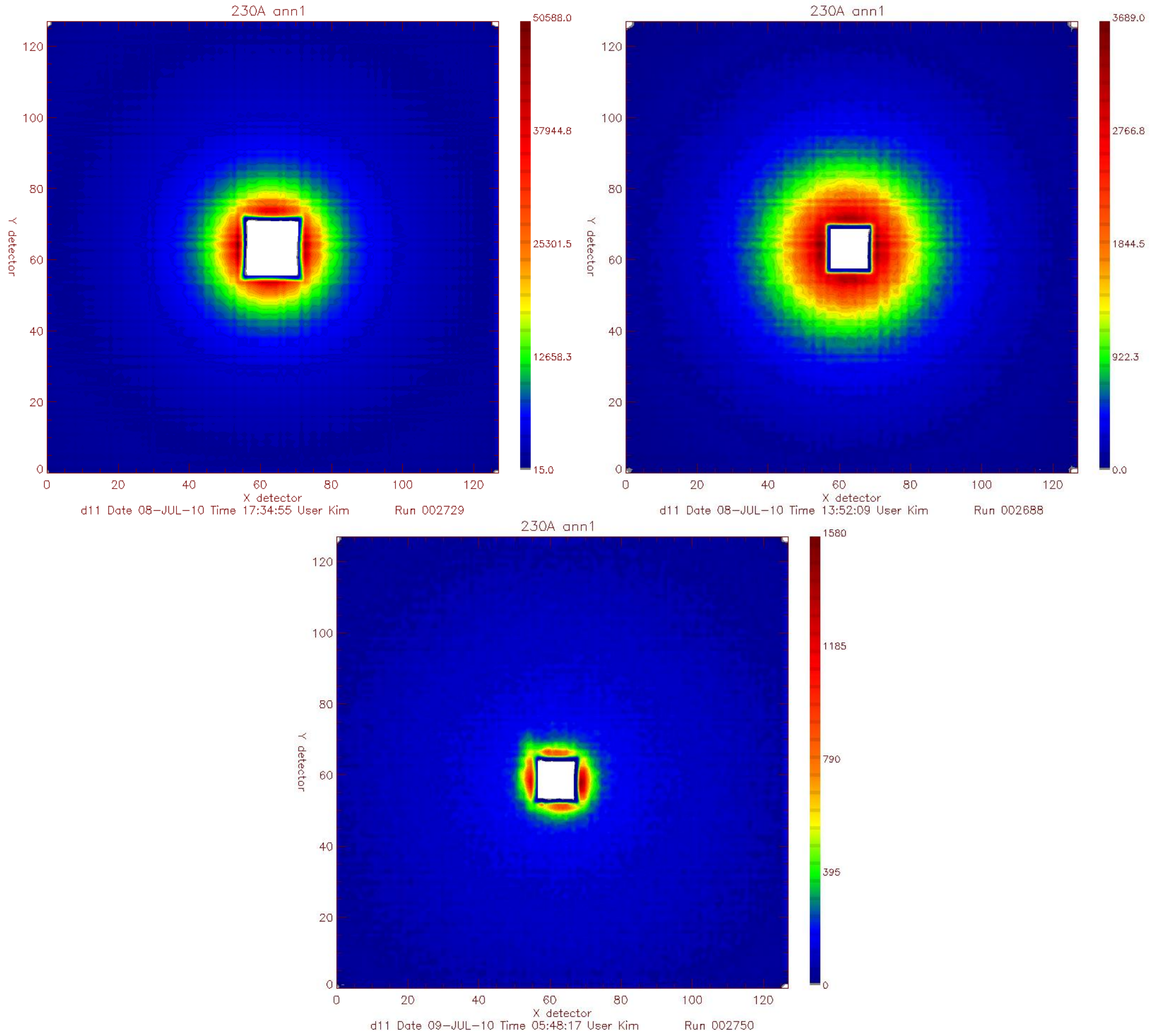

Figure 114: 2D SANS detector images for 230A_ann (230 kg mol^{-1} with 0 wt% SWCNTs, annealed). Sample–detector distances: top left: 1.50 m; top right: 8.00 m; bottom: 39.0 m.

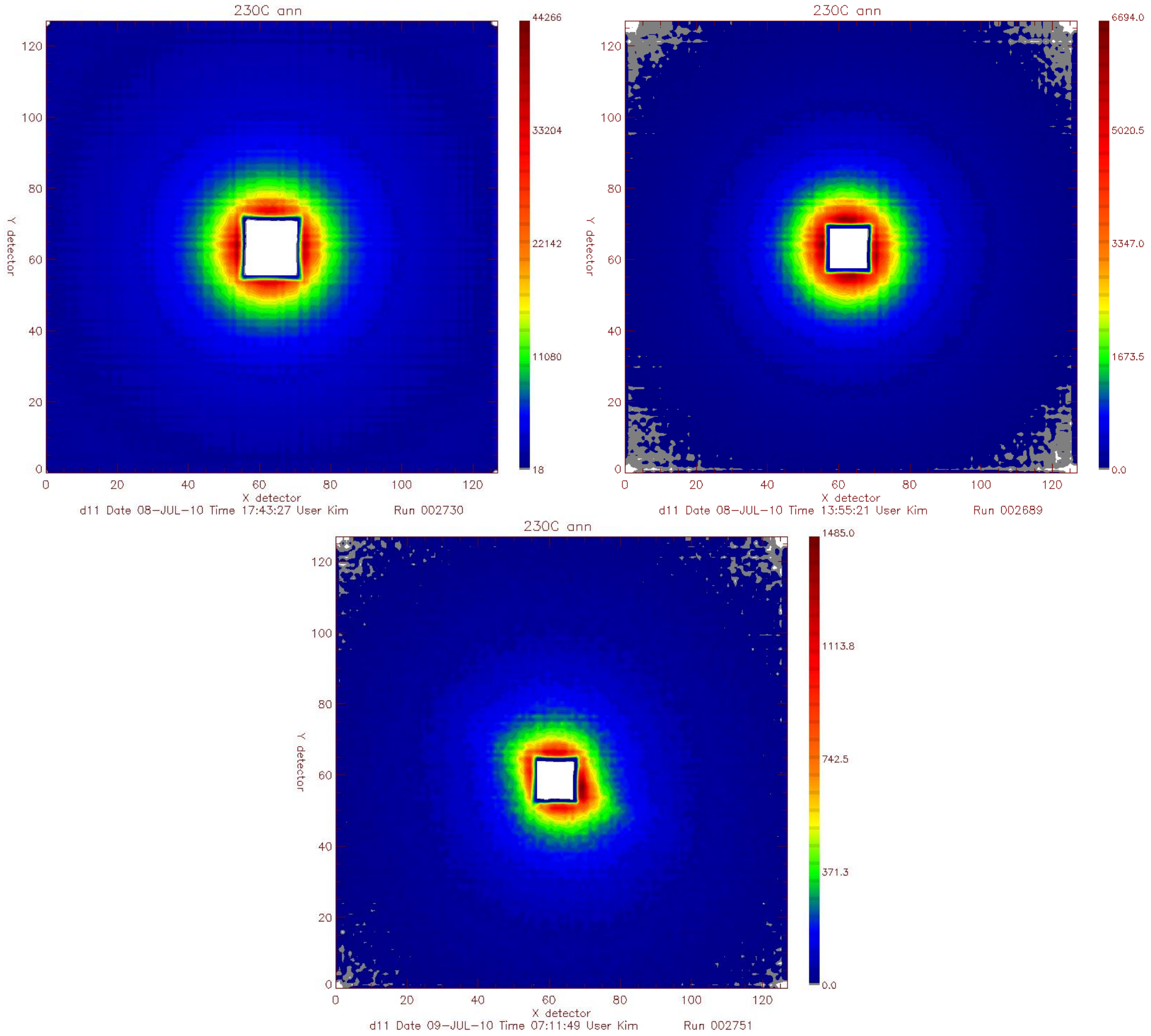

Figure 115: 2D SANS detector images for 230C_ann (230 kg mol^{-1} with 1 wt% SWCNTs, annealed). Sample–detector distances: top left: 1.50 m; top right: 8.00 m; bottom: 39.0 m.

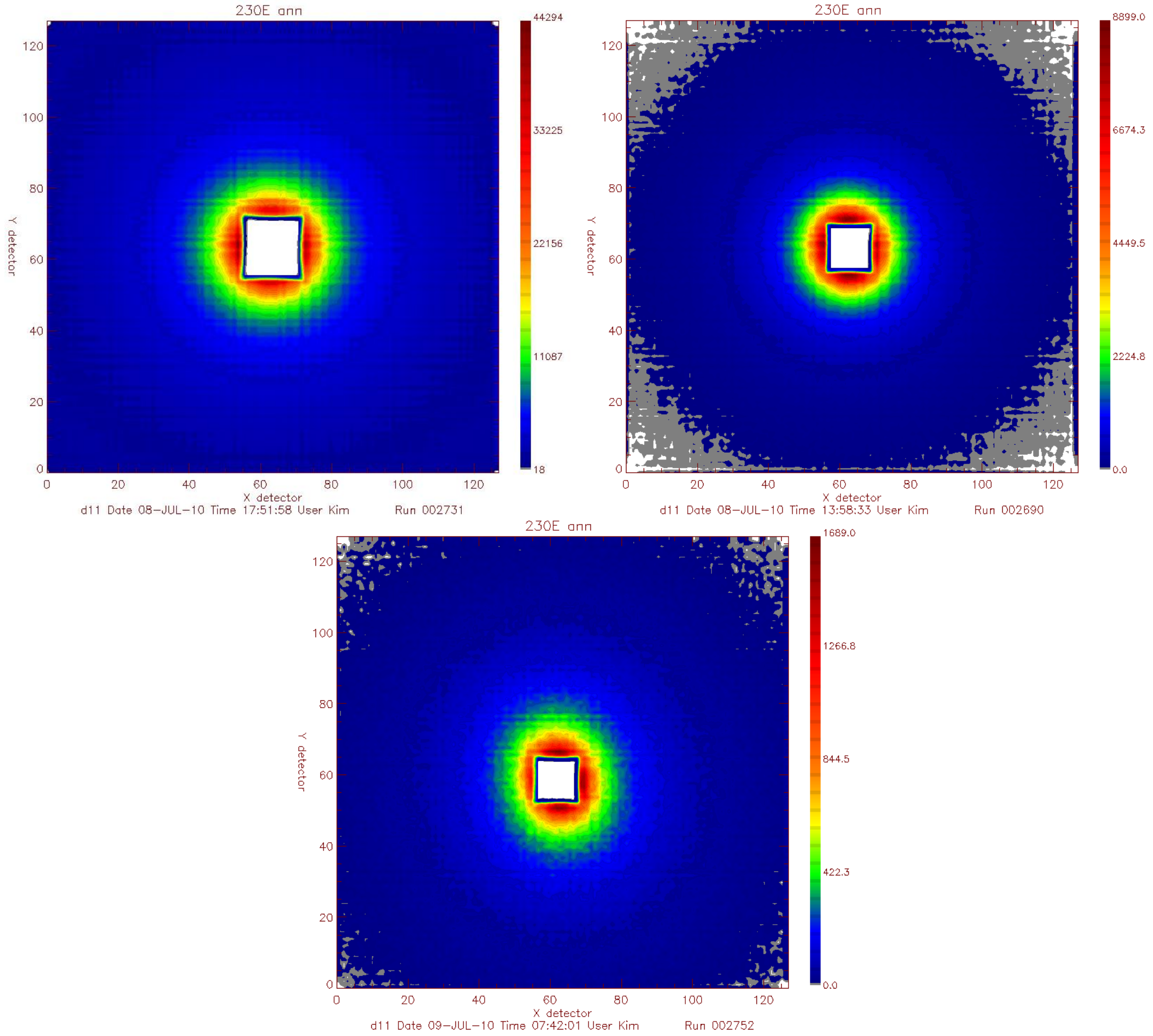

Figure 116: 2D SANS detector images for 230E_ann (230 kg mol^{-1} with 2 wt% SWCNTs, annealed). Sample–detector distances: top left: 1.50 m; top right: 8.00 m; bottom: 39.0 m.

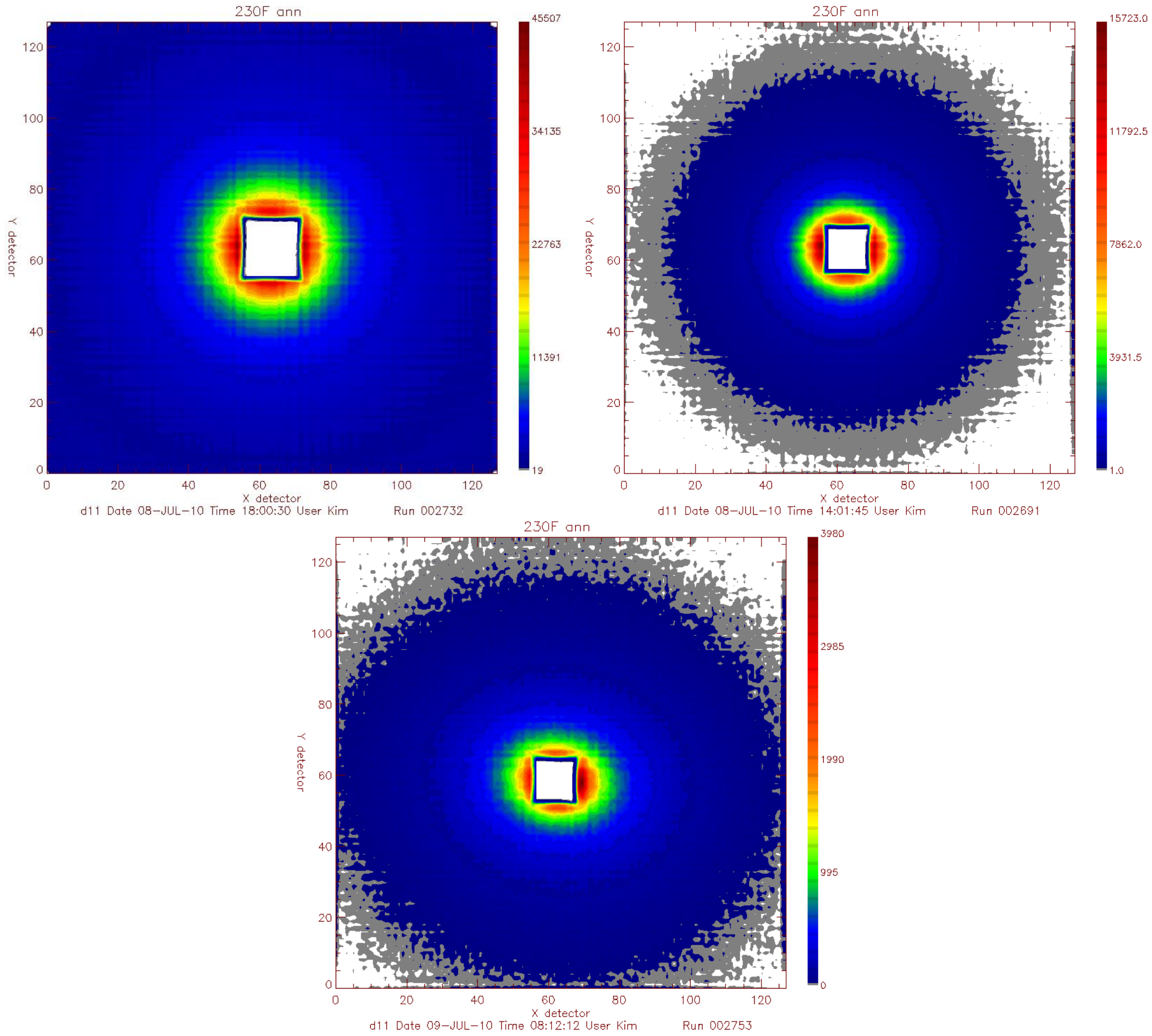

Figure 117: 2D SANS detector images for 230F_ann (230 kg mol^{-1} with 3 wt% SWCNTs, annealed). Sample–detector distances: top left: 1.50 m; top right: 8.00 m; bottom: 39.0 m.

Appendix 2: truncation times for $I(Q,t)$ data prior to KWW fitting

Table 34: Times at which the $I(Q,t)$ data were truncated prior to fitting with the KWW function for the h5 PS + 0 wt% SWCNTs sample

***Q* grouping**	**Time at which data is truncated prior to fitting/ns**				
	67 °C	**97 °C**	**127 °C**	**152 °C**	**177 °C**
1	0.02	0.015	0.03	0.03	0.045
2	0.02	0.02	0.02	0.045	0.11
3	0.02	0.02	0.02	0.045	0.055
4	0.025	0.02	0.02	0.035	0.06
5	0.015	0.03	0.07	0.06	0.105
6	—	—	—	—	—
7	0.13	0.11	0.115	0.125	0.15
8	0.015	0.03	0.05	0.075	0.125
9	0.15	0.03	0.07	0.11	0.135
10	0.075	0.07	0.1	0.095	0.15
11	0.06	0.1	0.08	0.15	0.15
12	0.15	0.15	0.145	0.15	0.15
13	—	—	—	—	—
14	0.05	0.05	0.05	0.09	0.15
15	0.035	0.08	0.105	0.11	0.15
16	0.055	0.085	0.15	0.13	0.15
17	0.06	0.05	0.11	0.15	0.15

Table 35: Times at which the *I*(*Q*,*t*) data were truncated prior to fitting with the KWW function for the h5 PS + 0.1 wt% SWCNTs sample

***Q* grouping**	**Time at which data is truncated prior to fitting/ns**				
	67 °C	**97 °C**	**127 °C**	**152 °C**	**177 °C**
1	0.02	0.02	0.02	0.05	0.045
2	0.02	0.02	0.02	0.115	0.06
3	0.02	0.015	0.025	0.08	0.045
4	0.02	0.015	0.025	0.08	0.075
5	0.03	0.03	0.045	0.11	0.09
6	0.1	0.05	0.15	0.15	—
7	0.15	0.1	0.15	0.125	0.125
8	0.06	0.03	0.03	0.15	0.01
9	0.05	0.035	0.065	0.15	0.105
10	0.15	0.08	0.115	0.15	0.115
11	0.1	0.15	0.095	0.15	0.095
12	0.15	0.15	0.15	0.15	0.15
13	0.15	0.115	0.15	0.15	—
14	0.15	0.08	0.15	0.15	0.12
15	0.15	0.09	0.15	0.1	0.135
16	0.15	0.13	0.12	0.15	0.15
17	0.15	0.15	0.15	0.135	0.15

Table 36: Times at which the $I(Q,t)$ data were truncated prior to fitting with the KWW function for the h5 PS + 0.4 wt% SWCNTs sample

***Q* grouping**	**Time at which data is truncated prior to fitting/ns**				
	67 °C	**97 °C**	**127 °C**	**152 °C**	**177 °C**
1	0.015	0.02	0.04	0.055	0.13
2	0.015	0.02	0.045	0.08	0.11
3	0.015	0.015	0.02	0.04	0.08
4	0.025	0.025	0.015	0.035	0.08
5	0.2	0.05	0.045	0.06	0.08
6	0.09	0.065	0.075	0.15	0.08
7	0.095	0.1	0.095	0.085	0.115
8	0.035	0.025	0.06	0.1	0.135
9	0.04	0.035	0.05	0.06	0.125
10	0.075	0.055	0.08	0.085	0.05
11	0.04	0.08	0.1	0.08	0.08
12	0.115	0.11	0.13	0.115	0.11
13	0.075	0.08	0.15	0.1	0.07
14	0.06	0.035	0.045	0.085	0.055
15	0.06	0.06	0.15	0.09	0.085
16	0.145	0.15	0.15	0.07	0.09
17	0.15	0.08	0.085	0.1	0.125

Table 37: Times at which the *I*(*Q*,*t*) data were truncated prior to fitting with the KWW function for the h5 PS + 1 wt% SWCNTs sample

***Q* grouping**	**Time at which data is truncated prior to fitting/ns**				
	67 °C	**97 °C**	**127 °C**	**152 °C**	**177 °C**
1	0.075	0.075	0.04	0.03	0.045
2	0.08	0.11	0.085	0.025	0.04
3	0.095	0.08	0.065	0.035	0.045
4	0.105	0.085	0.05	0.04	0.065
5	0.085	0.1	0.11	0.065	0.15
6	0.15	0.15	0.15	0.135	0.15
7	0.135	0.11	0.11	0.15	0.15
8	0.15	0.11	0.1	0.1	0.15
9	0.11	0.105	0.095	0.105	0.15
10	0.15	0.085	0.15	0.15	0.15
11	0.13	0.13	0.135	0.15	0.15
12	0.085	0.15	0.15	0.15	0.15
13	0.15	0.15	0.15	0.15	0.15
14	0.09	0.12	0.15	0.15	0.15
15	0.075	0.11	0.15	0.15	0.15
16	0.125	0.15	0.11	0.15	0.15
17	0.105	0.15	0.115	0.15	0.15

Table 38: Times at which the *I*(*Q*,*t*) data were truncated prior to fitting with the KWW function for the h5 PS + 2 wt% SWCNTs sample

***Q* grouping**	**Time at which data is truncated prior to fitting/ns**				
	67 °C	**97 °C**	**127 °C**	**152 °C**	**177 °C**
1	0.02	0.015	0.02	0.03	0.055
2	0.02	0.02	0.02	0.04	0.07
3	0.015	0.02	0.03	0.04	0.045
4	0.03	0.015	0.02	0.04	0.06
5	0.03	0.02	0.045	0.07	0.1
6	0.09	0.08	0.055	0.12	0.15
7	0.095	0.13	0.075	0.12	0.15
8	0.05	0.045	0.095	0.11	0.085
9	0.06	0.04	0.085	0.15	0.13
10	0.075	0.11	0.115	0.13	0.11
11	0.09	0.085	0.15	0.15	0.15
12	0.085	0.08	0.15	0.15	0.15
13	0.085	0.085	0.15	0.15	0.15
14	0.025	0.055	0.15	0.12	0.15
15	0.075	0.15	0.115	0.15	0.15
16	0.15	0.1	0.125	0.15	0.09
17	0.085	0.09	0.15	0.15	0.15

Table 39: Times at which the $I(Q,t)$ data were truncated prior to fitting with the KWW function for the h5 PS + 4 wt% SWCNTs sample

***Q* grouping**	**Time at which data is truncated prior to fitting/ns**				
	67 °C	**97 °C**	**127 °C**	**152 °C**	**177 °C**
1	0.015	0.02	0.025	0.03	0.03
2	0.02	0.02	0.025	0.05	0.025
3	0.02	0.02	0.02	0.045	0.035
4	0.02	0.02	0.025	0.045	0.04
5	0.02	0.02	0.03	0.075	0.06
6	—	—	—	—	—
7	0.095	0.105	0.08	0.105	0.105
8	0.025	0.03	0.065	0.11	0.09
9	0.025	0.025	0.075	0.085	0.06
10	0.04	0.045	0.085	0.135	0.125
11	0.045	0.06	0.15	0.15	0.105
12	0.125	0.15	0.105	0.15	0.15
13	—	—	—	—	—
14	0.06	0.045	0.13	0.15	0.15
15	0.075	0.12	0.15	0.15	0.15
16	0.15	0.125	0.09	0.15	0.15
17	0.125	0.15	0.11	0.12	0.15

Table 40: Times at which the *I*(*Q*,*t*) data were truncated prior to fitting with the KWW function for the h3 PS + 0 wt% SWCNTs sample

***Q* grouping**	**Time at which data is truncated prior to fitting/ns**				
	67 °C	**97 °C**	**127 °C**	**152 °C**	**177 °C**
1	0.015	0.02	0.02	0.02	0.055
2	0.02	0.015	0.02	0.035	0.085
3	0.02	0.02	0.015	0.035	0.045
4	0.02	0.02	0.02	0.03	0.07
5	0.02	0.02	0.02	0.035	0.06
6	0.02	0.02	0.025	0.09	0.12
7	0.02	0.025	0.02	0.08	0.12
8	0.02	0.02	0.02	0.03	0.085
9	0.02	0.02	0.02	0.045	0.115
10	0.02	0.02	0.03	0.065	0.1
11	0.02	0.02	0.04	0.06	0.15
12	0.07	0.06	0.15	0.15	0.15
13	0.025	0.02	0.045	0.085	0.15
14	0.02	0.02	0.035	0.08	0.11
15	0.02	0.02	0.04	0.15	0.135
16	0.15	0.02	0.1	0.15	0.15
17	0.045	0.04	0.08	0.15	0.15

Table 41: Times at which the *I*(*Q*,*t*) data were truncated prior to fitting with the KWW function for the h3 PS + 0.1 wt% SWCNTs sample

***Q* grouping**	**Time at which data is truncated prior to fitting/ns**				
	67 °C	**97 °C**	**127 °C**	**152 °C**	**177 °C**
1	0.015	0.015	0.015	0.02	0.05
2	0.015	0.025	0.045	0.055	0.075
3	0.02	0.015	0.035	0.07	0.045
4	0.015	0.015	0.015	0.045	0.05
5	0.02	0.03	0.025	0.045	0.08
6	0.08	0.055	0.06	0.06	0.11
7	0.04	0.085	0.09	0.075	0.085
8	0.03	0.025	0.045	0.075	0.095
9	0.015	0.025	0.045	0.06	0.1
10	0.015	0.045	0.05	0.1	0.11
11	0.06	0.08	0.06	0.1	0.1
12	0.115	0.15	0.11	0.15	0.15
13	0.07	0.15	0.095	0.15	0.15
14	0.045	0.15	0.15	0.08	0.15
15	0.03	0.15	0.15	0.15	0.15
16	0.15	0.15	0.15	0.15	0.15
17	0.055	0.15	0.15	0.15	0.15

Table 42: Times at which the *I*(*Q*,*t*) data were truncated prior to fitting with the KWW function for the h3 PS + 0.4 wt% SWCNTs sample

***Q* grouping**	**Time at which data is truncated prior to fitting/ns**				
	67 °C	**97 °C**	**127 °C**	**152 °C**	**177 °C**
1	0.015	0.015	0.02	0.025	0.04
2	0.015	0.015	0.015	0.04	0.06
3	0.015	0.015	0.015	0.04	0.04
4	0.015	0.015	0.02	0.025	0.04
5	0.015	0.015	0.03	0.04	0.055
6	0.02	0.025	0.04	0.05	0.1
7	0.04	0.035	0.045	0.06	0.1
8	0.015	0.02	0.03	0.055	0.08
9	0.015	0.015	0.025	0.04	0.055
10	0.02	0.015	0.045	0.06	0.08
11	0.025	0.03	0.055	0.07	0.09
12	0.09	0.15	0.085	0.11	0.125
13	0.03	0.045	0.09	0.085	0.15
14	0.015	0.025	0.05	0.065	0.15
15	0.015	0.035	0.15	0.095	0.15
16	0.04	0.105	0.15	0.15	0.15
17	0.09	0.15	0.15	0.15	0.15

Table 43: Times at which the *I*(*Q*,*t*) data were truncated prior to fitting with the KWW function for the h3 PS + 1 wt% SWCNTs sample

***Q* grouping**	**Time at which data is truncated prior to fitting/ns**				
	67 °C	**97 °C**	**127 °C**	**152 °C**	**177 °C**
1	0.015	0.02	0.03	0.045	0.06
2	0.045	0.045	0.055	0.06	0.09
3	0.025	0.025	0.025	0.045	0.065
4	0.02	0.02	0.045	0.06	0.08
5	0.045	0.04	0.045	0.065	0.085
6	0.095	0.05	0.08	0.09	0.09
7	0.075	0.06	0.065	0.095	0.105
8	0.055	0.04	0.05	0.09	0.115
9	0.035	0.05	0.045	0.075	0.095
10	0.035	0.035	0.05	0.085	0.085
11	0.045	0.045	0.055	0.08	0.15
12	0.09	0.12	0.15	0.15	0.15
13	0.09	0.075	0.075	0.13	0.13
14	0.05	0.03	0.07	0.085	0.15
15	0.06	0.105	0.055	0.15	0.145
16	0.13	0.085	0.115	0.13	0.15
17	0.1	0.105	0.15	0.15	0.15

Table 44: Times at which the *I*(*Q*,*t*) data were truncated prior to fitting with the KWW function for the h3 PS + 2 wt% SWCNTs sample

***Q* grouping**	**Time at which data is truncated prior to fitting/ns**				
	67 °C	**97 °C**	**127 °C**	**152 °C**	**177 °C**
1	0.045	0.02	0.04	0.04	0.08
2	0.03	0.045	0.06	0.05	0.09
3	0.025	0.04	0.04	0.06	0.06
4	0.025	0.015	0.02	0.06	0.045
5	0.025	0.035	0.035	0.06	0.08
6	0.035	0.045	0.075	0.08	0.09
7	0.055	0.055	0.085	0.09	0.105
8	0.04	0.04	0.04	0.065	0.085
9	0.02	0.02	0.045	0.045	0.1
10	0.04	0.04	0.06	0.07	0.15
11	0.04	0.055	0.06	0.08	0.105
12	0.0.65	0.085	0.11	0.09	0.15
13	0.065	0.06	0.105	0.12	0.15
14	0.04	0.04	0.095	0.06	0.115
15	0.085	0.11	0.085	0.07	0.15
16	0.08	0.105	0.11	0.12	0.15
17	0.095	0.115	0.14	0.15	0.115

Table 45: Times at which the *I*(*Q*,*t*) data were truncated prior to fitting with the KWW function for the h3 PS + 3 wt% SWCNTs sample

***Q* grouping**	**Time at which data is truncated prior to fitting/ns**				
	67 °C	**97 °C**	**127 °C**	**152 °C**	**177 °C**
1	0.03	0.02	0.025	0.025	0.06
2	0.045	0.045	0.07	0.065	0.08
3	0.045	0.025	0.035	0.045	0.08
4	0.015	0.03	0.025	0.04	0.045
5	0.045	0.05	0.025	0.05	0.075
6	0.075	0.05	0.06	0.06	0.085
7	0.05	0.07	0.085	0.07	0.08
8	0.06	0.035	0.05	0.06	0.095
9	0.04	0.25	0.04	0.055	0.075
10	0.06	0.06	0.045	0.06	0.07
11	0.06	0.05	0.065	0.13	0.105
12	0.095	0.15	0.095	0.095	0.15
13	0.085	0.095	0.105	0.15	0.125
14	0.125	0.045	0.06	0.12	0.135
15	0.095	0.12	0.15	0.13	0.15
16	0.15	0.1	0.15	0.15	0.15
17	0.09	0.15	0.15	0.13	0.125

Table 46: Times at which the *I*(*Q*,*t*) data were truncated prior to fitting with the KWW function for the h3 PS + 4 wt% SWCNTs sample

***Q* grouping**	**Time at which data is truncated prior to fitting/ns**				
	67 °C	**97 °C**	**127 °C**	**152 °C**	**177 °C**
1	0.015	0.025	0.03	0.045	0.08
2	0.02	0.02	0.045	0.065	0.08
3	0.03	0.02	0.035	0.035	0.055
4	0.02	0.02	0.025	0.04	0.06
5	0.02	0.02	0.03	0.075	0.075
6	0.065	0.04	0.09	0.1	0.085
7	0.045	0.025	0.04	0.07	0.075
8	0.02	0.02	0.03	0.05	0.09
9	0.025	0.02	0.04	0.045	0.065
10	0.035	0.03	0.07	0.095	0.15
11	0.02	0.035	0.04	0.095	0.15
12	0.09	0.12	0.075	0.095	0.15
13	0.065	0.065	0.06	0.13	0.15
14	0.025	0.04	0.05	0.08	0.11
15	0.045	0.07	0.08	0.15	0.15
16	0.105	0.095	0.135	0.15	0.135
17	0.06	0.07	0.07	0.15	0.15

References

1. S. Iijima, *Nature*, 1991, 354, 56-58.
2. M. Moniruzzaman and K. I. Winey, *Macromolecules*, 2006, 39, 5194-5205.
3. G. Mittal, V. Dhand, K. Y. Rhee, S.-J. Park and W. R. Lee, *J. Ind. Eng.*, 2015, 21, 11-25.
4. T. Guo, P. Nikolaev, A. Thess, D. T. Colbert and R. E. Smalley, *Chem. Phys. Lett.*, 1995, 243, 49-54.
5. Z. F. Ren, Z. P. Huang, J. W. Xu, J. H. Wang, P. Bush, M. P. Seigal and P. N. Provencio, *Science*, 1998, 282, 1105-1107.
6. *Carbon nanotubes: synthesis, structure, properties and applications*, Springer-Verlag, Berlin, 2001.
7. P. J. F. Harris, *Carbon nanotubes and related structures: new materials for the twenty-first century*, Cambridge University Press, Cambridge, 1999.
8. M. F. Yu, B. S. Files, S. Arepelli and R. S. Ruoff, *Phys. Rev. Lett.*, 2000, 84, 5552-5555.
9. J. N. Coleman, U. Khan, W. J. Blau and Y. K. Gun'ko, *Carbon*, 2006, 44, 1624-1652.
10. J. P. Salvetat, G. A. D. Briggs, J. M. Bonard, R. R. Bacsa, A. J. Kulik, T. Stockli, N. A. Burnham and L. Forro, *Phys. Rev. Lett.*, 1999, 82, 944-947.
11. J. W. G. Wildoer, L. C. Venema, A. G. Rinzler, R. E. Smalley and C. Dekker, *Nature*, 1998, 391, 59-62.
12. T. W. Ebbesen, H. J. Lezec, H. Hiura, J. W. Bennett, H. F. Ghaemi and T. Thio, *Nature*, 1996, 382, 54.
13. H. Dai, E. W. Wong and C. M. Lieber, *Science*, 1996, 272, 523.
14. S. Berber, Y. Kwon and D. Tomanek, *Phys. Rev. Lett.*, 2000, 84, 4613-4616.
15. Y. S. Touloukian, R. W. Powell, C. Y. Ho and P. G. Klemens, *Thermal conductivity: metallic elements and alloys*, Purdue University, West Lafayette, Indiana, USA, 1970.
16. D. M. Marquis, E. Guillaume and C. Chivas-Joly, in *Nanocomposites and Polymers with Analytical Methods*, ed. J. Cuppoletti, In Tech, Croatia and China, 2011, ch. 11.
17. *Nanocomposite Science and Technology*, Wiley-VCH Verlag GmbH, Weinheim, Germany, 2003.
18. P. M. Ajayan, O. Stephan, C. Colliex and D. Trauth, *Science*, 1994, 265, 1212-1214.
19. M. F. L. DeVolter, S. H. Tawfick, R. H. Baughman and J. A. Hart, *Science*, 2013, 339, 535-539.
20. O. Breuer and U. Sundararaj, *Polym. Composites*, 2004, 25, 630-645.
21. Carbon nanotubes from Sigma-Aldrich, http://www.sigmaaldrich.com/materials-science/material-science-products.html?TablePage=16376687, Accessed May 3rd, 2016.
22. Y.-L. Zhao and J. F. Stoddart, *Acc. Chem. Res.*, 2009, 42, 1161-1171.
23. P. Liu, *Eur. Phys. J.*, 2005, 41, 2693-2703.

24. M. T. Tchoul, W. T. Ford, M. L. P. Ha, I. Chavez-Summarriva, B. P. Grady, G. Lolli, D. E. Resasco and S. Arepelli, *Chem. Mater.*, 2008, 20, 3120-3126.

25. W. Huang, Y. Lin, S. Taylor, J. Gaillard, A. M. Rao and Y.-P. Sun, *Nano Lett.*, 2002, 2, 231-234.

26. S. Badaire, P. Poulin, M. Maugey and C. Zakin, *Langmuir*, 2004, 20.

27. J. Zhu, H. Peng, F. Rodriguez-Macias, J. L. Margrave, V. N. Khabashesku, A. M. Imam, K. Lozano and E. V. Barrera, *Adv. Funct. Mater.*, 2004, 14, 643-648.

28. L. Xie, F. Xu, F. Qiu, H. Lu and Y. Yang, *Macromolecules*, 2007, 40, 3296-3305.

29. S. Wang, R. Liang, B. Wang and C. Zhang, *Polym. Composites*, 2009, 30, 1050-1057.

30. F. Du, J. E. Fischer and K. I. Winey, *J. Polym. Sci., B: Polym. Phys.*, 2003, 41, 3333-3338.

31. J. S. Higgins and H. C. Benoît, *Polymers and neutron scattering*, Clarendon Press, Oxford, 1994.

32. K. Hong, D. Uhrig and J. W. Mays, *Curr. Opin. Solid State Mater. Sci.*, 1999, 4, 531-538.

33. H. S. Xia, Q. Wang, K. S. Li and G. H. Hu, *J. Appl. Polym. Sci.*, 2004, 93, 378-386.

34. S. Pujari, T. Ramanathan, K. Kasimatis, J. Masuda, R. Andrews, J. M. Torkelson, L. C. Brinson and W. P. Burghardt, *J. Polym. Sci., B: Polym. Phys.*, 2009, 47, 1426-1436.

35. A. Dufresne, M. Paillet, J. L. Putaux, R. Canet, F. Carmona, P. Delhaes and S. Cui, *J. Mater. Sci.*, 2002, 37, 3915-3923.

36. Y. Xu, B. Higgins and W. J. Brittain, *Polymer*, 2005, 46, 799-810.

37. N. Grossiord, J. Loos, L. van Laake, M. Maugey, C. Zakri, C. E. Koning and J. A. Hart, *Adv. Funct. Mater.*, 2008, 18, 3226-3234.

38. P. M. Ajayan and O. Z. Zhou, in *Carbon nanotubes: synthesis, structure, properties and applications*, eds. M. S. Dresselhaus, G. Dresselhaus and P. Avouris, Springer, Heidelberg, Germany, 2001.

39. S. J. V. Frankland, A. Caglar, D. W. Brenner and M. J. Griebel, *J. Phys. Chem. B*, 2002, 106, 3046-3048.

40. L. S. Schadler, S. C. Giannaris and P. M. Ajayan, *Appl. Phys. Lett.*, 1998, 73, 3842-3844.

41. P. M. Ajayan, L. S. Schadler, S. C. Giannaris and A. Rubio, *Adv. Mater.*, 2000, 12, 750-753.

42. D. Qian, E. C. Dickey, R. Andrews and T. Ratnell, *Appl. Phys. Lett.*, 2000, 76, 2868-2870.

43. C. A. Cooper, D. Ravitch, D. Lips, J. Mayer and H. D. Wagner, *Compos. Sci. Technol.*, 2002, 62, 1105-1112.

44. L. Chen, X. J. Pang and Z. L. Yu, *Mater. Sci. Eng.*, 2007, 457, 287-291.

45. T. V. Kosmidou, A. S. Vatalis, C. G. Delides, E. Logakis, P. Pissis and G. C. Papanicolaou, *eXPRESS Polym. Lett.*, 2008, 2, 364-372.

46. P. C. Ma, J. K. Kim and B. Z. Tang, *Compos. Sci. Technol.*, 2007, 67, 2965-2972.

47. J. A. King, D. L. Gaxiola, B. A. Johnson and J. M. Keith, *J. Compos. Mater.*, 2010, 44, 839-855.

48. C. Guthy, F. Du, S. Brand, K. I. Winey and J. E. Fischer, *J. Heat Transfer, Trans. ASME*, 2007, 129, 1096-1099.

49. Z. Han and A. Fina, *Prog. Polym. Sci.*, 2011, 36, 914-944.

50. J. P. Cotton, D. Decker, H. Benoit, B. Farnoux, J. S. Higgins, G. Jannick, R. Ober, C. Picot and J. des Cloizeaux, *Macromolecules*, 1974, 7, 863-872.

51. M. Rubinstein and R. H. Colby, *Polymer Physics*, Oxford University Press, New York, 2003.

52. M. Doi, *Introduction to Polymer Physics*, Oxford Science Publications, Oxford University Press, Oxford, UK, 1995.

53. S. Sen, Y. Xie, S. K. Kumar, H. Yang, A. Bansal, D. L. Ho, L. Hall, J. B. Hooper and K. S. Schweizer, *Phys. Rev. Lett.*, 2007, 98, 128302.

54. K. Nusser, S. Neueder, G. J. Schneider, A. Meyer, W. Pyckhout-Hintzen, L. Willner, A. Radulescu and D. Richter, *Macromolecules*, 2010, 43, 9837-9847.

55. M. Vacatello, *Macromolecules*, 2001, 34, 1946-1952.

56. M. Vacatello, *Macromol. Theory Simul.*, 2002, 11, 53-57.

57. M. A. Sharaf and J. E. Mark, *Polymer*, 2004, 45, 3943-3952.

58. M. A. Sharaf, A. Kloczowski, T. Z. Sen, K. I. Jacob and J. E. Mark, *Eur. Polym. J.*, 2006, 42, 796-806.

59. M. Y. Lin, H. M. Lindsay, D. A. Weitz, R. C. Ball, R. Klein and P. Meakin, *Phys. Rev. A*, 1990, 41, 2005-2020.

60. M. Y. Lin, H. M. Lindsay, D. A. Weitz, R. C. Ball, R. Klein and P. Meakin, *Nature*, 1989, 339, 360-362.

61. M. S. Ozmusul, R. C. Picu, S. S. Sternstein and S. K. Kumar, *Macromolecules*, 2005, 38, 4495-4500.

62. A. I. Nakatani, W. Chen, R. G. Schmidt, G. V. Gordon and C. C. Han, *Polymer*, 2001, 42, 3713-3722.

63. A. I. Nakatani, W. Chen, R. G. Schmidt, G. V. Gordon and C. C. Han, *Int. J. Thermophys.*, 2002, 23, 199-209.

64. Q. W. Yuan, A. Kloczkowski, J. E. Mark and M. A. Sharaf, *J. Polym. Sci., B: Polym. Phys.*, 1996, 34, 1647-1657.

65. M. Vacatello, *Macromolecules*, 2002, 8191-8193.

66. P. J. Dionne, R. Ozisik and R. C. Picu, *Macromolecules*, 2005, 38, 9351-9358.

67. N. Jouault, F. Dalmas, S. Said, E. Di Cola, R. Schweins, J. Justin and F. Boue, *Macromolecules*, 2010, 43, 9881-9891.

68. M. E. Mackay, A. Tuteja, P. M. Duxbury, C. J. Hawker, B. Van Horn, Z. Guan, G. Chen and R. S. Krishnan, *Science*, 2006, 311, 1740-1743.
69. A. Tuteja, P. M. Duxbury and M. E. Mackay, *Phys. Rev. Lett.*, 2008, 100, 077801.
70. M. Vacatello, *Macromol. Theory Simul.*, 2001, 10, 187-195.
71. F. W. Starr, T. B. Schroder and G. S. C., *Macromolecules*, 2002, 35, 4481-4492.
72. C. Mischler, J. Baschnagel, S. Dasgupta and K. Binder, *Polymer*, 2002, 43.
73. S. K. Kumar, M. Vacatello and D. Y. Yoon, *J. Chem. Phys.*, 1988, 89, 5206-5215.
74. S. K. Kumar, M. Vacatello and D. Y. Yoon, *Macromolecules*, 1990, 23, 2189-2197.
75. R. L. Jones, S. K. Kumar, D. L. Ho, R. M. Briber and T. P. Russell, *Nature (London)*, 1999, 400, 146-149.
76. F. M. Erguney, H. Lin and W. L. Mattice, *Polymer*, 2006, 47, 3689-3695.
77. F. M. Erguney and W. L. Mattice, *Polymer*, 2008, 49, 2621-2623.
78. Y. Termonia, *Polymer*, 2009, 50, 1062-1066.
79. A. L. Frischknecht, E. S. McGarrity and M. E. Mackay, *J. Chem. Phys.*, 2010, 132, 204901.
80. R. C. Picu and M. S. Ozmusul, *J. Chem. Phys.*, 2003, 118, 11239-11248.
81. A. Karatrantos, R. J. Composto, K. I. Winey and N. Clarke, *Macromolecules*, 2011, 44, 9830-9838.
82. E. Zaminpayma and K. Mirabbaszadeh, *Comp. Mater. Sci.*, 2012, 58, 7-11.
83. E. Zaminpayma and K. Mirabbaszadeh, *Polym. Composites*, 2012, 33, 548-554.
84. S. Haghighatpanah and K. Bolton, *Comp. Mater. Sci.*, 2013, 69, 443-454.
85. H. Eslami and M. Behrouz, *J. Phys. Chem. C*, 2014, 118, 9841-9851.
86. W. S. Tung, V. Bird, R. J. Composto, N. Clarke and K. I. Winey, *Macromolecules*, 2013, 46, 5345-5354.
87. W. S. Tung, R. J. Composto, N. Clarke and K. I. Winey, *ACS Macro Lett.*, 2015, 4, 916-920.
88. J. Colmenero, A. J. Moreno and A. Alegria, *Prog. Polym. Sci.*, 2005, 30, 1147-1184.
89. B. Frick, U. Buchenau and D. Richter, *Colloid Polym. Sci.*, 1995, 273, 413-420.
90. T. Kanaya, T. Ishida, T. Kawaguchi and K. Kaji, *Physica B*, 1995, 213 and 214, 502-505.
91. T. Kawaguchi, T. Kanaya and K. Kaji, *Physica B*, 1995, 213 and 214, 510-512.
92. T. Kanaya, T. Kawaguchi and K. Kaji, *J. Chem. Phys.*, 1996, 104, 3841-3850.
93. S. Arrese-Igor, A. Arbe, B. Frick and J. Colmenero, *Macromolecules*, 2011, 44, 3161-3168.
94. R. Inoue, T. Kanaya, T. Miyazaki, K. Nishida, I. Tsukushi and K. Shibata, *Mater. Sci. Eng. A*, 2006, 442, 367-370.
95. R. Inoue, T. Kanaya, K. Nishida, I. Tsukushi and K. Shibata, *Phys. Rev. Lett.*, 2005, 95, 056102.
96. R. Inoue, T. Kanaya, K. Nishida, I. Tsukushi and K. Shibata, *Phys. Rev. E*, 2006, 74, 021801.
97. R. Inoue, T. Kanaya, K. Nishida, I. Tsukushi and K. Shibata, *Phys. Rev. E*, 2008, 77, 032801.

98. R. Inoue, T. Kanaya, K. Nishida, I. Tsukushi, J. Taylor, S. Levett and B. J. Gabrys, *Eur. Phys. J. E*, 2007, 24, 55-60.

99. R. Inoue, T. Kanaya, K. Nishida, I. Tsukushi, M. T. F. Telling, B. J. Gabrys, M. Tyagi, C. Soles and W.-I. Wu, *Phys. Rev. E*, 2009, 80, 031802.

100. T. Kanaya, T. Miyazaki, R. Inoue and K. Nishida, *phys. stat. sol. (b)*, 2005, 242, 595-606.

101. G. Shirane, S. M. Shapiro and J. M. Tranquada, *Neutron scattering with a triple-axis spectrometer: basic techniques*, Cambridge University Press, Cambridge, UK, 2004.

102. A. Marruzzo, W. Schirmacher, A. Fratalocchi and G. Ruocco, *Sci. Rep.*, 2013, 3, 1407.

103. S. Arrese-Igor, A. Arbe, A. Alegria, J. Colmenero and B. Frick, *J. Chem. Phys.*, 2004, 120, 423-436.

104. S. Arrese-Igor, A. Arbe, A. Alegria, J. Colmenero and B. Frick, *J. Chem. Phys.*, 2005, 123, 014907.

105. R. J. Roe, *J. Non-Cryst. Solids*, 1998, 235-237, 308-313.

106. L. Saviot, E. Duval, A. J. Dianoux and J. F. Jal, *Physica B*, 2000, 276-278, 435-436.

107. J. L. Keddie, R. A. L. Jones and R. A. Cory, *Europhys. Lett.*, 1994, 27, 59-64.

108. W. J. Orts, J. H. van Zanten, W. Wu and S. K. Satija, *Phys. Rev. Lett.*, 1993, 71, 867-870.

109. G. Zaccai, *Science*, 2000, 288, 1604-1607.

110. J. E. Mark, *Polymer data handbook*, Oxford University Press, 2nd edn., 2009.

111. P. G. DeGennes, *Eur. Phys. J. E*, 2000, 2, 201-203.

112. J. R. Katz, *Transactions of the Faraday Society*, 1936, 32, 77-96.

113. S. M. Wecker, T. Davidson and J. B. Cohen, *Journal of Materials Science*, 1972, 7, 1249-1259.

114. G. R. Mitchell and A. H. Windle, *Polymer*, 1984, 25, 906-920.

115. H. R. Schubach, E. Nagy and B. Heise, *Colloid and Polymer Science*, 1981, 259, 789-796.

116. C. Ayyagari, D. Bedrov and G. D. Smith, *Macromolecules*, 2000, 33, 6194-6199.

117. V. Arrighi, J. S. Higgins, A. N. Burgess and G. Floudas, *Polymer*, 1998, 39, 6369-6376.

118. S. Gagliardi, V. Arrighi, R. Ferguson and M. T. F. Telling, *Physica B*, 2001, 301, 110-114.

119. T. Masui, H. Kishimoto, T. Kikuchi, S. Ohira-Kawamura, Y. Inamura, T. Koga and K. Nakajima, *J. Phys.: Conf. Series*, 2014, 502, 012057.

120. A. Sanz, M. Ruppel, J. F. Douglas and J. T. Cabral, *J. Phys., Condens. Matter*, 2008, 20, 104209.

121. J. M. Kropka, V. Garcia-Sakai and P. F. Green, *Nano Lett.*, 2008, 8, 1060-1065.

122. H. C. Wong, A. Sanz, J. F. Douglas and J. T. Cabral, *J. Mol. Liq.*, 2010, 153, 79-87.

123. T. Psurek, J. Obrzut, C. L. Soles, K. A. Page, M. Cicerone and J. F. Douglas, *J. Phys. Chem. B*, 2008, 112, 15980.

124. A. C. Balazs, T. Emrick and T. P. Russell, *Science*, 2006, 314, 1107-1110.

125. H. C. Wong, A. Sanz, J. F. Douglas and J. T. Cabral, *J. Mol. Liq.*, 2010, 153, 79-87.

126. A. Sanz, H. C. Wong, A. J. Nedoma, J. F. Douglas and J. T. Cabral, *Polymer*, 2015, 68, 47-56.

127. D. Bhowmik, J. A. Pomposo, F. Juranyi, V. Garcia-Sakai, M. Zampani, Y. Su, A. Arbe and J. Colmenero, *Macromolecules*, 2014, 47, 304-315.

128. B. Miller, A. E. Imel, W. Holley, D. Baskaran, J. W. Mays and M. D. Dadmun, *Macromolecules*, 2015, 48, 8369-8375.

129. M. Mu, N. Clarke, R. J. Composto and K. I. Winey, *Macromolecules*, 2009, 42, 7091-7097.

130. M. Mu, R. J. Composto, N. Clarke and K. I. Winey, *Macromolecules*, 2009, 42, 8365-8369.

131. Y. Li, M. Kroger and W. K. Liu, *Phys. Rev. Lett.*, 2012, 109, 118001.

132. A. Karatrantos, N. Clarke, R. J. Composto and K. I. Winey, *IOP Conf. Series: Mater. Sci. Eng.*, 2014, 64, 012041.

133. J. T. Kalathi, S. K. Kumar, M. Rubinstein and G. S. Grest, *Soft Matter*, 2015, 11, 4123-4132.

134. K. Chrissopoulou, S. H. Anastiadis, E. P. Giannelis and B. Frick, *J. Chem. Phys.*, 2007, 127, 144910.

135. F. Barroso-Bujans, F. Fernandez-Alonso, S. Cerveny, S. F. Parker, A. Alegria and J. Colmenero, *Soft Matter*, 2011, 7, 7173-7176.

136. C. Karlsson, A. S. Best, J. Swenson, W. S. Howells and L. Borjesson, *J. Chem. Phys.*, 2003, 118, 4206-4212.

137. P. G. deGennes, *J. Chem. Phys.*, 1971, 55, 572-579.

138. C. Maxwell, *Treatise on Electricity and Magnetism*, Oxford University Press, London, 1873.

139. W. S. Tung, N. Clarke, R. J. Composto and K. I. Winey, *Macromolecules*, 2013, 46, 2317-2322.

140. C.-C. Lin, K. Ohno, N. Clarke, K. I. Winey and R. J. Composto, *Macromolecules*, 2014, 47, 5357-5364.

141. A. Karatrantos and N. Clarke, *Soft Matter*, 2011, 7, 7334-7341.

142. A. Karatrantos, R. J. Composto, K. I. Winey and N. Clarke, *Mater. Sci. Eng.*, 2012, 40, 012027.

143. A. Karatrantos, R. J. Composto, K. I. Winey and N. Clarke, *Macromolecules*, 2012, 45, 7274-7281.

144. A. Karatrantos, N. Clarke, R. J. Composto and K. I. Winey, *Soft Matter*, 2013, 9, 3877-3884.

145. J. T. Kalathi, G. S. Grest and S. K. Kumar, *Phys. Rev. Lett.*, 2012, 109, 198301.

146. R. Ashkar, M. A. Baki, M. Tyagi, A. Faraone, P. Butler and R. Krishnomorti, *Macro Lett.*, 2014, 2014, 1262-1265.

147. J. M. G. Cowie and V. Arrighi, *Polymers: Chemistry and Physics of Modern Materials*, CRC Press, Boca Raton, Florida, USA, 3rd edn., 2008.

148. W. Zhou, Y. H. Ooi, R. Russo, P. Papanek, D. E. Luzzi, J. E. Fischer, M. J. Bronikowski, P. A. Willis and R. E. Smalley, *Chem. Phys. Lett.*, 2001, 350, 6-14.

149. S. Brand, Masters thesis, University of Pennsylvania, Philadelphia, 2004.

150. PYRIS Thermal Analysis Software (11.0.30.470), Perkin Elmer, 2009.

151. S. M. King, *Small angle neutron scattering*, ISIS Facility, STFC Rutherford Appleton Laboratory, Oxford, UK, 1995.

152. V. Garcia-Sakai, Quasi-elastic neutron scattering, http://www.oxfordneutronschool.org/2013/Lectures/GarciaSakai-QENS.pdf, Accessed 30th October, 2016.

153. G. D. Wignall and Y. B. Melnichenko, *Rep Prog Phys*, 2005, 68, 1761-1810.

154. A. L. Likhtman and T. C. B. McLeish, *Macromolecules*, 2002, 35.

155. ILL, D11 instrument layout, http://www.ill.eu/instruments-support/instruments-groups/instruments/d11/, Accessed 9th January, 2014.

156. LAMP, the Large Array Manipulation Program, http://www.ill.eu/data_treat/lamp/the-lamp-book/.

157. D. Richard, M. Ferrand and G. J. Kearley, *J. Neutron Res.*, 1996, 4, 33-39.

158. M. Bée, *Quasielastic neutron scattering*, Hilger, Bristol, 1988.

159. ISIS, Schematic of IRIS, http://www.isis.stfc.ac.uk/instruments/iris/iris4691.html, Accessed 22 January, 2014.

160. A. Meyer, R. M. Dimeo, P. M. Gehring and D. A. Neumann, *Rev Sci Instrum*, 2003, 74, 2759-2777.

161. NIST, Schematic of HFBS beamline, http://www.ncnr.nist.gov/instruments/hfbs/instr-details.html, Accessed 22 January, 2014.

162. Neutron scattering lengths and cross sections, http://www.ncnr.nist.gov/resources/n-lengths/, Accessed 12th November 2015.

163. I. Grillo, in *Soft Matter Characterisation*, eds. R. Borsali and R. Pecora, Springer, 2008, vol. 1, ch. 13.

164. P. Debye, H. R. Anderson and H. Brumberger, *J. Appl. Phys.*, 1957, 28, 679-683.

165. R. Ryong-Joon, *Methods of X-Ray and Neutron Scattering in Polymer Science*, Oxford University Press, New York, 2000.

166. W. Zhou, M. F. Islam, H. Wang, D. L. Ho, A. G. Yodh, K. I. Winey and J. E. Fischer, *Chem. Phys. Lett.*, 2004, 384, 185-189.

167. D. W. Schaefer, J. Zhao, J. M. Brown, D. P. Anderson and D. W. Tomlin, *Chem. Phys. Lett.*, 2003, 375, 369-375.

168. Origin 8 SR4, v. 8.0951, OriginLab Coporation, MA, USA, 2008.

169. L. J. Fetters, D. J. Lohse, D. Richter, T. A. Witten and A. Zirkel, *Macromolecules*, 1994, 27, 4639-4647.

170. M. Aubouy, G. H. Fredrickson, P. Pincus and E. Raphael, *Macromolecules*, 1995, 28, 2979-2981.

171. F. Akeroyd, S. Ansell, S. Antony, O. Arnold, A. Bekasovs, J. Bilheux, J. Borreguero, K. Brown, A. Buts, S. Campbell, D. Champion, L. Chapon, M. Clarke, S. Cottrell, R. Dalgliesh, D. Dillow, M. Doucet, N. Draper, R. Fowler, M. A. Gigg, G. Granroth, M. Hagen, W. Heller, A. Hillier, S. Howells, S. Jackson, D. Kachere, M. Koennecke, C. Le Bourlot, R. Leal, V. Lynch, P. Manuel, A. Markvardsen, R. McGreevy, D. Mikkelson, R. Mikkelson, R. Miller, S. Nagella, T. Nielsen, K. Palmen, P. G. Parker, M. Pascal, G. Passos, T. Perring, P. F. Peterson, F. Pratt, T. Proffen, P. Radaelli, J. Rainey, S. Ren, M. Reuter, L. Sastry, A. Savici, J. Taylor, R. J. Taylor, M. Thomas, R. Tolchenov, R. Whitley, M. Whitty, S. Williams, W. Zhou and J. Zikovsky, MANTID: Manipulation and Analysis Toolkit for Instrument Data, http://dx.doi.org/10.5286/software/mantid, MANTID Project, 2013.

172. IRIS technical information, http://www.isis.stfc.ac.uk/instruments/iris/technical/iris-technical-information7247.html, Accessed May 2nd, 2016.

173. G. R. Mitchell and A. H. Windle, *Polymer*, 1984, 25, 906-920.

174. M. C. Garcia-Gutierrez, A. Nogales, J. J. Hernandez, D. R. Rueda and T. A. Ezquerra, *Opt. Pura Apl.*, 2007, 40, 195-205.

175. S. M. Kimani, R. L. Thompson, L. R. Hutchings, N. Clarke, S. M. R. Billah, V. Garcia-Sakai and S. E. Rogers, *Macromolecules*, 2014, 47, 2062-2071.

176. High Flux Back Scattering Spectrometer (HFBS) Experiment, https://www.ncnr.nist.gov/summerschool/ss11/pdf/SS2011_StudentPresentation_HFBS.pdf, Accessed May 1st, 2016.

177. P. F. Green and E. J. Kramer, *Macromolecules*, 1986, 19, 1108-1114.

178. F. Kohlrausch, *Pogg. Ann. Physik*, 1863, 119, 352.

179. G. Williams and D. C. Watts, *Trans. Faraday Soc.*, 1970, 66, 80.

180. A. Arbe and J. Colmenero, *Phys. Rev. Lett.*, 1998, 81, 590-593.

181. A. Sanz, A. Nogales, T. A. Ezquerra, W. Haussler, M. Soccio, N. Lotti and A. Munari, *Macromolecules*, 2011, 44, 8124-8128.

182. F. Ganazzoli, G. Raffaini and V. Arrighi, *Phys. Chem. Chem. Phys.*, 2002, 4, 3734-3742.

183. J. Swenson, I. Koper and M. T. F. Telling, *J. Chem. Phys.*, 2002, 116, 5073-5079.

184. G. Arialdi, K. Karatasos, J.-P. Rychaert, V. Arrighi, F. Saggio, A. Triolo, A. Desmedt, J. Pieper and R. E. Lechner, *Macromolecules*, 2003, 36, 8864-8875.

185. V. Bird, *Thesis supplementary data: KWW fits to I(Q,t)*, 2016, doi:10.15128/r2cc08hf608.

186. D. Richter, M. Monkenbusch, A. Arbe and J. Colmenero, *Neutron Spin Echo in Polymer Systems*, Springer-Verlag, Heidelberg, Germany, 2005.

187. V. P. Privalko, *J. Non-Cryst. Solids*, 1999, 255, 259-263.

188. B. Frick, K. Dalnoki-Veress, J. A. Forrest, J. Dutcher, C. Murray and A. Higgins, *Eur. Phys. J. E*, 2003, 12, s93.

189. O. Ahumada, D. N. Theodorou, A. Triolo, V. Arrighi, C. Karatasos and J.-P. Ryckaert, *Macromolecules*, 2002, 35, 7110-7124.

190. M. P. Weir, D. W. Johnson, S. C. Boothroyd, R. C. Savage, R. L. Thompson, S. M. King, S. E. Rogers, K. S. Coleman and N. Clarke, *ACS Macro Lett.*, 2016, 5, 430-434.